THE MINISTRY OF SCIENCE AND HIGHER EDUCATION OF THE RUSSIAN FEDERATION

ST. PETERSBURG STATE POLYTECHNICAL UNIVERSITY JOURNAL

Physics and Mathematics

VOLUME 12, No.2, 2019

Peter the Great St. Petersburg
Polytechnic University
2019

**ST. PETERSBURG STATE POLYTECHNICAL UNIVERSITY JOURNAL.
PHYSICS AND MATHEMATICS**

The journal is included in the List of leading peer-reviewed scientific journals and other editions to publish major findings of theses for the research degrees of Doctor of Sciences and Candidate of Sciences.

The publications are presented in the VINITI RAS Abstract Journal and Ulrich's Periodical Directory International Database.

The journal is published since 2008 as part of the periodical edition 'Nauchno-tekhnicheskie vedomosti SPb-GPU'.

The journal is registered with the Federal Service for Supervision in the Sphere of Telecom, Information Technologies and Mass Communications (ROSKOMNADZOR). Certificate ПИ № ФС77-52144 issued December 11, 2012.

The journal is distributed through the CIS countries catalogue, the «Press of Russia» joint catalogue and the «Press by subscription» Internet catalogue. The subscription index is **71823.**

The journal is in the **Web of Science** (Emerging Sources Citation Index) and the **Russian Science Citation Index** (RSCI) databases.

Address: 195251 Politekhnicheskaya St. 29, St. Petersburg, Russia.

Phone: (812) 294-22-85.

http://ntv.spbstu.ru/physics

МИНИСТЕРСТВО НАУКИ И ВЫСШЕГО ОБРАЗОВАНИЯ РОССИЙСКОЙ ФЕДЕРАЦИИ

НАУЧНО-ТЕХНИЧЕСКИЕ ВЕДОМОСТИ

САНКТ-ПЕТЕРБУРГСКОГО ГОСУДАРСТВЕННОГО ПОЛИТЕХНИЧЕСКОГО УНИВЕРСИТЕТА

Физико-математические науки

ТОМ 12, №2

2019

Санкт-Петербургский политехнический
университет Петра Великого
2019

НАУЧНО-ТЕХНИЧЕСКИЕ ВЕДОМОСТИ САНКТ-ПЕТЕРБУРГСКОГО ГОСУДАРСТВЕННОГО ПОЛИТЕХНИЧЕСКОГО УНИВЕРСИТЕТА. ФИЗИКО-МАТЕМАТИЧЕСКИЕ НАУКИ

Журнал с 2002 г. входит в Перечень ведущих рецензируемых научных журналов и изданий, в которых должны быть опубликованы основные результаты диссертаций на соискание ученых степеней доктора и кандидата наук.

Сведения о публикациях представлены в Реферативном журнале ВИНИТИ РАН, в международной справочной системе «Ulrich's Periodical Directory».

С 2008 года выпускается в составе сериального периодического издания «Научно-технические ведомости СПбГПУ».

Журнал зарегистрирован Федеральной службой по надзору в сфере информационных технологий и массовых коммуникаций (Роскомнадзор). Свидетельство о регистрации ПИ № ФС77-52144 от 11 декабря 2012 г.

Распространяется по Каталогу стран СНГ, Объединенному каталогу «Пресса России» и по Интернет-каталогу «Пресса по подписке». Подписной индекс **71823**.

Журнал индексируется в базе данных **Web of Science** (Emerging Sources Citation Index), а также включен в базу данных **«Российский индекс научного цитирования»** (РИНЦ), размещенную на платформе Научной электронной библиотеки на сайте

http://www.elibrary.ru

При перепечатке материалов ссылка на журнал обязательна.

Точка зрения редакции может не совпадать с мнением авторов статей.

Адрес редакции и издательства:

Россия, 195251, Санкт-Петербург, ул. Политехническая, д. 29.

Тел. редакции (812) 294-22-85.

http://ntv.spbstu.ru/physics

Contents

Simulation of physical processes

Mathematical physics

Experimental technique and devices

Biophysics and medical physics

Nuclear physics

Mechanics

Содержание

Математическое моделирование физических процессовя

Математическая физика

Приборы и техника физического эксперимента

Биофизика и медицинская физика

Ядерная физика

Механика

DOI: 10.18721/JPM.12201
УДК 519.6:533.6.011

NUMERICAL SOLUTION OF A 3D PROBLEM ON A SUPERSONIC VISCOUS GAS FLOW PAST A PLATE-CYLINDRICAL BODY JUNCTION AT M 2.95

E.V. Kolesnik, E.M. Smirnov, A.A. Smirnovsky

Peter the Great St. Petersburg Polytechnic University, St. Petersburg, Russian Federation

In the paper, results of numerical simulation of a shock-wave pattern and vortex structures forming in supersonic flow past an adjacent-to-plate elongate cylindrical body, which penetrates the developing flat-plate boundary layer, have been presented. The laminar flow regime at Mach number 2.95 was considered, Reynolds number was taken 4000. The solutions were obtained using two schemes for convective flux (HLL and AUSM). Comparison of the flow fields computed with the mentioned schemes of the first and second orders of accuracy were conducted. Solution mesh sensitivity issues were discussed.

Keywords: high-speed flow, viscous-inviscid interaction, numerical simulation, AUSM and HLL schemes

Citation: Kolesnik E.V., Smirnov E.M., Smirnovsky A.A., Numerical solution of a 3D problem on a supersonic viscous gas flow past a plate-cylindrical body junction at M 2.95, St. Petersburg Polytechnical State University Journal. Physics and Mathematics. 12 (2) (2019) 7–22. DOI: 10.18721/JPM.12201

ЧИСЛЕННОЕ РЕШЕНИЕ ТРЕХМЕРНОЙ ЗАДАЧИ ОБТЕКАНИЯ УСТАНОВЛЕННОГО НА ПЛАСТИНЕ ЦИЛИНДРИЧЕСКОГО ТЕЛА СВЕРХЗВУКОВЫМ ПОТОКОМ ВЯЗКОГО ГАЗА ПРИ М = 2,95

Е.В. Колесник, Е.М. Смирнов, А.А. Смирновский

Санкт-Петербургский политехнический университет Петра Великого,
Санкт-Петербург, Российская Федерация

Представлены результаты численного моделирования ударно-волновых и вихревых структур, которые формируются при обтекании сверхзвуковым потоком удлиненного цилиндрического тела, которое примыкает к пластине и пронизывает развивающийся на пластине пограничный слой. Рассмотрен ламинарный режим течения при числе Маха набегающего потока, равном 2,95, и числе Рейнольдса, равном 4000. Решения получены с использованием двух схем для расчета конвективных потоков (HLL и AUSM). Проведено сравнение полей течения, рассчитанных с применением указанных численных схем первого и второго порядков точности. Обсуждаются вопросы сходимости численного решения по сетке.

Ключевые слова: высокоскоростное течение, вязко-невязкое взаимодействие, численное моделирование, схема AUSM, схема HLL

Ссылка при цитировании: Колесник Е.В., Смирнов Е.М., Смирновский А.А. Численное решение трехмерной задачи обтекания установленного на пластине цилиндрического тела сверхзвуковым потоком вязкого газа при М = 2,95// Научно-технические ведомости СПбГПУ. Физико-математические науки. 2019. Т. 12. № 2. С. 7–22. DOI: 10.18721/JPM.12201

Introduction

Practical problems of the aerospace industry and turbomachinery often involve studies on the structure of subsonic and supersonic flows around structural elements fixed on the streamlined surface. This includes, in particular, design of connections between wings, fuselage, tail and other elements, and optimization of interaction of supersonic flow with injected gas jets used in control elements.

Keen interest in this type of problems was instigated by development of supersonic and hypersonic aircraft construction started in the mid-20th century. One of the challenging tasks here is three-dimensional flow with a complex shock-wave structure, a wide separation region and a system of horseshoe-shaped vortices that takes place in supersonic viscous gas flow around the junction of a blunt body with a plate. In other words, the effects of viscous-inviscid interaction in supersonic flow of viscous gas can be clearly observed in this problem.

On the whole, sufficient detailed information has been ~~collected~~ obtained in recent years for the case of the interaction of a separating boundary layer with a bow shock. Reviews of literature on this topic can be found, for example, in [1, 2].

A case of a separation region forming in front of the body in subsonic flow is also of interest. For instance, this applies to problems of turbomachine engineering, where understanding the complex vortex structure of the flow near the leading edge of the blade is important for taking into account the heat transfer patterns in the region of the blade/endwall junction in ~~disks~~ vanes of high-temperature gas turbines. Many studies, both experimental and computational, have been dedicated to studying the flow structure in subsonic regime (see, for example, [3–6]).

The subject of this study is one of the model problems simulating the complex structure of three-dimensional flow. We have considered supersonic flow around an elongated cylindrical body mounted on a plate along which the boundary layer evolves (Fig. 1). A fairly large number of experimental works [7–13] addressed this problem. Some of the earliest studies of the flow structure in this configuration [7–9] revealed that local supersonic regions and bow shocks, inducing a secondary separation region inside the main zone, evolve in front of the cylindrical body.

One of the most important characteristic for high-speed aircraft is the intensity of heat transfer in front of the streamlined body; studies indicate strong intensification of heat transfer in this region. In particular, a recently published paper [13] considered local heat transfer on a plate with flow around a cylindrical body at a Mach number of 5.

It is rather problematic to experimentally obtain sufficient data on the detailed structure of three-dimensional supersonic flow in the entire region where it develops. For this reason, it would be of great interest to be able to predict the flow structure in the given model configuration based on computational fluid dynamics, providing high quality of resolution for the regions with viscous-inviscid interaction. The first studies on numerical simulation of laminar and turbulent flows in the given configuration [14, 15] used computational meshes that could not provide sufficient resolution of all flow features. A relatively recent work [16], detailing extensive study (both experimental and numerical) of the flow around a blunt body at Mach number M = 6.7 was performed, established, for example, that a sufficiently accurate resolution of the flow structure is obtained with a mesh size of about 15 million cells.

Numerical simulation of supersonic flow under given conditions may be complicated by the so-called carbuncle instability [17, 18], which leads to strong distortion of bow shock in the numerical solution. This instability may occur when using several well-known numerical schemes; different approaches (in particular,

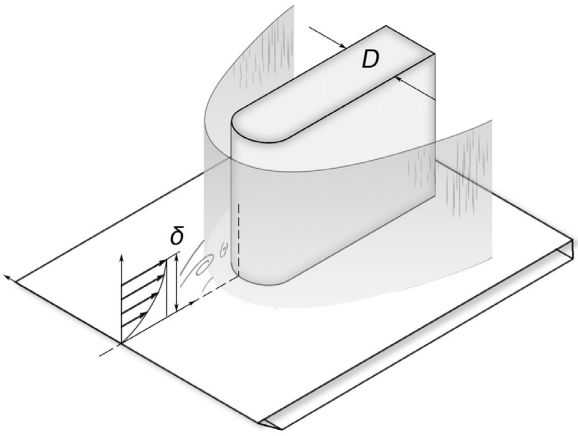

Fig. 1. Schematic representation of problem statement: viscous gas flow around elongated cylindrical body with diameter D of blunt part, mounted on plate; boundary layer develops along the plate (δ is the thickness of this layer)

hybrid schemes [18, 16] and introduction of additional artificial viscosity [19]) have been devised to suppress it. There are also schemes where the carbuncle instability is usually not observed. These include the Harten–Lax–van Leer (HLL) scheme [20], which is characterized by high dissipativity, and a family of schemes based on s flux vector splitting, proposed by Liou and Steffen (Advection Upstream Splitting Method (AUSM)) [21], which many authors have found to be stable to non-physical oscillations on the bow shock.

The majority of published works on numerical solution to the problem of high-speed flow of viscous gas around a blunt body mounted on a plate considered a case of hypersonic flow. However, little attention has been paid in literature to flows with moderate free-stream Mach numbers and the quality of numerical prediction of the effects of viscous-inviscid interaction.

In this paper, we present the results of a numerical solution to the problem of flow past an elongated blunt body mounted on a plate, with the free-stream Mach number equal to 2.95, and the Reynolds number based on the diameter of the blunt part equal to 4000. A moderate Reynolds number, ensuring laminar flow in the given region, was chosen because we focused on obtaining an accurate, almost grid-converged solution, with detailed resolution of both the complex structure of the flow in the viscous separation region with a system of horseshoe-shaped vortices, and the gas-dynamic structure characterized by detached shock and a system of oblique compression waves generated by flow around the separation region.

Numerical solutions were obtained by two schemes, HLL and AUSM; both of them allowed to avoid the carbuncle instability. Additionally, we have carried out comparative analysis of the solutions.

Numerical method for solving the problem

General formulation. The following numerical solutions for viscous gas flow were obtained using the finite volume method (FVM), based on integral formulation of the laws of conservation of mass, momentum and energy, as applied to computational cell (control volume):

$$\int_{\Omega} \frac{\partial \mathbf{w}}{\partial \tau} d\Omega + \sum_{M} \int_{S_m} \mathbf{F}^{\Sigma} dS = 0, \qquad (1)$$

where Ω is the control volume; M is the number of its faces; S_m is the area of the current face, m $= \overline{1,M}$, $\mathbf{F}^{\Sigma}$ is the vector of the fluxes on the face of the control volume; w = [ρ,ρu,ρv,ρw,ρE] is the vector of conservative variables ($u \equiv u_1$, $v \equiv u_2$, $w \equiv u_3$ are the components of the velocity vector **V** in the Cartesian coordinate system; E is the total energy; ρ is the density).

The vector $\mathbf{F}^{\Sigma}$ is the sum of vectors of inviscid and viscous fluxes $\mathbf{F}^{\Sigma} = \mathbf{F} + \mathbf{F}^{visc}$, defined by the expressions:

$$\mathbf{F} = \begin{bmatrix} \rho \mathbf{V} \cdot \mathbf{n} \\ \rho \mathbf{V} \cdot \mathbf{n} u + p \mathbf{n} \cdot \mathbf{i} \\ \rho \mathbf{V} \cdot \mathbf{n} v + p \mathbf{n} \cdot \mathbf{j} \\ \rho \mathbf{V} \cdot \mathbf{n} w + p \mathbf{n} \cdot \mathbf{k} \\ \rho \mathbf{V} \cdot \mathbf{n} H \end{bmatrix}, \qquad (2)$$

$$\mathbf{F}^{visc} = \begin{bmatrix} 0 \\ \mathbf{n} \cdot \boldsymbol{\tau} \cdot \mathbf{i} \\ \mathbf{n} \cdot \boldsymbol{\tau} \cdot \mathbf{j} \\ \mathbf{n} \cdot \boldsymbol{\tau} \cdot \mathbf{k} \\ \mathbf{n} \cdot (\boldsymbol{\tau} \cdot \mathbf{V} + \mathbf{q}) \end{bmatrix}, \qquad (2)$$

where p is the pressure; H is the total enthalpy; **n** is the normal to the face; **i**, **j**, **k** are the unit vectors of the Cartesian coordinate system ($x \equiv x_1$, $y \equiv x_2$, $z \equiv x_3$).

The components of the viscous stress tensor $\boldsymbol{\tau}$ and the heat flux density vector **q** are written as

$$\tau_{ij} = \mu \left[\left(\frac{\partial u_i}{\partial x_j} + \frac{\partial u_j}{\partial x_i} \right) - (2/3) \frac{\partial u_k}{\partial x_k} \delta_{ij} \right], \qquad (3)$$

$$q_j = -\lambda \left(\partial T / \partial x_j \right), \qquad (4)$$

where T is the temperature; μ is the dynamic viscosity of the gas whose dependence on temperature is determined by the Sutherland formula; λ is the thermal conductivity of the gas.

The total energy and enthalpy are determined by the expressions:

$$E = c_v T + V^2/2, \; H = c_p T + V^2/2,$$

where cv, cp are the specific heat capacities at constant volume and constant pressure,

respectively; they are assumed to be constant.

Pressure p, density ρ and internal energy e are related by the equation of state of a perfect gas:

$$p = (\gamma - 1)\rho e,$$

where γ is the adiabatic index ($\gamma = cp/cv$).

Simulation schemes for convective flows. The method for inviscid fluxes $\mathbf{F}$ approximation is especially important in simulation of supersonic flows. The approximation scheme should provide sufficiently accurate resolution of gas dynamic discontinuities with a small number of internal points in the absence of flow field oscillations near the discontinuities. The methods with desired behavior, which are based on characteristic properties of the system of equations, have gained great popularity over the past decades [22]. These include flux vector splitting schemes (for example, the Steger–Warming splitting scheme, the AUSM method), and schemes based on the Riemann solver for the discontinuity problem (for example, Godunov, Roe, HLL and HLLC schemes). Below, we consider ~~in detail~~ only the AUSM and HLL schemes selected for our computations.

Parameters for the "left" and "right" sides of a given face are widely used in flux computations (denoted by subscripts L and R below). If values from the centers of adjacent cells are used as such parameters, the numerical method is of the first order of accuracy. Special methods for evaluating the parameters to the left and right of the face (briefly discussed below) can be used to implement schemes with a higher order of accuracy.

AUSM scheme [21]. The flux vector $\mathbf{F}$ is represented as the sum of $\mathbf{F}^{(c)}$ (convective component) and $\mathbf{F}^{(p)}$ (component related to pressure):

$$\mathbf{F} = \begin{bmatrix} \rho\mathbf{V}\cdot\mathbf{n} \\ \rho\mathbf{V}\cdot\mathbf{n}u + p\mathbf{n}\cdot\mathbf{i} \\ \rho\mathbf{V}\cdot\mathbf{n}v + p\mathbf{n}\cdot\mathbf{j} \\ \rho\mathbf{V}\cdot\mathbf{n}w + p\mathbf{n}\cdot\mathbf{k} \\ \rho\mathbf{V}\cdot\mathbf{n}H \end{bmatrix} = \begin{bmatrix} \rho\mathbf{V}\cdot\mathbf{n} \\ \rho\mathbf{V}\cdot\mathbf{n}u \\ \rho\mathbf{V}\cdot\mathbf{n}v \\ \rho\mathbf{V}\cdot\mathbf{n}w \\ \rho\mathbf{V}\cdot\mathbf{n}H \end{bmatrix} + \begin{bmatrix} 0 \\ p\mathbf{n}\cdot\mathbf{i} \\ p\mathbf{n}\cdot\mathbf{j} \\ p\mathbf{n}\cdot\mathbf{k} \\ 0 \end{bmatrix} = \mathbf{F}^{(c)} + \mathbf{F}^{(p)}. \quad (5)$$

Accordingly, $\mathbf{F}_f$ (numerical flux on the face) is also found as the sum:

$$\mathbf{F}_f = \mathbf{F}_f^{(c)} + \mathbf{F}_f^{(p)}. \quad (6)$$

A specific splitting method is used for each of the components.

The convective flux $\mathbf{F}^{(c)}$ is expressed in terms of the Mach number M constructed from the normal velocity component:

$$\mathrm{M} = \mathbf{V}\cdot\mathbf{n}/a,$$

where $a = \sqrt{\gamma RT}$ is the speed of sound (R is the gas constant):

$$\mathbf{F}^{(c)} = \mathrm{M}\begin{bmatrix} \rho a \\ \rho a u \\ \rho a v \\ \rho a w \\ \rho a H \end{bmatrix} \equiv \mathrm{M}\hat{\mathbf{F}}^{(c)}. \quad (7)$$

Splitting of the convective flux is based on the sign of the Mach number at the face M_f in the following manner:

$$\mathbf{F}_f^{(c)} = \begin{cases} \mathrm{M}_f\left[\hat{\mathbf{F}}^{(C)}\right]_L, & \mathrm{M}_f \geq 0, \\ \mathrm{M}_f\left[\hat{\mathbf{F}}^{(C)}\right]_R, & \mathrm{M}_f < 0. \end{cases} \quad (8)$$

The Mach number at the face is found as the sum of the positive and negative components:

$$\mathrm{M}_f = \mathrm{M}_L^+ + \mathrm{M}_R^-,$$

where the splitting into components is carried out using the following relationship:

$$\mathrm{M}_{L/R}^{\pm} = \begin{cases} \pm\frac{1}{4}(\mathrm{M}_{L/R} \pm 1)^2, |\mathrm{M}_{L/R}| \leq 1; \\ \frac{1}{2}(\mathrm{M}_{L/R} \pm |\mathrm{M}_{L/R}|), |\mathrm{M}_{L/R}| > 1. \end{cases} \quad (9)$$

The component of the flux related to pressure is defined as

$$\mathbf{F}_f^{(\mathrm{p})} = \left(p_L^+ + p_R^-\right)\begin{bmatrix} 0 \\ \mathbf{n}\cdot\mathbf{i} \\ \mathbf{n}\cdot\mathbf{j} \\ \mathbf{n}\cdot\mathbf{k} \\ 0 \end{bmatrix}, \quad (10)$$

where the splitting of pressure into the positive and the negative component is also carried out depending on the Mach number:

$$p_{L/R}^{\pm} = \begin{cases} \pm \dfrac{p_{L/R}}{4}(\mathrm{M}_{L/R} \pm 1)^2 (2 \mp \mathrm{M}_{L/R}), \\ |\mathrm{M}_{L/R}| \le 1; \\ \dfrac{p_{L/R}}{2} \dfrac{(\mathrm{M}_{L/R} \pm |\mathrm{M}_{L/R}|)}{\mathrm{M}_{L/R}}, \\ |\mathrm{M}_{L/R}| > 1. \end{cases} \quad (11)$$

HLL scheme [20]. The scheme is based on the approximate Riemann solver for the discontinuity problem. It is assumed that the solution consists of two main discontinuities describing the propagation only of strong waves such as shock waves; other waves, such as contact or tangential discontinuities, are not taken into account.

The velocities of the main discontinuities (characteristics) S_L and S_R comprising solution are defined by the following expressions [23]:

$$S_L = \min\left(\mathbf{V}_L \cdot \mathbf{n} - a_L, \tilde{\mathbf{V}} \cdot \mathbf{n} - \tilde{a}\right), \quad (12)$$

$$S_R = \min\left(\mathbf{V}_R \cdot \mathbf{n} + a_R, \tilde{\mathbf{V}} \cdot \mathbf{n} + \tilde{a}\right), \quad (13)$$

where a_L and a_R are the speeds of sound computed by the parameters on the left and right sides of the face; the quantities $\tilde{a}$ and $\tilde{\mathbf{V}}$ are the variables computed for the current face by means of Roe averaging [24].

According to the approximate Riemann solver [20], the characteristics of S_L and S_R are separated from each other by three regions with constant gas parameters on the x–t diagram: two regions with undisturbed gas parameters "left" and "right" from the face, and the third region between them.

Numerical flux on the face depends on the configuration corresponding to the current face:

$$\mathbf{F}_f = \begin{cases} \mathbf{F}_L, \ 0 \le S_L; \\ \mathbf{F}^*, \ S_L \le 0 \le S_R; \\ \mathbf{F}_R, \ 0 \ge S_R, \end{cases} \quad (14)$$

where the flux $\mathbf{F}^*$ is found by the formula

$$\mathbf{F}^* = \frac{S_R \mathbf{F}_L - S_L \mathbf{F}_R + S_L S_R (\mathbf{w}_R - \mathbf{w}_L)}{S_R - S_L}. \quad (15)$$

Increasing the order of accuracy. The order of accuracy of a numerical scheme can be increased with a technique for quasi-monotonic interpolation of mesh solutions: the MUSCL approach (Monotonic Upstream-Centered Scheme for Conservation Laws) [25], which is used for piecewise polynomial reconstruction of the solution in each control volume and

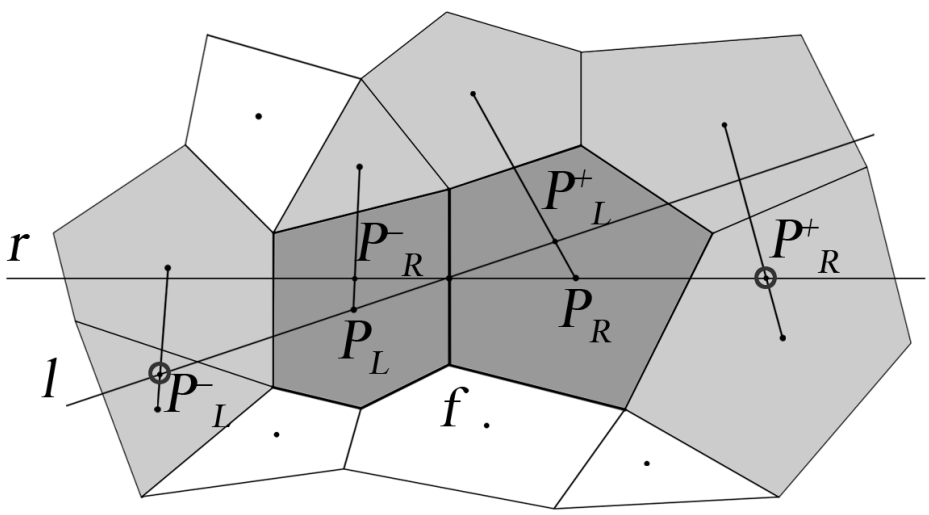

Fig. 2. Scheme for constructing algorithm for quasi-one-dimensional computations in two-dimensional case;
left and right cells adjacent to the given face f are highlighted in dark gray, all stencil cells used for determining the values at additional points (notations are given for them) are highlighted in light gray; r, l are direct reconstructions for face f

for reconstruction of the values on the face with increased accuracy. Total Variation Diminishing schemes (TVD) are applied to obtain monotonous solutions in computations by second-order accuracy schemes [26]. This approach can be generalized to the case of unstructured meshes by applying quasi-one-dimensional computations with some suitable direction (similar to the coordinate direction initially present in structured meshes) selected locally for each face. In other words, aside from the values of the variables in the centers of the cells located on both sides of the face, at least two more virtual points to the left and right of the center points (points P_L^+, P_L^-, P_R^+ and P_L^- in Fig. 2) are required, in which the values of variables can be reconstructed in some way.

The numerical solutions given below were obtained using the approach proposed in [27] and described in detail in [28]. Two straight lines (reconstruction beam) are drawn through the center of each face f and through the centers of the cells adjacent to the face (direct reconstructions are l and r in Fig. 2); two additional points are taken on each of these straight lines, with the values of the variables in these points ~~found~~ evaluated by interpolation based on the known values of the variables in certain neighboring centers of the cells (“interpolating triples”).

Such cells are found by the following algorithm [28]: first, a set N_1 is established, including all first-level neighbors for the current cell, i.e., the set of cells that have at least one common node with the current cell, excluding the cell itself. Next, all cells from the set N_1 are sorted by ascending cosine of the angle between the reconstruction beam emanating from the center of the current cell and the vector of direction to the center of the cell from this set. Next, an iterative search of the cell triplets is performed in ascending order of the sum of the indices of these cells in the sorted array and the first of the “interpolating triplets” found is used. By interpolating triplet we mean a triplet of cells whose centers form a triangle and the straight line of reconstruction intersects it.After the values at additional points have been computed, the values on the left and right sides of the face are found in accordance with one-sided linear extrapolation:

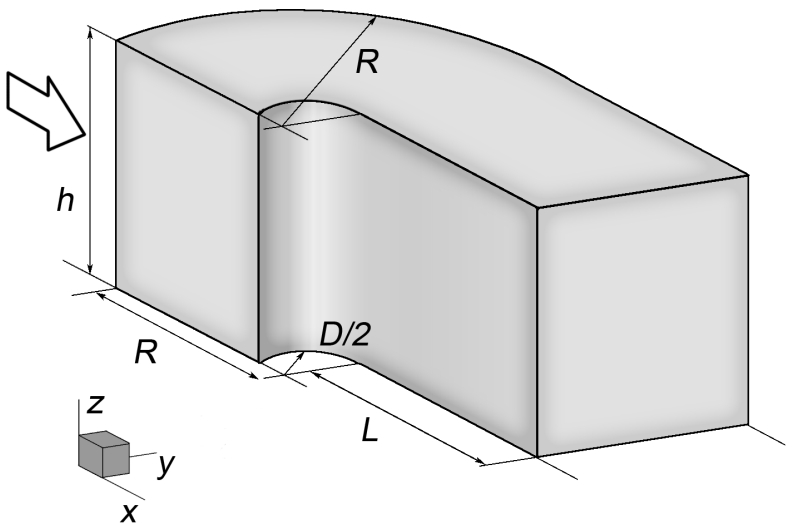

Fig. 3. Computational domain for problem of supersonic flow around elongated cylindrical body (see Fig. 1).
The figure shows the geometrical parameters: D is the diameter of the blunt part of the body, R, L, h are the dimensions of the computational domain, the arrow indicates the direction of the flux

$$u_L^f = u_L + \psi_L \left(u_L - u_L^-\right)/2, \quad (16)$$

$$u_R^f = u_R - \psi_R \left(u_R^+ - u_R\right)/2, \quad (17)$$

where u is any of the reconstructed variables; $\psi(r)$ is the limiter introduced to control oscillations and computed as a function of the ratio of two differences:

$$\psi_L = \psi_L \left(\left(u_L^+ - u_L\right)/\left(u_L - u_L^-\right)\right), \quad (18)$$

$$\psi_R = \psi_R \left(\left(u_R^- - u_R\right)/\left(u_R - u_R^+\right)\right). \quad (19)$$

We used Van Albada's TVD-limiter [29] as the function ψ in these computations.

Problem statement and computational tools

Fig. 3 shows the computational domain for the given problem of supersonic flow past an elongated cylindrical body mounted on an adiabatic plate along which a laminar boundary layer evolves. The flow is assumed to be symmetrical, so the computational domain covers only half of the initial configuration. The dimensions of the region are: $R = 15D$, $h = 10D$, $L = 8D$, where D is the diameter of the blunt part of the body, also assumed to be adiabatic.

The problem is governed by the following set of dimensionless parameters: the free-stream Mach number M, the Reynolds number Re_D, the Prandtl number Pr, the adiabatic index γ and the ratio D/δ of the body's diameter to the thickness of the incoming boundary layer. The numerical solutions in this study were obtained for M = 2.95, $\mathrm{Re}_D = 4000$, Pr = 0.71, $\gamma = 1.4$, $D/\delta_{95\%} = 1$. Velocity and temperature profiles for the boundary layer of a given thickness $\delta_{95\%}$ were prescribed at the inlet boundary of the computational domain.

We have implemented the above-described numerical method in combination with the implicit scheme in "increments" as one of the options of the finite-volume unstructured ~~program~~ code SINF/Flag-S, which is under development at the Hydroaerodynamics, Combustion and Heat Transfer Department of Peter the Great St. Petersburg Polytechnic University.

The resources of the Polytechnic Supercomputer Center (www.scc.spbstu.ru) were used for computations.

Computation results and discussion

Flow structure. The numerical solution obtained by the AUSM scheme on the most refined of the meshes used is shown in Figs. 4–6 (the issues of grid-converged solution are discussed below). In general, the structure of the computed flow field is similar to that described

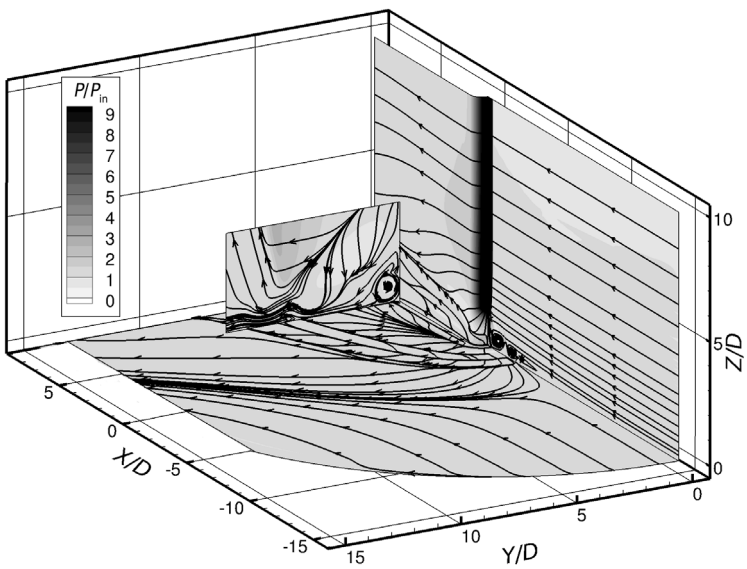

Fig. 4. Surface streamlines and flow structure in axial (*XZ* plane) and transverse (*XY*) cross-sections of flow. Pressure distributions in these cross sections and on the surface of the streamlined body are also shown

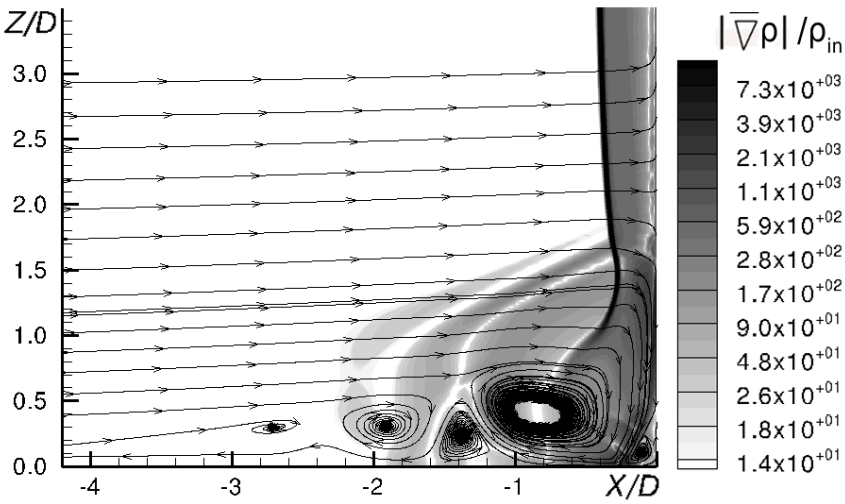

Fig. 5. Density gradient field and streamlines in symmetry plane.
The figure shows values of the density gradient, computed by differentiation from dimensionless coordinates and corresponding to free-stream densities ρ_{in}

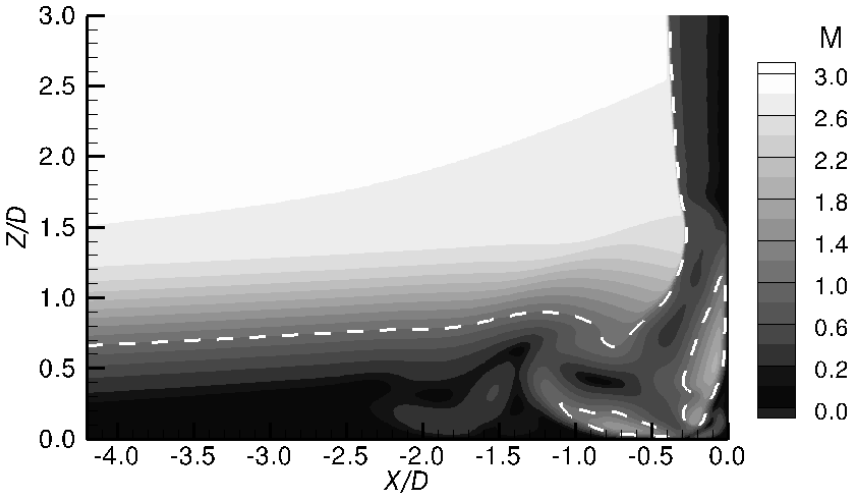

Fig. 6. Field of Mach number in symmetry plane;
dashed line indicates sonic line M = 1

earlier in studies carried out for higher Mach and Reynolds numbers [15, 16]. A bow shock that occurs in front of the body interacts with the boundary layer, causing it to separate. The separation region induces oblique compression waves intersecting with the bow shock. Zones with supersonic velocities and local compression waves appear within the separation region, inducing secondary separation of the near-wall flow. As a result, an extended separation region with a chain of vortices evolves in front of the body, each of them becomes the "head" of a horseshoe-shaped vortex that surrounds the body.

The surface streamlines in Fig. 4 indicate the regions where the boundary layer separates and reattaches. The figure also shows the pressure distribution (related to the free-stream pressure value P_{in}). In particular, it can be seen that maximum pressure in the frontal part of the streamlined body exceeds the inlet pressure by about ten times.

More detailed visualization of the flow in the symmetry plane is given in Fig. 5, illustrating the

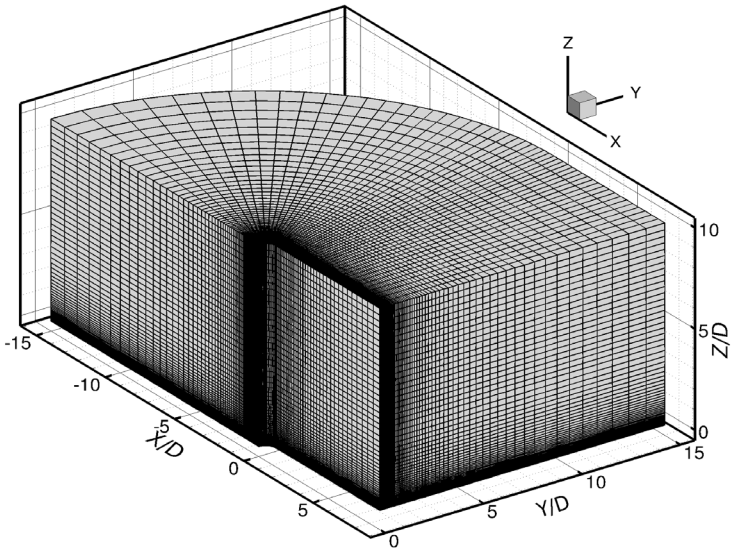

Fig. 7. Computational mesh 1, containing 0.3 million cells
(see the explanations in the text)

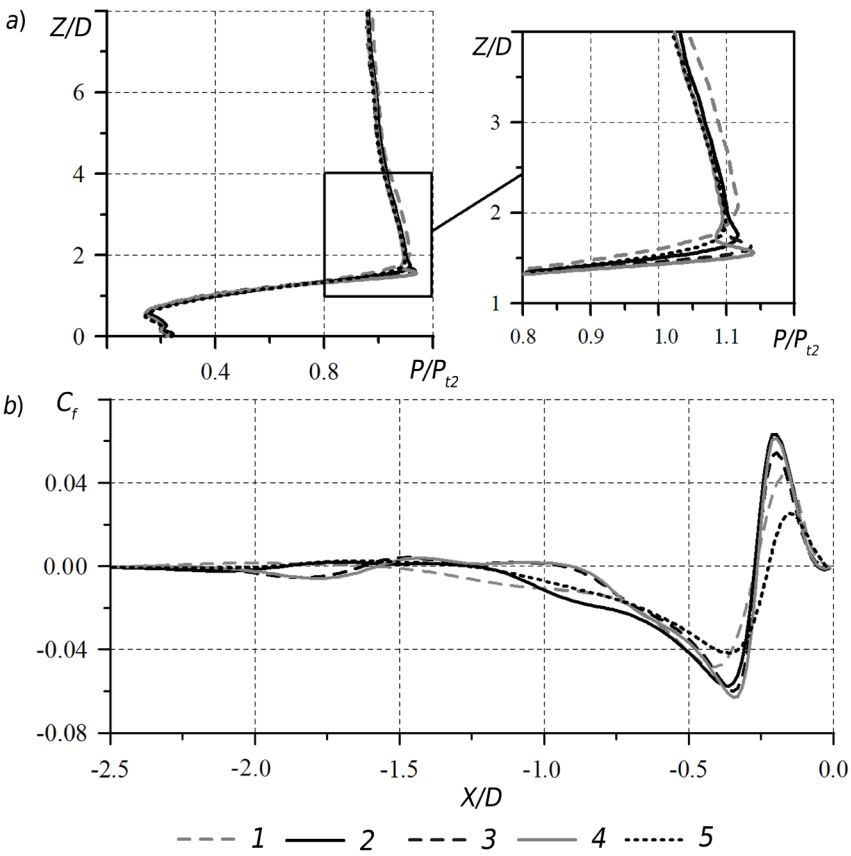

Fig. 8. Distributions of dimensionless pressure along frontal line (*a*)
and skin friction coefficient on plate along line of symmetry (*b*)
The figure shows computations by the AUSM scheme of second order of accuracy on meshes 1–4
(curve numbers coincide with mesh numbers) and first order of accuracy on mesh 4 (curve *5)*

shock wave structure with the density gradient field, combined with streamline patterns for the evolution of a vortex chain in the separation region. Analysis of the figure shows that the vortices filling the separation region induce oblique compression waves interacting with the bow shock. As a result of this interaction, the bow shock bends in the direction of the streamlined body, and a gas jet forms; as it flows onto the body, a zone of local pressure increasing arise. This effect is discussed in more detail below.

Fig. 6 shows the Mach number distribution in the symmetry plane; the dashed line indicates the sonic line (M = 1). While the flow is mainly subsonic in the ~~separated~~ separation region, two zones with supersonic flow are also observed. The flow moving from the stagnation region along the surface of the streamlined body towards the plate accelerates to supersonic speeds and then turns into a vortex, also reaching supersonic speed.

Mesh convergence. The study of mesh convergence was carried out using several quasi-structured meshes: mesh 1 contained 0.3 million cells, mesh 2 2.4 million cells, mesh 3 8.1 million cells and mesh 4 13.3 million cells. Mesh 2 was constructed by refining mesh 1 twice in each coordinate direction, mesh 3 by refining mesh 2 1.5 times, mesh 4 by refining mesh 3 only near the leading edge of the body (from 0 to 2.5 along the Z/D coordinate and from 2 to 0 along the X/D coordinate). All meshes had the same structure, with the mesh lines clustered to the streamlined body and to the surface of the plate. A general view of computational mesh 1 is shown in Fig. 7.

Fig. 8 shows the results obtained by the AUSM scheme using different meshes, including the pressure distribution along a front line on the surface of the body, and the distribution of the skin friction on the plate along a line of symmetry (the pressure was taken as the total pressure P_{t2} behind a normal shock wave, computed analytically). Notably, a characteristic increase in pressure was observed in the region at $Z/D \approx 1.5$, which is associated with a gas jet forming during the interaction of oblique compression waves with the bow shock. It is also interesting that the scheme with first-order accuracy does not reproduce this characteristic pressure peak even on the most refined mesh; this is primarily due to insufficient resolution of oblique compression waves. Moreover, a first-order scheme predicts a substantially simpler vortex structure of the separation region in front of the body.

The solution obtained on mesh 3 is very close to that obtained on mesh 4, both with respect to the pressure distribution and skin friction on the plate. This allows us to conclude that if schemes with second-order accuracy are used, mesh 4 is sufficiently refined for resolving all the details of the vortex structure near the junction between the body and the plate and also provides high-quality resolution of the shock-wave structure.

Comparison of solutions obtained by different schemes

Comparative computations were carried out on the most refined mesh (mesh 4) using the HLL and AUSM schemes of the first and second orders of accuracy. The most convenient way to compare the results obtained using different schemes is to analyze pressure distributions along selected lines on the streamlined body, as well as the predicted distributions of the skin friction along individual lines on the plate surface. The lines selected for analysis are shown in Fig. 9, and the distributions compared in Figs. 10 and 11.

Because schemes with first-order accuracy are highly dissipative, the solutions obtained by first-order and second-order schemes differ quite considerably in individual regions of the flow, both in the case of AUSM and in the case of the HLL scheme. Notably, however, the first-order AUSM scheme is fairly adequate in reproducing the shock-wave structure of the flow on the most refined mesh. Fig. 10 shows, in particular, that the pressure distribution over the body surface, obtained by the first-order AUSM scheme, is close to that computed by the second-order scheme (except for certain local regions); on the other hand, solution obtained with first-order HLL scheme strongly differs in the form.

Regarding the quality of viscous effects resolution ~~of viscous effects~~, as noted above, the first-order AUSM scheme turns out to be too dissipative: using it results in a decreased number of resolved vortices that have reduced intensities even in case of the most refined mesh (see. Fig. 11). Using the first-order HLL scheme yields even less acceptable results: a completely different level of friction is predicted on a large part of the plate (see Fig. 11). While the results obtained by the AUSM and HLL schemes of the second order of accuracy are fairly close, there are also some local differences. In particular, it follows from analysis of the pressure

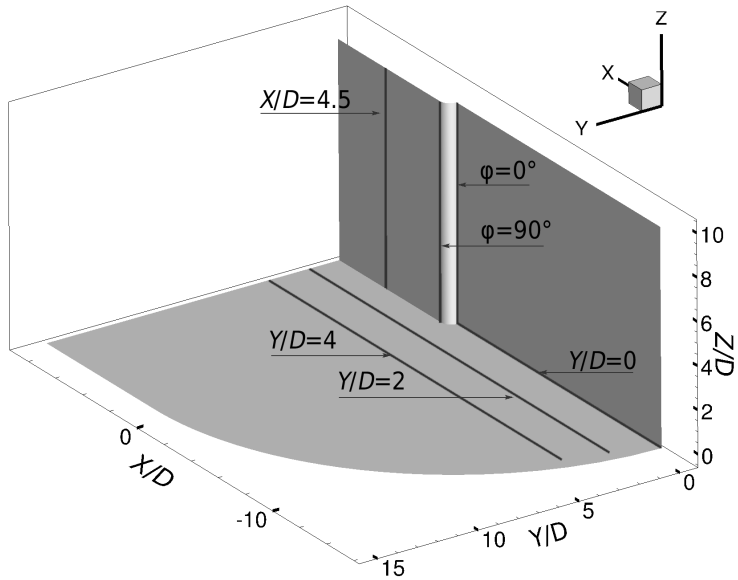

Fig. 9. Position of streamlines on body, selected for analysis of computed pressure and skin friction distributions
(see comparative analysis in Figs. 10, 11)

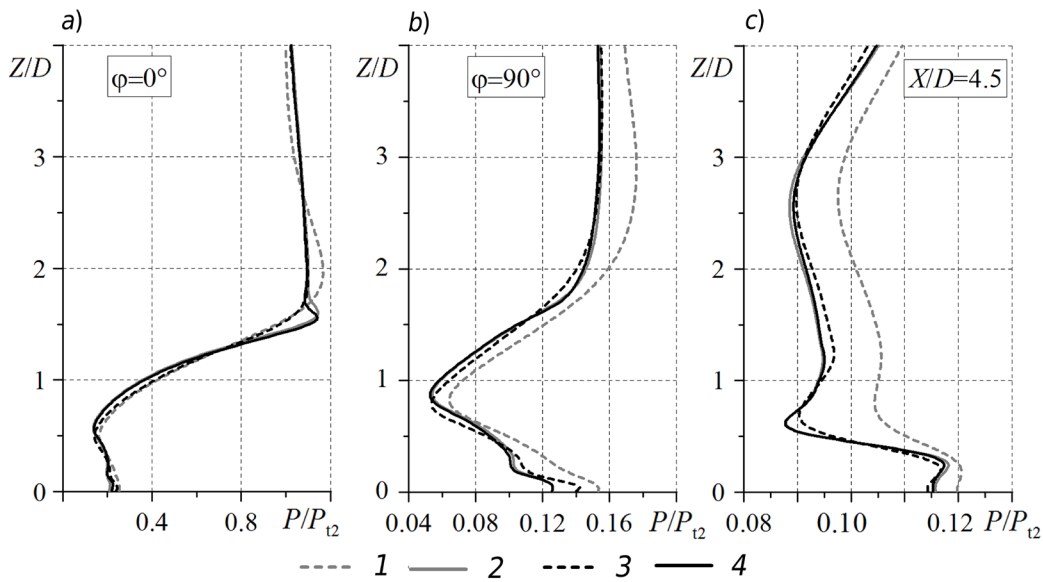

Fig. 10. Distributions of dimensionless pressure along vertical lines on surface of streamlined body (see Fig. 9): on frontal line (φ = 0°) (*a*), at the end of blunt part (φ = °90) (*b*), downstream (*X*/*D*) = 4.5 (*c*)
Computations were carried out by different schemes:
1, *2* correspond to HLL of first and second orders of accuracy, respectively;
3, *4* to AUSM of first and second orders of accuracy

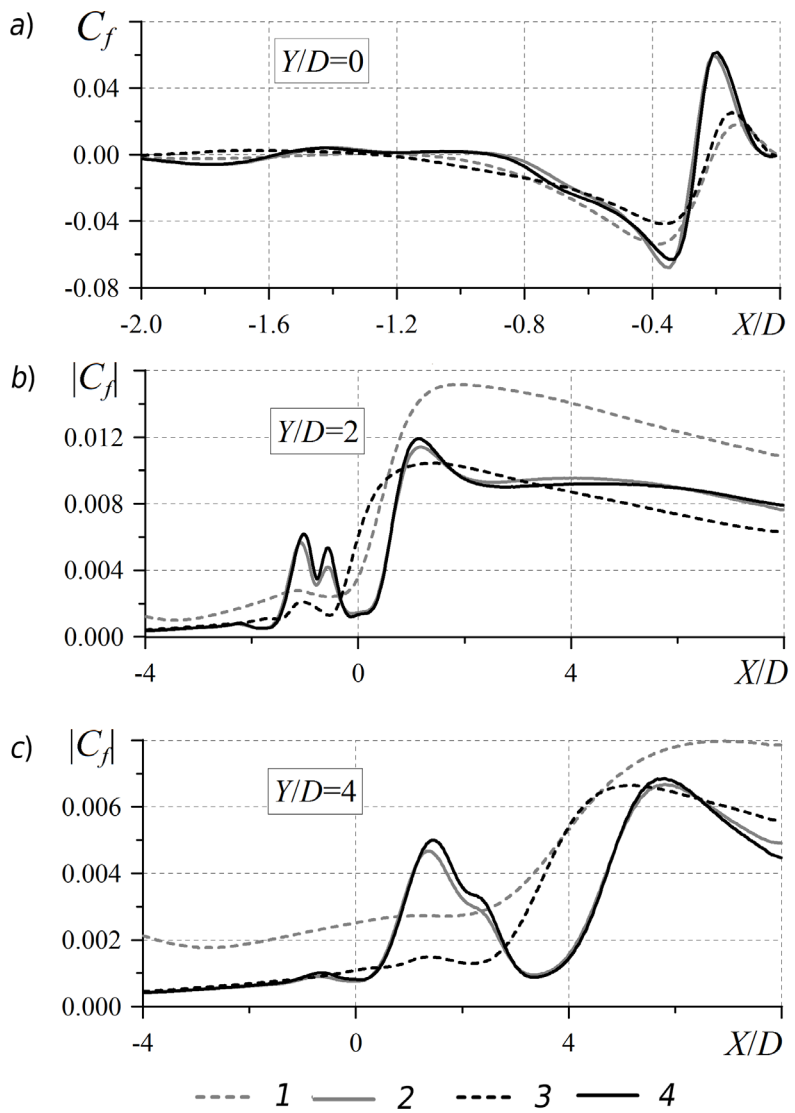

Fig. 11. Distributions of skin friction coefficient along several lines on plate surface: along line of symmetry (*a*) ($Y/D = 0$), at distances of two ($Y/D = 2$) and four ($Y/D = 4$) diameters from body, respectively (*b*, *c*). Computations were carried out by different schemes: *1*, *2* correspond to HLL of first and second orders of accuracy, respectively; *3*, *4* to AUSM of first and second orders of accuracy

distribution along the front line (see Fig. 10) that the local pressure peak has a noticeably smaller width in the solution obtained by to the AUSM scheme. Conversely, analysis of the skin friction distribution on the plate (see Fig. 11) shows that the vortex intensity in the solution obtained by the HLL scheme is slightly lower than in the case of the AUSM scheme.

Conclusion

We have obtained a family of numerical solutions for a model problem of interaction of supersonic viscous gas (air) flow with an elongated blunt body mounted on a plate along which a laminar boundary layer evolves. Solutions using two schemes (HLL and AUSM) for convective flux evaluation on meshes of different sizes were obtained with a free-stream Mach number of 2.95 and a Reynolds number of 4000.

The flow evolving in the given configuration is three-dimensional, with clear effects of viscous-inviscid interaction. The separation region in front of the body has a complex vortex structure, with a family of horseshoe-shaped vortices that spread along the plate and expands around the body. Supersonic flow around the separation region induces oblique

compression waves; interacting with the bow shock, these waves generate a gas jet, which causes a local increase in pressure on the body.

According to the results of the mesh convergence study, we have found that if schemes with second order of accuracy are used, meshes containing 13–15 million hexagonal cells allow to resolve all the details of the vortex structure ~~of the flow~~ near the region where the body is connected to the plate, as well as to obtain high-quality resolution of the shock-wave structure. Schemes of the first-order of accuracy do not allow to reproduce significant characteristics of the flow caused by viscous effects even on the most detailed mesh among those used. The solutions obtained by the AUSM and HLL schemes of the second-order of accuracy are in good agreement, but on the whole, the HLL scheme proves to be more dissipative.

REFERENCES

1. **Dolling D.S.** Fifty years of shock-wave/boundary layer research? What next?, AIAA Journal. 39 (8) (2001) 1517–1531.

2. **Babinsky H., Harvey J.K.,** Shock wave/boundary-layer interactions, Cambridge University Press, Cambridge (2011).

3. **Devenport W.J., Simpson R.L.,** Time-dependent and time-averaged turbulence structure near the nose of a wing-body juncture, Journal of Fluid Mechanics. 210 (1990) 23–55.

4. **Fleming J.L., Simpson R.L., Cowling J.E., Devenport W.J.,** An experimental study of a turbulent wing-body junction and wake flow, Experiments in Fluids. 14 (5) (1993) 366–378.

5. **Ballio F., Franzetti S.,** Topological analysis of a junction vortex flow, Proceedings of Advances in Fluid Mechanics, Montreal, Canada, 24–26 May, 2000. WIT Press, Southampton (2000) 255–264.

6. **Levchenya A.M., Smirnov E.M., Goryachev V.D.,** RANS-based numerical simulation and visualization of the horseshoe vortex system in the leading edge endwall region of a symmetric body, International Journal of Heat and Fluid Flow. 31 (6) (2010) 1107–1112.

7. **Voytenko D.M., Zubkov A.I., Panov Yu.A.,** Obtekaniye tsilindricheskogo prepyatstviya na plastine sverkhzvukovym potokom gaza [Flow past a cylindrical obstacle on the plate by a supersonic gas stream], Fluid Dynamics. (1) (1966) 121.

8. **Aduyevskiy B.C., Medvedev K.I.,** Fizicheskiye osobennosti techeniya v oblasti otryva pri trekhmernom vzaimodeystvii pogranichnogo sloya s udarnoy volnoy [Physical features of the flow in the separation region in three-dimensional interaction of the boundary layer with a shock wave], Fluid Dynamics. (1) (1967) 25 –34.

9. **Teterin M.P.** Issledovaniye techeniya gaza v oblasti padeniya skachka uplotneniya na tsilindr, obtekayemyy potokom bolshoy sverkhzvukovoy skorosti [Investigation of gas flow in the region of the shock drop sealing on a cylinder, streamlined by a large supersonic flow], Fluid Dynamics. (2) (1967) 143–147.

10. **Dolling D.S., Bogdonoff S.M.,** Blunt fin-induced shock wave/turbulent boundary-layer interaction, AIAA Journal. 20 (12) (1982) 1674–1680.

11. **Ozcan O., Holt M.,** Supersonic separated flow past a cylindrical obstacle on a flat plate, AIAA Journal. 22 (5) (1984) 611–617.

12. **Houwing A.F.P., Smith D.R., Fox J.S., et al.,** Laminar boundary layer separation at a fin-body junction in a hypersonic flow, Shock Waves. 11 (1) (2001) 31–42.

13. **Borovoy V., Mosharov V., Radchenko V., Skuratov A.**, The shock-waves interference in the flow around a cylinder mounted on a blunted plate, 7th European Conference for Aeronautics and Space Sciences (EUCASS). Report 2017-63. (2017) 1 – 8.

14. **Hung C.-M., Buning P.G.,** Simulation of blunt-fin-induced shock-wave and turbulent boundary-layer interaction, Journal of Fluid Mechanics. 154 (1985) 163–185.

15. **Lakshmanan B., Tiwari S.N.,** Investigation of three-dimensional separation at wing/body junctions in supersonic flows, Journal of Aircraft. 31 (1) (1994) 64–71.

16. **Tutty O.R., Roberts G.T., Schuricht P.H.,** High-speed laminar flow past a fin-body junction, Journal of Fluid Mechanics. 737 (2013) 19–55.

17. **Peery K.M., Imlay S.T.,** Blunt body flow simulations, AIAA, Paper 88-2924 (1988).

18. **Quirk J.J.,** A contribution to the great Riemann solver debate, International Journal for Numerical Methods in Fluids. 18 (6) (1994) 555–574.

19. **Rodionov V.,** Artificial viscosity to cure the carbuncle phenomenon: The three-dimensional case, Journal of Computational Physics. 361 (2018) 50–55.

20. **Harten A., Lax P.D., van Leer B.,** On

upstream differencing and Godunov-type schemes for hyperbolic conservation laws, SIAM Review. 25 (1) (1983) 35–61.

21. **Liou M.S., Steffen C.J.,** A new flux splitting scheme, Journal of Computational Physics. 107 (1) (1993) 23–39.

22. **Toro E.F.,** Riemann solvers and numerical methods for fluid dynamics, Springer-Verlag, Berlin, Heidelberg (2009).

23. **Einfeldt B.,** On Godunov-type methods for gas dynamics, SIAM Journal on Numerical Analysis. 25 (2) (1988) 294–318.

24. **Roe P.L.,** Approximate Riemann solvers, parameter vectors, and difference schemes, Journal of Computational Physics. 43 (2) (1981) 357–372.

25. **Van Leer B.,** Towards the ultimate conservative difference scheme. V. A second order sequel to Godunov's method, Journal of Computational Physics. 32 (1) (1979) 101–136.

26. **Harten A.,** High resolution schemes for hyperbolic conservation laws, Journal of Computational Physics. 49 (3) (1983) 357–393.

27. **Le Touze S., Murrone A., Guillard H.,** Multislope MUSCL method for general unstructured meshes, Journal of Computational Physics. 284 (2015) 389–418.

28. **Bakhvalov P.A., Kozubskaya T.K.**, Skhema s kvaziodnomernoy rekonstruktsiyey peremennykh, opredelennykh v tsentrakh elementov trekhmernoy nestrukturirovannoy setki [Cell-centered quasi-one-dimensional reconstruction scheme on 3D hybrid meshes], Matem. modelirovaniye. 28 (3) (2016)79 –95.

29. **Van Albada G.D., Van Leer B., Roberts W.W.,** A comparative study of computational methods in cosmic gas dynamics, Astronomy and Astrophysics. 108 (1) (1982) 76–84.

Received 26.03.2019, accepted 03.04.2019.

THE AUTHORS

KOLESNIK Elizaveta V.
Peter the Great St. Petersburg Polytechnic University
29 Politechnicheskaya St., St. Petersburg, 195251, Russian Federation
kolesnik_ev@mail.ru

SMIRNOV Evgueni M.
Peter the Great St. Petersburg Polytechnic University
29 Politechnicheskaya St., St. Petersburg, 195251, Russian Federation
smirnov_em@spbstu.ru

SMIRNOVSKY Alexander A.
Peter the Great St. Petersburg Polytechnic University
29 Politechnicheskaya St., St. Petersburg, 195251, Russian Federation
smirta@mail.ru

СПИСОК ЛИТЕРАТУРЫ

1. **Dolling D.S.** Fifty 2019s of shock-wave/boundary layer research? What next? // AIAA Journal. 2001. Vol. 39. No. 8. Pp. 1517–1531.

2. **Babinsky H., Harvey J.K.** Shock wave/boundary-layer interactions. Cambridge: Cambridge University Press, 2011. 461 p.

3. **Devenport W.J., Simpson R.L.** Time-dependent and time-averaged turbulence structure near the nose of a wing-body juncture // Journal of Fluid Mechanics. 1990. Vol. 210. Pp. 23–55.

4. **Fleming J.L., Simpson R.L., Cowling J.E., Devenport W.J.** An experimental study of a turbulent wing-body junction and wake flow // Experiments in Fluids. 1993. Vol. 14. No. 5. Pp. 366–378.

5. **Ballio F., Franzetti S.** Topological analysis of a junction vortex flow // Proceedings of Advances in Fluid Mechanics. Montreal, Canada. 2000. 24–26 May. WIT Press, Southampton. 2000. Pp. 255–264.

6. **Levchenya A.M., Smirnov E.M., Goryachev V.D.** RANS-based numerical simulation and visualization of the horseshoe vortex system in the leading edge endwall region of a symmetric body // International Journal of Heat and Fluid Flow. 2010. Vol. 31. No. 6. Pp. 1107–1112.

7. **Войтенко Д.М., Зубков А.И., Панов Ю.А**. Обтекание цилиндрического препятствия на пластине сверхзвуковым потоком газа //

Известия АН СССР. Механика жидкости и газа. 1 № .1966. С. 121.

8. **Адуевский В.С., Медведев К.И.** Физические особенности течения в области отрыва при трехмерном взаимодействии пограничного слоя с ударной волной // Известия АН СССР. Механика жидкости и газа. 1 № .1967. С. 25–34.

9. **Тетерин М.П.** Исследование течения газа в области падения скачка уплотнения на цилиндр, обтекаемый потоком большой сверхзвуковой скорости // Известия АН СССР. Механика жидкости и газа. 1967. № 2. С. 143 –147.

10. **Dolling D.S., Bogdonoff S.M.** Blunt fin-induced shock wave/turbulent boundary-layer interaction // AIAA Journal. 1982. Vol. 20. No. 12. Pp. 1674–1680.

11. **Ozcan O., Holt M.** Supersonic separated flow past a cylindrical obstacle on a flat plate // AIAA Journal. 1984. Vol. 22. No. 5. Pp. 611–617.

12. **Houwing A.F.P., Smith D.R., Fox J.S., Danehy D.M., Mudford N.R.** Laminar boundary layer separation at a fin-body junction in a hypersonic flow // Shock Waves. 2001. Vol. 11. No. 1. Pp. 31–42.

13. **Borovoy V., Mosharov V., Radchenko V., Skuratov A.** The shock-waves interference in the flow around a cylinder mounted on a blunted plate //7th European Conference for Aeronautics and Space Sciences (EUCASS). 2017. Report 2017-63. Pp. 1 – 8.

14. **Hung C.-M., Buning P.G.** Simulation of blunt-fin-induced shock-wave and turbulent boundary-layer interaction // Journal of Fluid Mechanics. 1985. Vol. 154. Pp. 163–185.

15. **Lakshmanan B., Tiwari S.N.** Investigation of three-dimensional separation at wing/body junctions in supersonic flows // Journal of Aircraft. 1994. Vol. 31. No. 1. Pp. 64–71.

16. **Tutty O.R., Roberts G.T., Schuricht P.H.** High-speed laminar flow past a fin–body junction // Journal of Fluid Mechanics. 2013. Vol. 737. Pp. 19–55.

17. **Peery K.M., Imlay S.T.** Blunt body flow simulations // AIAA. 1988. July. Paper 88-2924.

18. **Quirk J.J.** A contribution to the great Riemann solver debate // International Journal for Numerical Methods in Fluids. 1994. Vol. 18. No. 6. Pp. 555–574.

19. **Rodionov V.** Artificial viscosity to cure the carbuncle phenomenon: The three-dimensional case // Journal of Computational Physics. 2018. Vol. 361. Pp. 50–55.

20. **Harten A., Lax P.D., van Leer B.** On upstream differencing and Godunov-type schemes for hyperbolic conservation laws // SIAM Review. 1983. Vol. 25. No. 1. Pp. 35–61.

21. **Liou M.S., Steffen C.J.** A new flux splitting scheme // Journal of Computational Physics. 1993. Vol. 107. No. 1. Pp. 23–39.

22. **Toro E.F.** Riemann solvers and numerical methods for fluid dynamics. Berlin, Heidelberg: Springer-Verlag, 2009. 724 p.

23. **Einfeldt B.** On Godunov-type methods for gas dynamics // SIAM Journal on Numerical Analysis. 1988. Vol. 25. No. 2. Pp. 294–318.

24. **Roe P.L.** Approximate Riemann solvers, parameter vectors, and difference schemes // Journal of Computational Physics. 1981. Vol. 43. No. 2. Pp. 357–372.

25. **Van Leer B.** Towards the ultimate conservative difference scheme. V. A second order sequel to Godunov's method // Journal of Computational Physics. 1979. Vol. 32. No. 1. Pp. 101–136.

26. **Harten A.** High resolution schemes for hyperbolic conservation laws // Journal of Computational Physics. 1983. Vol. 49. No. 3. Pp. 357–393.

27. **Le Touze** C., **Murrone A., Guillard H.** Multislope MUSCL method for general unstructured meshes // Journal of Computational Physics. 2015. Vol. 284. Pp. 389–418.

28. Бахвалов П.А., Козубская **Т.К.** Схема с квазиодномерной реконструкцией переменных, определенных в центрах элементов трехмерной неструктурированной сетки // Математическое моделирование. 2016. Т. 28. № 3. С. 79–95.

29. **Van Albada G.D., Van Leer B., Roberts W.W.** A comparative study of computational methods in cosmic gas dynamics // Astronomy and Astrophysics. 1982. Vol. 108. No. 1. Pp. 76–84.

Статья поступила в редакцию 26.03.2019, принята к публикации 03.04.2019.

СВЕДЕНИЯ ОБ АВТОРАХ

КОЛЕСНИК Елизавета Владимировна – инженер кафедры «Гидроаэродинамика, *горение и теплообмен» Санкт-Петербургского политехнического университета Петра Великого.*
195251, Российская Федерация, г. Санкт-Петербург, Политехническая ул., 29
kolesnik_ev@mail.ru

СМИРНОВ Евгений Михайлович – доктор физико-математических наук, заведующий кафедрой «Гидроаэродинамика, *горение и теплообмен» Санкт-Петербургского политехнического университета Петра Великого.*
195251, Российская Федерация, г. Санкт-Петербург, Политехническая ул., 29
smirnov_em@spbstu.ru

СМИРНОВСКИЙ Александр Андреевич – кандидат физико-математических наук, доцент кафедры «Гидроаэродинамика, *горение и теплообмен» Санкт-Петербургского политехнического университета Петра Великого.*
195251, Российская Федерация, г. Санкт-Петербург, Политехническая ул., 29
smirta@mail.ru

DOI: 10.18721/JPM.12202
УДК 537.856

DEVELOPMENT OF INDUCTION SYSTEMS FOR DISK HEATING

E.R. Mannanov[1], S.A. Galunin[1], A.N. Nikanorov[2]
B. Nacke[2], T.P. Kozulina[1]

[1] St. Petersburg Electrotechnical University "LETI", St. Petersburg, Russian Federation;

[2] Institute for Electrotechnology of the Leibniz University of Hanover, Hannover, Germany

The paper presents the experimental and numerical results obtained by the induction heating a steel disk. This study has been aimed at realizing the local uniform heating the disk at minimum temperature departure from 450°C. The system-of-interest included 3-turn inducers and a steel disk heated up. The computer-based investigation results were implemented at a laboratory mock-up. The temperature distribution over the disk material and its changes were recorded by a infrared camera. Simulation of electromagnetic and thermal processes occurring in heating a rotating disk-shaped work piece was carried out using ANSYS APDL base. A comparison between the obtained numerical data and experimental one showed a disagreement of about 5 %. It pointed to an adequacy of simulation carried out. A detailed analysis of the disagreement sources was made.

Keywords: induction heating, electrothermal task, numerical simulation, heat treatment, heating with rotation

Citation: Mannanov E.R., Galunin S.A., Nikanorov A.N., Nacke B., Kozulina T.P. Development of induction systems for disk heating, St. Petersburg Polytechnical State University Journal. Physics and Mathematics. 12 (2) (2019) 23–31. DOI: 10.18721/JPM.12202

РАЗРАБОТКА ИНДУКЦИОННЫХ СИСТЕМ ДЛЯ НАГРЕВА ДИСКОВ

Э.Р. Маннанов[1], С.А. Галунин[1], А.Н. Никаноров[2]
Б. Наке[2], Т.П. Козулина[1]

[1] Санкт-Петербургский государственный электротехнический университет «ЛЭТИ» им. В.И. Ульянова (Ленина), Санкт-Петербург, Российская Федерация;

[2] Институт электротехнологий Ганноверского университета им. В. Лейбница, г. Ганновер, Германия

В статье представлены экспериментальные и численные результаты, полученные при нагреве стального диска индукционным методом. Исследование направлено на обеспечение локального равномерного нагрева диска при минимальном отклонении температуры от °450С. Рассматриваемая система включала трехвитковые индукторы и нагреваемый металлический диск. Результаты компьютерных исследований были реализованы на лабораторном макете. Температурное распределение по материалу диска и его изменения регистрировались с помощью тепловизора. Моделирование электромагнитных и термических процессов при нагреве вращающейся заготовки в форме диска выполнено на базе программного пакета ANSYS APDL. Сравнение полученных численных результатов с экспериментальными данными показало, что расхождение между ними составило около 5 %, что указывает на адекватность выполненного моделирования. Проведен детальный анализ источников отклонения модели от экспериментальных данных.

Ключевые слова: индукционный нагрев, численное моделирование, термообработка, нагрев вращением

Ссылка при цитировании: Маннанов Э.Р., Галунин С.А., Никаноров А.Н., Наке Б., Козулина Т.П. Разработка индукционных систем для нагрева дисков // Научно-технические ведомости СПбГПУ. Физико-математические науки. 2019. Т. 2 № .12. С. 23–31. DOI: 10.18721/JPM.12202

Introduction

Numerical methods are very efficient and straightforward, yielding highly accurate results, which is why they are widely used for constructing induction heating systems. These methods allow to use automatic parameterization, eliminating extremely high costs for a probabilistic range of experimental trial-and-error procedures. However, while reproducing all factors affecting metal heating in an electromagnetic field can improve the quality of the process and, accordingly, produce better results, it also considerably complicates the problem statement.

Parameters of nonlinear properties of materials depending on temperature should necessarily be considered to correctly reproduce the experimental results in numerical solution of the heating problem. Besides, magnetic permeability μ depends on the magnetic field resulting from magnetic saturation.

The nonlinear behavior of materials means that the problem should be solved in the time domain instead of the simpler data processing in the frequency domain.

The frequency of the current passing through the material can reach high values (up to hundreds of kHz for induction hardening), leading to significant fluctuations of the magnetic field per second. Thus, a periodic electromagnetic solution can be obtained for a short time interval, while the temperature distribution varies over wider time intervals (in seconds). This implies that the distribution of temperature over the material sample depends on the average flux density of the magnetic field. If μ is variable, its value can be updated over every short period of time while preserving computational efficiency, but this inevitably leads to unnecessarily lengthy computations.

The rapidly changing source term in the heat equation, expressing the specific power of internal heat sources, can be replaced by an average value over one period of electric current, calculated from the previously obtained value of the magnetic field, depending on time. This solution is optimal for updating the values of physical parameters characterizing the properties of materials taking into account the new temperature values in the grid nodes.

Numerical simulation

The goal of this study has consisted in maintaining local uniform heating of the disk with minimal temperature deviation from 450°C. This temperature value was chosen based on the results of [7], giving the data obtained after tempering a through-hardened metal sample 3 mm thick.

Each study developing new electrical tech-

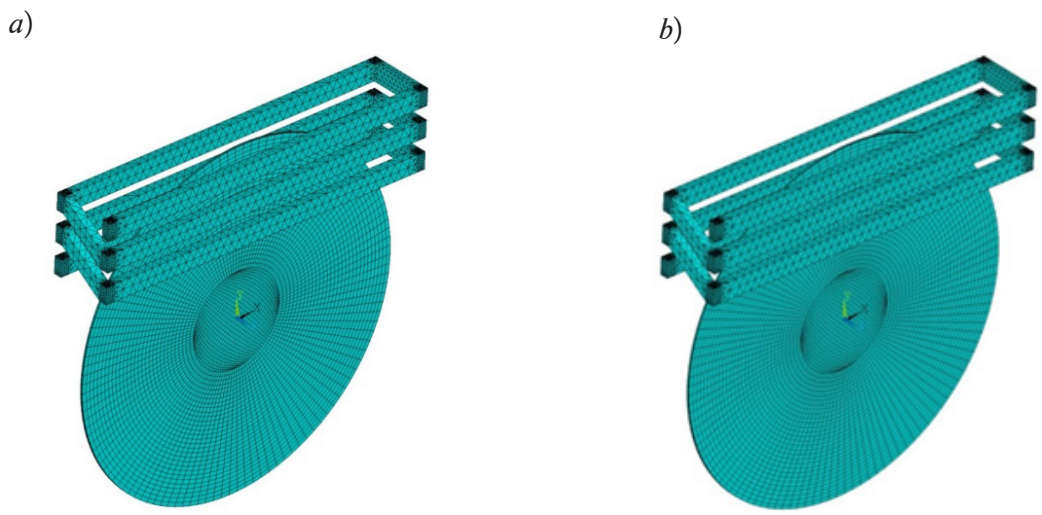

Fig. 1 .3D models of induction heating system in longitudinal (*a*) and transverse (*b*) magnetic fields

nologies or modernizing existing ones requires experimental verification. The results of computer studies [1–6] were tested using a laboratory model. A infrared camera was used as a tool for monitoring the temperature variation. The emissivity was set to 0.95 in the software. The temperature range was set from 200 to 1200°C. This way, the sensitivity of the device could be increased in the final temperature zone of 450°C.

Systems developed using the ANSYS APDL software package are 3D models of induction systems for simulating coupled electromagnetic and thermal problems of disk heating. The given system includes three-turn induction coils and a heated metal disk. The disk is made of hardened steel and has the following main dimensions: outer diameter of 410 mm, thickness of 3 mm. The operating frequency of the system is 2.5 kHz. A constant power was maintained in the object during heating. Air is the ambient environment; it is numerically described as a non-magnetic non-conductive medium that does not contain sources generating the electromagnetic field.

a)

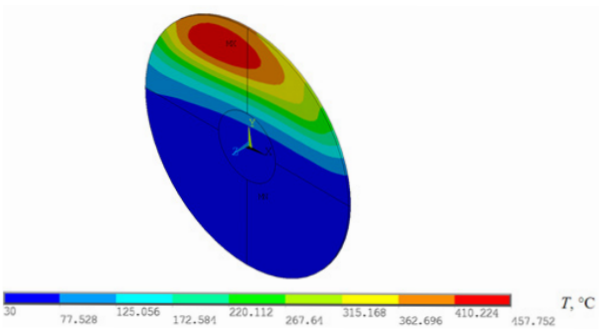

b)

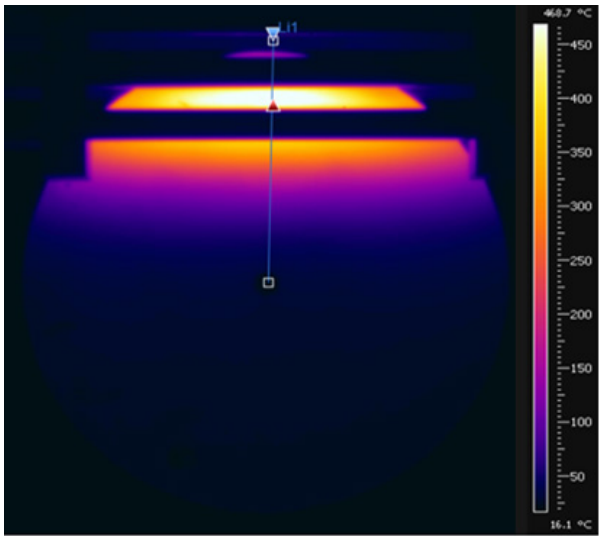

Fig. 2. Comparison of simulation results (*a*) with experimental data (*b*);
obtained for temperature distribution over workpiece surface with stationary disk heating in high-frequency longitudinal magnetic field;
b is the straight line passing from the edge of the disk to its center indicating the direction along which the temperature was measured; the dark triangle indicates the maximum temperature on the surface of the disk

The penetration depth of the current in steel depends on its brand, and was taken in the range of 1.5–0.77 mm for the current frequency of 2.5 kHz, while the relative magnetic permeability μ was taken in the range of 10–40.

As is known, highly efficient tempering is achieved if steel is heated to a depth exceeding its hardening depth. Volumetric induction heating with a small temperature difference across the cross-section is maintained due to a relatively low heating rate. Uniform temperature can be maintained in the given area both due to high thermal conductivity of the heated object, and by varying the time interval required for heating due to small thickness of the workpiece. The given temperature level can be also reached by using other frequencies; in that case, the temperature distribution over the disk surface would be different from the initial one provided that the initial data are unchanged. Additionally, assuming that a sample made by stamping has a complex profile, hot spots may appear if frequencies above 2500 Hz are used to heat such a sample for subsequent tempering.

The geometric shape of the induction coils and the positioning of the heated object fully replicate the actual samples in numerical models. The workpiece is attached to the torque transmission system of torque connected to the electric motor. Eddy currents generate heating (that is local by default) of an electrically conductive workpiece under the coil, but this phenomenon can only be detected with a infrared camera on the surface. This is the reason why numerical simulation is necessary in this case.

The results of the first stage of the study are shown in Figs. 1–3. The 3D model is partitioned into a finite element mesh in the following manner: there are five partitions per each millimeter of the disk thickness; the finite elements of the mesh along the disk diameter are larger but their size still makes it

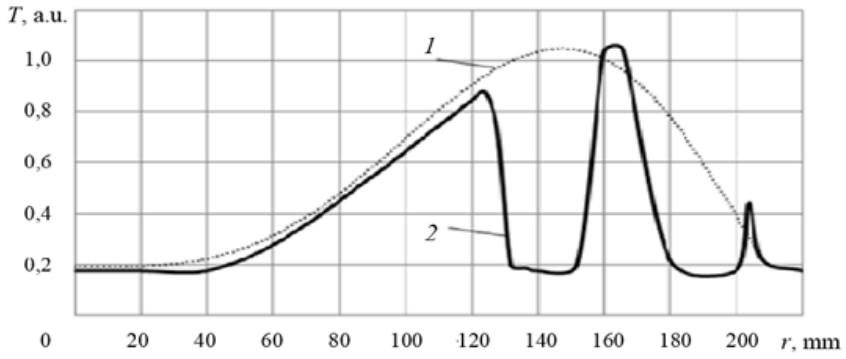

Fig. 3. Final temperature profile along workpiece radius according to results of numerical simulation (*1*) and experiment (*2*)

a)

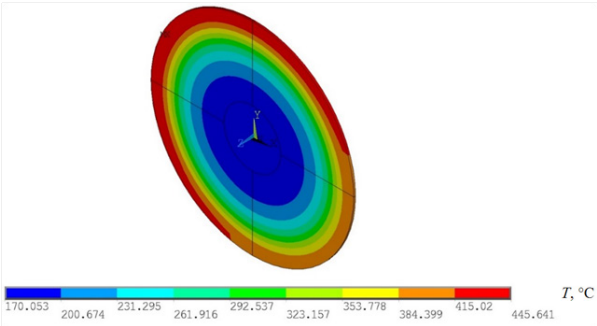

b)

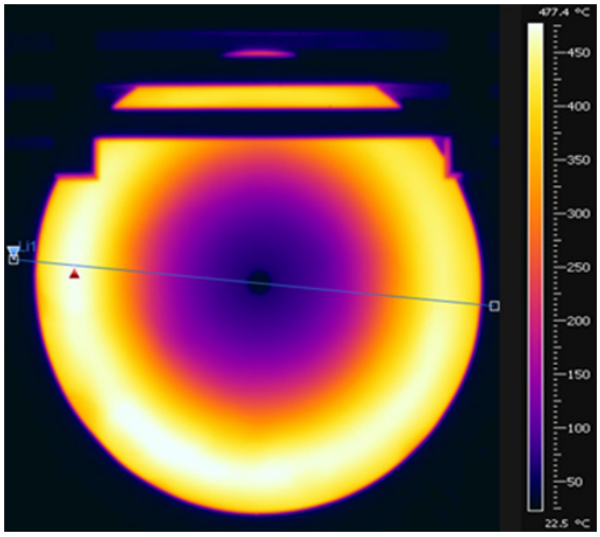

Fig. 4. Comparison of simulation results (*a*) with experimental data (*b*);

obtained for temperature distribution over workpiece surface with disk heated by rotation in high-frequency longitudinal magnetic field; *b* is the straight line passing through the center of the disk indicating the direction along which the temperature was measured; the dark triangle indicates the maximum temperature on the surface of the disk

possible to obtain fairly satisfactory results. We managed to plot the relationships between the main parameters and to assess the fit of the numerical results to the experimental data.

Electromagnetic and thermal characteristics, namely the relative magnetic permeability, resistivity, thermal conductivity, heat transfer coefficient and heat capacity are non-linear and depend on both the temperature of the hardened steel disk and the ambient temperature. The density of the disk material is assumed to be constant and uniform.

The purpose of the model was to solve the coupled electromagnetic and thermal problems, taking into account rotation, nonlinear magnetic permeability μ and the algorithm for updating data during dynamic temperature variation. The principles by which the model was constructed are described in detail in [4].

Comparison of experimental results and numerical simulation is shown in Fig. 2.

There are several objective reasons for the discrepancy between the simulation and the experimental data. Sharp dips in the temperature distribution along the workpiece radius (Fig. 3) are explained by the fact that the infrared camera was placed at some distance from the heating system. In the specific example, these dips depend on the temperature at the surface of the water-cooled turns of the coil. Because the workpiece was partially located inside the coil, there was no other way to measure the temperature.

We simulated the rotation of the disk at the second stage of the study. Heating to a temperature of 450°C was reached in 30 s with the workpiece rotated at a speed of 18 rpm (Figs. 4 and 5). The graphs are based on averaged results.

The heating time was selected assuming

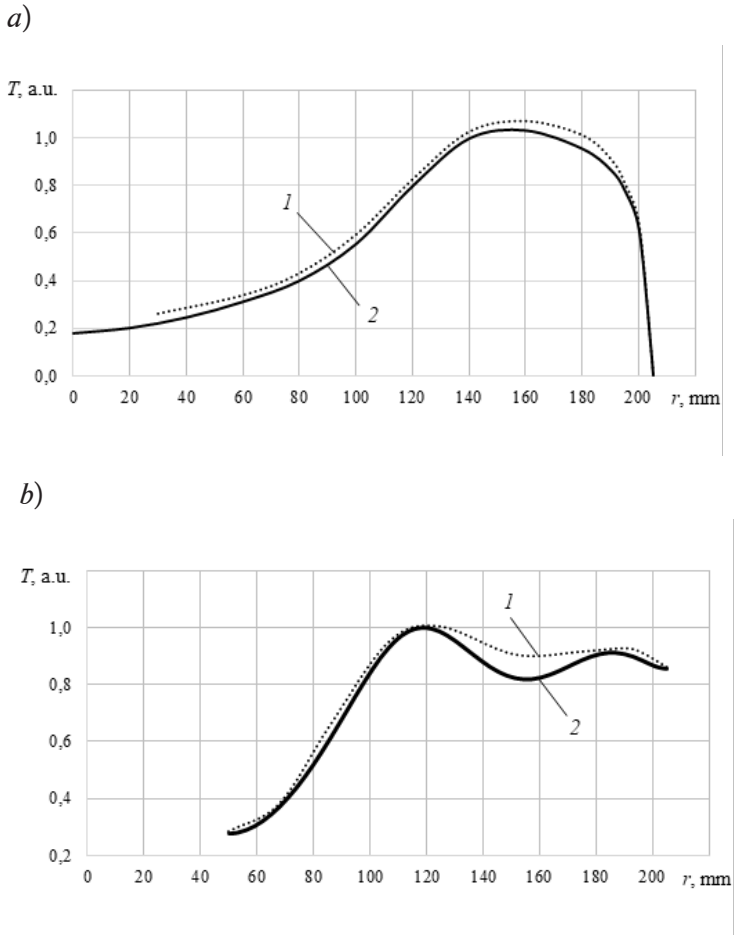

Fig. 5. Temperature profiles on workpiece surface along the radius with disk heated in the longitudinal (*a*) and transverse (*b*) magnetic fields: *1* corresponds to simulation results, *2* to experimental data

that tempering is done for a metal product. Tempering temperature has a significant effect on mechanical properties during high-frequency hardening. As mentioned above, this temperature was chosen based on the results of [7], presenting the data obtained after tempering a through-hardened metal sample with a thickness of 3 mm. A stable temperature field and, as a result, high strength, ductility and toughness of the metal can be maintained at a moderate heating rate. A further increase in tempering temperature inevitably leads to a decrease in strength and an increase in the toughness of the product.

The final temperature distribution at a low rotational speed of the metal disk is induced by thermal conductivity of the material and heat losses from its surfaces. The results obtained are in agreement with the data of [8–10], describing dependences of the allocated additional power in the disk on the rotational speed.

As seen from the data in this study, due to radiative heat losses, the edges of the disk have a lower temperature relative to the required level, while the maximum temperature along the disk radius is shifted towards the center of the heated sample.

In our simulation, the metal disk was heated through for tempering to account for the effects that the operating frequency and the construction of the induction coil system had on the disk's temperature profile. This made it possible to minimize the temperature difference over the cross-section of the disk in the heated zone. However, we did not take into account the presence of a hardened layer in the numerical study. We can predict without running a simulation that in practice this may manifest as an uneven decrease in hardness along the radius of the disk but the hardness can be reduced in an optimal manner.

The discrepancy between the numerical results and the experimental data is about 5%, which indicates that the simulation we have

carried out is adequate.

The natural construction of the heating system also includes a magnetic core, which allows to use a lower electromagnetic field frequency by controlling the pole pitch of the coil.

The results obtained indicate that the proposed induction system is sensitive to variation in geometric parameters such as coil geometry and position of the turns relative to the workpiece, as well as to variation in electrical parameters. Therefore, there is an optimal configuration of parameters allowing to achieve the best result, that is, uniform local heating of the product in the permissible range of temperature deviations from the given value in the shortest heat treatment time.

The study showed that non-standard solutions open up additional opportunities for regulating the heating process and improving the efficiency of heat treatment. Thus, the key step in improving the efficiency of induction systems for heating metal products by rotation is modernizing the existing induction heating systems and developing new ones based on automated optimization of geometric, positional and electrical parameters (combined with computer simulation). This should successfully solve the related physical problems during heat treatment, construct the shape of induction coils, select the optimal mode of operation, incorporate the properties of new materials in the design of the developed systems, produce reliable estimates for devising non-standard solutions to reduce material costs.

Conclusion

We have constructed problem-oriented 3D models of induction systems in the ANSYS APDL software package in order to calculate the coupled electromagnetic and thermal problems. The models developed have been tested and verified experimentally. The obtained results can be successfully applied to analyze and solve electrothermal problems for constructing induction systems and for parametric search of optimal configurations of these systems. In turn, optimal characteristics should ensure high quality of the final product and its maximum yield, minimum cost of equipment and maximum total efficiency.

Potential applications of the constructed models are lie in study of different induction systems for heating samples of different shapes. The developed methods and approaches can be applied to other electrical engineering processes. The proposed solutions allow to efficiently use the results obtained for steel rings, disks, gears, shafts, springs and other symmetrical workpieces of different types and sizes, for constructing induction systems and for parametric search of optimal system configurations.

REFERENCES

1. **Zlobina M., Nacke B., Nikanorov A.,** Numerical investigation of different concepts to control the temperature field at the induction heating of aluminium billets by rotation in superconductive magnets, Proceedings of the 6th International Conference on Electromagnetic Processing of Materials “EPM 2009”, Dresden (Germany), 19–23 October 2009, Dresden (2009) 177–180.

2. **Fabbri M., Morandi A., Negrini F.,** Temperature distribution in aluminium billets heated by rotation in static magnetic field produced by superconducting magnets, COMPEL – The International Journal for Computation and Mathematics in Electrical and Electronic Engineering. 24 (1) (2005) 281–290.

3. **Nacke B., Zlobina M., Nikanorov A.,** Ulferts: Numerical simulation of induction heating of aluminium billets by rotation in DC magnetic field, Proceedings of International Symposium on Heating by Electromagnetic Sources, Padua (2007) 497–504.

4. **Mannanov E., Galunin S., Nikanorov A., Nacke B.,** Simulation algorithm for induction heating of rotated workpieces with complex shape, Proceedings of the 18th International UIE-Congress “Electrotechnologies for Material Processing”, Hannover (Germany), June 6–9 (2017) 491–496.

5. **Mannanov E., Galunin S., Blinov K.,** Numerical optimization of transverse flux induction heating systems, Proceedings of the 2015 IEEE North West Russia Section Young Researchers in Electrical and Electronic Engineering Conference (ElConRusNW 2015), (2015) 241–244.

6. **Mannanov E., Muratov A., Galunin S.,** Numerical investigation of spatial control tools of temperature distribution in the heating systems by rotation, Research and Development of Young Scientists: The Collected Reports of the 6th International Youth Scientific and Practical

Conference, Novosibirsk, 16.10. 2015. (2015) 71–75.

7. **Shepelyakovskiy K.Z.,** Uprochneniye detaley mashin poverkhnostnoy zakalkoy pri induktsionnom nagreve [Machine parts strengthening by shell hardening in the induction heating], Mashinostroyeniye, Moscow, 1972.

8. **Lepeshkin S.A.,** Issledovaniye petlevykh induktorov dlya modelirovaniya i povysheniya effektivnosti nagreva vrashchayushchikhsya diskov GTD [Studies in the loop inducers for modeling and improvement of efficiency of rotating TE discs' heating], In collected book "Energy- and Resource- Saving – The 21th century", Proceedings of the 13th International Theoretical and Practical Internet Conference, "The Orel Region Center of Energy-Saving" (2015) 84– 87.

9. **Kuvaldin A.B., Lepeshkin A.R., Lepeshkin S.A.,** Modelirovaniye rezhimov induktsionnogo nagreva diskov turbin GTD s ispolzovaniyem spetsialnykh induktorov [Modeling of induction heating modes for turbines' disks using special inducers], "Electrotechnics, Electrotechnology, Energetics" – Coll. Book of Scientific Papers of the 7th Intern. Sci. Conf. for Youth Reseachers, Novosibirsk Oblast (2015) 70–73.

10. **Lepeshkin S.A.**, Modelirovaniye i issledovaniye raspredeleniy temperatur vo vrashchayushchikhsya diskakh s uchetom vzaimnogo vliyaniya [Modeling and investigation of temperature distribution in the rotating disks with consideration for their mutual coupling], In: "Energy- and Resourse-Saving – The 21th Century", Proceedings of the 12th International Research-to-Practice Internet Conference (2014) 77–79.

Received 20.01.2019, accepted 15.04.2019.

THE AUTHORS

MANNANOV Emil R.
St. Petersburg Electrotechnical University "LETI"
5 Professora Popova St., 197376, St. Petersburg, Russian Federation
emil-mannanov@mail.ru

GALUNIN Sergei A.
St. Petersburg Electrotechnical University "LETI"
5 Professora Popova St., 197376, St. Petersburg, Russian Federation
galunin@mail.ru

NIKANOROV Alexander N.
Institute for Electrotechnology of the Leibniz University of Hanover
Wilhelm-Busch-Str. 4, 30167, Hannover, Deutschland
nikanorov@etp.uni-hannover.de

NACKE Bernard
Institute for Electrotechnology of the Leibniz University of Hanover
Wilhelm-Busch-Str. 4, 30167, Hannover, Deutschland
etp@etp.uni-hannover.de

KOZULINA Tatiana P.
St. Petersburg Electrotechnical University "LETI"
5 Professora Popova St., 197376, St. Petersburg, Russian Federation
kozulina.tatiana@mail.ru

СПИСОК ЛИТЕРАТУРЫ

1. **Zlobina M., Nacke B., Nikanorov A.** Numerical investigation of different concepts to control the temperature field at the induction heating of aluminium billets by rotation in superconductive magnets // Proceedings of the 6th International Conference on Electromagnetic Processing of Materials "EPM 2009". Dresden (Germany), 19–23 October 2009. Dresden, 2009. Pp. 177–180.

2. **Fabbri M., Morandi A., Negrini F.** Temperature distribution in aluminium billets heated by rotation in static magnetic field produced

by superconducting magnets // COMPEL – The International Journal for Computation and Mathematics in Electrical and Electronic Engineering. 2005. Vol. 24. No. 1. Pp. 281–290.

3. **Nacke B., Zlobina M., Nikanorov A.** Ulferts: Numerical simulation of induction heating of aluminium billets by rotation in DC magnetic field// Proceedings of International Symposium on Heating by Electromagnetic Sources. Padua. 2007. Pp. 497–504.

4. **Mannanov E., Galunin S., Nikanorov A.**, **Nacke B.** Simulation algorithm for induction heating of rotated workpieces with complex shape // Proceedings of the 18th International UIE-Congress "Electrotechnologies for Material Processing". Hannover (Germany), June 6 – 9, 2017. Pp. 491–496.

5. **Mannanov E., Galunin S., Blinov K.** Numerical optimization of transverse flux induction heating systems // Proceedings of the 2015 IEEE North West Russia Section Young Researchers in Electrical and Electronic Engineering Conference (ElConRusNW 2015). Pp. 241–244.

6. **Mannanov E., Muratov A., Galunin S.** Numerical investigation of spatial control tools of temperature distribution in the heating systems by rotation // Research and Development of Young Scientists: The Collected Reports of the 6th International Youth Scientific and Practical Conference. Novosibirsk, 16.10. 2015. Pp. 71–75.

7. **Шепеляковский К.З.** Упрочнение деталей машин поверхностной закалкой при индукционном нагреве. М.: Машиностроение, 287 .1972 с.

8. **Лепешкин С.А**. Исследование петлевых индукторов для моделирования и повышения эффективности нагрева вращающихся дисков ГТД // «Энерго- и ресурсосбережение – XXI век». Сб. матер. XIII международной научно-практической интернет-конференции. Орловский гос. ун-т, «Орловский региональный центр энергосбережения». 2015. С. 87–84.

9. **Кувалдин А.Б., Лепешкин А.Р., Лепешкин С.А.** Моделирование режимов индукционного нагрева дисков турбин ГТД с использованием специальных индукторов // Электротехника. Электротехнология. Энергетика. Сб. научн. тр. VII Международной научной конференции молодых ученых. Межвузовский центр содействия научной и инновационной деятельности студентов и молодых ученых Новосибирской области. 2015. С. 70–73.

10. **Лепешкин С.А.** Моделирование и исследование распределений температур во вращающихся дисках с учетом взаимного влияния // «Энерго- и ресурсосбережение – XXI век». Матер. XII Междунар. научно-практ. интернет-конференции. 2014. С. 77–79.

Статья поступила в редакцию 20.01.2019, принята к публикации 15.04.2019.

СВЕДЕНИЯ ОБ АВТОРАХ

МАННАНОВ Эмиль Рамилевич – *аспирант кафедры электротехнологической и преобразовательной техники Санкт-Петербургского государственного электротехнического университета «ЛЭТИ» имени В.И. Ульянова (Ленина).*

197376, Российская Федерация, г. Санкт-Петербург, ул. Профессора Попова, 5.
emil-mannanov@mail.ru

ГАЛУНИН Сергей Александрович – *кандидат технических наук, заведующий кафедрой электротехнологической и преобразовательной техники Санкт-Петербургского государственного электротехнического университета «ЛЭТИ» имени В.И. Ульянова (Ленина).*

197376, Российская Федерация, г. Санкт Петербург, ул. Профессора Попова, 5.
galunin@mail.ru

НИКАНОРОВ Александр Николаевич – *кандидат технических наук, научный сотрудник Института электротехнологий Ганноверского университета им. В. Лейбница.*

Wilhelm-Busch-Str. 4, 30167, Hannover, Deutschland
nikanorov@etp.uni-hannover.de

НАКЕ Бернард – *доктор технических наук, директор Института электротехнологий Ганноверского университета им. В. Лейбница.*
Wilhelm-Busch-Str. 4, 30167, Hannover, Deutschland
etp@etp.uni-hannover.de

КОЗУЛИНА Татьяна Павловна – *аспирантка кафедры электротехнологической и преобразовательной техники Санкт-Петербургского государственного электротехнического университета «ЛЭТИ» имени В.И. Ульянова (Ленина).*
197376, Российская Федерация, г. Санкт Петербург, ул. Профессора Попова, 5.
kozulina.tatiana@mail.ru

DOI: 10.18721/JPM.12203
УДК 517.51; 517.28; 517.983; 537.213, 537.8

GENERALIZATION OF THE THOMSON FORMULA FOR GENERAL HARMONIC FUNCTIONS

A.S. Berdnikov[1], *L.N. Gall*[1], *N.R. Gall*[1], *K.V. Solovyev*[2,1]
[1]Institute for Analytical Instrumentation of the Russian Academy of Sciences, St. Petersburg, Russian Federation;
[2] Peter the Great St. Petersburg Polytechnic University, St. Petersburg, Russian Federation

The paper continues the investigation of electron and ion optical properties of electric and magnetic fields which can be represented in an analytical form. The target of this research is new recipes for generating analytical solutions of 3D Laplace equation, in particular, for generating 3D harmonic functions which are homogeneous in Euler terms. Linear algebraic expressions with first order partial derivatives which generalize the widely known Thomson formula (Kelvin transformation), are analyzed. The paper provides an exhaustive list of symmetric and homogeneous first order differentiating expressions that convert an arbitrary 3D harmonic function into some new 3D harmonic functions. The produced 3D expressions are generalized for the *n*-dimensional case.

Keywords: electrostatic field, magnetostatic field, scalar potential, Laplace's equation, Thomson formula

Citation: Berdnikov A.S., Gall L.N., Gall N.R., Solovyev, K.V. Generalization of the Thomson formula for general harmonic functions, St. Petersburg Polytechnical State University Journal. Physics and Mathematics. 12 (2) (2019) 32–47. DOI: 10.18721/JPM.12203

ОБОБЩЕНИЕ ФОРМУЛЫ ТОМСОНА ДЛЯ ГАРМОНИЧЕСКИХ ФУНКЦИЙ ОБЩЕГО ВИДА

А.С. Бердников[1], *Л.Н. Галль*[1], *Н.Р. Галль*[1], *К.В. Соловьев*[2,1]
[1]Институт аналитического приборостроения Российской академии наук, Санкт-Петербург, Российская Федерация;
[2]Санкт-Петербургский политехнический университет Петра Великого, Санкт-Петербург, Российская Федерация

Статья продолжает цикл работ, посвященный изучению электронно- и ионно-оптических свойств электрических и магнитных полей, представимых в аналитической форме. Целью исследования является поиск альтернативных рецептов для генерирования новых аналитических решений трехмерного уравнения Лапласа и, в частности, для генерирования трехмерных гармонических функций, являющихся однородными по Эйлеру. Рассматриваются обобщения широко известной алгебраической формулы Томсона (преобразование Кельвина), которые используют линейные алгебраические формы с частными производными первого порядка. Приведен исчерпывающий список симметризованных однородных дифференцирующих выражений первого порядка, преобразующих произвольные трехмерные гармонические функции в новые трехмерные гармонические функции. Дано обобщение полученных трехмерных формул на случай произвольного (конечного) числа измерений.

Ключевые слова: электростатическое поле, магнитостатическое поле, скалярный потенциал, уравнение Лапласа, формула Томсона

Ссылка при цитировании: Бердников А.С., Галль Л.Н., Галль Н.Р., Соловьев К.В. Обобщение формулы Томсона для гармонических функций общего вида // Научно-технические ведомости СПбГПУ. Физико-математические науки. 2019. Т. 12. № 2. С. 32–48. DOI: 10.18721/JPM.12203

Introduction

The Thomson formula [1–3] for 3D harmonic functions is a unique tool. Any other formula of this type may differ from the original Thomson formula only by a trivial change of variables, represented as a superposition of shifts, reflections, rotations, and proportional stretching of coordinates. Let us describe in detail how the Thomson formula works.

If $U(x,y,z)$ is an arbitrary harmonic function of three variables, i.e., it satisfies the Laplace equation

$$U_{xx} + U_{yy} + U_{zz} = 0 \qquad (1)$$

(from now on we use the subscripts composed of the symbols x, y, z to denote partial derivatives with respect to the corresponding variables), then the function

$$V(x,y,z) = \frac{1}{r} U\left(\frac{x}{r^2}, \frac{y}{r^2}, \frac{z}{r^2}\right), \qquad (2)$$

where $r = \sqrt{x^2 + y^2 + z^2}$, is also harmonic [1, 2]. Using Eq. (2) once again, we make the transition from the function $V(x,y,z)$ back to the function $U(x,y,z)$. We can verify that the function V obtained from Eq. (2) is harmonic (provided that the function U is harmonic) using the identity

$$V_{xx} + V_{yy} + V_{zz} \equiv \frac{1}{r^5}\left(U_{xx} + U_{yy} + U_{zz}\right),$$

where the function V is given by expression (2), and the function U is arbitrary.

The change of variables used for the arguments of the function U in Eq. (2) is the inversion in a sphere of unit radius with the center at the origin. Eq. (2) is named the Thomson formula after its author, the eminent British physicist William Thomson, Lord Kelvin [3–5]; sometimes this formula is also called the Kelvin transform [1, 6–10]. Transformation (2) preserves harmonic functions and can be used, in particular, not only for solving boundary problems with the Dirichlet condition (with the interior Dirichlet problem transformed into exterior and vice versa) but also for generating new analytical solutions for scalar potentials of electrostatic and magnetostatic fields, which is convenient in synthesizing electron and ion optical systems [11–13].

Euler-homogeneous electric and magnetic fields are a useful tool for synthesizing a special type of electron and ion optical systems [14–18]. The trajectories of charged particles in Euler-homogeneous electrostatic and magnetostatic fields obey the principle of similarity of trajectories described by Golikov [19, 20]; the unique optical properties of the devices controlling the motion of charged particles and using Euler-homogeneous electric and magnetic fields follow from this principle.

As a rule, these fields are characterized by a scalar electric or magnetic potential which is an Euler-homogeneous (or, more precisely, positively homogeneous) function in the sense given to this term in classical mathematical analysis [21, 22]:

$$\forall \lambda > 0: \; U(\lambda x, \lambda y, \lambda z) \equiv \lambda^k U(x,y,z), \qquad (3)$$

where k is the degree of homogeneity of the scalar function (that is not necessarily an integer) and, accordingly, the degree of homogeneity of the field.

Possible exceptions, when the scalar potential of a homogeneous field is not a homogeneous function, were considered in [23].

If $U(x,y,z)$ is a harmonic and Euler-homogeneous function with a degree of homogeneity k, then the harmonic function $V(x,y,z)$ calculated according to rule (2) is also Euler-homogeneous with a degree of homogeneity $(-k-1)$. Applying transformation (2) again, we make the transition from the function $V(x,y,z)$ back to the function $U(x,y,z)$. Therefore, a harmonic prototype with a degree of homogeneity $(-k-1)$ necessarily exists for each harmonic function that is Euler-homogeneous with a degree of homogeneity k, so that the function can be obtained from this prototype by Eq. (2). Combined with differentiation with respect to the variables x, y, z, which is a universal method for obtaining new homogeneous harmonic functions with reduced degree of homogeneity [24, 25], the Thomson formula (2) allows to obtain differential/algebraic equations of a general form for 3D homogeneous harmonic functions with any integer-valued degrees of homogeneity [24, 26]. Donkin's formula is used as the starting point for 3D homogeneous harmonic functions of zero degree [16, 17, 24, 27–31]. This issue is considered in more detail in [24, 26].

The common factor $1/r^2$ in Eq. (2) is taken out of the function arguments for Euler-homogeneous functions U satisfying identity (3). Eq. (2) then takes a simplified form (see Thomson's treatise [5], Appendix B to Chapter 1):

$$V(x,y,z) = r^{-2k-1} U(x,y,z). \qquad (4)$$

We can verify that if a homogeneous function U is substituted into Eq. (4), function (4) is homogeneous. The function V, calculated in accordance with rule (4), is harmonic, as follows from the identity

$$V_{xx} + V_{yy} + V_{zz} \equiv r^m(U_{xx} + U_{yy} + U_{zz}) + \\ + 2mr^{m-2}(xU_x + yU_y + zU_z - kU) + \\ + m(m + 2k + 1)r^{m-2}U, \quad (5)$$

valid for functions of the form $V(x,y,z) = r^m U(x,y,z)$ with an arbitrary exponent m and an arbitrary function U. Indeed, the right-hand side of identity (5) becomes zero at $m = 0$ and $m = -2k - 1$, since the function U must satisfy the Laplace equation (1) and the Euler differential equation for homogeneous functions [21, 22]:

$$xU_x + yU_y + zU_z = kU. \quad (6)$$

The goal of this study has consisted in finding alternative recipes for generating new analytical solutions of the Laplace equation and, in particular, for generating 3D harmonic functions that Euler-homogeneous.

Uniqueness of Thomson's algebraic formula

Let us consider the transformation of a three-dimensional harmonic function $U(x,y,z)$ in accordance with the rule

$$V(x,y,z) = S(x,y,z)\times \\ \times U\big(f(x,y,z), g(x,y,z), h(x,y,z)\big), \quad (7)$$

where S, f, g, h are some fixed functions.

Here we can confine ourselves to algebraic expressions linear with respect to U, since the Laplace equation (1) has the property of linearity and linear superposition of its solutions with constant coefficients is again a solution.

Let us impose the condition that expression (7) be a harmonic function for any harmonic functions U. After substituting expression (7) into the Laplace equation (1), we obtain a linear combination composed of partial derivatives U, U_x, U_y, U_z, U_{xx}, U_{yy}, U_{zz}, U_{xy}, U_{xz}, U_{yz}. Since the function U is harmonic, the derivative U_{zz} can be expressed in terms of partial derivatives U_{xx} and U_{yy}:

$$U_{zz} = -U_{xx} - U_{yy}. \quad (8)$$

This brings up the question whether the other partial derivatives can be regarded as independent. The answer is yes: the Cauchy problem for the Laplace equation (1) with initial conditions

$$U(x,y,z_0) = U^{(0)}(x,y),$$
$$U_z(x,y,z_0) = U^{(n)}(x,y),$$

set for the plane $z = z_0$, is solvable for any initial values of $U^{(0)}(x,y)$ and $U^{(n)}(x,y)$, at least in some neighborhood of the plane $z = z_0$. For example, this solution could be a Taylor series with respect to the variable z, where all coefficients are uniquely expressed in terms of the functions $U^{(0)}(x,y)$, $U^{(n)}(x,y)$ and their derivatives with respect to x, y. Therefore, the derivatives of the functions $U^{(0)}(x,y)$ and $U^{(n)}(x,y)$ with respect to the variables x and y, calculated at a fixed point, are independent numbers.

Consequently, if there are no additional constraints on the harmonic function U, then the remaining partial derivatives in the final linear combination of partial derivatives of the function U, obtained after substituting condition (8), should be assumed to be independent, and each of the factors grouped before these partial derivatives should be zero. The set of independent partial derivatives includes mixed derivatives of any order with respect to x, y, but only zero and first order with respect to z. This rule holds not only for derivatives whose order is not higher than the second, used in the given linear combination, but also in the general case (see the next section).

As a result, we obtain for the unknown functions S, f, g, h, assuming that $S(x,y,z) \neq 0$, a system of nine partial differential equations:

$$\begin{gathered} f_x g_x + f_y g_y + f_z g_z = 0, \\ f_x h_x + f_y h_y + f_z h_z = 0, \\ g_x h_x + g_y h_y + g_z h_z = 0, \\ f_x^2 + f_y^2 + f_z^2 = h_x^2 + h_y^2 + h_z^2, \\ g_x^2 + g_y^2 + g_z^2 = h_x^2 + h_y^2 + h_z^2, \\ S\left(f_{xx} + f_{yy} + f_{zz}\right) + \\ +2S_x f_x + 2S_y f_y + 2S_z f_z = 0, \\ S\left(g_{xx} + g_{yy} + g_{zz}\right) + \\ +2S_x g_x + 2S_y g_y + 2S_z g_z = 0, \\ S\left(h_{xx} + h_{yy} + h_{zz}\right) + \\ +2S_x h_x + 2S_y h_y + 2S_z h_z = 0, \\ S_{xx} + S_{yy} + S_{zz} = 0. \end{gathered} \quad (9)$$

This system of equations is overdetermined (there are more equations than unknown functions), so, generally speaking, it may not

have solutions [32–38]. However, the Thomson formula (2) guarantees that system (9) has non-degenerate non-zero solutions that interest us.

The first five equations of system (9) mean that a one-to-one, continuously differentiable mapping

$$x' = f(x,y,z),\ y' = g(x,y,z),\quad z' = h(x,y,z) \tag{10}$$

is conformal, that is, it locally preserves the angles between the lines at the point where they intersect regardless of the location of these lines, and converts infinitely small segments into proportional infinitely small segments with a proportionality coefficient that does not depend on direction. This mapping preserves the shape of infinitely small figures but does not preserve the length of the lines, their curvature, or the global shape of the figures and, possibly, the orientation of the local basis [39, 40].

The family of conformal transformations for a two-dimensional plane is very diverse and in fact coincides with the family of analytic functions of one complex variable [41–45]. However, this is not the case for three and higher dimensions: the Liouville theorem on conformal mappings in Euclidean spaces (see [46–52]) postulates that the family of conformal mappings coincides with the group of Möbius transformations in these cases [53–55] and no other multidimensional conformal mappings are available. Unfortunately, we have not managed to uncover the elementary proof of this important theorem; evidently, the simplest proof is given in [52].

In general, the Möbius group is a group generated by the following elementary transformations and their superpositions:

a) shifts (parallel translation),

$$x' = x + a,\ y' = y + b,\ z' = z + c;$$

b) three-dimensional rotations around a fixed point [56, section 14.10];

c) reflections with respect to hyperplanes, in particular, elementary symmetries

$$x' = -x,\ y' = -y,\ z' = -z;$$

d) proportional stretching in all coordinates relative to some center

$$x' = kx,\ y' = ky,\ z' = kz;$$

(the origin is used as the center here);

e) inversion relative to the sphere,

$$x' = xr_0^2/(x^2+y^2+z^2),\ y' = yr_0^2/(x^2+y^2+z^2),\quad z' = zr_0^2/(x^2+y^2+z^2)$$

(here r_0 is the radius of the sphere, and the origin is used as the center of the sphere).

Not all of the above transformations are independent. For example, stretching can be replaced by two successive inversions relative to spheres with a common center but with different radii, and reflections relative to hyperplanes $x = 0$, $y = 0$ or $z = 0$ can be replaced by stretching with a scaling factor of -1 combined with 180° rotation relative to one of the coordinate axes.

The Möbius group for the two-dimensional case that is the most typical for practical applications coincides with the group of linear fractional conformal transformations, to which complex conjugate linear fractional conformal transformations are added (anti-conformal, if conformal transformations are understood as those preserving not only local angles but also their direction, i.e., the orientation of the local basis).

We can prove that any element of the Möbius group can be reduced to one of two possible types:

$$\mathbf{r}' = \mathbf{b} + \frac{\lambda A(\mathbf{r}-\mathbf{a})}{|\mathbf{r}-\mathbf{a}|^2}, \tag{11}$$

$$\mathbf{r}' = \mathbf{b} + \lambda A(\mathbf{r}-\mathbf{a}), \tag{12}$$

where $\mathbf{r}$ is the radius vector (generally speaking, n dimensional) for the initial point; $\mathbf{r}'$ is the radius vector for the transformed point; $\mathbf{a}$ is the initial center of the geometric transformation; $\mathbf{b}$ is the final location of the center of the geometric transformation; λ is the stretch factor (real number); A is an orthogonal matrix satisfying the condition $AA^T = A^TA = E$ and describing rotation in n dimensional space relative to the origin (possibly with a change in the orientation of the local basis if the determinant of the matrix A is equal to -1).

To prove this statement, it is sufficient to verify that the composition of geometric transformation (11) or (12) is again reduced either to reference form (11) or to reference form (12) with each of the elementary transformations of the Möbius group given above.

Three-dimensional geometric transformations of the form (11) or (12) are obviously decomposed into a superposition of elementary transformations in the form of an initial shift, inversion with the center at the origin (for transformation (11)), three-dimensional rotations around the origin [56, section 14.10] (possibly combined with one of the symmetries changing the orientation of the system),

proportional stretching relative to the origin and the final shift to the new center. The harmonic function U remains harmonic with a shift, rotation, symmetric reflection and proportional stretching of the arguments, so in these cases the factor $S(x,y,z)$ for Eq. (7) is equal to unity (or, more precisely, to an arbitrary constant, as follows from Eqs. (9)). In case of inversion with the center at the origin, the factor $S(x,y,z)$ for Eq. (7) is determined up to a constant factor in accordance with the Thomson formula (2), and system of equations (9) confirms that this factor is unique.

Successively making these transformations, with the conformal transformation (10) is written either in the form (11) or (12), we obtain the final solution for the problem of finding algebraic formulas of the form (7) which remain harmonic. If, however, an Euler-homogeneous harmonic function is to be transformed into a homogeneous harmonic function, the answer is either the Thomson formula (2) or the identity equality $V(x,y,z) = U(x,y,z)$ up to a rotation and proportional stretching of the arguments x, y, z relative to the origin, and also up to the potential values at all points of space multiplied by a constant. Uniqueness of the Thomson formula is also proved in [8, 10].

Expanded form including first derivatives

The purely algebraic transformation (7) has no other meaningful solutions except the classical Thomson formula (2), leading us to search for other methods of generating new harmonic functions. Let us consider the transformation of the three-dimensional harmonic function $U(x,y,z)$ in accordance with the rule

$$\begin{aligned} &V(x,y,z)= \\ &=S(x,y,z)\cdot U\big(f(x,y,z),g(x,y,z),h(x,y,z)\big)+ \\ &+P(x,y,z)\cdot U_x\big(f(x,y,z),g(x,y,z),h(x,y,z)\big)+ \\ &+Q(x,y,z)\cdot U_y\big(f(x,y,z),g(x,y,z),h(x,y,z)\big)+ \\ &+R(x,y,z)\cdot U_z\big(f(x,y,z),g(x,y,z),h(x,y,z)\big), \end{aligned} \tag{13}$$

where S, P, Q, R, f, g, h are some fixed functions, U is an arbitrary harmonic function.

As before, let us impose that expression (13) be a harmonic function for the given functions S, P, Q, R, f, g, h and any harmonic functions U. To ensure that function (13) is a homogeneous function with homogeneous functions U, we impose that the functions S, P, Q, R, f, g, h also be Euler-homogeneous (it is easy to verify that this requirement is necessary as well as sufficient). To eliminate the freedom of choice in the form of three-dimensional rotations around the origin, which is excessive in our case, similar to Eq. (2), we confine ourselves to the case when $f(x,y,z) = x\varphi(x,y,z)$, $g(x,y,z) = y\varphi(x,y,z)$, $h(x,y,z) = z\varphi(x,y,z)$,
where the common factor $\varphi(x,y,z)$ is an Euler-homogeneous function.

We should however keep in mind that we run the risk of discarding any truly interesting solutions, and not just rotations.

It is convenient to write the homogeneous functions φ, S, P, Q, R in the following form:

$$\begin{aligned} \varphi(x,y,z) &= r^m\omega(x/r, y/r), \\ S(x,y,z) &= r^n s(x/r, y/r), \\ P(x,y,z) &= r^{n+m+1}u(x/r, y/r), \\ Q(x,y,z) &= r^{n+m+1}\nu(x/r, y/r), \\ R(x,y,z) &= r^{n+m+1}w(x/r, y/r), \end{aligned} \tag{14}$$

where m is the degree of homogeneity of the common factor for the arguments of the function U; n is the degree of homogeneity of the factor before the function U itself; $\omega(\chi,\eta)$, $s(\chi,\eta)$, $u(\chi,\eta)$, $\nu(\chi,\eta)$, $w(\chi,\eta)$ are some functions of two variables, unknown so far.

This formulation is a slightly modified universal representation [21, 22] for homogeneous functions of degree k:

$$f\left(x_1,x_2,\ldots,x_n\right)=x_1^k g\left(x_2/x_1,\ldots x_n/x_1\right) \tag{15}$$

and does not lead to loss of admissible solutions. Importantly, the change of variables used for constructing substitution (14) is reversible
:

$$\begin{cases} \chi = x\Big/\sqrt{x^2+y^2+z^2}, \\ \eta = y\Big/\sqrt{x^2+y^2+z^2}, \\ \rho = \sqrt{x^2+y^2+z^2}, \end{cases} \Leftrightarrow$$

$$\Leftrightarrow \begin{cases} x = \chi\rho, \\ y = \eta\rho, \\ z = \pm\rho\sqrt{1-\chi^2-\eta^2}. \end{cases}$$

After substituting Eqs. (13) into the Laplace equation (1), we obtain a linear combination with some factors independent of U, composed of partial derivatives

$$U,\ U_x,\ U_y,\ U_z,\ U_{xx},$$
$$U_{yy},\ U_{zz},\ U_{xy},\ U_{xz},\ U_{yz},$$
$$U_{xxx},\ U_{xxy},\ U_{xxz},\ U_{xyy},\ U_{xyz},$$
$$U_{xzz},\ U_{yyy},\ U_{yyz},\ U_{yzz},\ U_{zzz}.$$

Since the function U is harmonic, some of these derivatives can be expressed in terms of others:

$$U_{zz} = -U_{xx} - U_{yy},\ U_{xzz} = -U_{xxx} - U_{xyy},$$
$$U_{zzy} = -U_{xxy} - U_{yyy},\ U_{zzz} = -U_{xxz} - U_{yyz}.$$

The reasoning in the previous section proves that the remaining partial derivatives should be assumed to be independent. Therefore, after substitution into the resulting linear combination of the above expressions for dependent derivatives

$$U_{zz},\ U_{xzz},\ U_{yzz},\ U_{zzz}$$

and finding common factors before the remaining partial derivatives, each of the resulting factors should be identically zero.

The resulting system of partial differential equations with respect to the unknown functions turns out to be overdetermined.

$$\omega(\chi,\eta),\ s(\chi,\eta),\ u(\chi,\eta),\ v(\chi,\eta),\ w(\chi,\eta)$$

It has a rather complicated form, so it is not given here explicitly. By the same logic, we omitted the analysis of compatibility of the obtained system of equations and its solutions, since it is overly cumbersome and, apart from standard technical methods, does not provide any new information. Analysis of this system using the appropriate methods [32–38] yields the following solutions which exhaustively cover all possible cases:

a) when $m = 0$ and $n = -1$ or $m = -2$ and $n = 0$

$$\omega(\chi,\eta) = c,\ s(\chi,\eta) = 0,$$
$$u(\chi,\eta) = c_a,\ v(\chi,\eta) = c_b,\ w(\chi,\eta) = c_c,$$

where c, c_a, c_b, c_c are arbitrary constants;

b) with $m = 0$ and $n = 1$ or $m = n = -2$

$$\omega(\chi,\eta) = c, s(\chi,\eta) = (c_a / c)\chi + (c_b / c)\eta + (c_c / c)\sqrt{1-\chi^2-\eta^2},$$
$$u(\chi,\eta) = c_a\left(-1+2\chi^2\right) + 2c_b\chi\eta + 2c_c\chi\sqrt{1-\chi^2-\eta^2},$$
$$v(\chi,\eta) = 2c_a\chi\eta + c_b\left(-1+2\eta^2\right) + 2c_c\eta\sqrt{1-\chi^2-\eta^2},$$
$$w(\chi,\eta) = 2c_a\chi\sqrt{1-\chi^2-\eta^2} + 2c_b\eta\sqrt{1-\chi^2-\eta^2} + c_c\left(1-2\chi^2-2\eta^2\right),$$

where c, c_a, c_b, c_c are arbitrary constants;

c) with $m = n = 0$ or $m = -2$ and $n = -1$

$$\omega(\chi,\eta) = c, s(\chi,\eta) = c_e,$$
$$u(\chi,\eta) = c_d\chi + c_c\eta - c_b\sqrt{1-\chi^2-\eta^2},$$
$$v(\chi,\eta) = -c_c\chi + c_d\eta + c_a\sqrt{1-\chi^2-\eta^2},$$
$$w(\chi,\eta) = c_b\chi - c_a\eta + c_d\sqrt{1-\chi^2-\eta^2},$$

where c, c_a, c_b, c_c, c_d, c_e are arbitrary constants.

As a result, we obtain a list of basic formulas transforming the original harmonic functions into new harmonic functions

$$V(x,y,z) = U(x,y,z), \tag{16}$$

$$V(x,y,z) = U_x(x,y,z), \tag{17}$$

$$V(x,y,z) = U_y(x,y,z), \tag{18}$$

$$V(x,y,z) = U_z(x,y,z), \tag{19}$$

$$V(x,y,z) = xU(x,y,z) + \left(x^2-y^2-z^2\right)U_x(x,y,z) + 2xyU_y(x,y,z) + 2xzU_z(x,y,z); \tag{20}$$

$$V(x,y,z) = yU(x,y,z) + 2xyU_x(x,y,z) + \left(-x^2+y^2-z^2\right)\times U_y(x,y,z) + 2yzU_z(x,y,z); \tag{21}$$

$$V(x,y,z) = zU(x,y,z) + 2xzU_x(x,y,z) + 2yzU_y(x,y,z) + \left(-x^2-y^2+z^2\right)U_z(x,y,z); \tag{22}$$

$$V(x,y,z) = xU_x(x,y,z) + yU_y(x,y,z) + zU_z(x,y,z); \tag{23}$$

$$V(x,y,z) = yU_x(x,y,z) - xU_y(x,y,z); \tag{24}$$

$$V(x,y,z)=zU_x(x,y,z)-xU_z(x,y,z); \quad (25)$$

$$V(x,y,z)=zU_y(x,y,z)-yU_z(x,y,z); \quad (26)$$

$$V(x,y,z)=\frac{1}{r}U\left(\frac{x}{r^2},\frac{y}{r^2},\frac{z}{r^2}\right); \quad (27)$$

$$V(x,y,z)=\frac{1}{r}U_x\left(\frac{x}{r^2},\frac{y}{r^2},\frac{z}{r^2}\right); \quad (28)$$

$$V(x,y,z)=\frac{1}{r}U_y\left(\frac{x}{r^2},\frac{y}{r^2},\frac{z}{r^2}\right); \quad (29)$$

$$V(x,y,z)=\frac{1}{r}U_z\left(\frac{x}{r^2},\frac{y}{r^2},\frac{z}{r^2}\right); \quad (30)$$

$$V(x,y,z)=\frac{x}{r^3}U\left(\frac{x}{r^2},\frac{y}{r^2},\frac{z}{r^2}\right)+ \frac{x^2-y^2-z^2}{r^5}U_x\left(\frac{x}{r^2},\frac{y}{r^2},\frac{z}{r^2}\right)+ \frac{2xy}{r^5}U_y\left(\frac{x}{r^2},\frac{y}{r^2},\frac{z}{r^2}\right)+\frac{2xz}{r^5}U_z\left(\frac{x}{r^2},\frac{y}{r^2},\frac{z}{r^2}\right); \quad (31)$$

$$V(x,y,z)=\frac{y}{r^3}U\left(\frac{x}{r^2},\frac{y}{r^2},\frac{z}{r^2}\right)+\frac{2xy}{r^5}U_x(v)+ \frac{-x^2+y^2-z^2}{r^5}U_y\left(\frac{x}{r^2},\frac{y}{r^2},\frac{z}{r^2}\right)+ \frac{2yz}{r^5}U_z\left(\frac{x}{r^2},\frac{y}{r^2},\frac{z}{r^2}\right); \quad (32)$$

$$V(x,y,z)=\frac{z}{r^3}U\left(\frac{x}{r^2},\frac{y}{r^2},\frac{z}{r^2}\right)+ \frac{2xz}{r^5}U_x\left(\frac{x}{r^2},\frac{y}{r^2},\frac{z}{r^2}\right)+ \frac{2yz}{r^5}U_y\left(\frac{x}{r^2},\frac{y}{r^2},\frac{z}{r^2}\right)+ \frac{-x^2-y^2+z^2}{r^5}U_z\left(\frac{x}{r^2},\frac{y}{r^2},\frac{z}{r^2}\right); \quad (33)$$

$$V(x,y,z)=\frac{x}{r^3}U_x\left(\frac{x}{r^2},\frac{y}{r^2},\frac{z}{r^2}\right)+ +\frac{y}{r^3}U_y\left(\frac{x}{r^2},\frac{y}{r^2},\frac{z}{r^2}\right)+\frac{z}{r^3}U_z\left(\frac{x}{r^2},\frac{y}{r^2},\frac{z}{r^2}\right); \quad (34)$$

$$V(x,y,z)=\frac{y}{r^3}U_x\left(\frac{x}{r^2},\frac{y}{r^2},\frac{z}{r^2}\right)- -\frac{x}{r^3}U_y\left(\frac{x}{r^2},\frac{y}{r^2},\frac{z}{r^2}\right); \quad (35)$$

$$V(x,y,z)=\frac{z}{r^3}U_x\left(\frac{x}{r^2},\frac{y}{r^2},\frac{z}{r^2}\right)- -\frac{x}{r^3}U_z\left(\frac{x}{r^2},\frac{y}{r^2},\frac{z}{r^2}\right); \quad (36)$$

$$V(x,y,z)=\frac{z}{r^3}U_y\left(\frac{x}{r^2},\frac{y}{r^2},\frac{z}{r^2}\right)- -\frac{y}{r^3}U_z\left(\frac{x}{r^2},\frac{y}{r^2},\frac{z}{r^2}\right), \quad (37)$$

where $r=\sqrt{x^2+y^2+z^2}$.

Eqs. (16)–(19) are trivial but we still included them in this list for formal reasons. The origin of Eqs. (20)–(22) is not obvious at first glance but they are evidently obtained from the Thomson formula (2) after it is differentiated with respect to one of the variables x, y, z and the Thomson transformation (2) restoring the initial form of the arguments of the function U is applied again.

Eqs. (24)–(26) are mentioned in monograph [24] but for some reason only in relation to homogeneous harmonic functions of zero degree. We have not actually encountered Eq. (23), as well as Eqs. (20)–(22) before (which is not to say of course that there are no such references).

Eqs. (27)–(37) are obtained from Eqs. (16)–(26) using the Thomson transform. In particular, Eq. (27) is obtained from the identical transformation (16) and, by virtue of this, coincides with Eq. (2).

Unlike the original Thomson formula, repeated application of differentiating transformations (16)–(37) does not restore the initial form of the transformed functions. However, some combinations of transformations (16)–(37) may turn out to be identical or again one the formulas from the given set. The reason for this is that the higher derivatives of the function U, appearing from combining differentiating transformations (16)–(37), can eventually be reduced, since the function U satisfies the Laplace equation.

Eqs. (16) and (23)–(26) for Euler-homogeneous functions preserve the degree of homo-

geneity of the function. Eqs. (17)–(19) reduce the degree of homogeneity of the function by one, and Eqs. (20)–(22) increase the degree of homogeneity of the function by one. Accordingly, homogeneous functions of degree k are transformed by Eqs. (27) and (34)–(37) into homogeneous functions of degree $(-k-1)$, into homogeneous functions of degree $(-k)$ by Eqs. (28)–(30), and into homogeneous functions of degree $(-k-2)$ by Eqs. (31)–(33).

The same as Eq. (16), Eqs. (23) and (34) are completely useless for Euler-homogeneous harmonic functions. It follows from the differential Euler relation (6) for homogeneous functions [21, 22] that applying Eq. (23) yields the same homogeneous harmonic function, only multiplied by a constant (degree of homogeneity). Accordingly, applying Eq. (34) is equivalent to applying Eq. (27) multiplied by a constant.

Generalization to the case of *n* variables

It is known that the Thomson formula (2) for 3D harmonic functions can be generalized to the multidimensional case [7, 9]. If

$$V\left(x_1,x_2,\ldots x_n\right)=\frac{1}{r^{n-2}}U\left(\frac{x_1}{r^2},\frac{x_2}{r^2},\cdots,\frac{x_n}{r^2}\right), \quad (38)$$

where $r=\sqrt{x_1^2+x_2^2+\cdots+x_n^2}$, and the function U is harmonic (i.e., it satisfies the n dimensional Laplace equation), then the function V is also harmonic. The result of substituting the function

$$V\left(x_1,x_2,\ldots x_n\right)=\frac{1}{r^m}U\left(\frac{x_1}{r^2},\frac{x_2}{r^2},\cdots,\frac{x_n}{r^2}\right)=$$
$$=\frac{1}{r^m}U^*\left(x_1,x_2,\cdots,x_n\right)$$

into the Laplace equation is a chain of equalities

$$\sum_{i=1}^{n}\frac{\partial^2}{\partial x_i^2}\left(\frac{1}{r^m}U^*\right)=U^*\sum_{i=1}^{n}\frac{\partial^2}{\partial x_i^2}\left(\frac{1}{r^m}\right)+$$
$$+2\sum_{i=1}^{n}\frac{\partial U^*}{\partial x_i}\frac{\partial}{\partial x_i}\left(\frac{1}{r^m}\right)+\frac{1}{r^m}\sum_{i=1}^{n}\frac{\partial^2 U^*}{\partial x_i^2};$$
$$\frac{\partial U^*}{\partial x_i}=\sum_{k=1}^{n}\frac{\partial U}{\partial x_k}\left(\frac{-2x_ix_k}{r^4}\right)+\frac{\partial U}{\partial x_i}\frac{1}{r^2};$$
$$\frac{\partial^2 U^*}{\partial x_i^2}=\sum_{k=1}^{n}\frac{\partial U}{\partial x_k}\left(\frac{-2x_k}{r^4}+\frac{8x_i^2x_k}{r^6}\right)+\frac{\partial U}{\partial x_i}\left(\frac{-2x_i}{r^4}\right)+$$
$$+\sum_{s=1}^{n}\sum_{k=1}^{n}\frac{\partial^2 U}{\partial x_k\partial x_s}\left(\frac{4x_i^2x_kx_s}{r^8}\right)+\sum_{k=1}^{n}\frac{\partial^2 U}{\partial x_k\partial x_i}\left(\frac{-2x_ix_k}{r^6}\right)+$$
$$+\frac{\partial U}{\partial x_i}\left(\frac{-2x_i}{r^4}\right)+\sum_{k=1}^{n}\frac{\partial^2 U}{\partial x_k\partial x_i}\left(\frac{-2x_ix_k}{r^6}\right)+\frac{\partial^2 U}{\partial x_i^2}\frac{1}{r^4};$$
$$\frac{\partial}{\partial x_i}\left(\frac{1}{r^m}\right)=\frac{-mx_i}{r^{m+2}};$$
$$\frac{\partial^2}{\partial x_i^2}\left(\frac{1}{r^m}\right)=\frac{-m}{r^{m+2}}+\frac{m\left(m+2\right)x_i^2}{r^{m+4}},$$

using, as arguments for function U, the values

$$x_1/r^2,\ x_2/r^2,\ \ldots,\ x_n/r^2.$$

Ultimately, because $\sum_{i=1,n}x_i^2=r^2$, we obtain the identity

$$\sum_{i=1}^{n}\frac{\partial^2}{\partial x_i^2}\left(\frac{U^*}{r^m}\right)=\frac{m\left(m+2-n\right)}{r^{m+2}}U+$$
$$+\frac{2\left(m+2-n\right)}{r^{m+4}}\sum_{k=1}^{n}x_k\frac{\partial U}{\partial x_k}+\frac{1}{r^{m+4}}\sum_{i=1}^{n}\frac{\partial^2 U}{\partial x_i^2},$$

whose right-hand side for harmonic functions U becomes zero for $m=n-2$. Notably, Eq. (38) remains valid, including with $n=2$, when it turns out to be a particular case of a conformal transformation of a plane (or, more precisely, anti-conformal transform, i.e., with a change in the direction in which angles are measured):

$$V\left(x,y\right)=U\left(\frac{x}{x^2+y^2},\frac{y}{x^2+y^2}\right).$$

Formulas including partial derivatives of the first order from the previous section are also transferred to the multidimensional case:

$$V\left(x_1,x_2,\ldots x_n\right)=U\left(x_1,x_2,\ldots x_n\right); \quad (39)$$

$$V\left(x_1,x_2,\ldots x_n\right)=\frac{\partial U\left(x_1,x_2,\ldots x_n\right)}{\partial x_i}; \quad (40)$$

$$V\left(x_1,x_2,\ldots x_n\right)=\left(n-2\right)x_iU\left(x_1,x_2,\ldots x_n\right)+$$
$$+\left(2x_i^2-r^2\right)\frac{\partial U\left(x_1,x_2,\ldots x_n\right)}{\partial x_i}+ \quad (41)$$
$$+\sum_{k\neq i}2x_ix_k\frac{\partial U\left(x_1,x_2,\ldots x_n\right)}{\partial x_k};$$

$$V\left(x_1,x_2,\ldots x_n\right)=\sum_k x_k\frac{\partial U\left(x_1,x_2,\ldots x_n\right)}{\partial x_k};\quad (42)$$

$$V\left(x_1,x_2,\ldots x_n\right)=x_i\frac{\partial U\left(x_1,x_2,\ldots x_n\right)}{\partial x_j}-x_j\frac{\partial U\left(x_1,x_2,\ldots x_n\right)}{\partial x_i};\quad (43)$$

$$V\left(x_1,x_2,\ldots x_n\right)=\frac{1}{r^{n-2}}U\left(\frac{x_1}{r^2},\frac{x_2}{r^2},\cdots,\frac{x_n}{r^2}\right);\quad (44)$$

$$V\left(x_1,x_2,\ldots x_n\right)=\frac{1}{r^{n-2}}\frac{\partial U}{\partial x_i}\left(\frac{x_1}{r^2},\frac{x_2}{r^2},\cdots,\frac{x_n}{r^2}\right);\quad (45)$$

$$V\left(x_1,x_2,\ldots x_n\right)=\frac{(n-2)x_i}{r^n}U\left(\frac{x_1}{r^2},\frac{x_2}{r^2},\cdots,\frac{x_n}{r^2}\right)+\frac{\left(2x_i^2-r^2\right)}{r^{n+2}}\frac{\partial U}{\partial x_i}\left(\frac{x_1}{r^2},\frac{x_2}{r^2},\cdots,\frac{x_n}{r^2}\right)+\sum_{k\neq i}\frac{2x_ix_k}{r^{n+2}}\frac{\partial U}{\partial x_k}\left(\frac{x_1}{r^2},\frac{x_2}{r^2},\cdots,\frac{x_n}{r^2}\right);\quad (46)$$

$$V\left(x_1,x_2,\ldots x_n\right)=\sum_k\frac{x_k}{r^n}\frac{\partial U}{\partial x_k}\left(\frac{x_1}{r^2},\frac{x_2}{r^2},\cdots,\frac{x_n}{r^2}\right);\quad (47)$$

$$V\left(x_1,x_2,\ldots x_n\right)=\frac{x_i}{r^n}\frac{\partial U}{\partial x_j}\left(\frac{x_1}{r^2},\frac{x_2}{r^2},\cdots,\frac{x_n}{r^2}\right)-\frac{x_j}{r^n}\frac{\partial U}{\partial x_i}\left(\frac{x_1}{r^2},\frac{x_2}{r^2},\cdots,\frac{x_n}{r^2}\right),\quad (48)$$

where $r=\sqrt{x_1^2+x_2^2+\cdots+x_n^2}$.

In contrast to the three-dimensional case, we cannot be certain that the given formulas exhaust the entire list of symmetric homogeneous algebraic formulas including first derivatives transforming an arbitrary n dimensional harmonic function into a new n dimensional harmonic function.

Eq. (46) is obtained by differentiating Eq. (38) with respect to the variable x_i. Eq. (41) is obtained from Eq. (46) using substitution (38). Substitution (38) is also used to obtain Eq. (47) from Eq. (42) and Eq. (48) from Eq. (43). Finally, we can verify that Eq. (42) is valid by using the identity

$$\sum_i\frac{\partial^2V\left(x_1,\ldots x_n\right)}{\partial x_i^2}\equiv\sum_i\frac{\partial^2U\left(x_1,\ldots x_n\right)}{\partial x_i^2}+\sum_k\left(x_k\frac{\partial}{\partial x_k}\left(\sum_i\frac{\partial^2U\left(x_1,\ldots x_n\right)}{\partial x_i^2}\right)\right),$$

which is satisfied for any functions V of the form (42), that Eq. (43) is valid using the identity

$$\sum_k\frac{\partial^2V\left(x_1,\ldots x_n\right)}{\partial x_k^2}\equiv\equiv x_i\frac{\partial}{\partial x_j}\left(\sum_k\frac{\partial^2U\left(x_1,\ldots x_n\right)}{\partial x_k^2}\right)-x_j\frac{\partial}{\partial x_i}\left(\sum_k\frac{\partial^2U\left(x_1,\ldots x_n\right)}{\partial x_k^2}\right),$$

which is satisfied for any functions of V form (43).

Conclusion

The study presents an exhaustive list of homogeneous symmetric differentiating expressions of the first order transforming arbitrary 3D harmonic functions into new 3D harmonic functions. We have generalized the formulas obtained to the case of an arbitrary number of measurements.

There are similar formulas using partial derivatives of higher orders. In particular, such formulas can be obtained by multiple differentiation of the Thomson formula (2) with respect to the variables x, y and z, and by superposition of first-order differential transformations obtained in this study (16)–(37). Compiling a complete list of transforming formulas with derivatives of higher orders is beyond the scope of this study; it is a task that presents considerable technical difficulties and, in our opinion, has little practical meaning.

It should be borne in mind for transformations with derivatives of higher orders that some partial derivatives of the second order and higher are expressed through each other for harmonic functions. Any transforming formula can be supplemented with the three-dimensional Laplace equation (1) with an arbitrary factor, in original form or after it is differentiated with respect to x, y or z the necessary number of times. This does not change the nature of the transformation (only its algebraic form) and, while its basic property to transform the original harmonic functions into new harmonic ones is preserved, additional analytical

expressions for 3D harmonic functions are not generated.

Notably, the calculations implicitly led to the assumption that substitution (10) is nondegenerate (reversible). It is possible that there are some additional solutions using changes of degenerate variables, not considered in this study. However, such degenerate transformations of harmonic functions apparently have little practical value, even if they do exist. For example, substituting constants for the arguments of any harmonic function, we obtain a constant, which is, of course, a harmonic function formally speaking, but it is completely useless for practical purposes.

The weak point of the analysis carried out is the assumption that the change of variables has a symmetric form,

$$f(x, y, z) = x\varphi(x, y, z),$$
$$g(x, y, z) = y\varphi(x, y, z),$$
$$h(x, y, z) = z\varphi(x, y, z),$$

while all functions involved in the differential/algebraic Eq. (13) are Euler-homogeneous. We deliberately limited the list of solutions (16)–(37) to homogeneous symmetric linear differential expressions of the first order. There are perhaps additional differential/algebraic expressions of the form (13), different from solutions (16)–(37) and free from this constraint, which also transform 3D harmonic functions into new 3D harmonic functions. However, comprehensive analysis of such an extended [problem [57–60] is well beyond the goals set in our study.

We should also note that the approach described has proved useful and efficient for other equations of mathematical physics beside the Laplace equation (1). For example, similar differential transformations were considered in [61] for the multidimensional heat equation. Unfortunately, the results obtained in [61] cannot be directly transferred to the Laplace equation, even though it is the steady-state limit of the heat equation. The reason for this is that the transformations used in [61] explicitly include time in such a manner that stationary solutions are transformed into non-stationary.

Acknowledgments

This study continues the series of works considering the electron and ion optical properties of Euler-homogeneous electric and magnetic fields that can be represented in analytical form. This series carries on the tradition of analytical studies into the properties of electron and ion optical systems initiated by our mentor Yuri Konstantinovich Golikov (1942–2013), an outstanding theoretical physicist who worked at the Department of Physical Electronics of Peter the Great St. Petersburg Polytechnic University and generously shared with his students his deep encyclopedic knowledge of fundamental mathematical results obtained by prominent scholars of the 18th, 19th and early 20th centuries, more or less forgotten in this computer age.

We are deeply indebted to the creators, employees and sponsors of the websites of Bibliothиque Nationale de France [62] and Proceedings of the Royal Society of London [63], whose dedicated efforts made it possible for us to freely access unique archival materials [3 28, 29], for which we express our heartfelt gratitude. We also extend our gratitude to the creators, employees, and sponsors of the Numdam Digital Library [64] for providing open access to rare mathematical publications from French mathematical journals, in particular, the article published in 1883 [65]. Furthermore, the data we obtained from HathiTrust Digital Library [66] and Das Göttinger Digitalisierungszentrum (GDZ) [67] were incredibly useful for our studies of archival sources, providing access to the digitized version of Cambridge and Dublin Mathematical Journal, published at the end of the 19th century and containing the original publications by William Thomson and George Boole on the given subject. We express our sincere gratitude to these public organizations and foundations, selflessly engaged in preserving Europe's unique historical scientific heritage and granting open access to it.

The calculations given in this paper were carried out using the Wolfram Mathematica software [68].

This study was partially carried out within the framework of State Task No. 075-00780-19-00 of the Institute for Analytical Instrumentation of the Russian Academy of Sciences.

REFERENCES

1. **Sretensky L.N.,** Teoriya niyutonovskogo potentsiala [Theory of the Newtonian potential], Moscow, Leningrad, OGIZ-GITTL, 1946.

2. **Golikov Yu.K.,** Analytical ways of describing harmonic functions, Vestnik of Aktobe's K. Zhubanov Regional State University, Physics and Mathematics. (2(44)) (2016) 165–181.

3. **Thomson W.,** Extraits de deux Lettres adressйes a M. Liouville, Journal de mathйmatiques pures et appliquйs. 12 (1847) 256–264.

4. **Thomson W. (Lord Kelvin), Tait P.G.,** Treatise on natural philosophy, 2nd Ed., Part 1, University Press, Cambridge, 1912.

5. **Thomson W. (Lord Kelvin), Tait P.G.,** Treatise on natural philosophy, 2nd Ed., Part 2, University Press, Cambridge, 1912.

6. **Smirnov V.I.,** A course of higher mathematics, Vol. 4: Integral equations and partial differential equations, Pergamon Press, Oxford, 1964.

7. **Vladimirov V.S.,** Uravneniya matematicheskoy fiziki [Equations of mathematical physics], Mir Publishers, Moscow, 1984.

8. **Kellogg O.D.**, Foundations of potential theory, Springer-Verlag, Berlin, Heidelberg, New-York, 1967.

9. **Wermer J.,** Potential theory, 2nd Ed., Ser. "Lecture Notes in Mathematics", Vol. 408, Springer-Verlag, Berlin, Heidelberg, New-York, 1981.

10. **Helms L.L.** Potential theory, 2nd Ed., Springer, London, Heidelberg, New-York, Dordrecht, 2014.

11. **Golikov Yu.K., Utkin K.G., Cheparuhin V.V.,** Raschet elementov elektrostaticheskikh elektronno-opticheslikh sistem [Design of elements of electron optical systems], Leningrad Polytechnic Inst. Publishing, Leningrad, 1984.

12. **Golikov Yu.K., Solovyov K.V.,** Elektrostaticheskiye ionnyye lovushki [Electrostatic ion traps], Saint-Petersburg Polytechnic University Publishing, Saint-Petersburg, 2008.

13. **Golikov Yu.K., Krasnova N.K.,** Teoriya synteza elektrostaticheskikh energoanalizatorov [Theory of designing of electrostatic energy analyzers], Saint-Petersburg Polytechnic University Publishing, Saint-Petersburg, 2010.

14. **Golikov Yu.K., Krasnova N.K.,** Application of electric fields uniform in the Euler sense in electron spectrography, Technical Physics. 56 (2) (2011) 164–170.

15. **Krasnova N.K.,** Theory and synthesis of disperging and focusing electron optical media, Dr. Sci. Thesis. St. Petersburg, 2013. (in Russian).

16. **Gabdullin P.G., Golikov Yu.K., Krasnova N.K., Davydov S.N.,** The use of Donkin's formula in the theory of energy analyzers, I, Technical Physics. 45 (2) (2000) 232–235.

17. **Gabdullin P.G., Golikov Yu.K., Krasnova N.K., Davydov S.N.,** The use of Donkin's formula in the theory of energy analyzers, II, Technical Physics. 45 (3) (2000) 330–333.

18. **Golikov Yu.K., Krasnova N.K.,** Analytical structures of generalized homogeneous electrical spectrographic media, Nauchnoe priborostroenie (Scientific Instrumentation). 24 (1) (2014) 50–58.

19. **Golikov Yu.K., Krasnova N.K.,** Generalized similarity principle of similarity in electron spectrography, Prikladnaya fizika (Applied Physics). (2) (2007) 5–11.

20. **Averin I.A., Berdnikov A.S., Gall N.R.,** The principle of similarity of trajectories for the motion of charged particles with different masses in electric and magnetic fields that are homogeneous in Euler terms, Technical Physics Letters. 43 (2) (2017) 156–158.

21. **Fichtenholz G.M.,** Differential- und Integralrechnung, I, VEB Deutscher Verlag der Wissenschaften, Berlin. 1968.

22. **Smirnov V.I.**, A course of higher mathematics, Vol. I: Elementary Calculus, Pergamon Press, Oxford, 1964.

23. **Berdnikov A.S., Averin I.A., Krasnova N.K., Solovyev K.V.,** On homogeneity of scalar and vector potentials of electric and magnetic fields, homogeneous in Euler terms, Uspekhi Prikladnoi Fiziki (Advances in Applied Physics). 5 (1) (2017) 10–27.

24. **Hobson E.W.,** The theory of spherical and ellipsoidal harmonics, University Press, Cambridge, 2012.

25. **Berdnikov A.S., Krasnova N.K., Solovyev K.V.,** The theorem on the differentiation of three-dimensional electric and magnetic potentials, homogeneous in Euler terms, Nauchnoe priborostroenie (Scientific Instrumentation). 27 (3) (2017) 107–119.

26. **Berdnikov A.S., Averin I.A., Krasnova N.K., Solovyev K.V.,** General formulas for three-dimensional electric and magnetic potentials homogeneous in Euler terms with an integer order of homogeneity, Nauchnoe priborostroenie (Scientific Instrumentation). 2016. Vol. 26 (4) (2016) 13–30.

27. **Whittaker E.T., Watson G.N.,** A course of modern analysis, University Press, Cambridge, 1950.

28. **Donkin W.F.,** On the equation of Laplace's functions &c., Philosophical Transactions of the

Royal Society of London. 147 (1857) 43–57.

29. **Donkin W.F.,** On the equation of Laplace's functions &c., Philosophical Proceedings of the Royal Society of London. 8 (1856–1857) 307–310.

30. **Golikov Yu.K.,** Resheniye zadachi Koshy dlya odnorodnykh garmonicheskikh potentsialov nulevoy plotnosty [Solution of the Cauchy problem for homogeneous harmonic potentials of a zero power], Vestnik of Aktobe's K. Zhubanov Regional State University, Physics and Mathematics. (2 (44)) (2016) 59–62.

31. **Golikov Yu.K., Berdnikov A.S., Antonov A.S., et al.,** Application of the Donkin formula in the theory of electrostatic prisms, Technical Physics. 63 (11) (2018) 1659–1666.

32. **Gьnther N.M.,** Integrirovaniye uravneniy v chastnykh proizvodnykh pervogo poryadka [Integration of first-order partial differential equations], ONTI, Leningrad, Moscow, 1934.

33. **Tricomi F.G.,** Lezioni sulle equazioni a derivative parziali, Editrice Gherono, Torino, 1954.

34. **Rashevsky P.K.,** Geometricheskaya teoriya uravneniy s chastnymy proizvodnymy [Geometric theory of partial differential equations], OGIZ, Moscow, Leningrad, 1947.

35. **Finikov S.P.,** Metod vneshnikh form Kartana v differentsialnoy geometriy [Cartan's method of exterior forms in differential geometry], OGIZ, Moscow, Leningrad, 1948.

36. **Cartan Й.,** Les systиmes diffйrentiels extйrieurs et leurs applications gйomйtriques, Ser. "Actualitйs Scientifiques et Industrielles", No. 994, Hermann, Paris, 1945.

37. **Shcherbakov R.N.,** Osnovy metoda vneshnikh form i lineuchatoy differentsialnoy geometriy [Fundamentals of the method of external forms and differential line geometry], Tomsk State University Publishing House, Tomsk, 1973.

38. **Kaptsov O.V.,** Metody integrirovaniya uravneniy s chastnymy proizvodnymy [Methods for integrating partial differential equations], Fizmatlit, Moscow, 2009.

39. **Janushauskas A.,** Harmonic mappings as defined by M.A. Laurentiev, In: Partial Differential Equations, Banach Center Publications. 10 (1) (1983) 213–241.

40. **Janushauskas A.I.,** Tryokhmernyye analogui konformnykh otobrazheniy [Three-dimensional analogues of conformal mappings], Nauka, Novosibirsk, 1982.

41. **Koppenfels W., Stallmann F.,** Praxis der Konformen Abbildung, Springer-Verlag, Berlin, Göttingen, Heidelberg, 1959.

42. **Lavrent'ev M.A., Shabat B.V.,** Methoden der komplexen Funktionen-theorie, Verlag Wissenshaft, 1969.

43. **Markushevich A.I.,** Theory of functions of a complex variable, Vol. 1–3, Providence, US, Amer. Math. Society Publ., 2005.

44. **Evgrafov M.A.,** Analytic functions, Dover Publ., 1978.

45. **Hurwitz A., Courant R.,** Vorlesungen Uber Allgemeine Funktionentheorie und Elliptische Funktionen, Springer, Berlin. 1964.

46. **Klein F.,** Vorlesungen ьber höhere Geometrie, Verlag von Julius Springer, Berlin, 1926.

47. **Reshetnyak Yu.G.,** Teorema Liuvilya o konformnykh otobrazheniyakh pri minimalnykh predpolozheniyakh regulyarnosty [Liouville's theorem on conformal mappings for minimal regularity assumptions], Siberian Mathematical Journal. 8 (4) (1967) 631–634.

48. **Flanders H.,** Liouville's theorem on conformal mapping, Journal of Mathematics and Mechanics. 15 (1) (1966) 157–161.

49. **Phillips R.,** Liouville's theorem, Pacific Journal. 28 (2) (1969) 397–405.

50. **Blair D.E.,** Inversion theory and conformal mapping, Ser. "Student Mathematical Library", Vol. 9, American Mathematical Society, 2000.

51."Liouville's theorem (conformal_ mappings)", URL: https:// en.wikipedia. org/ wiki/.

52. **Rashevsky P.K.,** Introduction to Riemannian geometry and tensor analysis, ONTI NKTP USSR, Moscow, Leningrad, 1936.

53. **Kobayashi S.,** Transformation groups in differential geometry, Ser. "Classics in Mathematics", Vol. 70, New York: Springer-Verlag, Berlin, 1995.

54. **Wilker J.B.,** Inversive geometry, In: Davis C., Grьnbaum B., Sherk F.A. (Eds.) The Geometric Vein, Springer, New York (1981) 379–442.

55. "Möbius transformation", Section "Higher dimensions", URL: https://en.wikipedia.org/ wiki/.

56. **Korn G.A., Korn T.M.,** Mathematical handbook for scientists and engineers, Definitions, theorems and formulas for reference and review, 2nd Ed., McGraw-Hill Book Company, New York, San Francisco, Toronto, London, Sydney, 1968.

57. **Bulyanitsa A.L., Kurochkin V.E.,** Studying ordering processes in open systems (on the example of pattern evolution in colonies of imperfect mycelial fungi), Nauchnoye priborostroyeniye (Scientific Instrumentation). 10 (2) (2000) 43–49.

58. **Bulyanitsa A.L., Evstrapov A.A.,**

Rudnitskaya G.E., Calculation of microscale system channel parameters by the method of moments, Nauchnoye priborostroyeniye (Scientific Instrumentation). 13 (4) (2003) 28–40.

59. **Evstrapov A.A., Bulyanitsa A.L., Rudnitskaya G.E., et al.,** Characteristic features of digital signal filtering algorithms as applied to electrophoresis on a microchip, Nauchnoye priborostroyeniye (Scientific Instrumentation). 13 (2) (2003) 57–63.

60. **Bulyanitsa A.L.,** Mathematical modeling in microfluidics: basic concepts, Nauchnoye priborostroyeniye (Scientific Instrumentation). 15 (2) (2005) 51–66.

61. **Brzezina M., Šimůnková M.,** On the harmonic morphism for the Kolmogorov type operators, In: Král J., Lukeš J., Netuka I., Veselý J. (Eds.), Potential Theory – ICPT-94, Walter de Gruyter, Berlin, New York (1996) 341–358.

62. Bibliothèque nationale de France, URL: http://gallica.bnf.fr.

63. Proceedings of the Royal Society of London, URL: http://rspl.royalsocietypublishing.org.

64. Numdam, the French digital mathematics library, URL: http://www.numdam.org/.

65. **Floquet G.**, Sur les equations différentielles linéaires a coefficients périodiques, Annales scientifiques de l'École Normale Supérieure, 2e serій. 12 (1883) 47–88.

66. HathiTrust Digital Library, URL: https://www.hathitrust.org/.

67. Das Göttinger Digitalisierungszentrum (GDZ), URL: https://gdz.sub.uni-goettingen.de/.

68. Wolfram Mathematica, URL: http://wolfram.com/mathematica/.

Received 21.03.2019, accepted 15.04.2019.

THE AUTHORS

BERDNIKOV Alexander S.
Institute for Analytical Instrumentation of the Russian Academy of Sciences
26 Rizhsky Ave., St. Petersburg, 190103, Russian Federation
asberd@yandex.ru

GALL Lidia N.
Institute for Analytical Instrumentation of the Russian Academy of Sciences
26 Rizhsky Ave., St. Petersburg, 190103, Russian Federation
lngall@yandex.ru

GALL Nikolaj R.
Institute for Analytical Instrumentation of the Russian Academy of Sciences
26 Rizhsky Ave., St. Petersburg, 190103, Russian Federation
gall@ms.ioffe.ru

SOLOVYEV Konstantin V.
Peter the Great St. Petersburg Polytechnic University
29 Politechnicheskaya St., St. Petersburg, 195251, Russian Federation
k-solovyev@mail.ru

СПИСОК ЛИТЕРАТУРЫ

1. **Сретенский Л.Н.** Теория ньютоновского потенциала. Москва, Ленинград: ОГИЗ-ГИТТЛ, 318 .1946 с.

2. **Голиков Ю.К.** Аналитические способы описания гармонических функций // Вестник Актюбинского регионального государственного университета им. К. Жубанова. Физико-математические науки. 44) 2 № .2016). С. 165–181.

3. **Thomson W.** Extraits de deux Lettres adressées a M. Liouville // Journal de Mathématiques Pures et Appliquées. 1847. Tome XII. Pp. 256–264.

4. **Томсон У. (лорд Кельвин), Тэт П.Г.** Трактат по натуральной философии. Ч. I. Москва, Ижевск: НИЦ «Регулярная и хаотическая динамика», 2010. 572 с.

5. **Томсон У. (лорд Кельвин), Тэт П.Г.** Трактат по натуральной философии. Ч. II. Москва, Ижевск: НИЦ «Регулярная и

хаотическая динамика», 2011. 560 с.

6. **Смирнов В.И.** Курс высшей математики. Т. 4. Ч. 2. М.: Наука, 297 .1981 с.

7. Владимиров В.С. Уравнения математической физики. М.: Наука, 1981. 512 с.

8. **Kellogg O.D.** Foundations of potential theory. Berlin, Heidelberg, New-York: Springer-Verlag, 1967. 386 p.

9. **Уэрмлер Дж.** Теория потенциала. М.: Мир, 1980. 134 с.

10. **Helms L.L.** Potential theory. 2nd Ed. London, Heidelberg, New-York, Dordrecht: Springer, 2014. 485 p.

11. **Голиков Ю.К., Уткин К.Г., Чепарухин В.В.** Расчет элементов электростатических электронно-оптических систем. Ленинград: Изд-во ЛПИ, 79 .1984 с.

12. **Голиков Ю.К., Соловьёв К.В.** Электростатические ионные ловушки. СПб.: Изд-во Политехнического ун-та, 152 .2008 с.

13. **Голиков Ю.К., Краснова Н.К.** Теория синтеза электростатических энергоанализаторов. СПб.: Изд-во Политехнического ун-та, 409 .2010 с.

14. **Голиков Ю.К., Краснова Н.К.** Электрические поля, однородные по Эйлеру, для электронной спектрографии // Журнал технической физики. 2011. Т. 2 № .81. С. 9—15.

15. **Краснова Н.К.** Теория и синтез диспергирующих и фокусирующих электронно-оптических сред. Дис.... докт. физ.-мат. наук. 01.04.04. СПб.: СПбГПУ, 2013. 259 с.

16. **Габдуллин П.Г., Голиков Ю.К., Краснова Н.К., Давыдов С.Н.** Применение формулы Донкина в теории энергоанализаторов. I. // Журнал технической физики. 2000. Т. 70. № 2. С. 91—94.

17. **Габдуллин П.Г., Голиков Ю.К., Краснова Н.К., Давыдов С.Н.** Применение формулы Донкина в теории энергоанализаторов. II. // Журнал технической физики. 2000. Т. 70. № 3. С. 44—47.

18. **Голиков Ю.К., Краснова Н.К.** Аналитические структуры электрических обобщенно-однородных спектрографических сред // Научное приборостроение. 2014. Т. .24 1 №. С. 50—58.

19. **Голиков Ю.К., Краснова Н.К.** Обобщенный принцип подобия и его применение в электронной спектрографии // Прикладная физика. 2 № .2007. С. 11—5.

20. **Аверин И.А., Бердников А.С., Галль Н.Р.** Принцип подобия траекторий при движении заряженных частиц с разными массами в однородных по Эйлеру электрических и магнитных полях // Письма в Журнал технической физики. 2017. Т. 3 № .43. С. —39 43.

21. **Фихтенгольц Г.М.** Курс дифференциального и интегрального исчисления. Т. 1. М.: Физматлит, 616 .2001 с.

22. **Смирнов В.И.** Курс высшей математики. Т. 1. М.: Наука, 480 .1974 с.

23. **Бердников А.С., Аверин И.А., Краснова Н.К., Соловьёв К.В.** Об однородности скалярных и векторных потенциалов электрических и магнитных полей, однородных по Эйлеру // Успехи прикладной физики. 2017. Т. 1 № .5. С. 27—10.

24. **Гобсон Е.В.** Теория сферических и эллипсоидальных функций. М.: Изд-во иностр. лит-ры, 476 .1952 с.

25. **Бердников А.С., Краснова Н.К., Соловьёв К.В.** Теорема о дифференцировании трехмерных электрических и магнитных потенциалов, однородных по Эйлеру // Научное приборостроение. 2017. Т. 3 № .27. С. 107—119.

26. **Бердников А.С., Аверин И.А., Краснова Н.К., Соловьёв К.В.** Общие формулы для трехмерных электрических и магнитных потенциалов, однородных по Эйлеру, с целочисленным порядком однородности // Научное приборостроение. 2016. Т. 4 № .26. С. 13—30.

27. **Уиттекер Э.Т., Ватсон Дж.** Курс современного анализа. Ч. 2: Трансцендентные функции. М.: Гос. изд-во физ.-мат. лит-ры, 1963. 516 с.

28. **Donkin W.F.** On the equation of Laplace‘s functions &c. // Philosophical Transactions of the Royal Society of London. 1857. Vol. 147. Pp. 43—57.

29. **Donkin W.F.** On the equation of Laplace‘s functions &c. // Proceedings of the Royal Society of London. 1856 —1857. Vol. 8. Pp. 307—310.

30. **Голиков Ю.К.** Решение задачи Коши для однородных гармонических потенциалов нулевой кратности // Вестник Актюбинского регионального государственного университета им. К. Жубанова. Физико-математические науки. 44) 2 № .2016). С. 59—62.

31. **Голиков Ю.К., Бердников А.С., Антонов А.С., Краснова Н.К., Соловьёв К.В.** Применение формулы Донкина в теории электростатических призм // Журнал технической физики. 2018. Т. 11 № .88. С. 1711—1719.

32. **Гюнтер Н.М.** Интегрирование уравнений в частных производных первого порядка.

Ленинград, Москва: ОНТИ, 368 .1934 с.

33. **Трикоми Ф.** Лекции по уравнениям в частных производных. М.: Изд-во иностр. лит-ры, 443 .1957 с.

34. **Рашевский П.К.** Геометрическая теория уравнений с частными производными. Москва, Ленинград: ГИТТЛ, 362 .1947 с.

35. **Фиников С.П.** Метод внешних форм Картана в дифференциальной геометрии. Москва, Ленинград: ОГИЗ, 432 .1948 с.

36. **Картан Э.** Внешние дифференциальные системы и их геометрические приложения. М.: Изд-во Московского ун-та, 237 .1962 с.

37. **Щербаков Р.Н.** Основы метода внешних форм и линейчатой дифференциальной геометрии. Томск: Изд-во ТГУ, 236 .1973 с.

38. **Капцов О.В**. Методы интегрирования уравнений с частными производными. М.: Физматлит, 184 .2009 с.

39. **Янушаускас А.** Гармонические по М.А. Лаврентьеву отображения // Partial Differential Equations. Banach Center Publications. 1983. Vol. 10. No. 1. Pp. 213–241.

40. **Янушаускас А.И.** Трехмерные аналоги конформных отображений. Новосибирск: Наука, 173 .1982 с.

41. **Коппенфельс В., Штальман Ф.** Практика конформных отображений. М.: Изд-во иностр. лит-ры, 406 .1963 с.

42. **Лаврентьев М.А., Шабат Б.В.** Методы теории функций комплексного переменного. М.: Наука, 716 .1965 с.

43. **Маркушевич А.И.** Теория аналитических функций. В 2 тт. М.: Наука, 1968. Т. 1 – 486 с., Т. 2 – 624 с.

44. **Евграфов М.А.** Аналитические функции. -3е изд., перераб. и доп. М.: Наука, 448 .1991 с.

45. **Гурвиц А., Курант Р.** Теория функций. М.: Наука, 646 .1968 с.

46. **Клейн Ф.** Высшая геометрия. Москва, Ленинград: ГОНТИ, 400 .1939 с.

47. **Решетняк Ю.Г.** Теорема Лиувилля о конформных отображениях при минимальных предположениях регулярности // Сибирский математический журнал. 1967. Т. 8. № 4. С. 835–840.

48. **Flanders H.** Liouville's theorem on conformal mapping // Journal of Mathematics and Mechanics. 1966. Vol. 15. No. 1. Pp. 157–161.

49. **Phillips R.** Liouville's theorem // Pacific Journal. 1969. Vol. 28. No. 2. Pp. 397–405.

50. **Blair D.E.** Inversion theory and conformal mapping. Ser. "Student Mathematical Library". Vol. 9 // American Mathematical Society. 2000. 118 p.

51. "Liouville's theorem (conformal_mappings)" // URL: https://en.wikipedia. org/wiki/.

52. **Рашевский П.К.** Введение в Риманову геометрию и тензорный анализ. Москва, Ленинград: ОНТИ НКТП СССР, 1936. 199 с.

53. **Kobayashi S.** Transformation groups in differential geometry. Ser. "Classics in Mathematics". Vol. 70. Berlin, New York: Springer-Verlag, 1995. 182 p.

54. **Wilker J.B.** Inversive geometry // Davis C., Grünbaum B., Sherk F.A. (Eds.) The Geometric Vein. New York: Springer, 1981. Pp. 379–442.

55. "Möbius transformation". "Higher dimensions" // URL: https://en. wikipedia.org/wiki/

56. **Корн Г., Корн Т.** Справочник по математике для научных работников и инженеров. Определения, теоремы, формулы. Пер. со 2-го американского переработанного издания. М.: Наука, 1973. 831 с.

57. **Буляница А.Л., Курочкин В.Е.** Исследование процессов упорядочивания в открытых системах // Научное приборостроение. 2000. Т. 10. № 2. С. 43–49.

58. **Буляница А.Л., Евстрапов А.А., Рудницкая Г.Е.** Метод моментов при расчете параметров каналов в микроразмерных системах // Научное приборостроение. 2003. Т. 13. № 4. С. 28–40.

59. **Евстрапов А.А., Буляница А.Л., Рудницкая Г.Е., Беленький Б.Г., Петряков А.О., Курочкин В.Е.** Особенности применения алгоритмов цифровой фильтрации электрофореграмм при анализе веществ на микрочипе // Научное приборостроение. 2003. Т. 13. № 2. С. 57–63.

60. **Буляница А.Л.** Математическое моделирование в микрофлюидике: основные положения // Научное приборостроение. 2005. Т. 15. № 2. С. 51–66.

61. **Brzezina M., Šimůnková M.** On the harmonic morphism for the Kolmogorov type operators // Král J., Lukeš J., Netuka I., Veselý J. (Eds.) Potential Theory – ICPT-94. Berlin, New York: Walter de Gruyter, 1996. Pp. 341 –358.

62. Bibliothèque nationale de France // URL: http://gallica.bnf.fr.

63. Proceedings of the Royal Society of London // URL: http://rspl.royalsocietypublishing.org.

64. Numdam, the French digital mathematics library // URL: http://www.numdam.org/.

65. **Floquet G.** Sur les equations différentielles linéaires à coefficients périodiques // Annales scientifiques de l'École Normale Supérieure. 2e Serié. 1883. Vol. 12. Pp. 47–88.

66. HathiTrust Digital Library // URL:

https://www.hathitrust.org/.
67. Das Göttinger Digitalisierungszentrum (GDZ) // URL: https://gdz.sub.uni-goettingen.de/.
68. Wolfram mathematica // URL : http://wolfram.com/mathematica/

Статья поступила в редакцию 21.03.2019, принята к публикации 15.04.2019.

СВЕДЕНИЯ ОБ АВТОРАХ

БЕРДНИКОВ Александр Сергеевич – *доктор физико-математических наук, ведущий научный сотрудник Института аналитического приборостроения РАН, Санкт-Петербург, Российская Федерация.*
190103, Российская Федерация, г. Санкт-Петербург, Рижский пр., 26
asberd@yandex.ru

ГАЛЛЬ Лидия Николаевна – *доктор физико-математических наук, главный научный сотрудник Института аналитического приборостроения РАН, Санкт-Петербург, Российская Федерация.*
190103, Российская Федерация, г. Санкт-Петербург, Рижский пр., 26
lngall@yandex.ru

ГАЛЛЬ Николай Ростиславович – *доктор физико-математических наук, ведущий научный сотрудник Института аналитического приборостроения РАН, Санкт-Петербург, Российская Федерация.*
190103, Российская Федерация, г. Санкт-Петербург, Рижский пр., 26
gall@ms.ioffe.ru

СОЛОВЬЕВ Константин Вячеславович – *кандидат физико-математических наук, доцент кафедры физической электроники Санкт-Петербургского политехнического университета Петра Великого, младший научный сотрудник Института аналитического приборостроения РАН, Санкт-Петербург, Российская Федерация.*
195251, Российская Федерация, г. Санкт-Петербург, Политехническая ул., 29
k-solovyev@mail.ru

DOI: 10.18721/JPM.12204
УДК 517.51; 517.28; 517.983; 537.213, 537.8

GENERALIZATION OF THE THOMSON FORMULA FOR HOMOGENEOUS HARMONIC FUNCTIONS

A.S. Berdnikov[1], *L.N. Gall*[1], *N.R. Gall*[1], *K.V. Solovyev*[2,1]

[1]Institute for Analytical Instrumentation of the Russian Academy of Sciences, St. Petersburg, Russian Federation;

[2]Peter the Great St. Petersburg Polytechnic University, St. Petersburg, Russian Federation

In the paper, it has been shown that the Thomson formula for three-dimensional harmonic homogeneous functions in Euler terms can be generalized using a linear algebraic form involving the first order partial derivatives of the initial function instead of pure algebraic linear expressions. An exhaustive list of the formed first order expressions converting arbitrary three-dimensional harmonic functions in Euler terms into new three-dimensional homogeneous harmonic functions was presented.

Keywords: electrostatic field, magnetostatic field, scalar potential, homogeneous function, harmonic function

Citation: Berdnikov A.S., Gall L.N., Gall N.R., Solovyev K.V. Generalization of the Thomson formula for homogeneous harmonic functions, St. Petersburg Polytechnical State University Journal. Physics and Mathematics. 12 (2) (2019) 48–60. DOI: 10.18721/JPM.12204

ОБОБЩЕНИЕ ФОРМУЛЫ ТОМСОНА ДЛЯ ГАРМОНИЧЕСКИХ ОДНОРОДНЫХ ФУНКЦИЙ

А.С. Бердников[1], *Л.Н. Галль*[1], *Н.Р. Галль*[1], *К.В. Соловьев*[2,1]

[1]Институт аналитического приборостроения Российской академии наук, Санкт-Петербург, Российская Федерация;

[2]Санкт-Петербургский политехнический университет Петра Великого, Санкт-Петербург, Российская Федерация

В работе показано, что формулу Томсона для трехмерных гармонических функций, однородных по Эйлеру, можно обобщить, если вместо чисто алгебраических линейных выражений использовать линейную алгебраическую форму с участием частных производных первого порядка от исходной функции. Приводится исчерпывающий список получающихся выражений первого порядка, преобразующих произвольные трехмерные однородные гармонические функции в новые трехмерные гармонические функции.

Ключевые слова: Ключевые слова: электростатическое поле, магнитостатическое поле, скалярный потенциал, уравнение Лапласа, формула Томсона

Ссылка при цитировании: Бердников А.С., Галль Л.Н., Галль Н.Р., Соловьев К.В. Обобщение формулы Томсона для гармонических однородных функций // Научно-технические ведомости СПбГПУ. Физико-математические науки. 2019. Т. 12. № 2. С. 49–62. DOI: 10.18721/JPM.12204

Introduction

This paper continues the studies in [1], considering generalizations of the Thomson formula for 3D harmonic functions of a general form. Differential-algebraic transformations similar to the classical Thomson formula for homogeneous harmonic functions were discussed. These transformations can be used to generate new harmonic functions represented in analytical form that are Euler-homogeneous. Electric and magnetic fields whose scalar potential (3D harmonic function) is an Euler-homogeneous function obey the principle of similarity of trajectories described by Golikov [2, 3]. Such fields possess additional useful electron and ion-= optical properties [4–10].

Let $r=\sqrt{x^2+y^2+z^2}$ be the distance from a sample point (x,y,z) to the origin. The Thomson formula (Kelvin transform)

$$V(x,y,z)=\frac{1}{r}U\left(\frac{x}{r^2},\frac{y}{r^2},\frac{z}{r^2}\right). \qquad (1)$$

transforms the harmonic function $U(x,y,z)$, satisfying the Laplace equation

$$U_{xx}+U_{yy}+U_{zz}=0, \qquad (2)$$

into a new harmonic function $V(x,y,z)$ [11–18]. From now on we use the subscripts x, y, z to denote partial derivatives with respect to the corresponding variables.

In particular, the Thomson formula (1) serves as a useful mathematical tool for generating analytical expressions for scalar potentials of electric and magnetic fields that can be used for synthesizing new electron and ion optical systems [4–10, 19, 20].

The function $U(x,y,z)$ is called Euler-homogeneous (or, more precisely, positively homogeneous) if it satisfies the identity

$$\forall\lambda>0:\ U(\lambda x,\lambda y,\lambda z)\equiv\lambda^m U(x,y,z),$$

where m is the degree of homogeneity of the function (not necessarily an integer) [21, 22].

For a continuously differentiable function $U(x,y,z)$ to be positively homogeneous with degree m, it is necessary and sufficient that the Euler differential equation for homogeneous functions be satisfied at any point in space (except for the origin):

$$xU_x+yU_u+zU_z-mU=0. \qquad (3)$$

The proof of this important statement can be found in [21, 22].

Searching among linear algebraic formulas of the type

$$V(x,y,z)=S(x,y,z)\times \\ \times U\big(f(x,y,z),g(x,y,z),h(x,y,z)\big) \qquad (4)$$

(where S, f, g, h are some fixed functions) of other relations that can generate new harmonic functions $V(x,y,z)$ for any harmonic functions $U(x,y,z)$, we verified that the Thomson formula (1) is, in a sense, unique [1, 15, 17].

Specifically, the Thomson formula (1) and the trivial identity $V(x,y,z) = U(x,y,z)$ are the only expressions of form (4) that meet the requirements of the problem stated to within 3D rotations around the origin, shifts (parallel translations)

$$x' = x + a,\ y' = y + b,\ z' = z + c,$$

symmetries

$$x' = -x,\ y' = -y,\ z' = -z$$

and proportional scaling

$$x' = kx,\ y' = ky,\ z' = kz$$

(as well as multiplication of the potentials obtained by a constant factor).

Considering linear expressions including first partial derivatives of the function U, which have the form

$$\begin{aligned} V(x,y,z)&= \\ &=S(x,y,z)\cdot U\big(f(x,y,z),g(x,y,z),h(x,y,z)\big)+ \\ &+P(x,y,z)\cdot U_x\big(f(x,y,z),g(x,y,z),h(x,y,z)\big)+ \\ &+Q(x,y,z)\cdot U_y\big(f(x,y,z),g(x,y,z),h(x,y,z)\big)+ \\ &+R(x,y,z)\cdot U_z\big(f(x,y,z),g(x,y,z),h(x,y,z)\big) \end{aligned} \qquad (5)$$

(S, P, Q, R, f, g, h are some fixed functions), we found that additional formulas transforming 3D harmonic functions into new 3D harmonic functions could exist [1].

Now the transformations are not purely algebraic but differential-algebraic. This expands the range of mathematical tools available for generating new 3D harmonic functions that serve as scalar potentials for electric and magnetic fields.

Increasing the order of partial derivatives of the function U included in expressions of form (5) expands the list of such formulas even further but also makes operations with them somewhat inconvenient. In particular, such formulas cannot be uniquely defined because the second derivatives of harmonic functions depend on each other. This is to say that there is a wide variety of such formulas

for each transformation: while their forms are not algebraically equivalent to each other, they yield essentially the same results.

Notably, however, we found a smaller amount of transformations preserving 3D harmonic functions in [1] than we had expected. One of the reasons why the search for new first-order algebraic and differential-algebraic expressions for generating 3D harmonic functions yielded unsatisfactory results might be that the requirement for these expressions to work for any initial harmonic functions $U(x,y,z)$ is too strict. For example, it is well known that any conformal transformation of the arguments for two-dimensional harmonic functions $U(x,y)$ generates a new two-dimensional harmonic function [23–27]. Such a transformation of harmonic functions has the form (4) but it is considerably different from the Thomson formula (1).

Another example is the Thomson formula for homogeneous harmonic functions (see [28] and [29], Appendix B to Chapter 1), which has the form

$$V(x,y,z) = r^{-2m-1}U(x,y,z). \qquad (6)$$

Function (6) becomes harmonic if a homogeneous harmonic function U of degree m substituted into it, but this is definitely not the case for any harmonic function U.

Finally, let us consider transformations of the form

$$\begin{gathered}
V(x,y,z) = CU_x(x,y,z) + \\
+BU_y(x,y,z) + AU_z(x,y,z); \\
A = a(2m+1)xz + b(2m+1)yz + \\
+c\left(-mx^2 - my^2 + (m+1)z^2\right); \\
B = a(2m+1)xy + \\
+b\left(-mx^2 + (m+1)y^2 - mz^2\right) + \\
+c(2m+1)yz; \\
C = a\left((m+1)x^2 - my^2 - mz^2\right) + \\
+b(2m+1)xy + c(2m+1)xz,
\end{gathered} \qquad (7)$$

that can be obtained by analyzing the harmonic conditions for linear forms of partial derivatives U_x, U_y, U_z with coefficients that are general quadratic forms in terms of variables x, y, z. It follows from the identity

$$\begin{gathered}
V_{xx} + V_{yy} + V_{zz} \equiv \\
\equiv (4m+2)(ax+by+cz)(U_{xx} + U_{yy} + U_{zz}) + \\
+C(U_{xxx} + U_{xyy} + U_{xzz}) + B(U_{xxy} + U_{yyy} + U_{yzz}) + \\
+A(U_{xxz} + U_{yyz} + U_{zzz}) + \\
+2a(xU_{xx} + yU_{xy} + zU_{xz} - (m-1)U_x) + \\
+2b(xU_{xy} + yU_{yy} + zU_{yz} - (m-1)U_y) + \\
+2c(xU_{xz} + yU_{yz} + zU_{zz} - (m-1)U_z)
\end{gathered}$$

that, generally speaking, if the only requirement imposed on the function U is for it to be harmonic, expression (7) is a harmonic function only if

$$a = b = c = 0.$$

If U is a homogeneous function of degree m, satisfying both the Laplace equation (2) and the Euler differential equation (3), then the conditions

$$\begin{gathered}
U_{xxx} + U_{xyy} + U_{xzz} = 0, \\
U_{xxy} + U_{yyy} + U_{yzz} = 0, \\
U_{xxz} + U_{yyz} + U_{zzz} = 0, \\
xU_{xx} + yU_{xy} + zU_{xz} = (m-1)U_x, \\
xU_{xy} + yU_{yy} + zU_{yz} = (m-1)U_y, \\
xU_{xz} + yU_{yz} + zU_{zz} = (m-1)U_z,
\end{gathered}$$

obtained by differentiating (2) and (3) with respect to x, y, z, are satisfied.

Then expression (7) turns out to be a harmonic homogeneous function of degree $(m+1)$ for any a, b, c.

The goal of this study has consisted in searching for alternative expressions that could be applicable for 3D homogeneous harmonic functions and useful for generating analytical expressions for 3D harmonic functions that are Euler-homogeneous.

There is good reason to believe that the set of transformations can be significantly expanded by limiting the class of transformed harmonic functions.

Problem statement

Let us consider the transformation of a 3D homogeneous harmonic function $U(x,y,z)$ in accordance with rule (5), where S, P, Q, R, f, g, h are some fixed functions, and U is an arbitrary homogeneous harmonic function of

a fixed degree m. We require that expression (5) be an Euler-homogeneous function for the given functions S, P, Q, R, f, g, h and any homogeneous harmonic functions U of degree m.

Since the function U should satisfy the Euler differential equation (3), we can assume for expression (5) without loss of generality that

$$R(x, y, z) = 0$$

(the partial derivative of U_z can be expressed in terms of the functions U, U_x, U_y).

Furthermore, let us confine ourselves to a particular case

$$f(x,y,z) \equiv x,\ g(x,y,z) \equiv y,$$
$$h(x,y,z) \equiv z,$$

which is a consequence of the symmetric change of variables

$$f(x,y,z) = x\varphi(x,y,z),$$
$$g(x,y,z) = y\varphi(x,y,z),$$
$$h(x,y,z) = z\varphi(x,y,z)$$

considered in [1] (here the common factor $\varphi(x,y,z)$ is taken out of the arguments of the functions U, U_x, U_y and U_z because these functions are Euler-homogeneous).

Thus, we are going to consider transformations of the following type below:

$$\begin{aligned} V(x,y,z) &= S_0(x,y,z)\cdot U(x,y,z) + \\ &+ P_0(x,y,z)\cdot U_x(x,y,z) + \\ &+ Q_0(x,y,z)\cdot U_y(x,y,z), \end{aligned} \tag{8}$$

where S_0, P_0, Q_0 are some fixed functions preserving the function V homogeneous and harmonic provided that the function U with a given degree of homogeneity m is homogeneous and harmonic.

For expression (5) to be an Euler-homogeneous function when an arbitrary homogeneous harmonic function U is substituted into it, the functions S, P, Q, R, f, g, h in expression (5) should satisfy some additional conditions.

In particular, we can prove for expressions of form (8) that the condition that S_0 is Euler-homogeneous of degree $n - m$ and P_0 and Q_0 are Euler-homogeneous of degree $n - m + 1$, is sufficient as well as necessary for expression (8) to be a homogeneous function of degree n.

To prove that it is necessary for the functions S_0, P_0 and Q_0 to be Euler-homogeneous, we use the condition that the function U is Euler-homogeneous without invoking the condition that it is harmonic. We should also verify that there are no additional options for homogeneous harmonic functions that are missing in case of arbitrary homogeneous functions. However, the constraints

$$f(x,y,z) = x,\ g(x,y,z) = y,$$
$$h(x,y,z) = z,\ R(x,y,z) = 0$$

guarantee that there are no other possible options for the functions S_0, P_0 and Q_0.

The obvious method for solving the problem is to remove all dependent partial derivatives of the function U from the result of substituting the expression (5) or (8) into the Laplace equation and into the Euler differential equation. After that, the factors grouped before the remaining partial derivatives of the function U should be equal to zero separately and independently of each other. "Extra" derivatives should be excluded, using not only the Laplace equation

$$U_{xx} + U_{yy} + U_{zz} = 0,$$

as done in [1], but also the Euler differential equation

$$xU_x + yU_y + zU_z = mU$$

for homogeneous functions of degree m, as well as the results of differentiation of the given equations with respect to the variables x, y, z.

The task is somewhat complicated by the fact that differential relations dependent on each other appear upon independent differentiation of the Laplace equation and the Euler differential relation:

$$\begin{aligned} &\left(xU_{xxx} + yU_{xxy} + zU_{xxz} - (m-2)U_{xx}\right) + \\ &+\left(xU_{xyy} + yU_{yyy} + zU_{yyz} - (m-2)U_{yy}\right) + \\ &+\left(xU_{xzz} + yU_{yzz} + zU_{zzz} - (m-2)U_{zz}\right) \equiv \\ &\equiv x\left(U_{xxx} + U_{xyy} + U_{xzz}\right) + \\ &+ y\left(U_{xxy} + U_{yyy} + U_{yzz}\right) + \\ &+ z\left(U_{xxz} + U_{yyz} + U_{zzz}\right) - \\ &-(m-2)\left(U_{xx} + U_{yy} + U_{zz}\right). \end{aligned}$$

However, there is a more effective way to solve the problem. Since $U(x,y,z)$ is an Euler-homogeneous function of degree m, by applying the change of variables used for the Donkin formula [7–10, 30–34], we can formulate it as

$$U(x,y,z) = r^m F\left(\frac{x}{z+r}, \frac{y}{z+r}\right), \tag{9}$$

where $r=\sqrt{x^2+y^2+z^2}$ and F is some appropriate function of two variables.

This formulation is a slightly modified universal representation of homogeneous functions of degree k in accordance with the formula [21, 22]:

$$f\left(x_1,x_2,\ldots,x_n\right)=x_1^k g\left(x_2/x_1,\ldots x_n/x_1\right);$$

it does not lead to loss of admissible solutions.

Accordingly, the transformed function $V(x,y,z)$, which should be an Euler-homogeneous function of degree n, can be represented as

$$V\left(x,y,z\right)=r^n G\left(\frac{x}{z+r},\frac{y}{z+r}\right). \qquad (10)$$

The change of variables used to construct substitutions (9) and (10) is reversible:

$$\begin{cases} p=\dfrac{x}{z+\sqrt{x^2+y^2+z^2}}, \\ q=\dfrac{y}{z+\sqrt{x^2+y^2+z^2}}, \\ r=\sqrt{x^2+y^2+z^2}, \end{cases} \Leftrightarrow$$

$$\Leftrightarrow \begin{cases} x=\dfrac{2pr}{1+p^2+q^2}, \\ y=\dfrac{2qr}{1+p^2+q^2}, \\ z=\pm\dfrac{r\left(1-p^2-q^2\right)}{1+p^2+q^2}. \end{cases} \qquad (11)$$

For the function U, given by equality (9), to be harmonic, that is, to satisfy the 3D Laplace equation, it is necessary and sufficient that the function F satisfy the two-dimensional elliptic equation

$$\frac{\partial^2 F\left(p,q\right)}{\partial p^2}+\frac{\partial^2 F\left(p,q\right)}{\partial q^2}+ +\frac{4m\left(m+1\right)}{\left(1+p^2+q^2\right)^2}F\left(p,q\right)=0. \qquad (12)$$

Then any homogeneous harmonic function U of degree m corresponds to the function F, which satisfies Eq. (12), substitution (9) yields a homogeneous harmonic function of degree n from any solution of equation (12), and there is one-to-one correspondence between the functions F and U. This statement is verified by direct substitution of expression (9) into the 3D Laplace equation, followed by change of variables according to rule (11). A similar technique is used, for example, in [35–39].

Evidently, the transformation of the function U according to rule (8), which should generate a new homogeneous harmonic function V of degree n, is equivalent to transformation of the function F according to the rule

$$G\left(p,q\right)=s\left(p,q\right)F\left(p,q\right)+ +v\left(p,q\right)\frac{\partial F\left(p,q\right)}{\partial p}+w\left(p,q\right)\frac{\partial F\left(p,q\right)}{\partial q} \qquad (13)$$

with some fixed functions

$$s(p,q),\ v(p,q),\ w(p,q),$$

the function G should then satisfy the equation

$$\frac{\partial^2 G\left(p,q\right)}{\partial p^2}+\frac{\partial^2 G\left(p,q\right)}{\partial q^2}+ +\frac{4n\left(n+1\right)}{\left(1+p^2+q^2\right)^2}G\left(p,q\right)=0. \qquad (14)$$

In the end the task is reduced to finding such functions $s(p,q)$, $v(p,q)$, $w(p,q)$ and such indices m and n that would generate the solutions of differential equation (14) after transformation (13) for any solution of differential equation (12). In this case, no additional conditions except Eqs. (12) and (14) are imposed on the functions F and G.

Solution of the problem

After substituting expression (13) into equation (14), we obtain a linear combination of partial derivatives

$$F,\ F_p,\ F_q,\ F_{pp},\ F_{pq},$$
$$F_{qq},\ F_{ppp},\ F_{ppq},\ F_{pqq},\ F_{qqq}$$

(the subscripts denote the partial derivatives taken with respect to the corresponding variables).

Derivatives F_{qq}, F_{pqq}, F_{qqq} are dependent, and they can be expressed in terms of the remaining partial derivatives using Eq. (12). After that, the factors are grouped before the remaining partial derivatives

$$F,\ F_p,\ F_q,\ F_{pp},\ F_{pq},\ F_{ppp},\ F_{ppq},$$

should be zero if the function G is required to satisfy Eq. (14) for any solution of Eq. (12).

The resulting system of equations has the form:

$$v_p - w_q = 0,\ v_q + w_p = 0,$$

$$v_{pp} + v_{qq} + v\frac{4\left(n(n+1) - m(m+1)\right)}{\left(1+p^2+q^2\right)^2} = -2s_p,$$

$$w_{pp} + w_{qq} + w\frac{4\left(n(n+1) - m(m+1)\right)}{\left(1+p^2+q^2\right)^2} = -2s_q,$$

$$s_{pp} + s_{qq} + s\frac{4\left(n(n+1) - m(m+1)\right)}{\left(1+p^2+q^2\right)^2} =$$

$$= -\frac{16m(m+1)}{\left(1+p^2+q^2\right)^3}(pv+qw) +$$

$$+\frac{4m(m+1)}{\left(1+p^2+q^2\right)^2}\left(v_p + w_q\right).$$

Analysis of the obtained overdetermined system of partial differential equations with respect to the unknown functions $s(p,q)$, $v(p,q)$, $w(p,q)$ using the methods [40–46] leads to the following non-degenerate solutions that exhaust all possible cases.

a) $n = -2 - m$ or $n = 1 + m$:

$$\begin{cases} s(p,q) = \dfrac{(m+1)}{1+p^2+q^2}\times \\ \times\left(4c_a p + 4c_b q + c_c\left(1-p^2-q^2\right)\right), \\ v(p,q) = c_c p + 2c_b pq + c_a\left(-1+p^2-q^2\right), \\ w(p,q) = c_c q + 2c_a pq + c_b\left(-1-p^2+q^2\right), \end{cases}$$

where c_a, c_b, c_c are arbitrary constants;

b) $n = -1 + m$ or $n = -m$:

$$\begin{cases} s(p,q) = \dfrac{-m}{1+p^2+q^2}\times \\ \times\left(4c_a p + 4c_b q + c_c\left(1-p^2-q^2\right)\right), \\ v(p,q) = c_c p + 2c_b pq + c_a\left(-1+p^2-q^2\right), \\ w(p,q) = c_c q + 2c_a pq + c_b\left(-1-p^2+q^2\right), \end{cases}$$

where c_a, c_b, c_c are also arbitrary constants;

c) $n = m$ or $n = -1 - m$:

$$\begin{cases} s(p,q) = c, \\ v(p,q) = -c_c q + 2c_b pq + c_a\left(1+p^2-q^2\right), \\ w(p,q) = c_c p + 2c_a pq + c_b\left(1-p^2+q^2\right), \end{cases}$$

where c, c_a, c_b, c_c are also arbitrary constants.

There are also degenerate solutions. The first one has the form

$$s(p,q) = 0,\ v(p,q) = 0,\ w(p,q) = 0$$

and is of no particular interest.

The second solution corresponds to the choice

$$m = 0,\ n = 0,$$

$$\text{or } m = 0,\ n = -1,$$

$$\text{or } m = -1,\ n = 0,$$

$$\text{or } m = -1,\ n = -1.$$

In these cases, Eqs. (12) and (14) turn into two-dimensional Laplace equations, and transformation (13) takes the form

$$\begin{aligned} G(p,q) = cF(p,q) + v(p,q)F_p(p,q) + \\ + w(p,q)F_q(p,q), \end{aligned} \tag{15}$$

where c is constant, and functions $V(p,q)$ and $w(p,q)$ satisfy the Cauchy–Riemann conditions

$$v_p = w_q,\ v_q = -w_p,$$

i.e., are the real and the imaginary part of the analytical function of a complex variable

$$u(p + iq) = v(p,q) + iw(p,q).$$

The physical meaning of Eq. (15) is quite simple: multiplication by a constant transforms the solution of the two-dimensional Laplace equation into a solution of the two-dimensional Laplace equation, and the product of two analytical functions of a complex variable

$$v(p,q) + iw(p,q),\ F_p(p,q) - iF_q(p,q)$$

yields the analytical function of a complex variable whose real and imaginary parts should satisfy the two-dimensional Laplace equation [24–27, 36].

However, this curious degenerate solution is not very interesting as a generator of new homogeneous harmonic functions, since the real and imaginary parts of analytical functions of a complex variable provide enough resources for solving the two-dimensional Laplace equation. All 3D homogeneous harmonic functions with homogeneity degrees of 0 and −1 can be obtained using the Donkin formulas [7–10, 30–34]:

$$V(x,y,z) = H\left(\frac{x}{z+r}, \frac{y}{z+r}\right),$$

$$V(x,y,z) = \frac{1}{r}H\left(\frac{x}{z+r}, \frac{y}{z+r}\right),$$

where is H is the solution of the two-dimensional Laplace equation.

In the end, the following transforming expressions of the form (8) are obtained:

$$V(x,y,z)=U(x,y,z), \tag{16}$$

$$V(x,y,z)=U_x(x,y,z), \tag{17}$$

$$V(x,y,z)=U_y(x,y,z), \tag{18}$$

$$V(x,y,z)=\frac{m}{z}U(x,y,z)-\frac{x}{z}U_x(x,y,z)-\frac{y}{z}U_y(x,y,z), \tag{19}$$

$$V(x,y,z)=(2m+1)xU(x,y,z)-r^2U_x(x,y,z), \tag{20}$$

$$V(x,y,z)=(2m+1)yU(x,y,z)-r^2U_y(x,y,z), \tag{21}$$

$$V(x,y,z)=\frac{-mr^2+(2m+1)z^2}{z}U(x,y,z)+\frac{xr^2}{z}U_x(x,y,z)+\frac{yr^2}{z}U_y(x,y,z), \tag{22}$$

$$V(x,y,z)=yU_x(x,y,z)-xU_y(x,y,z), \tag{23}$$

$$V(x,y,z)=-\frac{mx}{z}U(x,y,z)+\frac{x^2+z^2}{z}U_x(x,y,z)+\frac{xy}{z}U_y(x,y,z), \tag{24}$$

$$V(x,y,z)=-\frac{my}{z}U(x,y,z)+\frac{xy}{z}U_x(x,y,z)+\frac{y^2+z^2}{z}U_y(x,y,z), \tag{25}$$

$$V(x,y,z)=\frac{1}{r^{2m+1}}U(x,y,z), \tag{26}$$

$$V(x,y,z)=\frac{1}{r^{2m-1}}U_x(x,y,z), \tag{27}$$

$$V(x,y,z)=\frac{1}{r^{2m-1}}U_y(x,y,z), \tag{28}$$

$$V(x,y,z)=\frac{m}{zr^{2m-1}}U(x,y,z)-\frac{x}{zr^{2m-1}}U_x(x,y,z)-\frac{y}{zr^{2m-1}}U_y(x,y,z), \tag{29}$$

$$V(x,y,z)=\frac{(2m+1)x}{r^{2m+3}}U(x,y,z)-\frac{1}{r^{2m+1}}U_x(x,y,z), \tag{30}$$

$$V(x,y,z)=\frac{(2m+1)y}{r^{2m+3}}U(x,y,z)-\frac{1}{r^{2m+1}}U_y(x,y,z), \tag{31}$$

$$V(x,y,z)=\frac{(2m+1)z^2-mr^2}{zr^{2m+3}}U(x,y,z)+\frac{x}{zr^{2m+1}}U_x(x,y,z)+\frac{y}{zr^{2m+1}}U_y(x,y,z), \tag{32}$$

$$V(x,y,z)=\frac{y}{r^{2m+1}}U_x(x,y,z)-\frac{x}{r^{2m+1}}U_y(x,y,z), \tag{33}$$

$$V(x,y,z)=-\frac{mx}{zr^{2m+1}}U(x,y,z)+\frac{x^2+z^2}{zr^{2m+1}}U_x(x,y,z)+\frac{xy}{zr^{2m+1}}U_y(x,y,z), \tag{34}$$

$$V(x,y,z)=-\frac{my}{zr^{2m+1}}U(x,y,z)+\frac{xy}{zr^{2m+1}}U_x(x,y,z)+\frac{y^2+z^2}{zr^{2m+1}}U_y(x,y,z), \tag{35}$$

where $r=\sqrt{x^2+y^2+z^2}$.

The variable z in the denominator typically indicates that the derivative U_z with some nonzero factor is implicitly present in formula; because the Euler equation (3) is used to eliminate the dependent derivative U_z, the derivative subsequently turns into a linear combination of functions U, U_x and U_y). As a result, some expressions can be simplified by eliminating the variable z in the denominator:

$$V(x,y,z)=U_z(x,y,z), \tag{19a}$$

$$V(x,y,z)=(2m+1)zU(x,y,z)-r^2U_z(x,y,z), \tag{22a}$$

$$V(x,y,z)=zU_x(x,y,z)-xU_z(x,y,z), \tag{24a}$$

$$V(x,y,z)=zU_y(x,y,z)-yU_z(x,y,z), \tag{25a}$$

$$V(x,y,z)=\frac{1}{r^{2m-1}}U_z(x,y,z), \tag{29a}$$

$$V(x,y,z)=\frac{(2m+1)z}{r^{2m+3}}U(x,y,z)-\frac{1}{r^{2m+1}}U_z(x,y,z), \tag{32a}$$

$$V(x,y,z)=\frac{z}{r^{2m+1}}U_x(x,y,z)-\frac{x}{r^{2m+1}}U_z(x,y,z), \tag{34a}$$

$$V(x,y,z)=\frac{z}{r^{2m+1}}U_y(x,y,z)-\frac{y}{r^{2m+1}}U_z(x,y,z). \tag{35a}$$

Conclusion

We have established that the Thomson formula for 3D harmonic functions that are Euler-homogeneous can be generalized if we use linear algebraic form (5) including first-order partial derivatives of the initial function instead of purely algebraic linear expressions. We have provided an exhaustive list of the obtained expressions of the first order, transforming arbitrary homogeneous 3D harmonic functions into new 3D harmonic functions which can be obtained without resorting to change of variables in the arguments of the function U.

Careful checking, however, has revealed that all the expressions obtained are in fact transforming formulas for 3D harmonic functions of a general form from [1], simplified by assuming that the function U and Euler's differential equation (3) for homogeneous functions are homogeneous [21, 22].

Other relations can also be obtained if we consider linear combinations with constant coefficients composed from the basic relations (16)–(35), corresponding to the same degree of homogeneity of the transformed function. Moreover, adding the Euler equation (3) multiplied by an arbitrary homogeneous function of the corresponding degree to any of the Eqs. (16)–(35), we obtain a new transformation.

For example, transformation (7) is such a linear combination; formally speaking, it is fundamentally different from the previously obtained basic Eqs. (16)–(35):

$$\begin{aligned}
L[U]=&\big(a(2m+1)xz+b(2m+1)yz+\\
&+c\big(-mx^2-my^2+(m+1)z^2\big)\big)U_x+\\
&+\big(a(2m+1)xy+b\big(-mx^2+(m+1)y^2-mz^2\big)+\\
&+c(2m+1)yz\big)U_y+\big(a\big((m+1)x^2-my^2-mz^2\big)+\\
&+b(2m+1)xy+c(2m+1)xz\big)U_z=\\
=&(2m+1)(cx+by+az)\big(xU_x+yU_y+zU_z-mU\big)+\\
&+mc\big((2m+1)xU-(x^2+y^2+z^2)U_x\big)+\\
&+mb\big((2m+1)yU-(x^2+y^2+z^2)U_y\big)+\\
&+ma\big((2m+1)xU-(x^2+y^2+z^2)U_z\big).
\end{aligned}$$

However, while such formulas can be considerably different (in the algebraic sense) from the list obtained earlier, they are fully equivalent to the basic Eqs. (16)–(35) serving as generators of new analytical expressions for 3D homogeneous harmonic functions. Similar problems with equivalent mathematical expressions that are not identically equal to each other in the algebraic sense are described, for example, in [47–50].

The calculations given in this paper were carried out using the Wolfram Mathematica software [51].

This study was partially carried out within the framework of State Task No. 075-00780-19-00 of the Institute for Analytical Instrumentation of the Russian Academy of Sciences.

REFERENCES

1. **Berdnikov A.S., Gall L.N., Gall N.R., et al.,** Generalization of the Thomson formula for general harmonic functions, St. Petersburg Polytechnical State University Journal. Physics and Mathematics. 12 (2) (2019) ... – ... .

2. **Golikov Yu.K., Krasnova N.K.,** Generalized similarity principle of similarity in electron spectrography, Prikladnaya fizika (Applied Physics). (2) (2007) 5–11.

3. **Averin I.A., Berdnikov A.S., Gall N.R.,** The principle of similarity of trajectories for the motion of charged particles with different masses in electric and magnetic fields that are homogeneous in Euler terms, Technical Physics Letters. 43 (2) (2017) 156–158.

4. **Golikov Yu.K., Krasnova N.K.,** Teoriya synteza elektrostaticheskikh energoanalizatorov [Theory of designing of electrostatic energy analyzers], Saint-Petersburg Polytechnic University Publishing, St. Petersburg, 2010 (in Russian).

5. **Golikov Yu.K., Krasnova N.K.,** Application of electric fields uniform in the Euler sense in electron spectrography, Technical Physics. 56 (2) (2011) 164–170.

6. **Krasnova N.K.,** Theory and synthesis of disperging and focusing electron optical media, Dr. Sci. Thesis. St. Petersburg, 2013 (in Russian).

7. **Gabdullin P.G., Golikov Yu.K., Krasnova N.K., Davydov S.N.,** The use of Donkin's formula in the theory of energy analyzers, I, Technical Physics. 45 (2) (2000) 232–235.

8. **Gabdullin P.G., Golikov Yu.K., Krasnova N.K., Davydov S.N.,** The use of Donkin's formula in the theory of energy analyzers, II, Technical Physics. 45 (3) (2000) 330–333.

9. **Golikov Yu.K., Krasnova N.K.,** Analytical structures of generalized homogeneous electrical spectrographic media, Nauchnoe priborostroenie (Scientific Instrumentation). 24 (1) (2014) 50–58.

10. **Golikov Yu.K., Berdnikov A.S., Antonov A.S., et al.,** Application of the Donkin formula in the theory of electrostatic prisms, Technical Physics. 63 (11) (2018) 1659–1666.

11. **Thomson W.,** Extraits de deux Lettres adressées a M. Liouville, Journal de Mathématiques Pures et Appliqués. 12 (1847) 256–264.

12. **Sretensky L.N.,** Teoriya niyutonovskogo potentsiala [Theory of the Newtonian potential], Moscow, Leningrad, OGIZ-GITTL, 1946.

13. **Smirnov V.I.,** A course of higher mathematics, Vol. 4: Integral equations and partial differential equations, Pergamon Press, Oxford, 1964.

14. **Vladimirov V.S.,** Uravneniya matematicheskoy fiziki [Equations of mathematical physics], Mir Publishers, Moscow, 1984.

15. **Kellogg O.D.**, Foundations of potential theory, Springer-Verlag, Berlin, Heidelberg, New-York, 1967.

16. **Wermer J.,** Potential theory, 2nd Ed., Ser. "Lecture Notes in Mathematics", Vol. 408, Springer-Verlag, Berlin, Heidelberg, New-York, 1981.

17. **Helms L.L.** Potential Theory, 2nd Ed., Springer, London, Heidelberg, New-York, Dordrecht, 2014.

18. **Golikov Yu.K.,** Analytical ways of describing harmonic functions, Vestnik of Aktobe's K. Zhubanov Regional State University, Physics and Mathematics. (2(44)) (2016) 165–181.

19. **Golikov Yu.K., Utkin K.G., Cheparuhin V.V.,** Raschet elementov elektrostaticheskikh elektronno-opticheslikh sistem [Design of elements of electron optical systems], Leningrad Polytechnic Inst. Publishing, Leningrad, 1984.

20. **Golikov Yu.K., Solovyev K.V.,** Elektrostaticheskiye ionnyye lovushki [Electrostatic ion traps], Saint-Petersburg Polytechnic University Publishing, St. Petersburg , 2008.

21. **Fichtenholz G.M.,** Differential- und Integralrechnung, I, VEB Deutscher Verlag der Wissenschaften, Berlin. 1968.

22. **Smirnov V.I.**, A course of higher mathematics, Vol. I: Elementary Calculus, Pergamon Press, Oxford, 1964.

23. **Koppenfels W., Stallmann F.,** Praxis der Konformen Abbildung, Springer-Verlag, Berlin, Göttingen, Heidelberg, 1959.

24. **Lavrent'ev M.A., Shabat B.V.,** Methoden der komplexen Funktionen-theorie, Verlag Wissenshaft, 1969.

25. **Markushevich A.I.,** Theory of functions of a complex variable, Vol. 1–3, Providence, US, Amer. Math. Society Publ., 2005.

26. **Evgrafov M.A.,** analytical functions, Dover Publ., 1978.

27. **Hurwitz A., Courant R.,** Vorlesungen Uber Allgemeine Funktionentheorie und Elliptische Funktionen, Springer, Berlin. 1964.

28. **Thomson W. (Lord Kelvin), Tait P.G.,** Treatise on natural philosophy, 2nd Ed., Part

1, University Press, Cambridge, 1912.

29. **Thomson W. (Lord Kelvin), Tait P.G.,** Treatise on natural philosophy, 2nd Ed., Part 2, University Press, Cambridge, 1912.

30. **Donkin W.F.,** On the equation of Laplace's functions &c., Philosophical Transactions of the Royal Society of London. 147 (1857) 43–57.

31. **Donkin W.F.,** On the equation of Laplace's functions &c., Philosophical Proceedings of the Royal Society of London. 8 (1856–1857) 307–310.

32. **Hobson E.W.,** The theory of spherical and ellipsoidal harmonics, University Press, Cambridge, 2012.

33. **Whittaker E.T., Watson G.N.,** A course of modern analysis, University Press, Cambridge, 1950.

34. **Berdnikov A.S., Averin I.A.,** Fringe fields of gridless electronic spectrographs with Euler's homogeneous electrostatic fields, Uspekhi prikladnoy fiziki (Advances in Applied Physics). 4 (1) (2016) 5–8.

35. **Berdnikov A.S., Averin I.A., Krasnova N.K., Solovyev K.V.,** Universal expressions for 3D electric and magnetic potentials which are uniform in Euler terms, Nauchnoye priborostroyeniye (Scientific Instrumentation). 26 (4) (2016) 13–30.

36. **Berdnikov A.S., Krasnova N.K., Solovyev K.V.,** Analysis of the general Whittaker' formula for 3D electric and magnetic potentials homogeneous in Euler terms, Nauchnoye priborostroyeniye (Scientific Instrumentation). 27 (4) (2017) 63–71.

37. **Berdnikov A.S., Krasnova N.K., Solovyev K.V.,** Whittaker' formula for 3D electric and magnetic potentials with a zero order of homogeneity and its consequencies // Nauchnoye priborostroyeniye (Scientific Instrumentation). 27 (4) (2017) 72–79.

38. **Golikov Yu.K., Berdnikov A.S., Antonov A.S., et al.,** Synthesis of electrode configurations that conserve fringing electric field homogeneity in Euler terms, Technical Physics. 63 (4) (2018) 593–597.

39. **Berdnikov A.S., Gall L.N., Antonov A.S., Solovyev K.V.,** Synthesis of fringing magnetic fields for static mass analyzers of the spectrographic type, Journal of Analytical Chemistry. 73 (14) (2018) 1301–1316.

40. **Günther N.M.,** Integrirovaniye uravneniy v chastnykh proizvodnykh pervogo poryadka [Integration of first-order partial differential equations], ONTI, Leningrad, Moscow, 1934.

41. **Tricomi F.G.,** Lezioni sulle equazioni a derivative parziali, Editrice Gherono, Torino, 1954.

42. **Rashevsky P.K.,** Geometricheskaya teoriya uravneniy s chastnymy proizvodnymy [Geometric Theory of Partial Differential Equations], OGIZ, Moscow, Leningrad, 1947.

43. **Finikov S.P.,** Metod vneshnikh form Kartana v differentsialnoy geometriy [Cartan's method of exterior forms in differential geometry], OGIZ, Moscow, Leningrad, 1948.

44. **Cartan É.,** Les systèmes différentiels extérieurs et leurs applications géométriques, Ser. "Actualités Scientifiques et Industrielles, No. 994, Hermann, Paris, 1945.

45. **Shcherbakov R.N.,** Osnovy metoda vneshnikh form i lineuchatoy differentsialnoy geometriy [Fundamentals of the method of external forms and differential line geometry], Tomsk State University Publishing House, Tomsk, 1973.

46. **Kaptsov O.V.,** Metody integrirovaniya uravneniy s chastnymy proizvodnymy [Methods for integrating partial differential equations], Fizmatlit, Moscow, 2009.

47. **Bulyanitsa A.L., Kurochkin V.E.,** Studying ordering processes in open systems (on the example of pattern evolution in colonies of imperfect mycelial fungi), Nauchnoye priborostroyeniye (Scientific Instrumentation). 10 (2) (2000) 43–49.

48. **Bulyanitsa A.L., Evstrapov A.A., Rudnitskaya G.E.,** Calculation of microscale system channel parameters by the method of moments, Nauchnoye priborostroyeniye (Scientific Instrumentation). 13 (4) (2003) 28–40.

49. **Evstrapov A.A., Bulyanitsa A.L., Rudnitskaya G.E., et al.,** Characteristic features of digital signal filtering algorithms as applied to electrophoresis on a microchip, Nauchnoye priborostroyeniye (Scientific Instrumentation). 13 (2) (2003) 57–63.

50. **Bulyanitsa A.L.,** Mathematical modeling in microfluidics: basic concepts, Nauchnoye priborostroyeniye (Scientific Instrumentation). 15 (2) (2005) 51–66.

51. Wolfram Mathematica, URL : http://wolfram.com/mathematica/

Received 21.03.2019, accepted 22.04.2019.

THE AUTHORS

BERDNIKOV Alexander S.
Institute for Analytical Instrumentation of the Russian Academy of Sciences
26 Rizhsky Ave., St. Petersburg, 190103, Russian Federation
asberd@yandex.ru

GALL Lidia N.
Institute for Analytical Instrumentation of the Russian Academy of Sciences
26 Rizhsky Ave., St. Petersburg, 190103, Russian Federation
lngall@yandex.ru

GALL Nikolay R.
Institute for Analytical Instrumentation of the Russian Academy of Sciences
26 Rizhsky Ave., St. Petersburg, 190103, Russian Federation
gall@ms.ioffe.ru

SOLOVYEV Konstantin V.
Peter the Great St. Petersburg Polytechnic University
29 Politechnicheskaya St., St. Petersburg, 195251, Russian Federation
k-solovyev@mail.ru

СПИСОК ЛИТЕРАТУРЫ

1. **Бердников А.С., Галль Л.Н., Галль Р.Н., Соловьев К.В.** Обобщение формулы Томсона для гармонических функций общего вида // Научно-технические ведомости СПбГПУ. Физико-математические науки. 2019. Т. 12. № 2. С.32–48.

2. **Голиков Ю.К., Краснова Н.К.** Обобщенный принцип подобия и его применение в электронной спектрографии // Прикладная физика. 2007. № 2. С. 5–11.

3. **Аверин И.А., Бердников А.С., Галль Н.Р.** Принцип подобия траекторий при движении заряженных частиц с разными массами в однородных по Эйлеру электрических и магнитных полях // Письма в Журнал технической физики. 2017. Т. 43. № 3. С. 39–43.

4. **Голиков Ю.К., Краснова Н.К.** Теория синтеза электростатических энергоанализаторов. СПб.: Изд-во Политехнического ун-та, 2010. 409 с.

5. **Голиков Ю.К., Краснова Н.К.** Электрические поля, однородные по Эйлеру, для электронной спектрографии // Журнал технической физики. 2011. Т. 81, № 2. С. 9–15.

6. **Краснова Н.К.** Теория и синтез диспергирующих и фокусирующих электронно-оптических сред. Дис. ... докт. физ.-мат. наук. 01.04.04. СПб.: СПбГПУ, 2013. 259 с.

7. **Габдуллин П.Г., Голиков Ю.К., Краснова Н.К., Давыдов С.Н.** Применение формулы Донкина в теории энергоанализаторов. I. // Журнал технической физики. 2000. Т. 70. № 2. С. 91–94.

8. **Габдуллин П.Г., Голиков Ю.К., Краснова Н.К., Давыдов С.Н.** Применение формулы Донкина в теории энергоанализаторов. II. // Журнал технической физики. 2000. Т. 70. № 3. С. 44–47.

9. **Голиков Ю.К., Краснова Н.К**. Аналитические структуры электрических обобщенно-однородных спектрографических сред // Научное приборостроение. 2014. Т. 24. № 1. С. 50–58.

10. **Голиков Ю.К., Бердников А.С., Антонов А.С., Краснова Н.К., Соловьев К.В**. Применение формулы Донкина в теории электростатических призм // Журнал технической физики. 2018. Т. 88. № 11. С. 1711–1719.

11. **Thomson W.** Extraits de deux Lettres adressées à M. Liouville // Journal de Mathématiques Pures et Appliquées. 1847. Tome XII. Pp. 256–264.

12. **Сретенский Л.Н.** Теория ньютоновского потенциала. Москва, Ленинград: ОГИЗ-ГИТТЛ, 1946. 318 с.

13. **Смирнов В.И.** Курс высшей математики. Т. 4. Ч. 2. М.: Наука, 1981. 297 с.

14. **Владимиров В.С.** Уравнения математической физики. М.: Наука, 1981. 512 с.

15. **Kellogg O.D.** Foundations of potential theory. Berlin, Heidelberg, New-York: Springer-Verlag, 1967. 386 p.

16. **Уэрмлер Дж.** Теория потенциала. М.: Мир, 1980. 134 с.

17. **Helms L.L.** Potential theory. 2nd Ed. London, Heidelberg, New-York, Dordrecht: Springer, 2014. 485 p.

18. **Голиков Ю.К.** Аналитические способы описания гармонических функций // Вестник Актюбинского регионального государственного университета им. К. Жубанова. Физико-математические науки. 2016. № 2 (44). С. 165–181.

19. **Голиков Ю.К., Уткин К.Г., Чепарухин В.В.** Расчет элементов электростатических электронно-оптических систем. Ленинград: Изд-во ЛПИ, 1984. 79 с.

20. **Голиков Ю.К., Соловьёв К.В.** Электростатические ионные ловушки. СПб.: Изд-во Политехнического ун-та, 2008. 152 с.

21. **Фихтенгольц Г.М.** Курс дифференциального и интегрального исчисления. Т. 1. М.: Физматлит, 2001. 616 с.

22. **Смирнов В.И.** Курс высшей математики. Т. 1. М.: Наука, 1974. 480 с.

23. **Коппенфельс В., Штальман Ф.** Практика конформных отображений. М.: Изд-во иностр. лит-ры, 1963. 406 с.

24. **Лаврентьев М.А., Шабат Б.В.** Методы теории функций комплексного переменного. М.: Наука, 1965. 716 с.

25. **Маркушевич А.И.** Теория аналитических функций. В 2 тт. М.: Наука, 1968. Т. 1. – 486 с., Т. 2 – 624 с.

26. **Евграфов М.А.** Аналитические функции. 3-е изд., перераб. и доп. М.: Наука, 1991. 448 с.

27. **Гурвиц А., Курант Р.** Теория функций. М.: Наука, 1968. 646 с.

28. **Томсон У. (лорд Кельвин), Тэт П.Г.** Трактат по натуральной философии. Ч. I. Москва, Ижевск: НИЦ «Регулярная и хаотическая динамика», 2010. 572 с.

29. **Томсон У. (лорд Кельвин), Тэт П.Г.** Трактат по натуральной философии. Ч. II. Москва, Ижевск: НИЦ «Регулярная и хаотическая динамика», 2011. 560 с.

30. **Donkin W.F.** On the equation of Laplace‘s functions &c. // Philosophical Transactions of the Royal Society of London. 1857. Vol. 147. Pp. 43–57.

31. **Donkin W.F.** On the equation of Laplace‘s functions &c. // Proceedings of the Royal Society of London. 1856 –1857. Vol. 8. Pp. 307–310.

32. **Гобсон Е.В.** Теория сферических и эллипсоидальных функций. М.: Изд-во иностр. лит-ры, 1952. 476 с.

33. **Уиттекер Э.Т., Ватсон Дж.** Курс современного анализа. Ч. 2: Трансцендентные функции. М.: Гос. изд-во физ.-мат. лит-ры, 1963. 516 с.

34. **Бердников А.С., Аверин И.А.** Краевые поля бессеточных электронных спектрографов с однородными по Эйлеру электростатическими полями // Успехи прикладной физики. 2016. Т. 4. № 1. С. 5–8.

35. **Бердников А.С., Аверин И.А., Краснова Н.К., Соловьёв К.В.** Общие формулы для трехмерных электрических и магнитных потенциалов, однородных по Эйлеру с целочисленным порядком однородности // Научное приборостроение. 2016. Т. 26. № 4. С. 13–30.

36. **Бердников А.С., Краснова Н.К., Соловьев К.В.** Анализ интегральной формулы Уиттекера общего вида для электрических и магнитных потенциалов, однородных по Эйлеру // Научное приборостроение. 2017. Т. 27. № 4. С. 63–71.

37. **Бердников А.С., Краснова Н.К., Соловьев К.В.** Интегральная формула Уиттекера для электрических и магнитных потенциалов с нулевым порядком однородности и ее следствия // Научное приборостроение. 2017. Т. 27. № 4. С. 72–79.

38. **Голиков Ю.К., Бердников А.С., Антонов А.С., Краснова Н.К., Соловьев К.В.** Синтез электродных конфигураций, сохраняющих для краевых электрических полей свойство однородности по Эйлеру // Журнал технической физики. 2018. Т. 88. № 4. С. 609–613.

39. **Бердников А.С., Галль Л.Н., Антонов А.С., Соловьев К.В.** Синтез краевых магнитных полей для статических масс-анализаторов спектрографического типа // Масс-спектрометрия. 2018. Т. 15. № 1. С. 26–43.

40. **Гюнтер Н.М.** Интегрирование уравнений в частных производных первого порядка. Ленинград, Москва: ОНТИ, 1934. 368 с.

41. **Трикоми Ф.** Лекции по уравнениям в частных производных. М.: Изд-во иностр. лит-ры, 1957. 443 с.

42. **Рашевский П.К.** Геометрическая теория уравнений с частными производными. Москва, Ленинград: ГИТТЛ, 1947. 362 с.

43. **Фиников С.П.** Метод внешних форм Картана в дифференциальной геометрии. Москва, Ленинград: ОГИЗ, 1948. 432 с.

44. **Картан Э.** Внешние дифференциальные системы и их геометрические приложения. М.: Изд-во Московского ун-та, 1962. 237 с.

45. **Щербаков Р.Н.** Основы метода внешних форм и линейчатой дифференциальной геометрии. Томск: Изд-во ТГУ, 1973. 236 с.

46. **Капцов О.В.** Методы интегрирования уравнений с частными производными. М.: Физматлит, 2009. 184 с.

47. **Буляница А.Л., Курочкин В.Е.** Исследование процессов упорядочивания в открытых системах // Научное приборостроение. 2000. Т. 10. № 2. С. 43–49.

48. **Буляница А.Л., Евстрапов А.А., Рудницкая Г.Е.** Метод моментов при расчете параметров каналов в микроразмерных системах // Научное приборостроение. 2003. Т. 13. № 4. С. 28–40.

49. **Евстрапов А.А., Буляница А.Л., Рудницкая Г.Е., Беленький Б.Г., Петряков А.О., Курочкин В.Е.** Особенности применения алгоритмов цифровой фильтрации электрофореграмм при анализе веществ на микрочипе // Научное приборостроение. 2003. Т. 13. № 2. С. 57–63.

50. **Буляница А.Л.** Математическое моделирование в микрофлюидике: основные положения // Научное приборостроение. 2005. Т. 15. № 2. С. 51–66.

51. Wolfram Mathematica. URL : http://wolfram.com/mathematica/

Статья поступила в редакцию 21.03.2019, принята к публикации 22.04.2019.

СВЕДЕНИЯ ОБ АВТОРАХ

БЕРДНИКОВ Александр Сергеевич – *доктор физико-математических наук, ведущий научный сотрудник Института аналитического приборостроения РАН.*

190103, Российская Федерация, г. Санкт-Петербург, Рижский пр., 26

asberd@yandex.ru

ГАЛЛЬ Лидия Николаевна – *доктор физико-математических наук, главный научный сотрудник Института аналитического приборостроения РАН.*

190103, Российская Федерация, г. Санкт-Петербург, Рижский пр., 26

lngall@yandex.ru

ГАЛЛЬ Николай Ростиславович – *доктор физико-математических наук, ведущий научный сотрудник Института аналитического приборостроения РАН.*

190103, Российская Федерация, г. Санкт-Петербург, Рижский пр., 26

gall@ms.ioffe.ru

СОЛОВЬЕВ Константин Вячеславович – *кандидат физико-математических наук, доцент кафедры физической электроники Санкт-Петербургского политехнического университета Петра Великого, младший научный сотрудник Института аналитического приборостроения РАН.*

195251, Российская Федерация, г. Санкт-Петербург, Политехническая ул., 29

k-solovyev@mail.ru

DOI: 10.18721/JPM.12205
УДК 531

NUMERICAL VERIFICATION OF WEAK SOLUTIONS OF THE CROCCO TYPICAL BOUNDARY PROBLEM USING AN IMPLICIT SECOND ORDER DIFFERENCE SCHEME

M.R. Petrichenko, E.V. Kotov

Peter the Great St. Petersburg Polytechnic University, St. Petersburg, Russian Federation

To verify the solution of a typical Crocco boundary problem, a numerical experiment has been performed using an implicit second-order difference scheme. The computational experiment showed uniform convergence in the $0 \le x \le 1$ interval for the numerical approximation of the solution to a weak solution with a small interval discrete sampling (of the order of $N =$ 104 nodes). It was shown that a numerical solution approximated a weak solution of the typical Crocco limit problem, except for the right end of the integration interval. The solution of the Crocco boundary problem could be continued to the left of the point $x = x_0$ while preserving the continuity and smoothness of the solution at this point. The point $x = 1$ represents the natural upper bound of the solution domain.

Keywords: Crocco's typical boundary problem, implicit difference scheme, weak solution, homotopy

Citation: Petrichenko M.R., Kotov E.V. Numerical verification of weak solutions of the Crocco typical boundary problem using an implicit second order difference scheme, St. Petersburg Polytechnical State University Journal. Physics and Mathematics. 12 (2) (2019) 62–71. DOI: 10.18721/JPM.12205

ЧИСЛЕННАЯ ВЕРИФИКАЦИЯ СЛАБЫХ РЕШЕНИЙ ТИПИЧНОЙ ПРЕДЕЛЬНОЙ ЗАДАЧИ КРОККО С ПОМОЩЬЮ НЕЯВНОЙ РАЗНОСТНОЙ СХЕМЫ ВТОРОГО ПОРЯДКА

М.Р. Петриченко, Е.В. Котов

Санкт-Петербургский политехнический университет Петра Великого,

Санкт-Петербург, Российская Федерация

Для верификации решения типичной предельной задачи Крокко проведен численный эксперимент с использованием неявной разностной схемы второго порядка. Вычислительный эксперимент показал равномерную на промежутке $0 \le x \le 1$ сходимость численной аппроксимации решения к слабому решению при небольшой плотности дискретизации промежутка (порядка $N = 10^4$ узлов). Показано, что численное решение аппроксимирует слабое решение типичной предельной задачи Крокко, кроме правого конца промежутка интегрирования – точки $x = 1$. Решение предельной задачи Крокко может быть продолжено левее точки x=0 с сохранением непрерывности и гладкости решения в этой точке. Точка $x = 1$ представляет естественную верхнюю границу области определения решения.

Ключевые слова: типичная предельная задача Крокко, неявная разностная схема, слабое решение, гомотопия

Ссылка при цитировании: Петриченко М.Р., Котов Е.В. Численная верификация слабых решений типичной предельной задачи Крокко с помощью неявной разностной схемы второго порядка // Научно-технические ведомости СПбГПУ. Физико-математические науки. 2019. Т. 12. № 2. С. 63–72. DOI: 10.18721/JPM.12205

Introduction

It is known that the typical Crocco boundary problem is stated as follows [1]:

$$yy'' + \gamma x = 0, D(y) = (x : 0 \le x_0 < x < 1);$$
$$\mathrm{Im}(y) = (y : y_0 > y > 0); \quad (1)$$
$$y'(x_0) = y(1) = 0,$$

where $y_0 := y(x_0) > 0$.

In the classic case of a typical boundary problem,

$$\gamma = 1/2,\ x_0 = 0,\ y_0 := y(0).$$

This study deals with this particular classical case.

We can prove that two-point boundary conditions (1) are equivalent to the Cauchy condition:

$$y(0) - a = y'(0) = 0.$$

Let $a = 0$. Then $y(x) = \pm\sqrt{2/3(-x)^3}$ is the solution of a homogeneous one-point problem for the Crocco equation on the negative semi-axis $x < 0$.

In hydrodynamic problems, $y(x)$ is the dimensionless friction factor, x is the dimensionless longitudinal component of velocity in the boundary layer on a plate in plane flow in the longitudinal direction.

Then $y(0) = a$ is the shear stress on the wall (Blasius constant) [2]. In seepage theory, x is the dimensionless depth of seepage flow through a scalar (homogeneous and isotropic) porous medium, y is the Crocco potential, defined as

$$y(x) = \int_x^1 s dx', \quad y(1) = y'(0) = 0,$$

where s is the longitudinal coordinate measured along the seepage flow.

The constant $y_0 = y(x_0)$ in seepage problems is proportional to seepage flow in the outflow face [3].

Steady-state solutions for free surface seepage in a scalar medium are found in terms of analytic theory of ordinary differential equations [3]. Modern results of such solutions are given in [4–6].

The following statements are true for a typical Crocco problem (1).

1. The Crocco equation has two solution branches: positive $y_+(x)$ and negative $y_-(x)$. The negative branch is defined as the solution to a boundary problem:

$$2y_-y_-'' + \gamma x = 0, \quad D(y_-) = (x : x_0 < x < 1),$$
$$y_-'(0) = y(1) = 0, \quad \mathrm{Im}(y_-) = (y_- : -y_0 > y_- > 0);$$

with $y_+(x) + y_-(x) = 0, \ \forall x \in (0,1)$.

The proof is trivial.

Below we consider only the positive branch of the solution of the Crocco equation, i.e., $y(x) := y_+(x)$.

2. The solution of a typical Crocco boundary problem (1) has the following properties:

$$y'(x) < 0, \ y''(x) < 0;$$
$$y'(x) \xrightarrow[x \to 1-0]{} -\infty,$$

so $y_0 = a > y(x)$, $0 < x < 1$.

To prove Statement 2, we formally reduce the order of the Crocco equation, reformulating it as an integral equation:

$$2y' = -\int_0^x \frac{tdt}{y(t)} \to y' \le 0, \quad 0 \le x < 1.$$

The integral on the right-hand side can be calculated using the Bonnet mean value theorem. We obtain:

$$2yy' = -1/2x^2(1-\theta^2), \quad (2)$$

where θ is a regular fraction, $0 < \theta < 1$.

Now we need only to pass to the limit for $x \to 1-0$, Q.E.D.

The solution of Eq. (2), such that the value of $y(1)$ is zero, $y(1) = 0$, has the following form:

$$y^2(x,\theta) = 1/6(1-\theta^2)(1-x^3). \quad (3)$$

Solution (3) continuously depends on the magnitude of the fraction θ. Its mean over θ is the so-called weak solution of the typical Crocco boundary problem, interpreted as the distribution over θ with a distribution density $y(x; \theta)$ [7].

In view of expression (3), the weak solution of the typical Crocco boundary problem is:

$$y(x) = 1/3\sqrt{1-x^3}, \quad (4)$$

and then $y_0 = y(0) = 1/3$, which is a good rational approximation for the Blasius constant. The exact value of the Blasius constant was calculated in Varin's study [8]. It can be seen from formula (4) that the weak solution can be continued to negative values of x while preserving the solution smooth and continuous at the point $x = 0$.

The solution of the typical Crocco boundary problem is related to the solution of a nonlinear integral equation:

$$y(x) = (1/2)\left\{\int_0^1 \frac{(1-s)sds}{y(s)} - \int_0^x \frac{(x-s)sds}{y(s)}\right\}, \quad (5)$$

which gives the following expression for the Blasius constant:

$$y_0 := y(0) = (1/2)\int_0^1 \frac{(1-s)sds}{y(s)}.$$

The solution of Eq. (5) can also be obtained in the form of a Lagrange series [9]. It was proved that the convergence radius of the Lagrange number is less than unity and the series diverges at $x \to 1-0$.

An alternative solution in the form of a Lagrange series is forming an iterative process:

$$y_k(x) = (1/2)\left\{\int_0^1 \frac{(1-s)sds}{y_{k-1}(s)} - \int_0^x \frac{(x-s)}{y_{k-1}(}\right.$$

$$k = 1(1)\infty,$$

where the subscript k indicates the iteration number.

The values of the Blasius constant obtained during the iterative process are found from the sequence

$$y_k(0) = (1/2)\int_0^1 \frac{(1-s)sds}{y_{k-1}(s)}.$$

We successively find the following values for different k:

$$k = 1: y_0(x) = y_0 = \sqrt{1/12} = 0.2887;$$

$$k = 2: y_1(x)\cdot y_0 = (1/12)(1-x^3),$$

$$y_1(x) = (1-x^3)/\sqrt{12},\ y_1(0) = 1/\sqrt{12};$$

$$k = 3:$$

$$y_2(x) = \sqrt{3}\left(\int_0^1 \frac{(1-s)sds}{1-s^3} - \int_0^x \frac{(x-s)sds}{1-s^2}\right) -$$

$$-\sqrt{3}\left\{\begin{array}{l} \ln\sqrt{3}\,\dfrac{x+2}{3}\ln\sqrt{1+x+x^2} + \\ +(1/3)(1-x)\ln\left(\dfrac{1}{1-x}\right) - \dfrac{\pi}{6\sqrt{3}} + \\ +\dfrac{1}{\sqrt{3}}\left(\operatorname{arctg}\dfrac{2x+1}{\sqrt{3}} - \dfrac{\pi}{6}\right) \end{array}\right\},$$

$$y_2(0) = \sqrt{3}\left(\ln\sqrt{3} - \frac{\pi}{6\sqrt{3}}\right)$$

and so on.

Accordingly, the first three iterated values of the Blasius constant form a sequence

$$y_0(0) = 1/\sqrt{12} = 0.2887...,$$

$$y_1(0) = 0.2887...,$$

$$y_3(0) = 0.4278...,$$

and, on average, $y(0)$ for the first three iterations lies in the range

$$0.3299 < y(0) < 0.3344.$$

The iterative process leads to trivial and lengthy calculations, which is already clear at the third iteration. Evidently, any iterated solution has all the basic properties of the solution to boundary problem (1):

$$\forall x \in (0,1),\ \forall k = 1(1)\infty,$$

$$y_k'(x) < 0,\ \ y_k''(x) < 0,$$

$$y'(x) \xrightarrow[x\to 1-0]{} -\infty.$$

The iterative process is inconvenient as the expressions for the iterated solutions are cumbersome and there is no proof for the convergence of the process. Both of these obstacles can be avoided by using the difference approximation of boundary problem (1).

Interest in numerical solutions to the Blasius equation appeared immediately after he published his study in 1908 [2], due to general disappointment in the integration method using power series (see [8] and its preprint detailing the history of the issue). Modern studies [10, 11, 13–21] mainly consist of attempts to improve the convergence of predictor-corrector methods for solving ordinary differential equations of the boundary layer. Ref. [22] is an exception,

developing Kaplun's method interpreted in terms of homotopy mappings of the integration interval on a compact set. In the case of boundary problem (1), the mappings are compact.

Let linear homotopy

$$F(t,x)\colon ((0 < t < 1) \times (0 < x < 1)) \to (0,\ a)$$

represent the solution to boundary problem (1).

Then $F(0,x)$ represents the solution in the neighborhood of the point $x = 0$, and $F(1,x)$ in the neighborhood of the point $x = 1$. For example, for a weak solution,

$$F(0,x) = (1/3)\left(1 - x^3/2 - x^6/8\right),$$

$$F(1,x) = \left(1/\sqrt{3}\right)\sqrt{1-x}.$$

A linear homotopy mapping has the form:

$$y(x) = F(t,x) = (1-t)F(0,x) + tF(1,x) =$$

$$= (1-t)/3\left(1 - x^3/3 - x^6/8\right) + t\sqrt{\frac{1-x}{3}}.$$

A weak solution also represents some homotopy with the parameter $\theta \in (0,1)$. Indeed,

$$y^2(x,\theta) = (1/6)\left(1-\theta^2\right)\left(1-x^3\right),$$

$$y^2(x,1) = 0,\ y^2(x,0) = (1/6)\left(1-x^3\right).$$

Finally, [12] reintroduces the method of power expansions. However, its results coincide with the data given in [8] on flat series, as well as preprints of this study in Keldysh Institute Preprints, published earlier.

The computational domain in the numerical solution of problem (1) on the interval $x \in (0,1)$ consists of N segments with a constant step $h = 1/N$ ($x_j = jh$, $j = 0, 1, \ldots, N$). We use a second-order difference scheme for discretizing Eq. (1)

$$\frac{y_{j-1} - 2y_j + y_{j+1}}{h^2} + \gamma\frac{x_j}{y_j} = 0. \qquad (6)$$

Equality (6) is a discrete equivalent of the exact equality

$$y'' = -\gamma\frac{x}{y}.$$

This expression is linear with respect to the component y_{j+1}, and therefore, if the components y_{j-1}, y_j (where $j = 1(1)$) of the vector **y** are known, a linear system of algebraic equations is obtained to calculate y_{j+1}.

The boundary conditions in problem (1) take the following form upon discretization:

$$\frac{3y_0 - 4y_1 + y_2}{2h} = 0,\ \ y_N = 0. \qquad (7)$$

If the differences in equalities (6), (7) are denoted by

$$\begin{cases} f_0 = 3y_0 - 4y_1 + y_2, \\ f_j = y_{j-1} - 2y_j + y_{j+1} + \gamma h^2\dfrac{x_j}{y_j}, \\ f_N = y_N, \end{cases} \qquad (8)$$

then problem (6)–(8) can be written in the form equivalent to a linear algebraic system

$$\mathbf{F(y)} = 0,$$

where **F, y** are vectors taking the form

$$F = [f_0 f_1 \ldots f_N]^T,$$

$$y = [y_0 y_1 \ldots y_N]^T.$$

The resulting nonlinear system is solved by the Newton iterative method:

$$y^{(k+1)} = y^{(k)} + \Delta y^{(k)},$$

where $\Delta y^{(k)}$ is the residual vector,

$$\Delta y^{(k)} = [\Delta y_0^{(k)}\ \Delta y_1^{(k)} \ldots\ \Delta y_N^{(k)}]^T.$$

It is obtained as a solution of the linearized matrix equation with the Jacobi matrix $\mathbf{J}_F(\mathbf{y})$ of order $N + 1$:

$$J_F(y^{(k)})\Delta y^{(k)} = -F(y^{(k)}), \qquad (9)$$

$$J_F(\mathbf{y}^{(k)}) = \frac{\partial(f_0,\ldots,f_N)}{\partial(y_0,\ldots,y_N)}. \qquad (10)$$

It is assumed that the matrix $\mathbf{J}_F(\mathbf{y})$ is well-conditioned. Then system (10) is correct and uniquely solvable:

$$\Delta\mathbf{y}^{(k)} = -\mathbf{J}_F^{-1}\left(\mathbf{y}^{(k)}\right)\mathbf{F}\left(\mathbf{y}^{(k)}\right).$$

Substituting equality (8) into Eq. (9), we obtain, in view of equality (10), the following expressions:

$$\begin{aligned} 3\Delta y_0^{(k)} - 4\Delta y_1^{(k)} + \Delta y_2^{(k)} &= -f_0^{(k)}, \\ f_0^{(k)} &= 3y_0^{(k)} - 4\Delta y_1^{(k)} + y_2^{(k)}, \end{aligned} \qquad (11)$$

$$f_j^{(k)} = y_{j-1}^{(k)} - 2y_j^{(k)} + y_{j+1}^{(k)} + \gamma h^2\frac{x_j}{y_j^{(k)}}, \qquad (12)$$

$$a_j \Delta y_{j-1}^{(k)} + b_j \Delta y_j^{(k)} + c_j \Delta y_{j+1}^{(k)} = -f_j^{(k)}, \quad (13)$$

$$a_j = 1,\ b_j = -2 - \gamma h^2 \frac{x_j}{\left(y_j^{(k)}\right)^2},\ c_j = 1, \quad (14)$$
$$\Delta y_N^{(k)} = -y_N^{(k)}.$$

Evidently, system of equations (11)–(14) contains three unknowns in each of the equations and is similar to a tridiagonal system. The first and the last equations in such systems usually contain only two unknowns. However, the first equation in this system contains three unknowns: $\Delta y_0^{(k)}$, $\Delta y_1^{(k)}$, $\Delta y_2^{(k)}$.

To eliminate the unknown $\Delta y_0^{(k)}$, Eq. (11) can be represented as follows:

$$\Delta y_0^{(k)} = \frac{1}{3}\left[4\Delta y_1^{(k)} - \Delta y_2^{(k)} - f_0^{(k)}\right]. \quad (15)$$

Next, substituting expressions (13) and (14) into Eq. (15) with $j = 1$, we obtain the expression:

$$\hat{b}_1 \Delta y_1^{(k)} + \hat{c}_1 \Delta y_2^{(k)} = -\hat{f}_1^{(k)}, \quad (16)$$

where

$$\hat{b}_1 = b_1 + 4/3a_1,$$
$$\hat{c}_1 = c_1 - 1/3a_1, \quad (17)$$
$$\hat{f}_1^{(k)} = f_1^{(k)} - 1/3 f_0^{(k)}.$$

The matrix of system of equations (11), (15), (16) is tridiagonal. This system can be solved by sweeping with respect to the indices j:

$$\Delta y_j^{(k)} = p_j - q_j \Delta y_{j+1}^{(k)}. \quad (18)$$

It follows from equality (16) that

$$p_1 = -\hat{f}_1^{(k)} / \hat{b}_1, q_1 = \hat{c}_1 / \hat{b}_1. \quad (19)$$

It follows from Eqs. (15), (19) that

$$a_j\left(p_{j-1} - q_{j-1}\Delta y_j^{(k)}\right) + b_j \Delta y_j^{(k)} + \quad (20)$$
$$+ c_j \Delta y_{j+1}^{(k)} + f_j^{(k)} = 0.$$

In view of the boundary condition $y_N = 0$, we obtain the following equalities for all k:

$$y_N^{(k)} = \Delta y_N^{(k)} = 0.$$

After calculating p_j and q_j for $j = 1, 2, \ldots, N - 1$ using expressions (18) and (19), we can calculate $\Delta y_j^{(k)}$ for $j = N - 1, N - 2, \ldots, 0$ using expression (18).

Calculations continue until a predetermined accuracy ε is reached:

$$\left\|\Delta \mathbf{y}^{(k)}\right\| \le \varepsilon,$$

where $\|*\|$ denotes, for example, sup that is the norm of the residual vector or any equivalent norm of the matrix.

Fig. 1 shows the numerical solution of problem (4), (5) on the interval $x \in [0, 1]$ for $\gamma = 1$ with a different number of steps N for $\varepsilon = 10^{-6}$. The fiber bundle of numerical solutions is small on the scale of the figure even when changing the number N of the nodes into which the integration interval $0 < x < 1$ is divided by 4(!) orders, $10^2 \le N \le 10^6$. The following expression is considered as the initial approximation:

$$y_0 = (1/2)\ (1 - x^2)^S.$$

The bold solid line in Fig. 1 corresponds to a weak solution (4) with the Blasius constant of 0.4714 (the exact value is 0.4696).

Table 1 lists the Blasius constants $y(0)$, calculated with $\gamma = 1$ and different numbers of steps N, and the values obtained by other authors [12–16].

It follows from the data given in Table that the first three exact significant digits of the Blasius constant can be calculated with a small number of nodes, with $N > 10{,}000$. The derivative of the numerical solution at the right endpoint of the integration interval, i.e., at $x = 1 - 0$, is bounded from below and no numerical solution curve has a vertical tangent (see Fig. 1). It is to be expected that the values of numerical derivatives should be bounded, since one-sided differences are used.

To extend the solution of problem (1) to the domain $x < 0$, a second-order difference scheme (6) is used with the following boundary conditions:

$$y(0) - \tilde{y}_0 = y'(0) = 0, \quad (21)$$

where $\tilde{y}_0$ is the value of $y(0)$ from the solution obtained on the interval $x \in [0, 1]$, i.e., the Blasius constant of the numerical solution.

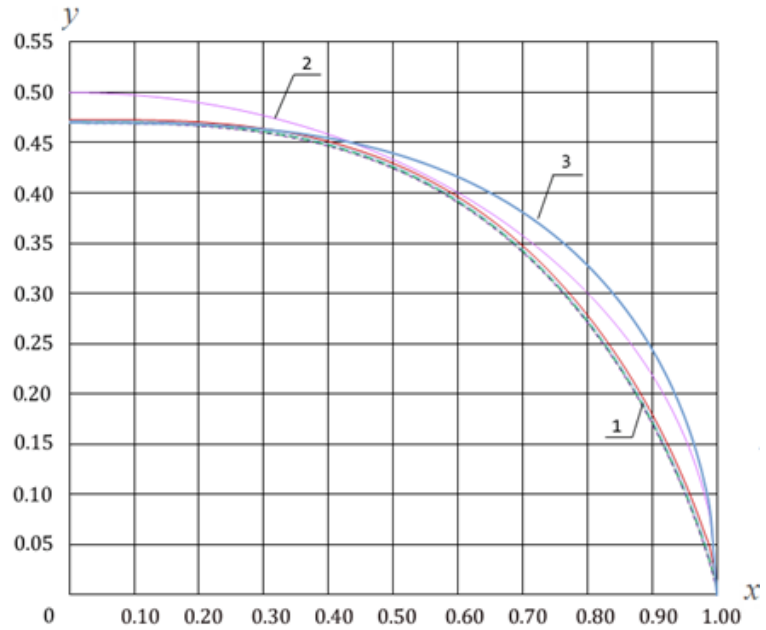

Fig. 1. Numerical solution of Crocco problem on interval $x \in [0, 1]$ with $\gamma = 1$, with a different number of steps N: 100, 1000, 10 000, 100 000, 10^6 (fiber bundle of lines *1*); line *2* is the initial approximation $y_0 = 1/2$, line *3* is weak solution (4) with the Blasius constant $y_0 = 0.4714$

Table

Calculated values of Blasius constant $y(0)$ with varying parameters and number of partitions of integration interval

Source	Number of steps N	Value of $y(0)$	
		$\gamma = 0.5$	$\gamma = 1.0$
This paper	100	0.339566	0.472865
	1000	0.335198	0.471984
	10,000	0.332051	0.470430
	100,000	0.332053	0.469855
	1,000,000	0.332053	0.469676
[13]	–	0.332057	0.469600
[14]		0.3320573362	0.4695999889
[15]		0.332057	0.469599

Upon discretization, boundary conditions (21) take the form

$$y_0 - \tilde{y}_0 = \left(y_0 - y_{-1}\right)/h = 0,$$

and it follows then that $y_0 = \tilde{y}_0 = y_{-1}$.

Therefore,

$$y_j = 2y_{j+1} - y_{j+2} - \gamma h^2 x_{j+1} / y_{j+1},$$
$$j = -2, -3, \ldots, -M,$$

where M is the number of calculation steps in the region $x < 0$ (a natural number).

Fig. 2 shows a positive numerical solution of boundary problem (1), extended to the negative semi-axis. The extended solution is preserved continuous and smooth at the point of contact $x = -0$.

Extension of the positive and negative branches of the weak solution to the negative semi-axis has the following form:

$$y(x) = \pm a\sqrt{1-(-x)^3},\ a = 1/\left(3\sqrt{\gamma}\right)$$

Evidently, if $-x >> 1$, a weak solution has an order that coincides with the order of the exact solution of boundary problem (1):

$$y(x) \sim (-x)^{3/2}.$$

Conclusions

The study we have carried out allows us to draw the following conclusions.

1. The weak solution of the Crocco problem has all the properties of an exact solution: there is a zero derivative at $x = 0$, an unbounded derivative at $x = 1$, the solution can be extended to the negative semi-axis $x < 0$ while preserving continuity and smoothness at $x = 0$.

2. The values of the Blasius constant that we have obtained for the weak solution were: $y(0) = 1/3$ with $\gamma = 1/2$ and $y(0) = 0.4714$ with $\gamma = 1$; the approximate value of the Blasius constant differs from the exact value

$$(y(0) = 0.332059,\ \gamma = 1/2 \text{ and}$$
$$y(0) = 0.4696,\ \gamma = 1)$$

by less than 0.4%.

3. The numerical experiment revealed that the numerical approximation of the solution uniformly converges on the interval $0 \le x \le 1$ to a weak solution with a small discretization of the interval (of the order of $N = 10^4$ nodes).

4. The derivative of the numerical solution is bounded from below at the right endpoint of the integration interval, $x = 1 - 0$, and the numerical solution curve does not have a vertical tangent. It is to be expected that the values of numerical derivatives should be bounded, since one-sided differences are used.

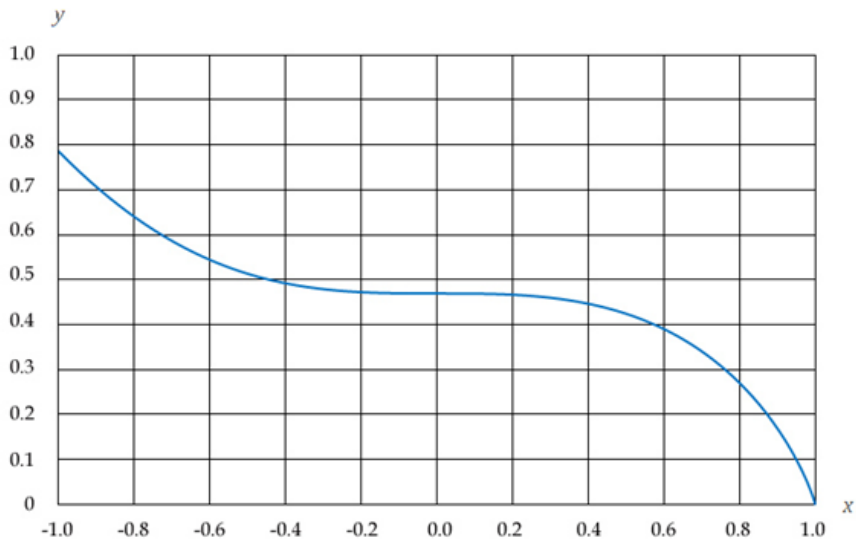

Fig. 2. Solution of Crocco problem on interval $x \in [-1, 1]$ with $\gamma = 1$

REFERENCES

1. **Crocco L.,** Sull strato limite laminare nei gas lungo una lamina plana, Rend. Math. Appl., Ser. 5. 21 (2) (1941) 138–152.

2. **Blasius H**., Grenzschichten in Flussigkeiten mit kleiner Reibung, Zeitschrift für Mathematik und Physik. 56 (1908) 1–37.

3. **Muskat M.,** Seepage of water through dams with vertical faces, Journal of General and Applied Physics. 6 (1935) 402–415.

4. **Anakhayev K.N.,** Raschet filtratsii cherez peremychku na nepronitsayemom osnovanii [The design of an impenetrable-based crosspiece filtration], News of Higher Educational Institutions. Construction. (7) (1990) 78–82.

5. **Anakhayev K.N.,** About filtration account the crosspiece, Matem. Mod. 23 (2) (2011) 148–158.

6. **Anakhayev K.N.,** About development of analytical methods of filtration calculation, Prirodoobustroystvo. (1) (2014) 72–75.

7. **Petrichenko M.R., Kotov E.V., Zaborova D.D., Musorina T.A.,** Weak solutions of the Crocco boundary problems, St. Petersburg State Polytechnical University Journal. Physics and Mathematics. 11(3) (2018) 27–38.

8. **Varin V.P**., Asymptotic expansion of Crocco solution and the Blasius constant, Computational Mathematics and Mathematical Physics. 58 (4) (2018) 517–528.

9. **Petrichenko M.R**., The integral equation of the Crocco boundary problem, Vestnik KRSU, Natural, Physical and Mathematical Sciences. 17 (12) (2017) 8–11.

10. **Azizi A., Latifizadeh H.,** On the efficiency of collocation method for solution of the Falkner – Skan boundary layer equation, Journal of Mathematical and Computational Science. 4 (2) (2014) 128–147.

11. **Kuo B-L.,** Heat transfer analysis for the Falkner – Skan wedge flow by the differential transformation method, International Journal of Heat and Mass Transfer. 48 (23–24) (2005) 5036–5046.

12. **Paul M.,** An accurate Taylor's series solution with high radius of convergence for the Blasius function and parameters of asymptotic variation, Journal of Applied Fluid Mechanics. 7 (4) (2014) 557–564.

13. **Liao S-J.,** An explicit, totally analytic approximate solution for Blasius' viscous flow problems, International Journal of Non-Linear Mechanics. 34 (4) (1999) 759–778.

14. **Liu C-S.,** An SL(3,R) shooting method for solving the Falkner – Skan boundary layer equation, International Journal of Non-Linear Mechanics. 49 (March) (2013) 145–151.

15. **Ding Xu, Xin Guo**, Fixed point analytical method for nonlinear differential equations, Journal of Computational and Nonlinear Dynamics. 8 (1) (2013) 011005.

16. **Aminikhah H.,** Analytical approximation to the solution of nonlinear Blasius viscous flow equation by LTNHPM, International Scholarly Research Network, ISRN Mathematical Analysis. 2012 (2012) ID 957473.

17. **Asaithambi A.,** Numerical solution of the Falkner – Skan equation using piecewise linear functions, Applied Mathematics and Computation. 159 (1) (2004) 267–273.

18. **Asaithambi A.,** Solution of the Falkner – Skan equation by recursive evaluation of Taylor coefficients, Journal of Computational and Applied Mathematics. 176 (1) (2005) 203–214.

19. **Boyd J.P.,** The Blasius function in the complex plane, Experimental Mathematics. 8 (4) (1999) 381–394.

20. **Varin V.P.,** Asymptotic expansion of Crocco solution and Blasius constant, Keldysh Institute preprints, Moscow, 106 (2016) 20 p.

21. **Zhang J., Chen B.,** An iterative method for solving the Falkner – Skan equation, Applied Mathematics and Computation. 2009. Vol. 210 (1) (2009) 215–222.

22. **Asaithambi A.,** Numerical solution of the Blassius equation with Crocco – Wang transformation, Journal of Applied Fluid Mechanics. 9 (5) (2014) 2595–2603.

23. **Zhao Y., Lin Z., Liao S.,** A modified homotopy analysis method for solving boundary layer equations, Applied Mathematics. 4 (1) (2013) 11–15.

Received 20.03.2019, accepted 20.04.2019

THE AUTHORS

PETRICHENKO Mikhail R.
Peter the Great St. Petersburg Polytechnic University
29 Politechnicheskaya St., St. Petersburg, 195251, Russian Federation
fonpetrich@mail.ru

KOTOV Eugeniy V.
Peter the Great St. Petersburg Polytechnic University
29 Politechnicheskaya St., St. Petersburg, 195251, Russian Federation
ekotov.cfd@gmail.com

СПИСОК ЛИТЕРАТУРЫ

1. **Crocco L.** Sull strato limite laminare nei gas lungo una lamina plana // Rend. Math. Appl. Ser. 5. 1941. Vol. 21. No. 2. Pp. 138–152.

2. **Blasius H.** Grenzschichten in Flussigkeiten mit kleiner Reibung // Zeitschrift für Mathematik und Physik. 1908. Band 56. S. 1–37.

3. **Muskat M.** Seepage of water through dams with vertical faces // Journal of General and Applied Physics. 1935. Vol. 6. Pp. 402–415.

4. **Анахаев К.Н.** Расчет фильтрации через перемычку на непроницаемом основании // Известия высших учебных заведений. Строительство и архитектура. 7 № .1990. С. 82–78.

5. **Анахаев К.Н.** О фильтрационном расчете перемычки // Математическое моделирование. 2011. Т. 2 № .23. С. 158–148.

6. **Анахаев К.Н.** О развитии аналитических методов расчета фильтрации // Природообустройство. 1 № .2014. С. 75–72.

7. **Петриченко** М.Р., **Котов Е.В.,** Заборова **Д.Д.,** Мусорина **Т.А.** Слабые решения предельных задач Крокко // Научно-технические ведомости Санкт-Петербургского государственного политехнического университета. Физико-математические науки. 2018. Т. 11. № 3. С. 27–38.

8. **Варин В.П.** Асимптотические разложения решения Крокко и ряд Блазиуса // Журнал вычислительной математики и математической физики. 2018. Т. 58. № 4. С. 530–540.

9. **Петриченко М.Р.** Интегральное уравнение предельной задачи Крокко // Вестник Кыргызско-Российского славянского университета. Естественные и физико-математические науки. 2017. Т. 17. № 12. С. 8–11.

10. **Azizi A., Latifizadeh H.** On the efficiency of collocation method for solution of the Falkner – Skan boundary layer equation // Journal of Mathematical and Computational Science. 2014. Vol. 4. No. 2. Pp. 128–147.

11. **Kuo B-L.** Heat transfer analysis for the Falkner – Skan wedge flow by the differential transformation method // International Journal of Heat and Mass Transfer. 2005. Vol. 48. No. 23–24. Pp. 5036–5046.

12. **Paul M.** An accurate Taylor's series solution with high radius of convergence for the Blasius function and parameters of asymptotic variation // Journal of Applied Fluid Mechanics. 2014. Vol. 7. No. 4. Pp. 557–564.

13. **Liao S-J.** An explicit, totally analytic approximate solution for Blasius' viscous flow problems // International Journal of Non-Linear Mechanics. 1999. Vol. 34. No. 4. Pp. 759–778.

14. **Liu C-S.** An SL(3,R) shooting method for solving the Falkner – Skan boundary layer equation // International Journal of Non-Linear Mechanics. 2013. Vol. 49. March. Pp. 145–151.

15. **Ding Xu, Xin Guo**. Fixed point analytical method for nonlinear differential equations // Journal of Computational and Nonlinear Dynamics. 2013. Vol. 8. No. 1. P. 011005 (9 p.)

16. **Aminikhah H.** Analytical approximation to the solution of nonlinear Blasius viscous flow equation by LTNHPM // International Scholarly Research Network. ISRN Mathematical Analysis. 2012. Vol. 2012. Article ID 957473 (10 p.).

17. **Asaithambi A.** Numerical solution of the Falkner – Skan equation using piecewise linear functions // Applied Mathematics and Computation. 2004. Vol. 159. No. 1. Pp. 267–273.

18. **Asaithambi A.** Solution of the Falkner – Skan equation by recursive evaluation of Taylor coefficients // Journal of Computational and Applied Mathematics. 2005. Vol. 176. No.1. Pp. 203–214.

19. **Boyd J.P.** The Blasius function in the complex plane // Experimental Mathematics.

1999. Vol. 8. No. 4. Pp. 381–394.

20. **Варин В.П.,** Асимптотическое разложение решения Крокко и константа Блазиуса. Препринты ИПМ им. Келдыша РАН. № 106, 20 с. http://keldysh.ru/paθpers/2016/prep2016_106.pdf.

21. **Zhang J., Chen B.** An iterative method for solving the Falkner – Skan equation // Applied Mathematics and Computation. 2009. Vol. 210. No. 1. Pp. 215–222.

22. **Asaithambi A.** Numerical solution of the Blassius equation with Crocco – Wang transformation // Journal of Applied Fluid Mechanics. 2014. Vol. 9. No. 5. Pp. 2595–2603.

23. **Zhao Y., Lin Z., Liao S.** A modified homotopy analysis method for solving boundary layer equations // Applied Mathematics. 2013. Vol. 4. No. 1. Pp. 11–15.

Статья поступила в редакцию 20.03.2019, принята к публикации 20.04.2019.

СВЕДЕНИЯ ОБ АВТОРАХ

ПЕТРИЧЕНКО Михаил Романович – *доктор технических наук, заведующий кафедрой гидравлики и прочности Санкт-Петербургского политехнического университета Петра Великого.*

195251, Российская Федерация, г. Санкт-Петербург, Политехническая ул., 29
fonpetrich@mail.ru

КОТОВ Евгений Владимирович – *ассистент кафедры гидравлики и прочности Санкт-Петербургского политехнического университета Петра Великого.*

195251, Российская Федерация, г. Санкт-Петербург, Политехническая ул., 29
ekotov.cfd@gmail.com

DOI: 10.18721/JPM.12206
УДК 535.36, 535.4, 57.088

MODIFICATION OF LASER CORRELATION SPECTROSCOPY METHOD FOR ANALYZING POLYDISPERSE NANOPARTICLE SUSPENSIONS

E.K. Nepomnyashchaya, E.N. Velichko

Peter the Great St. Petersburg Polytechnic University, St. Petersburg, Russian Federation

The paper proposes a modification of the laser correlation spectroscopy method to improve the accuracy of determining the size of polydisperse nanoparticles in suspensions. The essence of the modification is to create an original scheme and an experimental data processing algorithm, which makes it possible to determine the size of highly polydisperse as well as nonspherical nanoparticles. A theory is given for calculating the size and shape of nanoparticles, as well as an algorithm for solving the inverse ill-posed problem of laser correlation spectroscopy. The approbation of the developed software and hardware complex is performed using model signals with different noise levels, as well as in the study of monodisperse and polydisperse suspensions of spherical and ellipsoidal particles with known sizes.

Keywords: laser correlation spectroscopy, nanoparticle, dimension, software and hardware complex

Citation: Nepomnyashchaya E.K., Velichko E.N., Modification of laser correlation spectroscopy method for analyzing polydisperse nanoparticle suspensions, St. Petersburg Polytechnical State University Journal. Physics and Mathematics. 12 (2) (2019) 72–85. DOI: 10.18721/JPM.12206

МОДИФИКАЦИЯ МЕТОДА ЛАЗЕРНОЙ КОРРЕЛЯЦИОННОЙ СПЕКТРОСКОПИИ ДЛЯ АНАЛИЗА ПОЛИДИСПЕРСНЫХ СУСПЕНЗИЙ НАНОЧАСТИЦ

Э.К. Непомнящая, Е.Н. Величко

Санкт-Петербургский политехнический университет Петра Великого,
Санкт-Петербург, Российская Федерация

В работе предлагается модификация метода лазерной корреляционной спектроскопии для повышения точности определения размеров полидисперсных наночастиц в составе суспензий. Суть модификации состоит в создании оригинальной схемы и алгоритма обработки экспериментальных данных и позволяет определять размеры сильно полидисперсных, а также несферических наночастиц. Приводится теория для расчета размеров и формы наночастиц, а также алгоритм для решения обратной некорректной задачи лазерной корреляционной спектроскопии. Апробация разработанного программно-аппаратного комплекса производится с использованием модельных сигналов с различным уровнем шума, а также при исследовании монодисперсных и полидисперсных суспензий сферических и эллипсоидальных частиц с известными размерами.

Ключевые слова: лазерная корреляционная спектроскопия, наночастица, размер, программно-аппаратный комплекс

Ссылка при цитировании: Непомнящая Э.К., Величко Е.Н. Модификация метода лазерной корреляционной спектроскопии для анализа полидисперсных суспензий наночастиц // Научно-технические ведомости СПбГПУ. Физико-математические науки. 2019. Т. 12. № 2. С. 73–87. DOI: 10.18721/JPM.12206

Introduction

There is growing interest in synthesis and study of nanoparticles and nanoparticle suspensions. While existing methods such as electron and atomic force microscopy have been recognized as effective, they do not allow to monitor changes in size and dynamics of particle aggregation in real time [1, 2]. Besides, these methods have severe limitations in studies of biological suspensions.

Methods based on dynamic light scattering, including laser correlation spectroscopy (LCS) [1, 3], have proved their efficiency in this situation. LCS is widely used in synthesis of nanoparticles and biomolecules for rapid analysis of particle size distributions. Unfortunately, commercially available laser correlation spectrometers cannot reliably analyze multicomponent polydisperse solutions with sufficient accuracy [4]. Furthermore, all sizes are calculated under the assumption that the scattering particles are spherical, while in fact nanoparticles of other shapes are often found, and biomolecules frequently form non-spherical clusters [5, 6]. In view of these limitations, it is important to improve the existing method of laser correlation spectroscopy and the data processing algorithms for increasing the accuracy with which particle sizes can be measured in polydisperse suspensions and for determining the longitudinal and transverse dimensions of non-spherical particles.

This paper describes the hardware and software system we have developed based on laser correlation spectroscopy. This system makes it possible to solve the problems posed, obtaining the distributions of sizes and their evolution trends for non-spherical particles in polydisperse suspensions.

Implementation scheme of modified LCS method

The LCS method is based on detecting and analyzing the light scattered by particles in Brownian motion in liquid. The scattered light forms a dynamic speckle pattern in the observation plane [7]. The intensity of this pattern at a point varies with time due to motion of scattering particles in liquid. Monitoring the intensity variation of the speckle pattern in a small region, we can assess the motion of particles and their sizes [8]. In this case, the motion of particles is characterized by the diffusion coefficient.

The scheme of the hardware and software system developed is shown in Fig. 1. A single-mode laser module *1* with 5 mW continuous-wave output power and a wavelength of 650 nm was chosen as the radiation source. Power was supplied to the module through a rechargeable battery, providing highly stable lasing output. An aspheric short-focus lens *3* is used, allowing to focus the beam to a diameter of 500 μm, with a caustic length in solution equal to 5 mm. Scattered radiation can be detected in a range of angles from 5 to 175°. The aperture and multimode fiber serve to limit the region from which radiation is

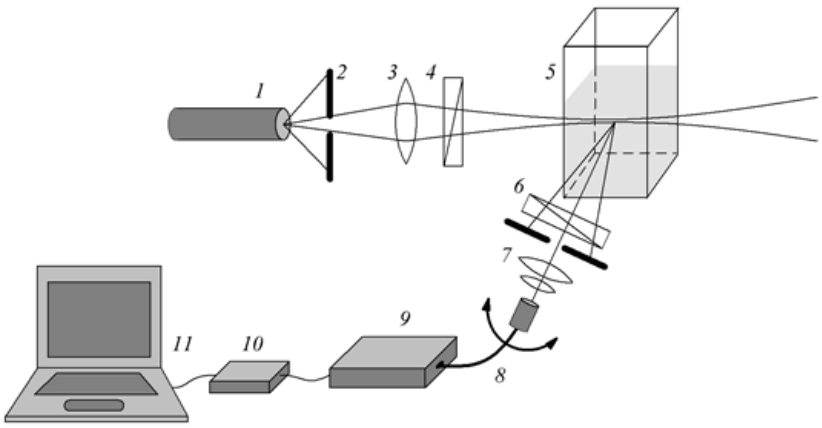

Fig. 1. Scheme of laser correlation spectrometer:
laser *1*, screen *2* with aperture, focusing lens *3*, polarizer *4*, cell *5* with test solution, output rotary analyzing polarizer *6*, collimating system *7*, input connector *8* of single-mode optical fiber, photomultiplier *9*, ADC module *10*, computer *11* with processing software

scattered (setting the effective scattering volume). The effective scattering length, calculated for a scattering angle of 90°, is 4.8 mm. The signal from photomultiplier *9* is digitized by ADC module *10* at frequencies of 50 kHz–50 MHz and processed with the software.

The hardware components could be fit in a small package with the given modification of the LCS method (the dimensions were 25 × 15 × 5 cm), allowing to construct a portable laser correlation spectrometer (weighing up to 2 kg) [9].

Polarizing plates *4* were added to the scheme for analyzing non-spherical nanoparticles [10].

The scattered radiation was detected in two orthogonal positions of the analyzing polarizer, so that the translational and rotational diffusion coefficients could be calculated separately. The longitudinal and transverse dimensions of non-spherical particles were estimated by both of these components.

Analysis of nanoparticle sizes using autocorrelation functions

The signal recorded using the given scheme is a pseudo-random dependence of the intensity of scattered radiation on time. The frequency of this signal depends on intensity fluctuations in the light scattered in the observation plane, which depend, in turn, on the coefficient of Brownian diffusion of particles in the solution. Fourier transforms can be used to find the characteristic frequencies but this approach does not yield accurate results because signals from several particles are recorded simultaneously and noise is generated. As a rule, time-domain rather than frequency-domain representation of the signal spectrum is used in such cases, i.e., the autocorrelation function is calculated.

Let us consider the diffusion of particles in solution in more detail. Brownian motion is a random process, so when a cell with the solution is illuminated with a laser beam, the number of scattering particles in the measuring volume is random, as is the intensity of the scattered light.

The scattering signal is processed in LCS by calculating the autocorrelation function of the signal:

$$G^{(1)}(\tau) = \langle E_S^*(t) E_S(t+\tau)\rangle, \quad (1)$$

where $E_s(t)$ is the light field in the observed region; $G^{(1)}(\tau)$ is called the autocorrelation function of the first kind; τ is the correlation time.

Quadratic detectors (photomultipliers) are typically used in real experiments; they register fluctuations of scattered radiation intensity rather than the field. In this case, an autocorrelation function of the second kind is calculated, taking the following form:

$$G^{(2)}(\tau) = \langle E_S^*(t) E_S(t) E_S^*(t+\tau) E_S(t+\tau)\rangle. \quad (2)$$

If the scattered light is a stationary Gaussian random process, the autocorrelation function of the second kind is connected to the autocorrelation function of the first kind by the Siegert relation [11]:

$$G^{(2)}(\tau) = \left|G^{(1)}(\tau)\right|^2 + 1. \quad (3)$$

This relation allows to make a transition from the measured function $G^{(2)}(\tau)$ to the function $G^{(1)}(\tau)$. The autocorrelation function for identical spherical diffusers whose positions are not correlated can be rewritten in the following form [11]:

$$G^{(1)}(\tau) = S(\mathbf{q}, d)\langle e^{i\mathbf{q}(\mathbf{r}(\tau)-\mathbf{r}(0))}\rangle e^{-i\omega_0\tau}. \quad (4)$$

In this equation, $S(\mathbf{q},d)$ is the amplitude of the scattered radiation; $\mathbf{q}$ is the scattering vector whose modulus is calculated as follows:

$$|\mathbf{q}| = \frac{4\pi n_0}{\lambda_0}\sin\left(\frac{\theta}{2}\right). \quad (5)$$

This expression is further simplified for free and isotropic diffusion:

$$G^{(1)}(\tau) = S(\mathbf{q}, d)\langle e^{-\mathbf{q}^2 D_T \tau}\rangle e^{-i\omega_0\tau}. \quad (6)$$

Here D_T is the translational diffusion coefficient, which, according to the Stokes–Einstein formula, is given as follows [11]:

$$D_T = 2k_B T / 6\pi\eta d, \quad (7)$$

where η, Pa·s, is the viscosity of the liquid; k_B, J/K, is the Boltzmann constant; T, K, is the temperature; d, m, is the hydrodynamic diameter of the diffusers.

The above formulas are sufficient for calculating the diffusion coefficients and the size of molecules in equilibrium. Additionally, agglomerations of biological molecules or metals can be monitored, allowing to qualitatively characterize the activity of various molecules, assessing the composition of the solution.

This theory is only valid for spherical scatterers and in the absence of polarizability anisotropy of radiation. Rotational diffusion also has to be taken into account for more detailed study. If we abandon the spherical approximation and assume that the amplitudes of the scattered light field depend on particle orientation in space, the expression for the

autocorrelation function for objects with rotational symmetry (cylinders, ellipsoids) is rewritten as follows [10, 12]:

$$G^{(1)}(\tau) = S_1(\mathbf{q}, d_1, d_2)e^{-q^2 D_T \tau} + \\ + S_2(\mathbf{q}, d_1, d_2)e^{-(q^2 D_T + 6D_R)\tau}, \quad (8)$$

where $S_0(\mathbf{q},d)$, $S_1(\mathbf{q},d)$ are the constant and the variable amplitude of scattered radiation, respectively, the latter depending on particle rotation; d_1, d_2 are arbitrary values of diameter and length of particles, D_R is the translational diffusion coefficient.

The first term in this expression is responsible for ordinary translational diffusion, the second usually depends on rotational diffusion.

Angular dependences of $S_0(q,d)$ and $S_1(q,d)$ suggest that only translational diffusion makes a significant contribution to the scattering signal at small angles (in our case, $\theta < 60°$) [12]. As the viewing angle increases, the contribution of rotational motion increases as well, but angular dependences of scattering should be measured to separate translational from rotational motion.

In case of polarizability anisotropy of the scatterers (or in case of non-spherical particles), the autocorrelation function of the depolarized scattering component can also be measured:

$$G^{(1)}_{Dep}(\tau) = S_{Dep}(\mathbf{q}, d)e^{-(q^2 D_T + 6D_R)\tau}. \quad (9)$$

Evidently, the component responsible solely for translational motion is absent, which makes it possible to avoid measuring the angular dependences and limit measurement of polarized and depolarized components at small (in the range of 20–50°) angles.

The diffusion coefficients depend on the shape of the diffuser. The diffusion coefficients for ellipsoids of revolution, which are the main form of nanoparticles observed in experiments, can be written as follows [12]:

$$D_T = \frac{k_B T}{3\pi\eta d_a} F(d_a, d_b),$$

$$D_R = \frac{k_B T}{\pi\eta d_a^3} \frac{\left(2 - \left(\frac{d_b}{d_a}\right)^2\right) F(d_a, d_b) - 1}{1 - \left(\frac{d_b}{d_a}\right)^4},$$

$$F(d_a, d_b) = \frac{1}{\sqrt{1 - \left(\frac{d_b}{d_a}\right)^2}} \times \\ \times \ln\left(\frac{1 + \sqrt{1 - \left(\frac{d_b}{d_a}\right)^2}}{\frac{d_b}{d_a}}\right), \quad (10)$$

where d_a, d_b are the semi-axes of the ellipsoids.

Based on measuring the translational and rotational diffusion coefficients, we can separately calculate the sizes of non-spherical particles.

Thus, the task of determining the sizes of nanoparticles consists in constructing the autocorrelation function of the scattering signal, solving the inverse ill-posed problem to find the diffusion coefficients and calculating particle sizes by Eq. (7) or (10).

Methods for solving the inverse LCS problem

As already noted, the problem of approximating experimental data is simple for the given case of light scattering by monodisperse spherical particles. However, it is more difficult to interpret the experimental data if the samples are polydisperse. Only two or three parameters of the polydisperse distribution can be obtained for achievable measurement accuracy: the average particle size, the width of the distribution, and its asymmetry.

The form of the correlation curve of the field function, which is an exponential function in case of monodisperse spheres, i.e.,

$$|g^{(1)}|(\tau) = e^{-\Gamma}$$

(where $\Gamma = D_T q^2$), changes for polydisperse particles and is generally written as a superposition of exponential functions:

$$\left|g^{(1)}(\tau)\right| = \int_0^\infty F(\Gamma) e^{-\Gamma\tau} d\Gamma, \quad (11)$$

where $F(\Gamma)$ is the contribution to total intensis ty from the radiation component scattered by particles of the same size.

Eq. (11) is solved by finding a set of diffusion coefficients for each particle size. The expression for the function contains experimental errors, which leads to a systematic error in the desired distribution $F(\Gamma)$.

There are many methods for finding solutions to equations of type (11) [13]. These methods can be divided into several main categories: statistical, variational, iterative and projective. The specific method selected for a particular task of LCS depends on its advantages and disadvantages for each case.

Projective methods. These methods are used for increasing the stability of the problem and are based on projection of an unstable functional on a compact. However, it is too difficult to define a compact for solving the right-hand side of the equation in real problems. So projective methods are commonly used to apply a priori limitations to the desired solution. A method that can be used for integral equations is the Fourier transform. If we know the right-hand side of the equation only approximately, then the Fourier transform using the filter function can suppress the effects of high frequency.

Statistical methods. These methods are based on a priori statistical information about the properties of the matrix represented as an approximate integral operator. The discrete equivalent of integral equations is taken in these methods:

$$Ax + \xi = y.$$

A common method in industrial operation is the method of cumulants [14]. It is quick and easy, so this method is described in the international standard ISO 13321:1996. However, only the average diffusion coefficient and its moments can be found by this method without a priori information. What is more, the method of cumulants is verifiable with a unimodal distribution, yielding distorted results in case of polydisperse solutions [9].

The distribution of decay rates $F(\Gamma)$ is found from the condition that $F(\Gamma)d\Gamma$ is the fraction of the total scattering intensity due to molecules whose $D_T q^2$ values lie in the interval between Γ, $\Gamma + d\Gamma$

$$\int_0^\infty F(\Gamma)\,d\Gamma = 1.$$

Cumulants $K_m(\Gamma)$ of the distribution $F(\Gamma)$ were calculated by the experimental data in [15] based on Koppel's approach. The first cumulant ($m = 1$) gives the "Z-average" value of the diffusion coefficient, the second ($m = 2$) characterizes the width of the distribution, the third ($m = 3$) characterizes the asymmetry, etc. Cumulants are also used as a sensitive method for finding deviations from monodispersity.

This method is still the most popular in commercial production, but it does not yield accurate measurement results when the expected particle sizes are unknown. Besides, commercial spectrometers often produce incorrect results for polydisperse multicomponent mixtures.

Bayesian methods use a posteriori probability density as a function of uncertainty $P(x|y)$ for the solution vector x and the experimental data y. This method is very effective and can provide the required solution with any background noise in the matrix and on the right-hand side of the equation. The only problem is that the most complete a priori information about the desired solution has to be obtained to apply the method, which is currently impossible in experiments with biological fluids.

Iterative methods. The central idea behind these methods is to formulate an iterative scheme converging to an exact solution if $\delta = 0$ on the right-hand side of the equation or there are no errors in the operator, or if $\delta \neq 0$ when a divergent iterative process is interrupted for a number of iterations. Nonlinear optimization (the Levenberg–Marquart method) can be used for solving the inverse problem in polydisperse solutions. Unfortunately, this method requires accurate a priori information about the form and number of components in the distribution, so it is not particularly useful in actual processing.

The non-negative least squares method is also iterative. It is useful as part of other algorithms but the data it yields may be too fragmented [15]. The simplest and most effective of the iterative methods is the Friedman method [16] allowing to take into account almost any a priori information about the required solution. On the other hand, this method's robustness against noise in the original data is poor and, besides, it is not quite suitable for solving equations with an exponential kernel.

Variational methods. Substantial progress in solving ill-posed problems was made through Tikhonov's general theory of regularization [17]. The method consists in finding a solution not in the class of all integrable functions but in a narrower class that satisfies some additional conditions. Until recently, CONTIN was one of the most popular methods. However, this method is too specific for the regularization parameter and does not allow for narrow peaks to be resolved. We compared Tikhonov's regularization and CONTIN in our previous paper [4].

Tikhonov's regularization stabilizes the deviations of the theoretical curve from the ex-

Table 1

Comparison of benefits and drawbacks of different methods for solving inverse ill-posed problems

Methods	Benefits	Drawbacks
Projection (e.g., Fourier filtering)	1. No need for a priori information. 2. No need for least-squares fitting procedures	1. Oscillations present 2. Filtering function has to be selected 3. Adjacent lines with different intensities are difficult to reconstruct 4. Negative values present in solution
Statistical (e.g., Bayesian)	1. Yield necessary solution with any background noise 2. Default level can be set individually for each matrix element	Greatest amount of a priori information needed
Iterative (e.g., Friedman method)	Virtually any a priori information can be taken into account.	1. Large number of iterations 2. Values of expected results have to be set 3. Possible errors accumulated
Variational (e.g., Tikhonov's method)	1. Cross-functionality 2. Minimum a priori information required 3. Smooth solution	1. Regularization parameter has to be chosen 2. Narrow lines are difficult to reconstruct

perimental one by means of an additional composite stabilizing functional $\Omega(x)$. The main advantage is cross-functionality of the method, as it uses a minimum of a priori information. Another variational method is truncated singular-value decomposition [18]. Its algorithm is close to Tikhonov's method, but it can be used to reduce rounding errors.

Comparison of the methods. The above methods are summarized and compared in Table 1. As evident from the data, variational methods are optimal for use in LCS problems with no a priori information about the scattering particles. The existing drawbacks of these methods can be avoided by introducing some modifications in the common algorithms and conducting model experiments to refine the regularization parameter.

Algorithm developed for solving inverse problem of LCS

As noted above, if suspended particles of different sizes are found in the liquid, their sizes can be determined by solving the inverse LCS problem (11), that is, reconstructing the function $F(\Gamma)$ from the known function $g^{(1)}(\tau)$. This inverse problem is ill-posed in the sense that the small error of the experimental data produces a large error in the calculated dependence $F(\Gamma)$.

Because the dependence $F(\Gamma)$ is measured in a discrete and finite set of points, and because a numerical solution has to be obtained for (11), the problem is reduced to a system of equations that is written in matrix form as

$$A\mathbf{f} = \mathbf{g} \qquad (12)$$

Certain a priori conditions which differ depending on the problem solved are imposed on the solution of this system if regularization is used. The conditions that the solution be non-negative (bounded in a compact set $M \geq 0$) and smooth (i.e., without outliers) are commonly accepted.

According to Tikhonov's method, an approximate solution of system of linear algebraic equations (12), resistant to small changes in the right-hand side, is found by replacing system (12) with the minimization problem with the added regularizing term:

$$\left\| A\mathbf{f} - \tilde{\mathbf{g}} \right\|^2 + \alpha\Omega(\mathbf{f}) \to \min, \qquad (13)$$

where α is the smoothing parameter ($\alpha > 0$); $\Omega(\mathbf{f})$ is the stabilizing functional that is selected separately for each problem; $\tilde{\mathbf{g}} \to \mathbf{g}$.

The stabilizing functional is chosen in laser correlation spectroscopy to reduce the jumps of the zero derivative for obtaining smooth solutions:

$$\Omega(\mathbf{f}) = \|\mathbf{f}\|^2 .$$

Minimization of this kind stabilizes the solution of the system, improving its conditioning; the agreement between the real and desired solutions is also increased. However, this choice often leads to excessive smoothing of solutions; if the solution is a combination of several narrow peaks, it can be difficult to separate them.

The regularizing parameter α is selected based on the input data, which is to say that a too high α produces "smoothed" solutions, and a too low value makes the problem unstable.

The starting value of the parameter α in our algorithm was chosen to be 1% of the maximum diagonal element of the matrix *A*. After the first iteration of solving system (13), the residual $\|A\mathbf{f} - \tilde{\mathbf{g}}\|^2$ was calculated, the parameter α was reduced by 90% of the initial value and the system was solved again. After the second iteration, the residual was again calculated and compared with the residual obtained at previous iteration. If they differed by more than 10%, the parameter α was again reduced by 90%, and the next iteration started. Since the proposed algorithm uses comparison of residuals, there is no need to set the noise level in the experiment, which is often not known exactly [19].

System of equations (13) is solved by the modernized Gauss method with the eigenvalues of the matrix shifted towards higher values because a regularizing term is introduced; this makes the solution more robust to noise.

After the solution cycle ends and the final distribution **f** is obtained, the solution is checked for negative components. Two different methods for eliminating negative solutions are included in the software.

In the first case, with $f_i < 0$, we take $f_j = 0$ for all extreme values of *j* in this Gaussian and exclude these points from further calculations. After that, we return to setting the initial value of α.

Values of f_j exceeding 60% of the minimum, rather than extreme points, are excluded from the calculations in the second method. This calculation is faster, but yields less accurate results, therefore it is suitable for preliminary analysis of particle size distributions. System (13) is recalculated until all negative components are completely eliminated.

Setting a fairly high initial value of α could produce unnecessarily smoothed solutions, however, the regularization algorithm eliminates positive values in addition to discarding negative values. Extreme points in the Gaussian are excluded from the solution one by one until a given width is reached, which makes it possible to calculate the sizes in highly polydisperse mixtures with resolutions up to 0.5 nm.

There is constant background illumination in addition to the variable component in real experiments. As a result, the autocorrelation function does not drop to zero at infinity, but rests on a pedestal whose height is proportional to the intensity of the background noise. A cycle removing the constant component was added to the program's algorithm to eliminate background noise.

The algorithm can be described as follows:

Step 1. Set initial (sufficiently high) value of α.

Step 2. Solve system of equations (13) and find the solution **f**.

Step 3. Calculate the residual

$$\|A\mathbf{f} - \tilde{\mathbf{g}}\|^2$$

(decrease α by 90% after the first iteration and return to Step 1).

Step 4. Compare the residuals by the inequality

$$\|A\mathbf{f} - \tilde{\mathbf{g}}\|_i^2 < 0{,}1 \cdot \|A\mathbf{f} - \tilde{\mathbf{g}}\|_{i-1}^2 ;$$

if it is satisfied, reduce α by 90% and return to Step 1, if not, go to Step 5.

Step 5. Check for negative components of the solution **f**. If there are $f_i < 0$, assume that $f_j = 0$ and return to step 1. The corresponding component is excluded from further calculations.

Step 6. If there are no $f_i < 0$, check the number of distribution points $n > N$ (set prior to solution); if yes, then set $f_{\min} = 0$ and return to Step 1; if no, end the calculation.

The domain of expected solutions and the desired accuracy should be set before start to speed up the calculations. Solution in the entire range of permissible values is also possible but it takes much longer because there is a cubic relationship between the time to solve the problem by the Gauss method and the number of points. The method for eliminating negative values (as described above) and the number of points left at the peak (more are taken if there are weak components) should be also chosen. The correlations obtained from experimental data can be averaged for greater accuracy.

Verification of the method

We tested the developed hardware and software system using computer simulation and experiments with objects of known diameters, polydisperse biological suspensions and suspensions containing non-spherical clusters of particles.

The first stage of testing involved analyzing model signals with different noise levels (from 0 to 10% of the useful signal) and with a different number of components. The results indicate that the accuracy with which the center of the Gaussian is reconstructed for unimodal distributions is close to 100% for any values of the noise level. The noise value of 10% for model signals corresponds to a signal-to-noise ratio of 21.6 dB in actual experiments (for a single measurement). To increase the signal-to-noise ratio, we recorded from 50 to 100 signals whose autocorrelation functions were averaged. This considerably reduced the contribution of the noise component to the useful signal.

Since the main purpose of the hardware and software system was to study the dynamics of cluster formation in polydisperse biological fluids, we found it interesting to calculate the accuracy with which model signals containing information about polydisperse particles with sizes from 1 to 100 nm are reconstructed. {Fig. 2 shows the reconstructed size distributions (calculation) for a signal with the given particle sizes, nm: 4, 10 and 21 (model).

Evidently, relative concentrations are not always reconstructed correctly but the position of the central peak and its width is calculated with an error not exceeding 5.7%.

The actual experiments were carried out using a quasi-monodisperse suspension of

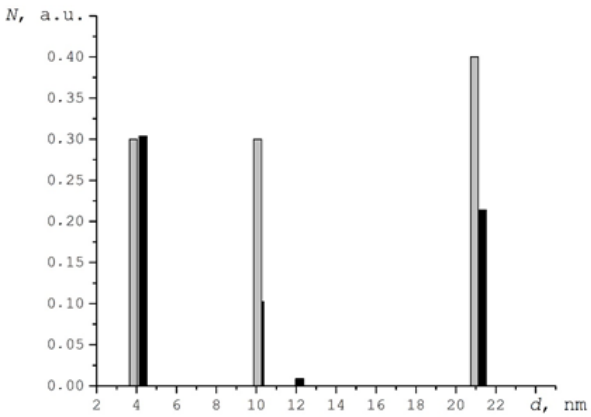

Fig. 2. Reconstructed distributions of model concentrations for particles with sizes of 4, 10 and 21 nm
Black columns correspond to calculated values, gray columns to model values

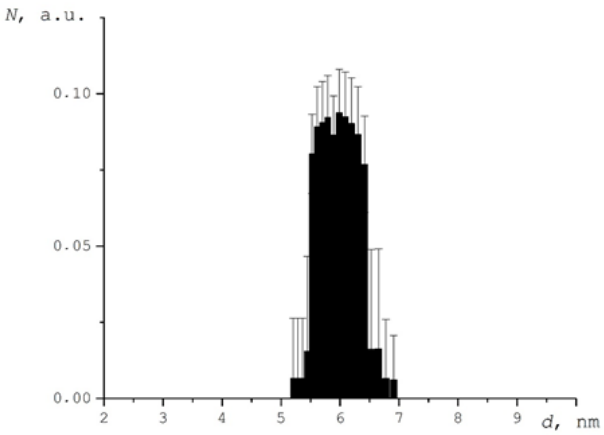

Fig. 3. Calculated particle size distribution in aqueous suspension of albumin protein at neutral pH

egg albumin protein in water. According to theoretical data, the albumin molecule has a diameter $d = 6$ nm in equilibrium (at neutral pH) [20]. Fig. 3 shows the size distribution of albumin in an aqueous suspension. It can be seen that the central position of the peak corresponds to the theoretical value, and the shape is described by the Gaussian curve.

To confirm that it was possible to describe the dynamics of particle aggregation in solutions, we measured the sizes of albumin protein aggregates in solutions with a varying pH. Albumin tends to aggregate forming large clusters near the isoelectric point (pH = 4.8) [21]. As the pH of the solution decreases further, protein aggregates disintegrate and the protein denatures [22]. The pH value in our experiments varied from 8.0 to 1.6 [23]. The calculated average sizes of aggregates are given in Table 2.

Table 2

Average particle sizes in albumin solutions with different pH values

pH	*R*, nm
8.0	6.00.4±
7.0	6.00.4±
6.0	9.00.5±
5.0	29.02.3±
4.2	30.02.4±
3.6	20.02.2±
2.5	16.01.8±
1.6	5.00.4±

As evident from the data in Table 2, when the pH of the solution changes from acidic to alkaline, albumin aggregation is observed near the isoelectric point, followed by de-aggregation with further increase in acidity. Thus, the proposed hardware and software system allows not only to detect particle sizes the size of particles, but also to observe their variation.

To confirm that this method can be applied to studying the composition of real biological fluids, the distribution of particle size in serum was measured in [24]. The result is shown in Fig. 4.

It is known that the sizes of particles in serum are different for different types of proteins. For example, albumin and amino acids have particle sizes from 1 to 10 nm, globulins from 11 to 30 nm; high-density lipoproteins and low-molecular circulating immune complexes have sizes from 31 to 70 nm; high-molecular circulating immune complexes have sizes greater than 150 nm [25].

Thus, we can divide the obtained size distribution into separate groups of proteins, analyzing their relative concentrations and tracing the dynamics of cluster formation in case of certain effects, and determine some important diagnostic parameters [26, 27]. Since the sizes of proteins in circulating immune complexes are drastically different from the sizes of other components, we can draw certain conclusions about the state of human immune system in terms of the size distribution and relative concentration of circulating immune complexes [24].

All of the results given above were obtained assuming that the scattering particles were approximately spherical. We used a solution of the magnetic fluid Fe_3O_4 to assess non-spherical particles. Magnetic fluid in equilibrium consists of an aqueous suspension of particles with diameters of about 10 nm [28]; however, it was found that magnetic particles lose equilibrium upon dilution, forming clusters of elongated ellipsoidal shape. The magnetic fluid in our experiments was diluted to a concentration of 0.15 mg/ml and tested using the proposed hardware and software system.

The translational and rotational diffusion coefficients for the agglomerates of magnetic particles and for single nanoparticles were calculated using the obtained values of the exponents G for polarized and depolarized components of scattered light. The diameters of the ellipsoids in two orthogonal sections d_b and d_a were calculated by Eqs. (10). We ultimately concluded that the nanoparticles were non-spherical judging from the calculated aspect ratio $\varepsilon = d_b/d_a$ (Table 3). The obtained data show that single nanoparticles predominantly have shapes close to spherical; this is confirmed by the results of scanning electron microscopy [29], while their aggregates have more elongated ellipsoidal shapes. Similar data were also obtained using other methods but the exact dimensions were not calculated. The size ranges given in Table 3 indicate that the given magnetic fluid is polydisperse and describe the sizes

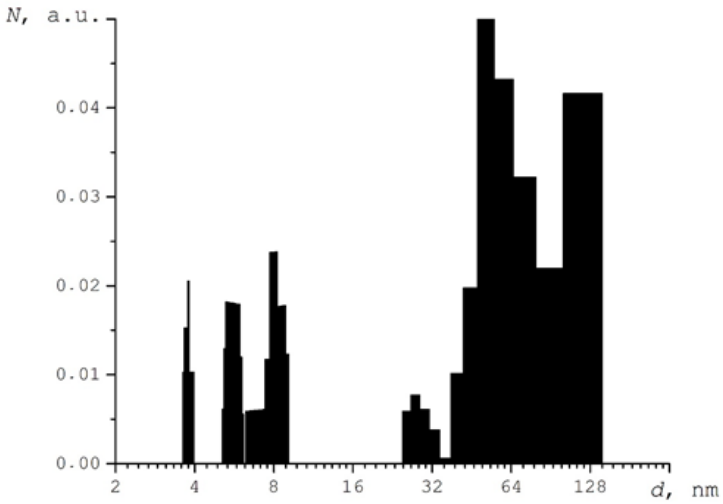

Fig. 4. Experimentally obtained particle size distribution in blood serum

and shapes of the clusters forming, which complicates analysis related to determining the shapes of nanoparticles. At the same time, the obtained result indicates that the classical spherical approximation cannot be applied to study of aggregates in magnetic fluids.

Table 3

Calculated sizes of magnetic particles and their aggregates

Parameter	Value	
	Aggregates	Single particles
D_T, (μm)^2/s	2.8–3.5	58–80
D_R, s^{-1}	700–1060	(4–6)·10^5
d_a, nm	73–94	4.1–5.0
d_b, nm	48–70	3.5–4.7
ε	0.50–0.96	0.85–1.00

Notation: d_a, d_b *are* the diameters of ellipsoids in two orthogonal sections, D_T is the translational diffusion coefficient; D_R is the rotational diffusion coefficient; $\varepsilon = d_b/d_a$

Conclusion

We have introduced a modified method of laser correlation spectroscopy and a hardware and software system developed based on this method, making it possible to detect the sizes of individual molecules and nanoparticles, as well as the dynamics of their clusterization in liquid media, including in blood serum [30]. The algorithm for solving the inverse problem of laser correlation spectroscopy described in this paper allows to calculate the sizes of polydisperse particles with an error not exceeding 6%. The modification proposed for the scheme of the laser correlation spectrometer and the approaches used to analyze the experimental data made it possible to determine the longitudinal and transverse dimensions of non-spherical nanoparticles in polydisperse solutions for the first time ever.

Testing the developed hardware and software system, we have proved that the accuracy with which dimensions are measured is not inferior to the commercially available spectrometers (Zetasizer Nano ZS and Photocor) for single-component solutions [4] and is considerably better that the known equivalents for multicomponent solutions.

The study was financially supported by the Innovation Promotion Fund (contract no. 13463GU/2018 of 20/07/2018).

REFERENCES

1. **Marakhova A., Zhilkina V., Blynskaya E., et al.,** Determination of nanoparticle size in colloidal solutions by dynamic light scattering, Nanoindustry. 63 (1) (2016) 88–93.

2. **Xu R.,** Light scattering: a review of particle characterization applications, Particuology. 18 (2014) 11–21.

3. **Sergeeva I.A., Khitrina K.A., Krot A.R., et al.,** Investigation of the interaction and dynamics of collagen and collagenase molecules in solutions by dynamic light scattering, Izvestiya of Saratov University, New series. Series Physics. 17 (3) (2017) 171–178.

4. **Nepomnyashchaya E., Velichko E., Aksenov E.,** Inverse problem of laser correlation spectroscopy for analysis of polydisperse solutions of nanoparticles, Journal of Physics: Conference Series. 769 (1) (2016) 012025.

5. **Yudin I.K., Deshabo V.A., Shalayev P.V., Tereshchenko S.A.**, Depolarization of light scattered in water dispersions of nanoparticles of different shapes, Biomedical Engineering. 49 (6) (2016) 394–397.

6. **Vlasova I.M., Zhuravleva V.V., Saletskiy A.M.,** Rotational diffusion of bovine serum albumin, denaturated with sodium dodecyl sulfate, according to tryptophan fluorescence, Russian Journal of Physical Chemistry A. 88 (3) (2014) 538–544.

7. **Ryabukho V.P.,** Speckle interferometry, Sorosovskiy Obrazovatelnyy Zhurnal. 7 (5) (2001) 102–109.

8. **Velichko E.N., Nepomnyashchaya E.K., Aksenov E.T.,** Modification of the laser correlation spectrometer for analysis of biological fluids, Uchenye Zapiski Kazanskogo Universiteta. Seriya Fiziko-Matematicheskie Nauki. 160 (1) (2018) 51–60.

9. **Nepomnyashchaya E., Zabalueva Z., Velichko E., Aksenov E.** Modifications of laser correlation spectrometer for investigation of biological fluids // EPJ Web of Conf. 161 (2017) 02017.

10. **Tereshchenko S.A., Burnayevskiy I.S., Dolgushin S.A., Shalaev P.V., Yudin I.K., Deshabo V.A.,** Determination of the composition of liquid polydispersions of cylinder-like microorganisms from the laser depolarization degree, Biomedical Engineering. 50 (6) (2017) 385–389.

11. **Stetefeld J., McKenna S.A., Patel T.R.,** Dynamic light scattering: a practical guide and applications in biomedical sciences, Biophys. Rev. 8 (4) (2016) 409–427.

12. **Nepomnyashchaya E., Aksenov E., Velichko E.,** Molecular dynamics as studied by laser correlation spectroscopy, Progress in Electromagnetics Research Symposium-Spring (PIERS). St. Petersburg (2017) 3556–3562.

13. **Nemtsova O.M.,** Methods for solving inverse problems involving by the Fredholm equation of the first kind, Vestnik Udmurtskogo Universiteta. Fizika. 4 (2005) 23–34.

14. **Koppel D.E.,** Analysis of macromolecular polydispersity in intensity correlation spectroscopy: the method of cumulants, J. Chem. Phys. 57 (11) (1972) 4814–4820.

15. **Mailer A.G., Clegg P.S., Pusey P.N.,** Particle sizing by dynamic light scattering: non-linear cumulant analysis, Journal of Physics.: Condense Matter. 27 (14) (2015) 145102.

16. **Bro R., de Jong S.,** A fast non-negativity-constrained least squares algorithm, Journal of Chemometrics. 11 (5) (1997) 393–401.

17. **Yankovskiy G.M., Kuznetsov D.V., Kondakov S.E., Melnikov M.Ya.,** Solution of the inverse problem of light beating spectroscopy using singular value decomposition for analyzing the composition of polydisperse suspensions of nanoparticles, Moscow University Chemistry Bulletin. 54 (5) (2013) 278–287.

18. **Yankovskiy G.M., Kuznetsov D.V., Kondakov S.E., Melnikov M.Ya,** Solution of the inverse problem of light beating spectroscopy using singular value decomposition (SVD) method for the analysis of polydisperse suspensions of nanoparticles, Moscow University Chemistry Bulletin. 54 (6) (2013) 312–320.

19. **Nepomnyashchaya E.K., Velichko E.N., Aksenov E.T.,** Solution of the laser correlation spectroscopy inverse problem by the regularization method, Humanities and Science University Journal. 13 (13) (2015) 13–21.

20. **Vlasova O.L.**, The multiple parameter approach to the optical analysis of model dispersions of bovine serum albumin, St. Petersburg Polytechnical University Journal. Physics and Mathematics. 2(77) (2009) 39–44.

21. **Baranov A.N., Vlasova I.M., Saletskiy A.M.**, Investigation of serum-albumin aggregation, Journal of Applied Spectroscopy. 71 (2) (2004) 222–226.

22. **Baranov A.N., Vlasova I.M., Mikrin V.E., Saletskiy A.M.,** Laser correlation spectroscopy of the processes of serum albumin denaturation, Journal of Applied Spectroscopy. 71 (6) (2004) 911-915.

23. **Nepomniashchaya E.K., Aksenov E.T., Bogomaz, Velichko E.N.,** Use of laser correlation spectroscopy to investigate the parameters

of biological suspensions, Journal of Optical Technology. 82 (3) (2015) 162–165.

24. **Nepomnyashchaya E., Velichko E., Bogomaz T.,** Diagnostic possibilities of dynamic light scattering technique, Proceedings of SPIE, Nanoscale Imaging, Sensing, and Actuation for Biomedical Applications, 16th. 10891 (2019) 108910J.

25. **Pluzhnikov M.S., Govorun M.I., Migmanova K.L.,** Vozmozhnosti lazernoy korrelyatsionnoy spektroskopii syvorotki krovi v diagnostike opukholey golovy i shei [Possibilities of laser serum correlation spectroscopy in the diagnosis of head and neck tumors], Russian Otorhinolaryngology. 27(2) (2007) 77–83.

26. **Gibizova V.V., Anenkova K.A., Maslennikova A.D., et al.,** Determination of fundamental physical parameters of blood serum proteins for development the methods for cancer diagnosis, Almanac of Clinical Medicine. 44 (2) (2016) 158–164.

27. **Kapralova V.M., Nazarova E.A., Ivanova N.E., Shadrin E.B.,** Albumin conformational changes as a diagnostic parameter, St. Petersburg Polytechnical University Journal. Physics and Mathematics. 3 (153) (2012) 83–91.

28. **Nepomnyashchaya E.K., Prokofiev A.V., Velichko E.N., et al.,** Investigation of magneto-optical properties of ferrofluids by laser light scattering techniques, Journal of Magnetism and Magnetic Materials. 431 (2017) 24–26.

29. **Prokofiev A.V., Pleshakov I.V., Kuzmin Y.I., Bibik E.E.,** An optical investigation of the geometric characteristics of aggregates formed by particles of magnetic fluid, Technical Physics Letters. 43(2) (2017) 194–196.

30. **Karganov M.Yu., Alchinova I.B., Yakovenko E.N., et al.,** Primeneniye metoda lazernoy korrelyatsionnoy spektroskopii v laboratornoy meditsine [An application of laser correlation spectroscopy in laboratory medicine], Russian Clinical Laboratory Diagnostics. 61(9) (2016) 533–534.

Received 31.03.2019, accepted 24.04.2019.

THE AUTHORS

NEPOMNYASHCHAYA Elina K.
Peter the Great St. Petersburg Polytechnic University
29 Politechnicheskaya St., St. Petersburg, 195251, Russian Federation
elina.nep@gmail.com

VELICHKO Elena N.
Peter the Great St. Petersburg Polytechnic University
29 Politechnicheskaya St., St. Petersburg, 195251, Russian Federation
velichko-spbstu@yandex.ru

СПИСОК ЛИТЕРАТУРЫ

1. **Марахова А., Жилкина В.,** Блынская **Е., Алексеев К.,** Станишевский **Я.** Определение размеров наночастиц в коллоидных растворах методом динамического рассеяния света // Наноиндустрия. 2016. Т. 63. № 1. С. 88–93.

2. **Xu R.** Light scattering: a review of particle characterization applications. Particuology. 2014. Vol. 18. Pp. 11–21.

3. **Сергеева И.А., Хитрина К.А., Крот А.Р., Сукнева А.В., Петрова Г.П.** Исследование взаимодействия и динамики молекул в растворах коллагена и коллагеназы методом динамического рассеяния света // Известия Саратовского университета. Новая серия. Серия Физика. 2017. Т. 17. № 3. С. 171–178.

4. **Nepomnyashchaya E., Velichko E., Aksenov E.,** Inverse problem of laser correlation spectroscopy for analysis of polydisperse solutions of nanoparticles // Journal of Physics: Conference Series. 2016. Vol. 769. No. 1. P. 012025.

5. **Юдин И.К., Дешабо В.А., Шалаев П.В., Терещенко С.А.** Деполяризация рассеянного света в водных дисперсиях наночастиц различной формы // Медицинская техника. 2015. Т. 294 № .6. С. 55–52.

6. **Власова И.М., Журавлева В.В.,** Салецкий **А.М.** Вращательная диффузия бычьего сывороточного альбумина, денатурированного додецилсульфатом натрия, по данным флуоресценции триптофана // Журнал физической химии. 2014. Т. 3 № .88. С. 544–538.

7. **Рябухо В.П.** Спекл-интерферометрия // Соросовский образовательный журнал. 2001.

Т. 5 № .7. С. 109–102.

8. **Величко Е.Н., Непомнящая Э.К., Аксенов Е.Т.** Модификация лазерного корреляционного спектрометра для анализа биологических жидкостей // Ученые записки Казанского университета. Серия Физико-математические науки. 2018. Т. 160. № 1. С. 51–60.

9. **Nepomnyashchaya E., Zabalueva Z., Velichko E., Aksenov E.** Modifications of laser correlation spectrometer for investigation of biological fluids // EPJ Web of Conferences. 2017. Vol. 161. P. 02017.

10. **Терещенко С.А., Бурнаевский И.С., Долгушин С.А., Шалаев П.В., Юдин И.К.,** Дешабо **В.А.** Определение состава жидких полидисперсий цилиндроподобных микроорганизмов по степени деполяризации лазерного излучения // Медицинская техника. 2016. Т. 300. № 6. С. 17–20.

11. **Stetefeld J., McKenna S.A., Patel T.R.** Dynamic light scattering: a practical guide and applications in biomedical sciences // Biophys. Rev. 2016. Vol. 8. No. 4. Pp. 409–427.

12. **Nepomnyashchaya E., Aksenov E., Velichko E.** Molecular dynamics as studied by laser correlation spectroscopy // Progress in Electromagnetics Research. Symposium-Spring (PIERS). St. Petersburg, 2017. Pp. 3556–3562.

13. **Немцова О.М.** Методы решения обратных задач, выраженных интегральными уравнениями Фредгольма первого рода // Вестник Удмуртского университета. Серия 4. Физика и химия. 2005. № 4. С. 23–34.

14. **Koppel D.E.** Analysis of macromolecular polydispersity in intensity correlation spectroscopy: the method of cumulants // J. Chem. Phys. 1972. Vol. 57. No. 11. Pp. 4814–4820.

15. **Mailer A.G., Clegg P.S., Pusey P.N.** Particle sizing by dynamic light scattering: non-linear cumulant analysis // Journal of Physics.: Condense Matter. 2015. Vol. 27. No. 14. P. 145102.

16. **Bro R., de Jong S.** A fast non-negativity-constrained least squares algorithm // Journal of Chemometrics. 1997. Vol. 11. No. 5. Pp. 393–401.

17. **Янковский Г.М., Кузнецов Д.В., Кондаков С.Э., Мельников М.Я.** Особенности решения обратной задачи оптического смешения методом регуляризации Тихонова для анализа состава полидисперсных взвесей наночастиц // Вестник Московского университета. Сер. 2. Химия. 2013. Т. № .54 5. С. 287–278.

18. **Янковский Г.М., Кузнецов Д.В., Кондаков С.Э., Мельников М.Я.** Особенности решения обратной задачи оптического смешения методом сингулярного разложения матрицы для анализа состава полидисперсных взвесей наноразмерных частиц // Вестник Московского университета. Сер. 2. Химия. 2013. Т. 6 № .54. С. 320–312.

19. **Непомнящая Э.К., Величко Е.Н., Аксенов Е.Т.** Решение обратной задачи лазерной корреляционной спектроскопии методом регуляризации // Университетский научный журнал. 2015. Т. 13 № .13. С. 21–13.

20. **Власова О.Л.** Многопараметрический подход к оптическому анализу модельных дисперсий бычьего сывороточного альбумина // Научно-технические ведомости Санкт-Петербургского государственного политехнического университета. Физико-математические науки. 2009. Т. 2 № .77. С. 44–39.

21. **Баранов А.Н., Власова И.М., Салецкий А.М.** Исследование процессов агрегации сывороточного альбумина // Журнал прикладной спектроскопии. 2004. Т. № .71 2. С. 207-204.

22. **Баранов А.Н., Власова И.М., Микрин В.Е., Салецкий А.М.** Лазерная корреляционная спектроскопия процессов денатурации сывороточного альбумина // Журнал прикладной спектроскопии. 2004. Т. 6 № .71. С. 835-831.

23. **Непомнящая Э.К., Величко Е.Н., Аксенов Е.Т., Богомаз Т.А.** Применение лазерной корреляционной спектроскопии для исследования биологических суспензий // Оптический журнал. 2015. Т. 82. № 3. С. 43–45.

24. **Nepomnyashchaya E., Velichko E., Bogomaz T.** Diagnostic possibilities of dynamic light scattering technique // Proceedings of SPIE. Nanoscale Imaging, Sensing, and Actuation for Biomedical Applications XVI. D.V. Nicolau, D. Fixler, E.M. Goldys (Eds.). 2019. Vol. 10891. P. 108910J.

25. **Плужников М.С., Говорун М.И., Мигманова К.Л.** Возможности лазерной корреляционной спектроскопии сыворотки крови в диагностике опухолей головы и шеи // Российская оториноларингология. 2007. Т. 2 № .27. С. 83–77.

26. **Гибизова В.В., Аненкова К.А., Масленникова** А.Д., **Федорова К.В., Сергеева И.А., Петрова Г.П.** Определение фундаментальных физических параметров белков сыворотки крови для развития методов диагностики злокачественных новообразований // Альманах клинической

медицины. 2016. Т. 2 № .44. С. 164–158.

27. **Капралова В.М., Назарова Е.А., Иванова Н.Е., Шадрин Е.Б.** Конформационные изменения альбумина как диагностический параметр // Научно-технические ведомости Санкт-Петербургского государственного политехнического университета. Физико-математические науки. 2012. № 3 (153) С. 83–91.

28. **Nepomnyashchaya E.K., Prokofiev A.V., Velichko E.N., Pleshakov I.V., Kuzmin Yu.I.** Investigation of magneto-optical properties of ferrofluids by laser light scattering techniques // Journal of Magnetism and Magnetic Materials. 2017. Vol. 431. 1 June. Pp. 24–26.

29. **Прокофьев А.В., Плешаков И.В., Бибик Е.Е., Кузьмин Ю.И.** Оптическое исследование геометрических характеристик агрегатов, образованных частицами магнитной жидкости // Письма в Журнал технической физики. 4 № .2017. С. 31–26.

30. **Карганов М.Ю., Алчинова И.Б., Яковенко** Е.Н., **Ковалева О.И., Медведева Ю.С.,** Вялкина **М.В.** Применение метода лазерной корреляционной спектроскопии в лабораторной медицине // Клиническая лабораторная диагностика. 2016. Т. 9 № .61. С. 534–533.

Статья поступила в редакцию 31.03.2019, принята к публикации 24.04.2019.

СВЕДЕНИЯ ОБ АВТОРАХ

НЕПОМНЯЩАЯ Элина Константиновна – *инженер Высшей школы прикладной физики и космических технологий Санкт-Петербургского политехнического университета Петра Великого.*

195251, Российская Федерация, г. Санкт-Петербург, Политехническая ул., 29

elina.nep@gmail.com

ВЕЛИЧКО Елена Николаевна – *кандидат технических наук, директор Высшей школы прикладной физики и космических технологий Санкт-Петербургского политехнического университета Петра Великого.*

195251, Российская Федерация, г. Санкт-Петербург, Политехническая ул., 29

velichko-spbstu@yandex.ru

DOI: 10.18721/JPM.12207
УДК 577.35, 57.087, 57.087.2, 57.87.1

ANALYSIS OF DENDRITIC SPINES MORPHOLOGY: FROM CLASSICAL DIVISION TO TYPES TOWARD ALTERNATIVE APPROACHES

E.I. Pchitskaya, I.S. Krylov, O.L. Vlasova, M.V. Bolsunovskaya, I.B. Bezprozvanny

Peter the Great St. Petersburg Polytechnic University, St. Petersburg, Russian Federation

This article provides a brief overview of the existing methods and approaches to analyzing the dendritic spines morphology playing an important role in the functioning of synaptic plasticity and memory formation mechanisms. Both various mathematical algorithms that classify spines according to their shape (thin, mushroom and stubby) and emerging alternative approaches have been considered. The reported scientific results point to uniform distribution of the main morphological parameters of dendritic spines; a number of authors cast some doubt on the often used division of spines into types and argue in favor of the existence of a shape continuum. Relying on this, a new approach to an analysis of dendritic spines morphology and to data presentation was advanced. It combines classification with the study of the distribution of dendritic spines by key morphological parameters.

Keywords: neuronal morphology, mushroom spine, thin spine, stubby spine, headed spine

Citation: Pchitskaya E.I., Krylov I.S., Vlasova O.L., Bolsunovskaya M.V., Bezprozvanny I.B., Analysis of dendritic spines morphology: from classical division to types toward alternative approaches, St. Petersburg Polytechnical State University Journal. Physics and Mathematics. 12 (2) (2019) 86–97. DOI: 10.18721/JPM.12207

ПЕРЕХОД ОТ КЛАССИЧЕСКОГО ДЕЛЕНИЯ ДЕНДРИТНЫХ ШИПИКОВ НЕЙРОНОВ НА ТИПЫ К АЛЬТЕРНАТИВНЫМ МЕТОДАМ АНАЛИЗА

Е.И. Пчицкая, И.С. Крылов, О.Л. Власова, М.В. Болсуновская, И.Б. Безпрозванный

Санкт-Петербургский политехнический университет Петра Великого, Санкт-Петербург, Российская Федерация

В статье представлен краткий обзор существующих методов и подходов к анализу морфологии дендритных шипиков, которые играют важную роль в функционировании механизмов синаптической пластичности и формировании памяти. Рассмотрены как различные математические алгоритмы, подразделяющие шипики на классы по признаку их формы (тонкие, грибовидные и пеньковые), так и новые альтернативные подходы. Результаты опубликованных исследований указывают на нормальный характер распределения основных морфологических параметров дендритных шипиков, ряд авторов ставят под сомнение часто используемое разделение шипиков на типы и свидетельствуют в пользу существования континуума форм. На этом основании в статье предложен новый подход к анализу морфологии дендритных шипиков и представлению данных. Он объединяет классификацию с изучением распределения дендритных шипиков по ключевым морфологическим параметрам.

Ключевые слова: морфология нейрона, грибовидный шипик, тонкий шипик, пеньковый шипик, филоподия

Ссылка при цитировании: Пчицкая Е.И., Крылов И.С., Власова О.Л., Болсуновская М.В., Безпрозванный И.Б. Переход от классического деления дендритных шипиков нейронов на типы к альтернативным методам анализа // Научно-технические ведомости СПбГПУ. Физико-математические науки. 2019. Т. 12. № 2. С. 88–100. DOI: 10.18721/JPM.12207

Introduction

A synapse is commonly understood as the zone of specialized contact between two neurons, serving to transmit information from cell to cell. An intrinsic property of neurons is that they can form synaptic connections, transmitting signals through them by means of electrical impulses that trigger the release of neurotransmitters. Most synapses form between the axonal bouton and the dendritic spine, which is a specialized protrusion from the dendritic membrane.

Dendritic spines come in a variety of shapes and sizes, differing greatly across different brain areas, cell types, and animal species [1]. The dendritic spine is an active element of synaptic transmission, capable of functional and morphological rearrangements in response to changes in the incoming signal. Synapses can modulate the efficiency of information transfer; for this reason, they are believed to serve as sites for memory formation and storage, initiating memory consolidation through mechanisms of potentiation and depression of synaptic activity [2–5]. Detailed analysis of synaptic morphology, reflecting the functional state of neurons, is an important task for neurobiology.

Dendritic spines are traditionally grouped into four large classes according to their morphological features: mushroom, thin, stubby and filopodia (Fig. 1).

Mushroom spines have a large head and a small neck, are relatively stable, form strong synaptic connections and supposedly act as memory storage sites [3, 6].

Thin spines have a small head and a long narrow neck, are more dynamic and are believed to be “learning spines”, responsible for forming new memories [3].

Stubby spines typically do not have a neck. They are known to be the predominant type in early stages of postnatal development but are also still found in small amounts in adulthood, where they are likely formed due to disappearance of mushroom spines [7].

Filopodia are long, thin spines without a clear head, commonly observed in developing neurons. These spines may also be found in mature neurons, but under specific conditions, for example, induction of plasticity after

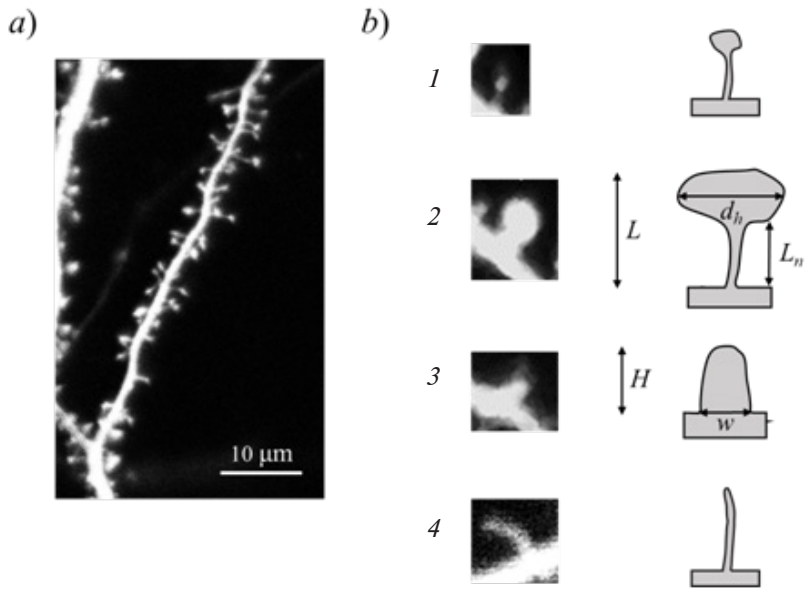

Fig. 1. Morphology of dendritic spines: micrograph of hippocampal neuron *in vitro* (confocal microscopy, ×60) (*a*); schematic representations of main types of dendritic spines with key morphological parameters (*b*).
Types of spines: thin (*1*), mushroom (*2*), stubby (*3*), filopodia (*4*);
L, L_n are the lengths of the spine and its neck, respectively;
d_h is the head width; H and w are the height and width of the base of the stubby spine

different types of brain injury [8]. Compared to other types of dendritic spines, filopodia are very mobile and flexible structures with a short lifetime. Electron micrographs show that filopodia mostly lack postsynaptic density and the apposing axon terminal contains only a few synaptic vesicles. Because of this, it was proposed to exclude filopodia from spine counts used to estimate synaptic density [9].

The morphology of the dendritic spine corresponds to its functional role and developmental stage at a given time, and the changes in its shape and size reflect changes in the activity of the given synaptic connection or in the environment surrounding the neuron and physiological processes in the neuron.

Various psychiatric and neurodegenerative diseases, such as Alzheimer's disease (AD) [10, 11], Parkinson's disease [12], Huntington's disease [13], schizophrenia [14], autism [15], depression [16], etc., are characterized by changes in the density and shape of dendritic spines of neurons in brain areas affected by these diseases. For example, it is believed that Huntington's chorea stems from dysfunction of the corticostriatal pathway [17]. Progressive memory loss in Alzheimer's disease is associated with a decrease in the number of mushroom spines in brain areas involved in memory formation, such as the hippocampus and the cortex [18].

Notably, synaptic degeneration is the initial stage of irreversible changes in the affected neuron, followed by atrophy of neurites and subsequent cell death. A recent study found that the number of mushroom and thin spines in pyramidal neurons of the prefrontal cortex was significantly lower in patients with Alzheimer-type dementia than in cognitively normal controls with AD pathology [19]. It was suggested that such spine morphology helps prevent the onset of dementia, despite the presence of characteristic AD pathology in the brain. These data are another argument supporting the position that using pharmacological agents to restore or stabilize dendritic spines in AD patients can prevent memory loss [18, 20–22].

Analysis of the number and shape of dendritic spines can provide insights into molecular mechanisms and signaling pathways involved in formation and functioning of synapses, the functional state of neurons, and mechanisms of neurodegenerative diseases, serving as a tool for assessing the effectiveness of pharmacological agents for treating these diseases [23–27]. Developing methods that can make this analysis accurate and quick is of key importance.

This paper provides a brief overview of the existing methods and approaches to studies of morphology of dendritic spines and suggest a new approach to classification of spines and presentation of the data obtained.

Review of existing methods for analysis of synaptic morphology

Analysis of morphology of dendritic spines is important for neurobiological studies, as it can shed light on the relationship between the structure of synaptic contacts and their function. There is currently no reliable automated software yielding accurate results, which means that experimenters have to resort to manual analysis of neuron images. This method is extremely time-consuming, and also completely depends on the opinion of the expert performing the analysis, which means that it lacks objectivity. In view of this, attempts were made to develop semi-automated and automated algorithms for analysis and subsequent classification of dendritic spines on images obtained by both confocal and multiphoton laser scanning microscopy [28–34].

One of the first attempts at automated classification of spines with software methods was undertaken in 2002, when advances in technologies for laser scanning microscopy made it possible to obtain high-resolution images of neurons on a spatial scale sufficient to visualize such small cell structures as dendritic spines [28]. The proposed approach to classification of spines [28] was based on the results discussed in [35], performing manual analysis of synaptic morphology on a series of slices of spine images obtained by electron microscopy. The authors found that neck diameter d_n, head width d_h and spine length L (see Fig. 1) were the most important morphological characteristics for classifying the spine into a specific category. The classification was based on the assumption that the length of thin spines is much greater than the diameter of their neck ($L >> d_n$), while head width cannot be substantially greater than neck diameter. Head width should be considerably larger than neck diameter ($d_h >> d_n$) for mushroom spines, and neck diameter is comparable to spine length ($d_n \approx L$) for stubby spines. Ratios L/d_n and L/d_h were used as criteria in the algorithm developed by the authors for assigning spines to

one of four classes [28].

Later, another research group developed the NeuronStudio software, classifying spines using a decision tree based on parameters such as the aspect ratio, head-to-neck ratio, and head diameter [29]. This software module subsequently became part of Neurolucida 360, a commercial package for analyzing the morphology of neuron cells [30]. Another classification based on a decision tree used such spine parameters as neck diameter, head diameter, shape criterion, area, spine length and perimeter [31]. The 2dSpAn software [32] also uses a set of rules incorporated in the decision tree for classification; the key parameters are neck length, the ratio of the locally deepest point to spine length and the ratio of base-to-head distance L_n/L to spine length. Notably, the authors excluded thin spines from consideration, regarding them as an intermediate type, but included spine-head protrusions as a separate type, combining them with filopodia in subsequent analysis. The software was later improved with a new algorithm for spine segmentation and extraction of morphometric data, but the principle of classification remained unchanged [33].

An algorithm for analyzing spines proposed in 2014 was based on semi-supervised learning (SSL) [34]. In this approach, spines are first segmented in three-dimensional space using wavelet functions, with the object's boundary defined as the position where the response of the wavelet on the spine section changes quickly. Spine parameters such as length, volume, neck and head diameters, etc., constituting the matrix of parameters, are calculated after segmentation. To form a training set, a neurobiology expert decides which class a small portion of the total number of detected spines belongs to, and the system sorts each of the remaining spines into the given classes at the final stage following training. One of the benefits of this approach is that it requires minimal operator intervention (only at the training stage), so, accordingly, the errors resulting from the experimenter's personal assessment of spine types that we have mentioned earlier are eliminated. However, a drawback of this approach is that the method's accuracy and performance strongly depend on the size of the training set and on the parameters included in the training vector.

Another new approach to classical methods of morphological analysis described above is classification of dendritic spines by appearance and shape [1]. Spine shape was represented in parametric form as a result of segmentation of the dendrite image using the recently proposed disjunctive normal shape model (DNSM). A histogram of oriented gradients (HOG) was used to extract the appearance parameters. The authors suggested kernel density estimation for classification based on the selected parameters, calculating three non-parametric density estimates for three spine classes based on the training set assigned by the expert. The accuracy of classification using a similar combination of methods significantly exceeded that of the above-mentioned classical approaches [28, 29, 32]. The highest accuracy, which was 87%, was obtained by combining DNSM segmentation and HOG with a classification using a neural network.

To validate the accuracy of their approach, the authors compared spine types detected by the program with the labels manually assigned to the spines by one or several experts [1, 29, 31, 32]. Notably, there was significant variation in classifications of spines made by different experts. In some cases, the expert had difficulties in assigning the type of spine; moreover, the same expert could assess the given sample differently on different days (the percentage of coincidences is 82.9%) [29]. This is to say that it is difficult to estimate the accuracy of classification algorithms due to lack of objective reference.

Continuum of spine shapes

The common approach to analysis of morphology of dendritic spines is dividing spines into the subgroups described above: stubby, thin, mushroom, and filopodia. Even though this classification is used in many studies, the question remains open whether there are actually different classes of spines or whether they should be modeled using a continuum of shape variations. It is also important to note that the existing classification of spine shapes does not provide a clear standardized definition for each group. Experimenters are free to select their own criteria, which introduces significant uncertainty to interpreting the data obtained by different research groups.

The study carried out by Yuste et al. [36]), analyzing the morphology of neurons in layers II and III of mouse visual cortex, found that a continuous distribution rather than several discrete peaks (which would have been an argument in favor of separate classes of spines) was observed for each of the morphological parameters of the spines. Another study

analyzing the morphology of neurons in cortical layer III [37] also found a continuous and smooth distribution of spine length and head diameter in the sample.

The authors of [38], where clustering of parameters which could be indicative of distinct spine types was not detected (similar to the above-mentioned works), suggested that classical categories of spines are just typical examples from a continuum of shapes. A recent review [9] also concluded based on data on the dynamics of dendritic spines that the shapes of synaptic contacts are a continuum; the stability of the spine and the strength of the synaptic connection it forms increase with increasing spine size. A multi-method study of the link between spine shape and compartmentalization of synapses [39] also observed a great diversity in spine morphology, which is further evidence against standard classification systems.

A radically new approach to analysis of spine shapes was proposed in 2016 based on these data. The authors applied a clustering method to study subpopulations of spines. Spines were not divided into predefined types; instead, spine groups (clusters) with similar features were detected by mathematical methods, and the distribution of their morphological parameters was analyzed.

To get a full picture, the authors of [40] used the data given in literature to compose a set of eleven most frequently used morphological parameters, which were reduced, using the method of principal components, to two parameters that were a linear combination of the initial ones. The first parameter included the components describing spine size and, accordingly, it was interpreted as a generalized size descriptor. Similarly, the second parameter was interpreted as the contour descriptor. After all spines from the sample were distributed into a two-dimensional orthogonal space formed by descriptors, hierarchical clustering was performed. Ten clusters were obtained, including both small peripheral clusters and clusters with insufficient separation. The authors selected three images of spines from each cluster, most closely reflecting the empirical morphological features of this group, to illustrate the results. Predictably, the clusters corresponding to the classical thin and mushroom types turned out to be the most dense and poorly separated, and stubby spines were represented by a single cluster with only a few spines. Importantly, the number and composition of the clusters obtained strongly depend on the chosen clustering algorithm and the properties of the initial data. The authors also proposed a model for analyzing the transitions between clusters under chemically stimulated long-term potentiation. Thus, it was proved mathematically that there are might be much more groups of spines similar in morphological structure than the four classical types. While the approach proposed in [40] can be extremely useful for fundamental study of synapses, it is ill-suited for wide practical use, where analysis of synaptic morphology is part of general analysis of the functional state of neurons, since presenting and interpreting data can be difficult. In view of the above, we can conclude that developing alternative automated methods for classification is an urgent task.

New approach to collection and presentation of numerical data on morphology of dendritic spines

Since an increasing number of studies indicate that there is a continuum of spine shapes, it is important to develop a new simple method of analysis for practical purposes that could be used to present the experimental data most fully, reliably and clearly.

Most errors in classification of spines happen in separating thin and mushroom spines, as these two types have the same shape and the only critical parameter by which they can be differentiated is the size of the head. Studies indicate that head size is directly proportional to the area of postsynaptic density and is correlated with the number of postsynaptic receptors and synaptic strength [36, 41–43], while neck length and width of the spines are directly related to the magnitude of postsynaptic potential [39]. The morphology of synapses varies depending on the strength of synaptic contact. Changes in synaptic strength during long-term potentiation and long-term depression are associated, respectively, with enlargement or shrinkage of the spine head [44, 45]. Thus, the shape of the dendritic spine determines the strength of synaptic connections; changes in spine shape are believed to be involved in coding information and storing memory in the brain.

As discussed above, the head size distribution has a continuous shape [9, 36–39], which casts doubt on whether such classes as thin and mushroom spines actually exist. For this reason, we propose to categorize all spines with a pronounced head in a separate group called “headed spines”. According to our observations, confirmed by another research group [32], one

of the potential critical parameters for this type of spines is the ratio L_n/L of neck length to total spine length. This parameter is of interest because the proportion of the neck from total spine length is more often smaller in spines with large heads than in spines with smaller heads.

Stubby spines have a pronounced shape, completely lacking a neck, and thus stand out clearly among diverse synaptic morphologies. This is confirmed by results of cluster analysis carried out earlier in [40], where stubby spines could be clearly detected as a separate group. It is difficult to determine the head width of the stubby spine because of this shape, since its widest part coincides with the base in most cases. We assume that spine length L and base width b_w can serve as critical parameters for stubby spines, and we plan to test this hypothesis in future studies. Electron microscopy of synapses revealed another structure, the filopodia, which are thin hair-like protrusions of the dendritic membrane [9]. As filopodia are characterized by very rapid changes in shape and do not form active synaptic contacts, there are probably no critical parameters for their morphology. In view of this, methods of intravital microscopy should be used for focused analysis of morphology of this type of dendritic spines, allowing to analyze their behavior in dynamics. Notably, the total content of stubby spines and filopodia in mature neurons does not exceed 10%, according to estimates [9], and, therefore, synaptic contacts of this type are few in number.

A histogram is obtained by dividing spines into classical groups, showing either the percentage of spines of a certain type or their density. Standard methods like the *t*- test or ANOVA are used to identify statistically significant differences between the control and experimental groups. A reasonable question, then, would be how to visualize the data, since they are characterized by a continuous distribution.

We propose to combine a pie chart (Fig. 2), where the size of the sector corresponds to the percentage of the group it contains, with a plotted distribution by parameters, which makes it possible to represent the most important parameter that is the change in the size of spine heads as a continuum. It is proposed for spines with pronounced heads to plot the head width d_h normalized to the average value along the inner circumference, and the point corresponding to the ratio L_n/L (neck length to total spine length) in the range from 0 to 1 along the radius. If there are enough spines without necks (stubby type), their distribution can be also represented as follows: spine height H is plotted along the inner circumference, and the point corresponding to the ratio H/w (spine height to base width) along the radius. Another sector should correspond to filopodia (if there are any). We also propose to introduce a sector reflecting the percentage of spines with

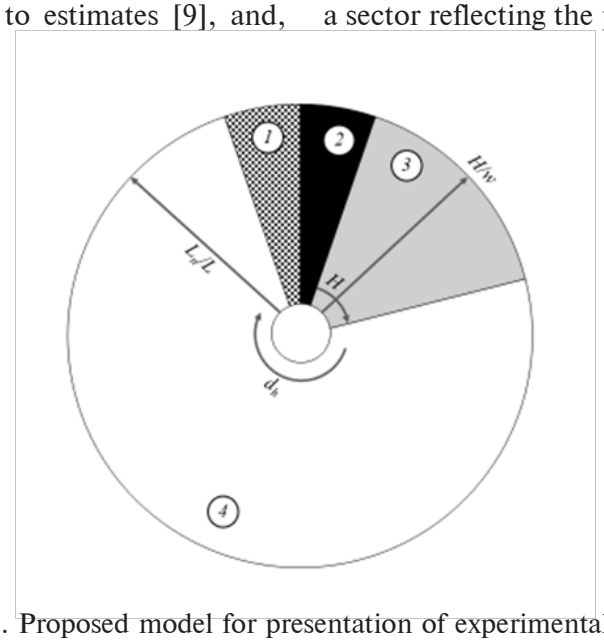

Fig. 2. Proposed model for presentation of experimental data, showing percentage of different types of dendritic spines and their distribution by key morphological parameters (see the explanations in the text)
Types of spines: filopodia (*1*), stubby (*2*), headed (*3*), with anomalous shape (*4*)

anomalous shapes that cannot be classified as any of the types by algorithm.

We offer the software tool we have developed for detecting and recording the metric of dendritic spines. At the first stage of its operation, the image is processed using the Otsu filter to eliminate noise and noisy areas. At the second stage, a neuron stem model is constructed using binarization and subsequent skeletonization of the image, while spine detection is performed by subtracting the resulting stem model from the filtered image with the necessary correction determined algorithmically. The obtained data on the morphology of dendritic spines is used to perform classification with help of a previously trained neural network. We plan to use the opinion formulated in consultation with a group of neuroscientists to generate a training set and monitor the performance and accuracy of the algorithm. Such critical morphological parameters as head size, neck length and neck height are carried out after classification using mathematical algorithms specially adapted to a certain type of spines, which should reduce potential errors. Subsequent manual analysis of the shape of anomalous spines recorded in experiments with the control and experimental groups might reveal new processes and changes in the morphology of synapses that could not be detected in studies using rigid classification methods. The diagram in Fig. 2 illustrates our model for representing the experimental data; its efficiency and practical value are to be assessed in forthcoming studies.

This study was supported by the RFBR grant no. 18-34-00183 (E.I. Pchitskaya). E.I. Pchitskaya is the recipient of the scholarship of the President of the Russian Federation no. SP—1929.2018.4.

REFERENCES

1. **Ghani M.U., Mesadi F., Kanik S.D., et al.,** Dendritic spine classification using shape and appearance features based on two-photon microscopy, J. Neurosci. Methods. 279 (2017) 13—21.

2. **Kasai H., Hayama T., Ishikawa M., et al.,** Learning rules and persistence of dendritic spines, Eur. J. Neurosci. 32 (2) (2010) 241—249.

3. **Bourne J., Harris K.M.,** Do thin spines learn to be mushroom spines that remember? Curr. Opin. Neurobiol. 17 (3) (2007) 381—386.

4. **Bailey C.H., Kandel E.R., Harris K.M.,** Structural components of synaptic plasticity and memory consolidation, Cold Spring Harb. Perspect Biol. 7 (7) (2015) a021758.

5. **Zhou Q., Homma K.J., Poo M.M.,** Shrinkage of dendritic spines associated with long-term depression of hippocampal synapses, Neuron. 44 (5) (2004) 749—757.

6. **Hayashi Y., Majewska A.K.,** Dendritic spine geometry: functional implication and regulation, Neuron. 46 (4) (2005) 529—532.

7. **Hering H., Sheng M.,** Dentritic spines: structure, dynamics and regulation, Nat. Rev. Neurosci. 2 (12) (2001) 880—888.

8. **Yoshihara Y., de Roo M., Muller D.,** Dendritic spine formation and stabilization, Current Opinion in Neurobiology. 19 (2) (2009) 146—153.

9. **Berry K.P., Nedivi E.,** Spine dynamics: are they all the same? Neuron. 96 (1) (2017) 43—55.

10. **Koffie R.M., Hyman B.T., Spires-Jones T.L.,** Alzheimer's disease: synapses gone cold, Mol. Neurodegener. 6 (2011) 63.

11. **Tu S., Okamoto S.-I., Lipton S.A., Xu H.,** Oligomeric Aβ-induced synaptic dysfunction in Alzheimer's disease, Mol. Neurodegener. 9 (2014) 48.

12. **Villalba R.M., Smith Y.,** Differential striatal spine pathology in Parkinson's disease and cocaine addiction: a key role of dopamine? Neuroscience. 251 (2013) 2—20.

13. **Nithianantharajah J., Hannan A.J.,** Dysregulation of synaptic proteins, dendritic spine abnormalities and pathological plasticity of synapses as experience-dependent mediators of cognitive and psychiatric symptoms in Huntington's disease, Neuroscience. 251 (2013) 66—74.

14. **Herms J., Dorostkar M.M.,** Dendritic spine pathology in neurodegenerative diseases, Annu. Rev. Pathol. 11 (2016) 221—250.

15. **Phillips M., Pozzo-Miller L.,** Dendritic spine dysgenesis in autism related disorders, Neuroscience Letters. 601 (2015) 30—40.

16. **Qiao H., Li M.-X., Xu C., et al.,** Dendritic spines in depression: what we learned from animal models, Neural Plasticity. 2016 (2016) 8056370.

17. **Cepeda C., Wu N., Andre V.M., et al.,** The corticostriatal pathway in Huntington's disease, Prog. Neurobiol. 81 (5—6) (2007) 253—271.

18. **Tackenberg C., Ghori A., Brandt R.,** Thin, stubby or mushroom: spine pathology in Alzheimer's disease, Curr. Alzheimer Res. 6 (3) (2009) 261—268.

19. **Boros B.D., Greathouse K.M., Gentry**

E.G., et al., Dendritic spines provide cognitive resilience against Alzheimer's disease, Ann. Neurol. 82 (4) (2017) 602–614.

20. **Popugaeva E., Pchitskaya E., Bezprozvanny I.,** Dysregulation of neuronal calcium homeostasis in Alzheimer's disease – a therapeutic opportunity? Biochemical and Biophysical Research Communications. 483 (4) (2017) 998–1004.

21. **Pchitskaya E., Popugaeva E., Bezprozvanny I.,** Calcium signaling and molecular mechanisms underlying neurodegenerative diseases, Cell Calcium. 70 (2018) 87–94.

22. **Popugaeva E., Supnet C., Bezprozvanny I.,** Presenilins, deranged calcium homeostasis, synaptic loss and dysfunction in Alzheimer's disease, Messenger. 1 (1) (2012) 53–62.

23. **Zhang H., Sun S., Wu L., et al.,** Store-operated calcium channel complex in postsynaptic spines: a new therapeutic target for Alzheimer's disease treatment, The Journal of Neuroscience. 36 (47) (2016) 11837–11850.

24. **Pchitskaya E.I., Zhemkov V.A., Bezprozvanny I.B.,** Dynamic microtubules in Alzheimer's disease: association with dendritic spine pathology, Biochemistry (Moscow). 83 (9) (2018) 1068–1074.

25. **Krasnov I.B., D'iachkova N.L., Burtseva T.D., Krasnikova I.V.,** Ultrastructure of dendritic spines in the somatosensory cortex of rat's brain following 5- and 33-day hypergravity, Aerospace and Environmental Medicine. 46 (5) (2012) 46–51.

26. **Zhuravleva Z.N., Zhuravlev G.I., Khutsian S.S.,** Inductive role of mossy fibers of hippocampus in the development of dendritic spines in aberrant synaptogenesis at neurotransplantation, Russian Journal of Developmental Biology. 45 (1) (2014) 42–49.

27. **Popov V.I., Deev A.A., Klimenko O.A., et al.,** Three-dimensional reconstruction of synapse and dendritic spines in the hippocampus of rats and ground squirrels: new paradigms of the structure and function of a synapse, The I.P. Pavlov Journal of Higher Nervous Activity. 54(1) (2004) 120–129.

28. **Koh I.Y.Y., Lindquist W.B., Zito K., et al.,** An image analysis algorithm for dendritic spines, Neural Computation. 14 (6) (2002) 1283–1310.

29. **Rodriguez A., Ehlenberger D.B., Dickstein D.L., et al.,** Automated three-dimensional detection and shape classification of dendritic spines from fluorescence microscopy images, PLoS One. 3(4) (2008) e1997.

30. **Dickstein D.L., Dickstein D.R., Janssen W.G., et al.,** Automatic dendritic spine quantification from confocal data with *Neurolucida* 360, Curr. Protoc. Neurosci. 77 (1) (2016) 1–1.

31. **Son J., Song S., Lee S., et al.,** Morphological change tracking of dendritic spines based on structural features, Journal of Microscopy. 241 (3) (2011) 261–272.

32. **Basu S., Plewczynski D., Saha S., et al.,** 2dSpAn: semiautomated 2-D segmentation, classification and analysis of hippocampal dendritic spine plasticity, Bioinformatics. 32 (16) (2016) 2490–2498.

33. **Basu S., Saha P.K., Roszkowska M., et al.,** Quantitative 3-D morphometric analysis of individual dendritic spines, Scientific Reports. 8 (2018) 3545.

34. **Shi P., Huang Y., Hong J.,** Automated three-dimensional reconstruction and morphological analysis of dendritic spines based on semi-supervised learning, Biome. Opt. Express. 5 (5) (2014) 1541–1553.

35. **Harris K.M., Jensen F.E., Tsao B.,** Three-dimensional structure of dendritic spines and synapses in rat hippocampus (CA1) at postnatal day 15 and adult ages: implications for the maturation of synaptic physiology and long-term potentiation, J. Neurosci. 12 (7) (1992) 2685–2705.

36. **Arellano J.I., Benavides-Piccione R., Defelipe J., Yuste R.,** Ultrastructure of dendritic spines: correlation between synaptic and spine morphologies, Front. Neurosci. 1 (1) (2007) 131–143.

37. **Wallace W., Bear M.F.,** A morphological correlate of synaptic scaling in visual cortex, The Journal of Neuroscience. 24 (31) (2004) 6928–6938.

38. **Loewenstein Y., Yanover U., Rumpel S.,** Predicting the dynamics of network connectivity in the neocortex, The Journal of Neuroscience. 35 (36) (2015) 12535–12544.

39. **Tonnesen J., Katona G., Rozsa B.,** Spine neck plasticity regulates compartmentalization of synapses, Nat. Neurosci. 17 (5) (2014) 678–685.

40. **Bokota G., Magnowska M., Kuśmierczyk T., et al.,** Computational approach to dendritic spine taxonomy and shape transition analysis, Frontiers in Computational Neuroscience. 10 (2016) 140.

41. **Kharazia V.N., Weinberg R.J.,** Immunogold localization of AMPA and NMDA receptors in somatic sensory cortex of albino rat, J. Comp. Neurol. 412 (2) (1999) 292–302.

42. **Takumi Y., Ramirez-Leon V., Laake P.,**

et al., Different modes of expression of AMPA and NMDA receptors in hippocampal synapses, Nat. Neurosci. 2 (7) (1999) 618–624.

43. **Ganeshina O., Berry R.W., Petralia R.S., et al.,** Differences in the expression of AMPA and NMDA receptors between axospinous perforated and nonperforated synapses are related to the configuration and size of postsynaptic densities, J. Comp. Neurol. 468 (1) (2004) 86–95.

44. **Yuste R., Bonhoeffer T.,** Morphological changes in dendritic spines associated with long-term synaptic plasticity, Annu. Rev. Neurosci. 24 (2001) 1071–1089.

45. **Holtmaat A., Svoboda K.,** Experience-dependent structural synaptic plasticity in the mammalian brain, Nat. Rev. Neurosci. 10 (9) (2009) 647–658.

Received 19.02.2019, accepted 05.06.2019.

THE AUTHORS

PCHITSKAYA Ekaterina I.
Peter the Great St. Petersburg Polytechnic University
29 Politechnicheskaya St., St. Petersburg, 195251, Russian Federation
katrincreative@yandex.ru

KRYLOV Ivan S.
Peter the Great St. Petersburg Polytechnic University
29 Politechnicheskaya St., St. Petersburg, 195251, Russian Federation
ivan.krylov@spbpu.com

VLASOVA Olga L.
Peter the Great St. Petersburg Polytechnic University
29 Politechnicheskaya St., St. Petersburg, 195251, Russian Federation
olvlasova@yandex.ru

BOLSUNOVSKAYA Marina V.
Peter the Great St. Petersburg Polytechnic University
29 Politechnicheskaya St., St. Petersburg, 195251, Russian Federation
bolsun_hht@mail.ru

BEZPROZVANNY Ilya B.
Peter the Great St. Petersburg Polytechnic University
29 Politechnicheskaya St., St. Petersburg, 195251, Russian Federation
mnlabspb@gmail.com

СПИСОК ЛИТЕРАТУРЫ

1. **Ghani M.U., Mesadi F., Kanik S.D., Argunsah A.O., Hobbiss A.F., Israely I., Unay D., Tasdizen T., Cetin M.** Dendritic spine classification using shape and appearance features based on two-photon microscopy // J. Neurosci. Methods. 2017. Vol. 279. Pp. 13–21. https://www.sciencedirect.com/science/ article/pii/S0165027016302928?via%3Dihub.

2. **Kasai H., Hayama T., Ishikawa M., Watanabe S., Yagishita S., Noguchi J.** Learning rules and persistence of dendritic spines // Eur. J. Neurosci. 2010. Vol. 32. No. 2. Pp. 241–249.

3. **Bourne J., Harris K.M.** Do thin spines learn to be mushroom spines that remember?// Curr. Opin. Neurobiol. 2007. Vol. 17. No. 3. Pp. 381–386.

4. **Bailey C.H., Kandel E.R., Harris K.M.** Structural components of synaptic plasticity and memory consolidation // Cold Spring Harb Perspect Biol. 2015. Vol. 7. No. 7. P. a021758; https://www.ncbi.nlm.nih.gov/pubmed/26134321.

5. **Zhou Q., Homma K.J., Poo M.M.** Shrinkage of dendritic spines associated with long-term depression of hippocampal synapses // Neuron. 2004. Vol. 44. No. 5. Pp. 749–757.

6. **Hayashi Y., Majewska A.K.** Dendritic spine geometry: functional implication and regulation // Neuron. 2005. Vol. 46. No. 4. Pp. 529–532.

7. **Hering H., Sheng M.** Dentritic spines :

structure, dynamics and regulation // Nat. Rev. Neurosci. 2001. Vol. 2. No. 12. Pp. 880–888.

8. **Yoshihara Y., de Roo M., Muller D.** Dendritic spine formation and stabilization // Current Opinion in Neurobiology. 2009. Vol. 19. No. 2. Pp. 146–153.

9. **Berry K.P., Nedivi E.** Spine dynamics: are they all the same? // Neuron. 2017. Vol. 96. No. 1. Pp. 43–55.

10. **Koffie R.M., Hyman B.T., Spires-Jones T.L.** Alzheimer's disease: synapses gone cold // Mol. Neurodegener. 2011. Vol. 6. P. 63.

11. **Tu S., Okamoto S.-I., Lipton S.A., Xu H.** Oligomeric Aβ-induced synaptic dysfunction in Alzheimer's disease // Mol. Neurodegener. 2014. Vol. 9. P. 48.

12. **Villalba R.M., Smith Y.** Differential striatal spine pathology in Parkinson's disease and cocaine addiction: a key role of dopamine? // Neuroscience. 2013. Vol. 251. Pp. 2–20; https://www.sciencedirect.com/science/ article/abs/pii/S0306452213005861?via%3Dihub.

13. **Nithianantharajah J., Hannan A.J.** Dysregulation of synaptic proteins, dendritic spine abnormalities and pathological plasticity of synapses as experience-dependent mediators of cognitive and psychiatric symptoms in Huntington's disease // Neuroscience. 2013. Vol. 251. Pp. 66–74; https://www.sciencedirect. com/science/ article/abs/pii/S0306452212005118?via%3Dihub.

14. **Herms J., Dorostkar M.M.** Dendritic spine pathology in neurodegenerative diseases // Annu. Rev. Pathol. 2016. Vol. 11. Pp. 221–250. https://www.ncbi.nlm.nih.gov/pubmed/26907528.

15. **Phillips M., Pozzo-Miller L.** Dendritic spine dysgenesis in autism related disorders // Neuroscience Letters. 2015. Vol. 601. Pp. 30–40; https://www.ncbi. nlm.nih.gov/pmc/articles/ PMC4496332/.

16. **Qiao H., Li M.-X., Xu C., Chen H.-B., An S.-C., Ma X.-M.** Dendritic spines in depression: what we learned from animal models // Neural Plasticity. 2016. Vol. 2016. P. 8056370. https://www.ncbi.nlm.nih. gov/pmc/articles /PMC 4736982/.

17. **Cepeda C., Wu N., Andre V.M., Cummings D.M., Levine M.S.** The corticostriatal pathway in Huntington's disease // Prog. Neurobiol. 2007. Vol. 81. No. 5–6. Pp. 253–271.

18. **Tackenberg C., Ghori A., Brandt R.** Thin, stubby or mushroom: spine pathology in Alzheimer's disease // Curr. Alzheimer Res. 2009. Vol. 6. No. 3. Pp. 261–268.

19. **Boros B.D., Greathouse K.M., Gentry E.G., Curtis K.A., Birchall E.L., Gearing M., Herskowitz J.H.** Dendritic spines provide cognitive resilience against Alzheimer's disease // Ann. Neurol. 2017. Vol. 82. No. 4. Pp. 602–614.

20. **Popugaeva E., Pchitskaya E., Bezprozvanny I.** Dysregulation of neuronal calcium homeostasis in Alzheimer's disease – A therapeutic opportunity?// Biochemical and Biophysical Research Communications. 2017. Vol. 483. No. 4. Pp. 998–1004.

21. **Pchitskaya E., Popugaeva E., Bezprozvanny I.** Calcium signaling and molecular mechanisms underlying neurodegenerative diseases // Cell Calcium. 2018. Vol. 70. Pp. 87–94. https://www.sciencedirect.com/science /article/pii/S0143416017300660?via%3Dihub.

22. **Popugaeva E., Supnet C., Bezprozvanny I.** Presenilins, deranged calcium homeostasis, synaptic loss and dysfunction in Alzheimer's disease // Messenger. 2012. Vol. 1. No. 1. Pp. 53–62.

23. **Zhang H., Sun S., Wu L., Pchitskaya E., Zakharova O., fon Tacer K., Bezprozvanny I.** Store-operated calcium channel complex in postsynaptic spines: a new therapeutic target for Alzheimer's disease treatment //The Journal of Neuroscience. 2016. Vol. 36. No. 47. Pp. 11837–11850.

24. **Пчицкая Е.И., Жемков В.А., Безпроа званный И.Б.** Динамические микротрубочки при болезни Альцгеймера: связь с патологией дендритных шипиков // Биохимия. 2018. Т. 83. № 9. С. 1343–1350.

25. **Краснов И.Б., Дьячкова Л.Н., Бурцева Т.Д., Красникова И.В.** Ультраструктура дендритных шипиков в соматосенсорной коре мозга крыс после -5 и -33суточного воздействия гипергравитации // Авиакосмическая и экологическая медицина. 2012. Т. 46. № 5. С. 46–51.

26. **Журавлева Н.З., Журавлев Г.И., Хуцян С.С.** Индуктивная роль мшистых волокон гиппокампа в развитии дендритных шипиков при аберрантном синаптогенезе в условиях нейротрансплантации // Онтогенез. 2014. Т. 45. № 1. С. 42–49.

27. **Попов В.И, Деев А.А., Клименко О.А., Краев И.В., Кузьминых С.Б., Медведев Н.И., Патрушев И.В., Попов Р.В., Рогачевский В.В., Хуцян С.С., Стьюарт М.Г., Фесенко Е.Е.** Трехмерные реконструкции синапсов и дендритных шипиков в гиппокампе крыс и сусликов: новые структурно-функциональные парадигмы работы синапса // Журнал высшей нервной деятельности им. И.П. Павлова. 2004. Т. 1 № .54. С. 129–120.

28. **Koh I.Y.Y., Lindquist W.B., Zito K., Nimchinsky E.A., Svoboda K.** An image analysis algorithm for dendritic spines // Neural

Computation. 2002. Vol. 14. No. 6. Pp. 1283–1310.

29. **Rodriguez A., Ehlenberger D.B., Dickstein D.L., Hof P.R., Wearne S.L.** Automated three-dimensional detection and shape classification of dendritic spines from fluorescence microscopy images // PLoS One. 2008. Vol. 3. No. 4. P. e1997.

30. **Dickstein D.L., Dickstein D.R., Janssen W.G., Hof P.R., Glaser J.R., Rodriguez A., O'Connor N., Angstman P., Tappan S.J.** Automatic dendritic spine quantification from confocal data with *Neurolucida* 360 // Curr. Protoc. Neurosci. 2016. Vol. 77. No. 1. Pp. 1–1.

31. **Son J., Song S., Lee S., Chang S., Kim M.** Morphological change tracking of dendritic spines based on structural features // Journal of Microscopy. 2011. Vol. 241. No. 3. Pp. 261–272.

32. **Basu S., Plewczynski D., Saha S., Roszkowska M., Magnowska M., Baczynska E., Wlodarczyk J.** 2dSpAn: semiautomated 2-D segmentation, classification and analysis of hippocampal dendritic spine plasticity // Bioinformatics. 2016. Vol. 32. No. 16. Pp. 2490–2498.

33. **Basu S., Saha P.K., Roszkowska M., Magnowska M., Baczynska E., Das N., Plewczynski D., Wlodarczyk J.** Quantitative 3-D morphometric analysis of individual dendritic spines // Scientific Reports. 2018. Vol. 8. P. 3545.

34. **Shi P., Huang Y., Hong J.** Automated three-dimensional reconstruction and morphological analysis of dendritic spines based on semi-supervised learning // Biomed. Opt. Express. 2014. Vol. 5. No. 5. Pp. 1541–1553.

35. **Harris K.M., Jensen F.E., Tsao B.** Three-dimensional structure of dendritic spines and synapses in rat hippocampus (CA1) at postnatal day 15 and adult ages: implications for the maturation of synaptic physiology and long-term potentiation // J. Neurosci. 1992. Vol. 12. No. 7. Pp. 2685–2705.

36. **Arellano J.I., Benavides-Piccione R., Defelipe J., Yuste R.** Ultrastructure of dendritic spines: correlation between synaptic and spine morphologies // Front. Neurosci. 2007. Vol. 1. No. 1. Pp. 131–143.

37. **Wallace W., Bear M.F.** A morphological correlate of synaptic scaling in visual cortex // The Journal of Neuroscience. 2004. Vol. 24. No. 31. Pp. 6928–6938.

38. **Loewenstein Y., Yanover U., Rumpel S.** Predicting the dynamics of network connectivity in the neocortex //The Journal of Neuroscience. 2015. Vol. 35. No. 36. Pp. 12535–12544.

39. **Tonnesen J., Katona G., Rozsa B., Nagerl U.V.** Spine neck plasticity regulates compartmentalization of synapses // Nat. Neurosci. 2014. Vol. 17. No. 5. Pp. 678–685.

40. **Bokota G., Magnowska M., Kuśmierczyk T., Łukasik M., Roszkowska M., Plewczynski D.** Computational approach to dendritic spine taxonomy and shape transition analysis //Frontiers in Computational Neuroscience. 2016. Vol. 10. P. 140. https://www.ncbi.nlm.nih.gov/pmc/articles/PMC5180374/.

41. **Kharazia V.N., Weinberg R.J.** Immunogold localization of AMPA and NMDA receptors in somatic sensory cortex of albino rat // J. Comp. Neurol. 1999. Vol. 412. No. 2. Pp. 292–302.

42. **Takumi Y., Ramirez-Leon V., Laake P., Rinvik E., Ottersen O.P.** Different modes of expression of AMPA and NMDA receptors in hippocampal synapses // Nat. Neurosci. 1999. Vol. 2. No. 7. Pp. 618–624.

43. **Ganeshina O., Berry R.W., Petralia R.S., Nicholson D.A., Geinisman Y.** Differences in the expression of AMPA and NMDA receptors between axospinous perforated and nonperforated synapses are related to the configuration and size of postsynaptic densities //J. Comp. Neurol. 2004. Vol. 468. No. 1. Pp. 86 –95.

44. **Yuste R., Bonhoeffer T.** Morphological changes in dendritic spines associated with long-term synaptic plasticity // Annu. Rev. Neurosci. 2001. Vol. 24. Pp. 1071–1089; http://www.biomedsearch.com/nih/Morphological-changes-in-dendritic-spines/11520928.html.

45. **Holtmaat A., Svoboda K.** Experience-dependent structural synaptic plasticity in the mammalian brain // Nat. Rev. Neurosci. 2009. Vol. 10. No. 9. Pp. 647–658.

Статья поступила в редакцию 19.02.2019, принята к публикации 06.05.2019.

СВЕДЕНИЯ ОБ АВТОРАХ

ПЧИЦКАЯ Екатерина Игоревна – *лаборантка лаборатории молекулярной нейродегенерации Высшей школы биомедицинских систем и технологии Санкт-Петербургского политехнического университета Петра Великого.*

195251, Российская Федерация, г. Санкт-Петербург, Политехническая ул., 29
katrincreative@yandex.ru

КРЫЛОВ Иван Сергеевич – *студент Высшей школы биомедицинских систем и технологии Санкт-Петербургского политехнического университета Петра Великого.*

195251, Российская Федерация, г. Санкт-Петербург, Политехническая ул., 29
ivan.krylov@spbpu.com

ВЛАСОВА Ольга Леонардовна – *доктор физико-математических наук, профессор Высшей школы биомедицинских систем и технологии Санкт-Петербургского политехнического университета Петра Великого.*

195251, Российская Федерация, г. Санкт-Петербург, Политехническая ул., 29
olvlasova@yandex.ru

БОЛСУНОВСКАЯ Марина Владимировна – *кандидат технических наук, доцент Высшей школы биомедицинских систем и технологии Санкт-Петербургского политехнического университета Петра Великого.*

195251, Российская Федерация, г. Санкт-Петербург, Политехническая ул., 29
bolsun_hht@mail.ru

БЕЗПРОЗВАННЫЙ Илья Борисович – *доктор биологических наук, заведующий лабораторией молекулярной нейродегенерации Высшей школы биомедицинских систем и технологии, профессор той же Высшей школы Санкт-Петербургского политехнического университета Петра Великого; именной профессор отдела физиологии Юго-западного медицинского центра Университета штата Техас; именной профессор Карла и Хортензии Томпсен в исследованиях болезни Альцгеймера.*

195251, Российская Федерация, г. Санкт-Петербург, Политехническая ул., 29
mnlabspb@gmail.com

DOI: 10.18721/JPM.12208
УДК 539.126.3

THE MEASUREMENT OF ETA MESON NUCLEAR MODIFICTION FACTORS IN BINARY COLLISIONS OF URANIUM NUCLEI

P.V. Radzevich, A.Ya. Berdnikov, Ya.A. Berdnikov, D.O. Kotov, S.V. Zharko

Peter the Great St. Petersburg Polytechnic University, St. Petersburg, Russian Federation

Invariant spectra of η mesons production and nuclear modification factors of η и π^0 mesons produced in binary collisions of uranium nuclei at energy of 192 GeV have been presented in the paper. This data was obtained using the PHENIX spectrometer of RHIC. These experimental results were analyzed and compared with similar data on binary collisions of gold nuclei at 200 GeV. The η и π^0 mesons yields in central collisions of both uranium and gold nuclei (at energy values mentioned) were established to be suppressed equally. In the peripheral collisions, the nuclear modification factors of η и π^0 mesons measured in the uranium nuclei collisions were suppressed more than those obtained in the gold ones. An analysis of a ratio of the η meson to π^0 meson production spectra in the uranium nuclei collisions (at 192 GeV) revealed that the ratio was independent of the centrality class and the transverse momenta.

Keywords: quark-gluon plasma, eta meson, jet-quenching effect, nuclear modification factor

Citation: P.V. Radzevich, A.Ya. Berdnikov, Ya.A. Berdnikov, D.O. Kotov, S.V. Zharko, The measurement of eta meson nuclear modification factors in binary collisions of uranium nuclei, St. Petersburg Polytechnical State University Journal. Physics and Mathematics. 12 (2) (2019) 98–107. DOI: 10.18721/JPM.12208

ИЗМЕРЕНИЕ ФАКТОРОВ ЯДЕРНОЙ МОДИФИКАЦИИ ЭТА-МЕЗОНОВ ПРИ СТОЛКНОВЕНИЯХ ЯДЕР УРАНА

П.В. Радзевич, А.Я. Бердников, Я.А. Бердников, Д.О. Котов, С.В. Жарко

Санкт-Петербургский политехнический университет Петра Великого, Санкт-Петербург, Российская Федерация

В статье представлены инвариантные спектры рождения η-мезонов и факторы ядерной модификации η- и π^0-мезонов, рожденных в парных столкновениях ядер урана при энергии 192 ГэВ. Эти данные получены на спектрометре PHENIX, расположенном на релятивистском коллайдере RHIC. Проведен анализ этих экспериментальных результатов, и они сопоставлены с аналогичными данными для парных столкновений ядер золота при энергии 200 ГэВ. Установлено, что выходы η- и π^0-мезонов в центральных парных столкновениях ядер как урана, так и золота (при указанных значениях энергии) подавлены в равной степени. В периферийных же столкновениях факторы ядерной модификации η- и π^0-мезонов, измеренные в столкновениях ядер урана, подавлены сильнее, чем данные факторы, полученные в столкновениях ядер золота. Анализ отношения спектров рождения η-мезонов к спектрам π^0-мезонов, рожденных в парных столкновениях ядер урана при энергии 192 ГэВ, показал, что оно не зависит ни от класса центральности, ни от поперечного импульса.

Ключевые слова: кварк-глюонная плазма, эта-мезон, эффект гашения струй, фактор ядерной модификации

Ссылка при цитировании: Радзевич П.В., Бердников А.Я., Бердников Я.А., Котов Д.О., Жарко С.В. Измерение факторов ядерной модификации эта-мезонов при парных столкновениях ядер урана // Научно-технические ведомости СПбГПУ. Физико-математические науки. 2019. Т. 12. № 2. С. 101–110. DOI: 10.18721/JPM.

Introduction

Transition of nuclear matter to quark-gluon plasma (QGP) at high energy densities and/or temperatures ($\varepsilon \approx 1$ GeV/fm^3, $T \approx 170$ MeV) was first predicted in 1970 using calculations of quantum chromodynamics (QCD) [1–5]. Phase transitions from colorless hadronic matter to QGP are studied in experiments on collisions of ultrarelativistic nuclei. QGP studies contribute substantially to modern understanding of the evolution of the early Universe, as the temperature of the Universe was at one stage equivalent to the temperature of QGP ($T \approx 10^{12}$ K) [6]. The behavior of nuclear matter at high temperatures and energy densities carries information on the nature of forces between quarks and gluons; these studies are in great demand in cosmology, providing insights on the properties of neutron stars [7, 8].

The properties of QGP in collisions of ultrarelativistic nuclei are detected by analyzing the effects of the initial and final states of nuclear matter. The effect of quenching of hadronic jets is related to phenomena occurring in the final state of nuclear matter and manifests itself in collisions of heavy nuclei with high energy [9]. Jet quenching is a result of hard scattering of partons produced in collisions of heavy ultrarelativistic nuclei. This effect is studied by measuring the production spectra and nuclear modification factors of the hadrons produced in interactions of nuclei. It is convenient to use η mesons to estimate the degree of suppression of hadron yields in the region of high transverse momenta.

Production spectra and nuclear modification factors of η mesons are measured with the purpose of studying the jet quenching effect in a specific system of colliding nuclei. Comparing the production spectra and nuclear modification factors of η mesons with those for π^0 mesons allows to obtain the dependence of jet quenching on the masses of produced particles and on their quark composition.

The binary system of colliding uranium nuclei (U + U) with the energy $\sqrt{s_{NN}} = 192$ GeV is particularly interesting. Uranium nuclei have a non-spherical shape, so the effects of QGP can be studied with different geometrical configurations of colliding nuclei. In central collisions, The U + U system of colliding nuclei has the maximum energy density available at the Relativistic Heavy Ion Collider (RHIC) [10].

Problem statement and description

The goal of this study has been to investigate the production of η mesons in collisions of uranium nuclei (U + U) at an energy $\sqrt{s_{NN}} = 192$ GeV.

To identify the mechanisms for production of particles in scattering of hard partons produced in collisions of U + U nuclei at $\sqrt{s_{NN}} = 192$ GeV, we had to measure the production spectra of η mesons and calculate their nuclear modification factors. The invariant production spectra and nuclear modification factors of η mesons were analyzed taking into account their centrality class and depending on the transverse momentum.

The transverse momentum p_T characterizes the interaction energy in a system of colliding nuclei. Centrality, measured as a percentage, is the degree of overlap of colliding nuclei with a fixed impact parameter. Collisions with the maximum degree of overlap correspond to a centrality of 0–20% and are called central, and collisions with the minimum degree of overlap are called peripheral and correspond to a centrality of 60–80%.

Study procedure

We have developed a procedure for studying the effect of jet quenching with the help of η mesons produced in collisions of U + U nuclei at $\sqrt{s_{NN}} = 192$ GeV. The procedure includes the following steps:

processing the experimental data;

measuring the yields of η mesons in different p_T ranges and centrality classes;

calculating the particle reconstruction efficiency for the detector;

measuring the invariant spectra of η meson production in collisions of U + U nuclei at $\sqrt{s_{NN}} = 192$ GeV in different p_T ranges and centrality classes;

assessing the systematic measurement errors;

measuring the nuclear modification factors of η mesons in U + U collisions at $\sqrt{s_{NN}} = 192$ GeV in different p_T ranges and centrality

classes.

The experimental data used in the study were obtained with the PHENIX spectrometer at RHIC. Electromagnetic calorimeters were used to detect the decay products of η mesons in the $\eta \to \gamma\gamma$ channel. Such devices measure the energy and coordinates of photons, electrons and hadrons emitted from the region of nuclear interaction. The electromagnetic calorimeter system at the PHENIX experiment provided an overall acceptance $\varphi = 2 \cdot \pi/2$ in the azimuth and $|\eta| < 0.35$ in pseudorapidity.

The system of electromagnetic calorimeters consisted of two subsystems: the lead scintillation sampling calorimeter (PbSc) and the lead-glass Cherenkov calorimeter (PbGl). Each of the devices had its own segmentation. Using both types of calorimeters made it possible to cross-check the results obtained separately for the PbSc and PbGl subsystems within a single experiment.

Processing the experimental data. The data were prepared by establishing the criteria for selecting the desired events recorded by the electromagnetic calorimeter.

Constraints were imposed on the shape of detected electron showers yo separate the signals recorded during interaction of hadrons and photons with the active volume of the electromagnetic calorimeter. The constraint $\chi^2 < 3$ was imposed in the PbSc subsystem, and *photon_prob* > 0.02 in the PbGl subsystem. Here χ^2 and *photon_prob* are statistical variables described in [11].

The average energy transferred by charged hadrons is $E \approx 300$ MeV. Therefore, to better separate the signals from hadrons, we impose an additional constraint on the energy of reconstructed clusters: $E_\gamma > 400$ MeV.

To improve the signal-to-background ratio, we use the constraint on energy asymmetry between the photons combined in reconstruction of η mesons:

$$\frac{|E_{\gamma 1} - E_{\gamma 2}|}{E_{\gamma 1} + E_{\gamma 2}} < 0.8.$$

Particles were detected in collisions of uranium nuclei for 22 days. Equipment malfunctions could have occurred for a variety of reasons during this period. In view of this, we discarded data segments with a small number of recorded events in our analysis.

The interaction vertex (z_{coll}) is one of the main parameters in the system of colliding nuclei. This parameter was determined using the beam-beam counter in the PHENIX experiment. To select the data, we used a constraint on the vertex

$$-20 < z_{coll} < +20,$$

since the efficiency of the collision counter, measured in U + U collisions, is constant in this interval.

Measuring the yields of η mesons in different p_T ranges and centrality classes. This procedure is done by constructing the effective mass distribution of two gammas, selected after processing the experimental data, in different p_T ranges and centrality classes. To find the yields of η mesons, the useful signal recorded as a result of decay of η mesons is separated from the background, which is divided into the correlated (a pair of γ quanta is the product of particle decay) and uncorrelated (random combination of γ quanta) components.

To separate the uncorrelated background, γ pairs taken from two different events with similar characteristics (vertex and centrality) are combined. The distribution of effective mass of combined γ quanta (background) is constructed, normalized in the range

$$0.7 < M_{\gamma\gamma} < 0.8 \text{ GeV}/c^2$$

by the distribution of effective mass of real events (signal and background) and subtracted from it.

The result of subtracting two distributions is approximated by a Gaussian function to describe the signal from the reconstructed η mesons and by a second-degree polynomial to describe the residual correlated background, in the interval

$$0.40 < M_{\gamma\gamma} < 0.75 \text{ GeV}/c^2$$

in the range $p_T < 10$ GeV/c
and

$$0.35 < M_{\gamma\gamma} < 0.75 \text{ GeV}/c^2$$

in the range $p_T > 10$ GeV/c.

Yields of η mesons are measured by counting the number of samples and subtracting the integral under the second-degree polynomial. The region where η meson yields are counted lies in the range

$$0.48 < M_{\gamma\gamma} < 0.62 \text{ GeV}/c^2.$$

Calculating the particle reconstruction efficiency for the detector. This procedure allows to separate the number of η mesons reconstructed in the electromagnetic calorimeter from the

number of η mesons in the active volume of the detector.

The reconstruction efficiency is found by simulating the passage of η mesons in the PHENIX spectrometer by the Monte Carlo method. The specialized PISA package implemented in GEANT-3 [11] is used for this simulation.

The reconstruction efficiency is calculated as the ratio of the number of particles reconstructed during simulation to the initial number of particles.

Measuring the invariant spectra of η meson production in collisions of U + U nuclei at $\sqrt{s_{NN}}$ = 192 GeV in different p*T* ranges and centrality classes. The following formula is used for these measurements:

$$I_\eta(p_T) = dN_{AA}(p_T) = \\ = \frac{1}{2\pi p_T}\frac{N_\eta(p_T)}{N_{event}\Delta p_T \varepsilon_{rec.ef}(p_T)}, \quad (1)$$

where N_η is the yield of neutral η mesons; $\varepsilon_{rec.ef}$ is the reconstruction efficiency; N_{event} is the number of events analyzed.

Invariant spectra of particle production are measured in different centrality classes.

Assessing the systematic measurement errors. This is done by varying different parameters (energy scale, energy resolution, weighting factors, parameters of detected particles, boundaries of detected γ clusters, conversion, geometry of the experimental setup and model) used to measure the yields of η mesons.

Statistical and systematic errors of nuclear modification factors are calculated as the sum of the squares of statistical and systematic errors of the numerator and denominator of formula (1).

Measuring the nuclear modification factors of η mesons in U + U collisions at $\sqrt{s_{NN}}$ = 192 GeV in different p_T ranges and centrality classes. The following formula is used for this purpose:

$$R_{AA} = \frac{1}{\langle N_{coll}\rangle}\frac{dN_{AA}}{dN_{pp}}, \quad (2)$$

where dN_{AA}, dN_{pp} are hadron yields in (A + A) and proton (p + p) collisions, respectively, in a given range of transverse momenta; $\langle N_{coll}\rangle$ is the average number of inelastic nucleon-nucleon collisions.

The value of $\langle N_{coll}\rangle$ is found by Monte Carlo simulation based on the Glauber theory taking into account the geometry of colliding nuclei. Normalization to this number is based on the assumption that hadrons are produced in elementary parton-parton interactions.

To study collective effects (effects of the final and initial states of nuclear matter) in the system of colliding nuclei, we used nuclear modification factors R_{AA}. If R_{AA} = 1, then there are no collective effects in the system of colliding nuclei. If R_{AA} is different from unity, this points to either suppressed or excessive particle yield.

Results and discussion

Fig. 1 shows invariant spectra of η mesons production measured in collisions of uranium nuclei (U + U) at $\sqrt{s_{NN}}$ = 192 GeV depending on the transverse momentum for different centrality classes.

The spectra were measured in a wide range of transverse momenta in central collisions (up to 14 GeV/*c*). There were limitations to measuring the production spectra in the region of low transverse momenta due to small capacity of the detector setup. The limitations in the region of high momenta were due to insufficient statistical data.

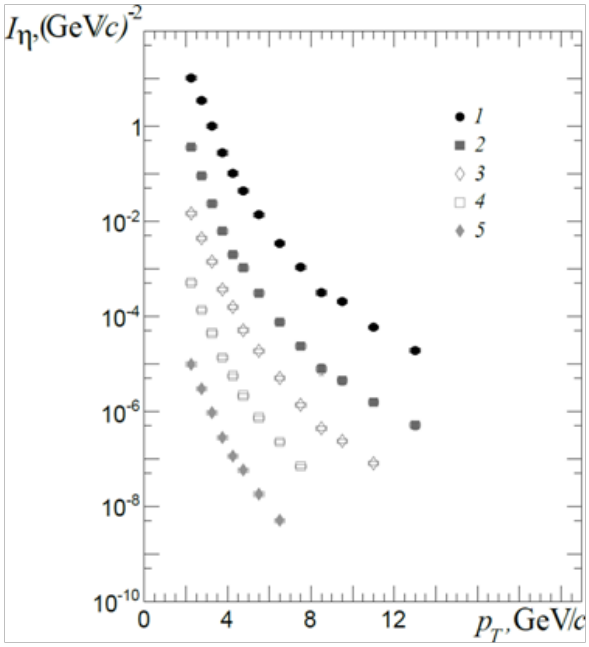

Fig. 1. Invariant spectra of η mesons measured in U + U collisions as function of transverse momentum for different centrality classes, %: 0–80 (*1*), 0–20 (*2*), 20–40 (*3*), 40–60 (*4*), 60–80 (*5*); $\sqrt{s_{NN}}$ = 192 GeV.

The vertical bars and the horizontal grey rectangles on the points here and below correspond to statistical and systematic measurement error, respectively

Fig. 2 shows a comparison of nuclear modification factors of η mesons measured in collisions of uranium (U + U) and gold (Au + Au) nuclei [12, 13] at energies $\sqrt{s_{NN}}$ = 192 and 200 GeV, respectively, with close values of N_{coll} (see Table). The nuclear modification factors of η mesons (see Fig. 2) were calculated by formula (2) using two different sets of average number N_{coll} of nucleon-nucleon collisions in different centrality classes in U + U collisions at $\sqrt{s_{NN}}$ = 192 GeV. Two sets of N_{coll} are used because of uneven distribution of nucleons in spherically asymmetric uranium nuclei.

The nuclear modification factors measured in collisions of uranium and gold nuclei at $\sqrt{s_{NN}}$ = 192 and 200 GeV, respectively, coincide for high values of N_{coll}, which indicates that the jet quenching effect does not depend on the geometric shape of colliding nuclei.

The nuclear modification factors obtained in

Table

Number of collisions N_{coll} as function of centrality for different types of interactions (see Fig. 2)

Centrality, %	N_{coll}	Fig. 2
Au + Au (*set 1*), 200 GeV		
0–5	1065.4105.3±	*a*)
20–40	300.832.6±	*b*)
40–50	120.313.7±	*c*)
60–92	17.13.9±	*d*)
Au + Au (*set 2*), 200 GeV		
0–10	967.392.9±	*a*)
60–92	17.23.5±	*d*)
U + U (*variant I*), 192 GeV		
0–20	934.597.5±	*a*)
20–40	335.033.0±	*b*)
40–60	95.913.0±	*c*)
60–80	17.53.8±	*d*)
U + U (*variant II*), 192 GeV		
0–20	999.0114.0±	*a*)
20–40	375.045.0±	*b*)
40–60	110.014.6±	*c*)
60–80	19.74.4±	*d*)

Note. Different variants possible for collisions of uranium nuclei are due to different degrees of deformation of uranium nuclei in calculations of the nucleon number N_{coll} in the Glauber model [12, 13].

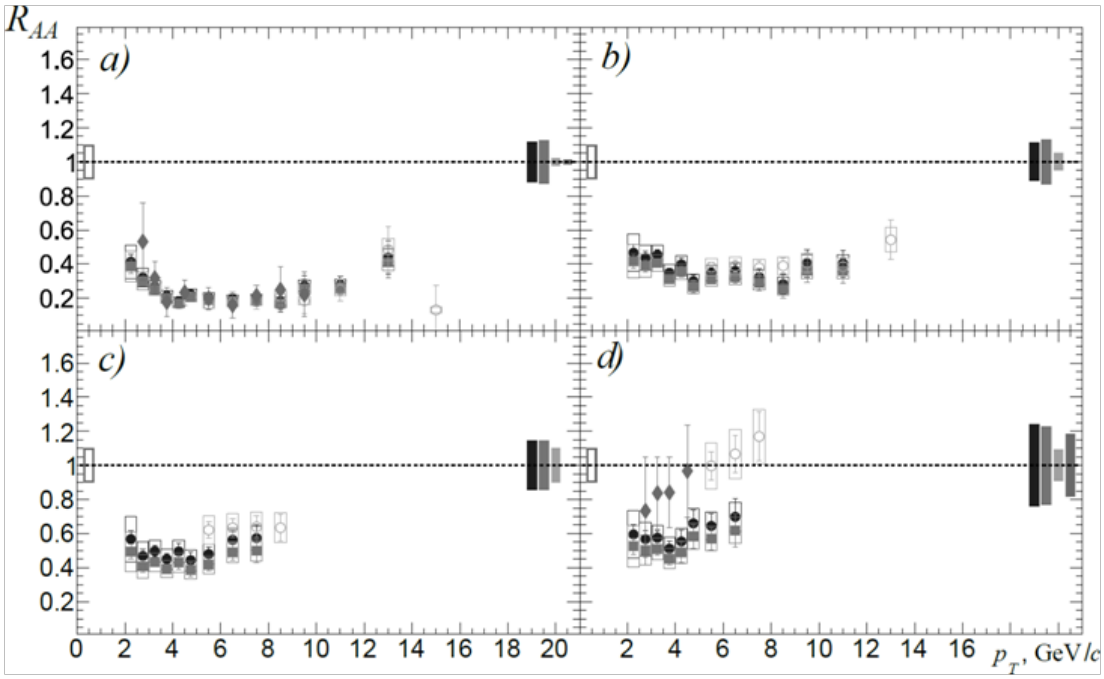

Fig. 2. Nuclear modification factor R_{AA} as function of transverse momentum p_T for η mesons in (U + U) interactions (solid circles and squares) and (Au + Au) interactions (circles and diamonds) [12, 13] with energies of 192 and 200 GeV, respectively (see Table)
Rectangles over the dashed lines indicate the systematic error for N_{coll}

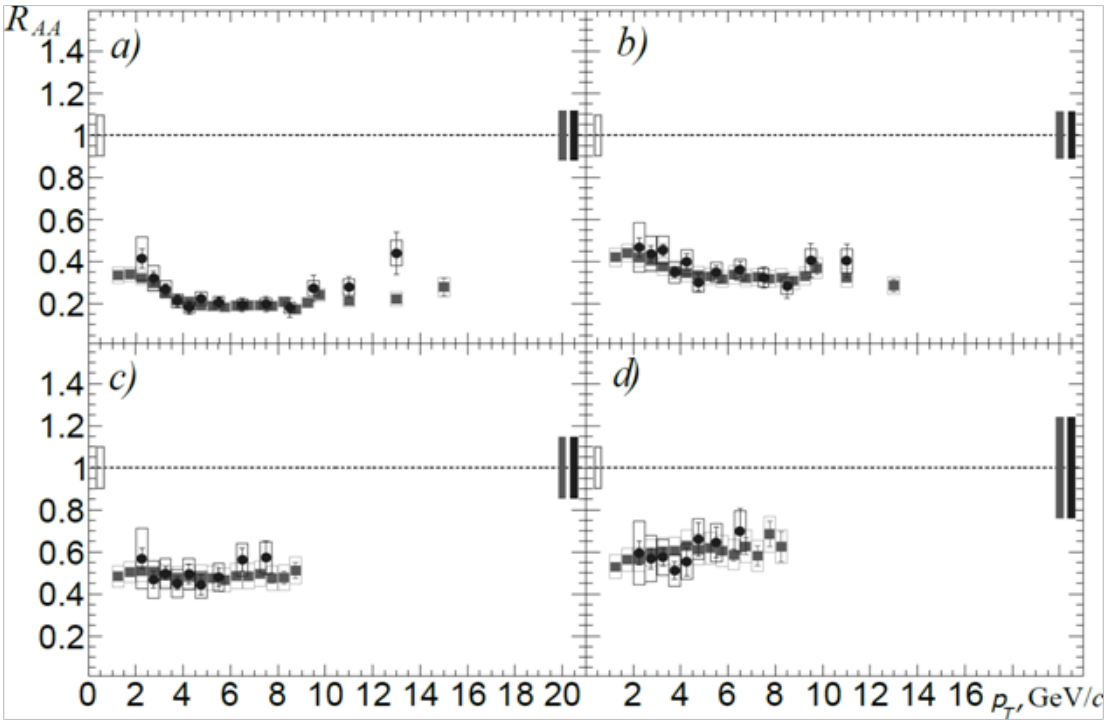

Fig. 3. Nuclear modification factor R_{AA} as function of transverse momentum p_T for π^0 mesons (squares) and η mesons (circles) in (U + U) interactions with energies of 192 and 200 GeV, respectively, for different centrality classes, %: 0–20 (*a*), 20–40 (*b*), 40–60 (*c*), 60–80 (*d*).
Rectangles over the dashed lines indicate the systematic error for N_{coll}

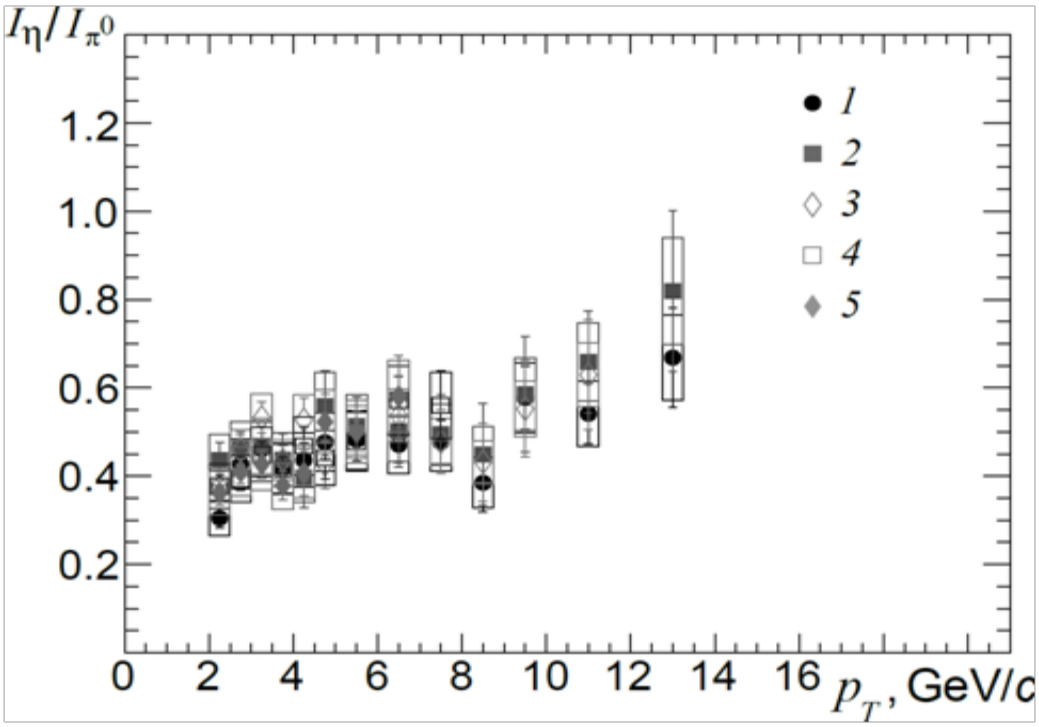

Fig. 4. Ratios for η meson production spectra to π^0 meson production spectra measured in U + U collisions at $\sqrt{s_{NN}}$ = 192 GeV as function of transverse momentum for different centrality classes, %: 0–80 (*1*), 0–20 (*2*), 20–40 (*3*), 40–60 (*4*), 60–80 (*5*)

collisions of uranium and gold nuclei at $\sqrt{s_{NN}}$ = 192 and 200 GeV, respectively, are somewhat different for small values of N_{coll}; however, the given quantities cannot be clearly separated due to large systematic error.

Fig. 3 shows a comparison of nuclear modification factors for π^0 and η mesons measured in collisions of uranium nuclei (U + U) at $\sqrt{s_{NN}}$ = 192 GeV, in different centrality classes. Evidently, these values coincide within systematic and statistical error in the entire range of transverse momenta and in all centrality classes.

Ultimately, the behavior of the ratios of η/π^0 spectra measured in collisions of uranium nuclei at $\sqrt{s_{NN}}$ = 192 GeV (Fig. 4) does not depend on centrality and transverse momentum within the systematic error.

Conclusion

Invariant spectra of η mesons have been measured in this study in five classes of centrality and nuclear modification factors of η mesons have been measured in four classes of centrality depending on the transverse momentum at an energy of $\sqrt{s_{NN}}$ = 192 GeV in pair collisions of uranium nuclei (U + U).

Coinciding nuclear modification factors of η mesons have been obtained for colliding uranium (U + U) and gold (Au + Au) systems with equal average numbers of inelastic nucleon-nucleon collisions in the region of high transverse momenta for central and semi-central collisions, which indicates that the effects of the final state do not depend on the geometric properties of the colliding nuclei.

We have established that the yields of η mesons in peripheral collisions of uranium (U + U) at $\sqrt{s_{NN}}$ = 192 GeV were suppressed more strongly than in collisions of gold (Au + Au) at $\sqrt{s_{NN}}$ = 200 GeV, but it proved impossible to clearly separate the obtained values due to large systematic and statistical error.

Analyzing the data for the ratios of η/π^0 spectra and comparing the nuclear modification factors of π^0 and η mesons, we have found that fragmentation of hard partons does not depend on the mass and composition of π^0 and η meson quarks produced in pair collisions of uranium nuclei at $\sqrt{s_{NN}}$ = 192 GeV.

The results of this study were obtained within the framework of State Task of the Ministry of Education and Science of Russian Federation 3.1498.2017/4.6.

REFERENCES

1. **Greutz M.,** Gauge fixing, the transfer matrix, and confinement on a lattice, Phys. Rev. D. 15 (4) (1977) 1128–1136.
2. **Wilson K.G.,** Confinement of quarks, Phys. Rev. D. 10 (8) (1974) 2445–2459.
3. **Wilson K.G., Walhout T.S., Harindranath A., et al.,** Nonperturbative QCD: A weak-coupling treatment on the light front, Phys. Rev. D. 49 (12) (1994) 6720–6766.
4. **Laermann E., Philipsen O.,** The status of lattice QCD at finite temperature, Annual Review of Nuclear and Particle Science. 53 (2003) 163–198.
5. **Adcox K., Adler S.S., Afanasiev S., et al.,** Formation of dense partonic matter in relativistic nucleus-nucleus collisions at RHIC: experimental evaluation by the PHENIX collaboration, Nucl. Phys. A. 757 (1–2) (2005) 184–283.
6. **Karsch F.,** Lattice QCD at high temperature and density, In: Lectures on quark matter, W. Plessas, L. Mathelitsch (Eds), Lecture Notes in Physics, Berlin: Springer. 582 (2002) 209–249.
7. **Collins J.C.,** Superdense matter: neutrons or asymptotically free quarks? Phys. Rev. Lett. 34 (21) (1975) 1353–1356.
8. **Rajagopal** K., The phases of QCD in heavy ion collisions and compact stars, AIP Conference Proceedings. 549 (1) (2000) 95–119.
9. **Berdnikov A.Ya., Berdnikov Ya.A., Zharko S.V., et al.,** Experimental study of pion production in U + U interactions at 192 GeV, Bulletin of the Russian Academy of Sciences: Physics. 82 (10) (2018) 1262–1265.
10. **Iordanova A.,** U+U and Cu+Au results from PHENIX , Journal of Physics: Conference Series. 458 (2013) 012004.
11. **Adler S.S., Chujo T., Desmond E.J., et al.,** PHENIX on-line and off-line computing, Nuclear Instruments and Methods in Physics Research, Section A: Accelerators, Spectrometers, Detectors and Associated Equipment. 499 (2/3) (2003) 593–602.
12. **Adler** S.S., **et al. (PHENIX Collaboration),** High transverse momentum η meson production in $p + p$, d + Au and Au + Au collisions at $\sqrt{s_{NN}}$ = 200 GeV, Phys. Rev. C. 75 (2) (2007) 024909.
13. **Adare A., et al. (PHENIX Collaboration),** Transverse momentum dependence of η meson suppression in Au+Au collisions at $\sqrt{s_{NN}}$ = 200 GeV, Phys. Rev. C. 82 (1) (2010) 011902.

Received 04.02.2019, accepted 11.03.2019.

THE AUTHORS

RADZEVICH Pavel V.
Peter the Great St. Petersburg Polytechnic University
29 Politechnicheskaya St., St. Petersburg, 195251, Russian Federation
radzevichp@gmail.com

BERDNIKOV Alexandr Ya.
Peter the Great St. Petersburg Polytechnic University
29 Politechnicheskaya St., St. Petersburg, 195251, Russian Federation
alexber@phmf.spbstu.ru

BERDNIKOV Yaroslav A.
Peter the Great St. Petersburg Polytechnic University
29 Politechnicheskaya St., St. Petersburg, 195251, Russian Federation
berdnikov@spbstu.ru

KOTOV Dmitry O.
Peter the Great St. Petersburg Polytechnic University
29 Politechnicheskaya St., St. Petersburg, 195251, Russian Federation
dmitriy.kotov@gmail.com

ZHARKO Sergei V.
Peter the Great St. Petersburg Polytechnic University
29 Politechnicheskaya St., St. Petersburg, 195251, Russian Federation
zharkosergey94@gmail.com

СПИСОК ЛИТЕРАТУРЫ

1. **Greutz M.** Gauge fixing, the transfer matrix, and confinement on a lattice // Phys. Rev. D. 1977. Vol. 15. No. 4. Pp. 1128–1136.

2. **Wilson K.G.** Confinement of quarks // Phys. Rev. D. 1974. Vol. 10. No. 8. Pp. 2445–2459.

3. **Wilson K.G., Walhout T.S., Harindranath A., Zhang W.-M., Perry R.J., Glazek D.S.** Nonperturbative QCD: A weak-coupling treatment on the light front // Phys. Rev. D. 1994. Vol. 49. No. 12. Pp. 6720–6766.

4. **Laermann E., Philipsen O.** The status of lattice QCD at finite temperature // Annual Review of Nuclear and Particle Science. 2003. Vol. 53. Pp. 163––198.

5. **Adcox K., Adler S.S., Afanasiev S., et al.** Formation of dense partonic matter in relativistic nucleus-nucleus collisions at RHIC: experimental evaluation by the PHENIX Collaboration // Nucl. Phys. A. 2005. Vol. 757. No. 1–2. Pp. 184–283.

6. **Karsch F.** Lattice QCD at high temperature and density // Lectures on quark matter. Plessas W., Mathelitsch L. (Eds). Lecture Notes in Physics. 2002. Vol. 583. Berlin: Springer. Pp. 209–249.

7. **Collins J.C.** Superdense matter: neutrons or asymptotically free quarks? // Phys. Rev. Lett. 1975. Vol. 34. No. 21. Pp. 1353–1356.

8. **Rajagopal K.** The phases of QCD in heavy ion collisions and compact stars // AIP Conference Proceedings. 2000. Vol. 549. No. 1. Pp. 95–119.

9. **Бердников А.Я., Бердников Я.А., Жарко С.В., Котов Д.О., Радзевич П.В.** Эксперименн тальные исследования рождения π-мезонов в U+U-взаимодействиях при энергии 192 Гэв // Известия РАН. Сер. физическая. 2018. Т. 82. № 10. С. 1391–1394.

10. **Iordanova A.** U+U and Cu+Au results from PHENIX // Journal of Physics: Conference Series. 2013. Vol. 458. P. 012004.

11. **Adler S.S., Chujo T., Desmond E.J., et al.** PHENIX on-line and off-line computing // Nuclear Instruments and Methods in Physics Research. Section A: Accelerators, Spectrometers, Detectors and Associated Equipment. 2003. Vol. 499. No. 2/3. Pp. 593–602.

12. **Adler S.S., et al.** (PHENIX Collaboration), High transverse momentum η meson production in $p + p$, d + Au and Au + Au collisions at $\sqrt{s_{NN}}$ = 200 GeV // Phys. Rev. C. 2007. Vol. 75. No. 2. P. 024909.

13. **Adare A., et al.** (PHENIX Collaboration), Transverse momentum dependence of η meson suppression in Au+Au collisions at $\sqrt{s_{NN}}$ = 200 GeV // Phys. Rev. C. 2010. Vol. 82. No. 1. P. 011902.

Статья поступила в редакцию 04.02.2019, принята к публикации 11.03.2019.

СВЕДЕНИЯ ОБ АВТОРАХ

РАДЗЕВИЧ Павел Владиславович – *аспирант кафедры экспериментальной ядерной физики Санкт-Петербургского политехнического университета Петра Великого.*

195251, Российская Федерация, г. Санкт-Петербург, Политехническая ул., 29
radzevichp@gmail.com

БЕРДНИКОВ Александр Ярославич – *кандидат физико-математических наук, доцент кафедры экспериментальной ядерной физики Санкт-Петербургского политехнического университета Петра Великого.*

195251, Российская Федерация, г. Санкт-Петербург, Политехническая ул., 29
alexber@phmf.spbstu.ru

БЕРДНИКОВ Ярослав Александрович – *доктор физико-математических наук, профессор, заведующий кафедрой экспериментальной ядерной физики Санкт-Петербургского политехнического университета Петра Великого.*

195251, Российская Федерация, г. Санкт-Петербург, Политехническая ул., 29
berdnikov@spbstu.ru

КОТОВ Дмитрий Олегович – *кандидат физико-математических наук, доцент кафедры экспериментальной ядерной физики Санкт-Петербургского политехнического университета Петра Великого.*

195251, Российская Федерация, г. Санкт-Петербург, Политехническая ул., 29
dmitriy.kotov@gmail.com

ЖАРКО Сергей Вячеславович – *ассистент кафедры экспериментальной ядерной физики Санкт-Петербургского политехнического университета Петра Великого.*

195251, Российская Федерация, г. Санкт-Петербург, Политехническая ул., 29
zharkosergey94@gmail.com

DOI: 10.18721/JPM.12209
УДК 539.126.3

SUPPRESSION OF THE HADRONIC YIELDS IN THE URANIUM NUCLEI COLLISIONS AT THE DIFFERENT QUARK'S COMPOSITION OF THE PRODUCED PARTICLES

P.V. Radzevich, A.Ya. Berdnikov, Ya.A. Berdnikov
S. V. Zharko, D.O. Kotov

Peter the Great St. Petersburg Polytechnic University, St. Petersburg, Russian Federation

This paper presents invariant spectra, nuclear modification factors and ratio of invariant spectra of light mesons, obtained in collisions of heavy uranium nuclei at 192 GeV. These values are studied with respect to transverse momenta, numbers of nucleon-nucleon collisions, numbers of participants and centrality. Light mesons production measurements are important in the study of heavy ion collisions, serving as hard probes of the quark-gluon plasma (QGP). The research of light mesons in U + U collisions at 192 GeV allows discriminating the effects of hot matter depending on the geometric characteristics of the colliding heavy nuclei. The obtained results showed independence of the fragmentation of hard partons on the mass and composition of quarks and the absence of the influence of the geometric form of the colliding nuclei on the jet-quenching effect.

Keywords: quark-gluon plasma, light meson, nuclear modification factor, collision of heavy nuclei

Citation: Radzevich P.V., Berdnikov A.Ya., Berdnikov Ya.A., Zharko S.V., Kotov D.O., Suppression of the hadronic yields in the uranium nuclei collisions at the different quark's composition of the produced particles, St. Petersburg Polytechnical State University Journal. Physics and Mathematics. 12 (2) (2019) 108–117. DOI: 10.18721/JPM.12209

ПОДАВЛЕНИЕ ВЫХОДОВ АДРОНОВ В СТОЛКНОВЕНИЯХ ЯДЕР УРАНА ПРИ РАЗЛИЧНОМ КВАРКОВОМ СОСТАВЕ РОЖДАЮЩИХСЯ ЧАСТИЦ

П.В. Радзевич, А.Я. Бердников, Я.А. Бердников
С.В. Жарко, Д.О. Котов

Санкт-Петербургский политехнический университет Петра Великого,
Санкт-Петербург, Российская Федерация

В статье представлены экспериментальные инвариантные спектры рождения, факторы ядерной модификации и отношения интенсивностей спектров легких мезонов, полученные в столкновении тяжелых ядер урана при энергии 192 ГэВ. Данные характеристики частично отражают свойства кварк-глюонной плазмы (КГП), рождающейся в столкновении тяжелых ядер урана при различном размере взаимодействующей системы и кварковом составе рождающихся частиц. Приведенные данные представлены в зависимости от поперечного импульса, среднего числа нуклон-нуклонных столкновений, среднего числа участников столкновения и класса по центральности. Предполагалось опытным путем дискриминировать эффекты горячей и плотной материи в зависимости от геометрических характеристик сталкивающихся тяжелых ядер из-за сферической несимметричности ядер урана. Анализ полученных данных привел к выводам о независимости фрагментации жестких партонов от массы и состава кварков легких мезонов и об отсутствии влияния геометрической формы сталкивающихся ядер на проявление эффекта гашения адронных струй.

Ключевые слова: кварк-глюонная плазма, легкий мезон, фактор ядерной модификации, столкновение тяжелых ядер

Ссылка при цитировании: Радзевич П.В., Бердников А.Я., Бердников Я.А., Жарко С.В., Котов Д.О. Подавление выходов адронов в столкновениях ядер урана при различном кварковом составе рождающихся частиц // Научно-технические ведомости СПбГПУ. Физико-математические науки. 2019. Т. 12. № 2. С. 111–120. DOI: 10.18721/JPM.12209

Introduction

The generally accepted definition of quark-gluon plasma is a state of matter where the degrees of freedom are color-charged quarks and gluons. Systematic observations of quark-gluon plasma forming in collisions of ultrarelativistic heavy nuclei (A + A) were first carried out at the Relativistic Heavy Ions Collider (RHIC) at collision energies $\sqrt{s_{NN}}$ = 130 and 200 GeV (per nucleon) [1–4] and later at the Large Hadron Collider (LHC) in collisions of lead nuclei at $\sqrt{s_{NN}}$ = 2.76 TeV [5].

Production of hadrons in collisions of ultrarelativistic ions for high transverse momenta, p_T > 5 GeV/c is due to fragmentation of hard partons produced in deep inelastic collisions. Cross sections of hadron production in elementary proton collisions (p + p) are adequately described by the next-to-leading order formalism of perturbative quantum chromodynamics (NLO pQCD) [6]. Production of hadrons in A + A collisions is influenced by the quark-gluon medium: hard partons passing through it lose some of their energy, which leads to suppressed hadron yield in fragmentation (compared to their yield in elementary proton-proton collisions). This effect is known as jet quenching [6, 7]. Considering the production of different types of light mesons (for example, π^0, η, K_S) in (A + A) collisions is a step towards systematic study of the effects of quark-gluon plasma and, in particular, the effect of jet quenching depending on the main characteristics, such as mass and quark composition of these particles.

The jet quenching effect is assessed quantitatively by calculating the nuclear modification factor found depending on transverse momentum and centrality according to the expression:

$$R_{AA} = \frac{1}{\langle N_{coll} \rangle} \frac{dN_{AA}}{dN_{pp}}, \qquad (1)$$

where dN_{AA}, dN_{pp} are hadron yields in (A + A) and (p + p) collisions, respectively; $\langle N_{coll} \rangle$ is the average number of inelastic nucleon-nucleon collisions in a given centrality class of (A + A) interactions.

Particle yield in (A + A) collisions is typically measured as a function of transverse momentum and collision centrality. Centrality is measured as a percentage and determines the impact parameter and the degree of overlap of colliding nuclei [8]. Collisions with small impact parameter and centrality in the range of 0–20% are characterized by high multiplicity of particles and are called central collisions. Only a small fraction of interacting nucleons participate in peripheral collisions with centrality in the range of 60–80%.

Yields of K_S mesons are measured in the $K_S \to \pi^0\pi^0$ channel. Daughter particles of K_S meson decay (π^0 mesons) were measured earlier in [9]. K_S mesons consist of strange quarks, which makes it possible to study the production of light mesons depending on the quark composition of the given particles in comparing the nuclear modification factors of K_S, π^0 and η mesons [9]. The difference in the masses of K_S, π^0 and η mesons [9] allows to study the effect of jet quenching depending on the mass component of the given particles.

The system of colliding nuclei of uranium-238 (U + U) at $\sqrt{s_{NN}}$ = 192 GeV is of particular interest for studying the jet quenching effect. Uranium nuclei have a pronounced spherical asymmetry, so collisions of these nuclei have a peculiar collision geometry, different from that of symmetric nuclei (for example, gold or copper). Besides, uranium nuclei are the heaviest used in collider experiments: their collisions have the highest energy density and, as a result, the highest multiplicity of particles among all (A + A) systems in this energy range [10]. Thus, analyzing the characteristics of production of neutral light mesons in (U + U) collisions at $\sqrt{s_{NN}}$ = 192 GeV is an important part of systematic studies on the jet quenching effect that should make it possible to additionally discriminate between free parameters of different models describing the energy losses of hard partons in quark-gluon plasma.

This paper reports on jet quenching in production of π^0, η and K_S mesons in collisions of uranium nuclei at $\sqrt{s_{NN}}$ = 192 GeV.

Study procedure

Raw data on collisions of uranium nuclei at $\sqrt{s_{NN}}$ = 192 GeV were collected using the PHENIX spectrometer at RHIC (Brookhaven National Laboratory, USA) in 2012. The centralities and coordinates of the vertex along the beam axis (z_{vert}) for each interaction of uranium nuclei were found using a system of beam-beam counters (BBC) [11]. The BBC counters determine the Minimum Bias trigger, selecting all the events of nucleus-nucleus collisions where at least one inelastic nucleon-nucleon interaction has occurred. The coordinate z_{vert} lies in the range $|z_{vert}| < 20$ cm in this case. The BBC response together with the spectrometer response simulated by the Monte Carlo method based on the Glauber theory [12] is used to determine the average number of collisions N_{coll} and the average number $\langle N_{part} \rangle$ of nucleons participating in the nucleus-nucleus interaction.

Light K_S, π^0 and η mesons are detected in the $K_S \to \pi^0\pi^0$ (BR = 30.69±0.05%), $\pi^0 \to \gamma\gamma$ (BR = 98.82±0.03%) and $\eta \to \gamma\gamma$ (BR = 72.12±0.34%) channels [10] in the system of electromagnetic calorimeters of the PHENIX spectrometer. Geometry and characteristics of the calorimeters were described in [13]. Some kinematic constraints are imposed to improve the signal-to-background ratio. In particular, the constraints imposed on the minimum energy E_γ and the photon energy asymmetry are, respectively,

$$E_\gamma > 400 \text{ MeV and } \frac{|E_{\gamma 1} - E_{\gamma 2}|}{E_{\gamma 1} - E_{\gamma 2}} < 0.8.$$

The procedure for measuring the π^0 and η meson yields in collisions of uranium nuclei at $\sqrt{s_{NN}}$ = 192 GeV was described in [8, 14].

To produce candidates for the role of π^0 mesons (referred to as π^0 candidates from now on) in $K_S \to \pi^0\pi^0$ decay, the invariant mass of a pair of γ quanta should be in the range of 1.5σ (σ is the standard deviation) of the measured masses of π^0 mesons, depending on their transverse momenta, and in the same arm of the PHENIX spectrometer. A pair of γ quanta should have a total momentum in the ranges

$$2 < p_T < 11 \text{ and } 2 < p_T < 14 \text{ GeV}/c$$

in the PbSc and PbGl subsystems [13] of the electromagnetic calorimeter, respectively. An additional adjustment is introduced for all γ pairs selected as π^0 candidates to re-

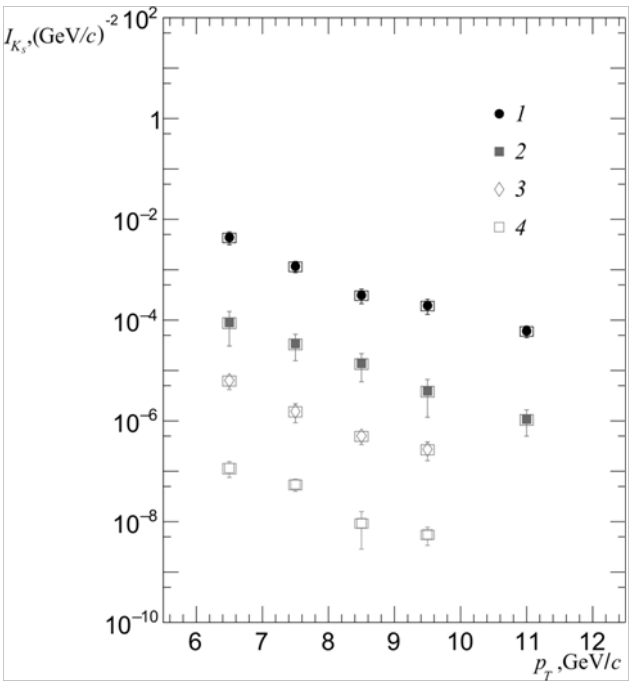

Fig. 1. Invariant spectra of K_S meson production as function of transverse momentum, measured in collisions of uranium nuclei at $\sqrt{s_{NN}}$ = 192 GeV for different centrality classes, %
0–80 (*1*), 0–20 (*2*), 20–40 (*3*), 40–80 (*4*)
The vertical bars and the horizontal grey rectangles on the points here and below correspond to statistical and systematic measurement error, respectively

duce the mass of the π^0 candidate to the table value m_{tabl} = 134.977 MeV, which allows to increase the signal-to-background ratio in the distributions over the invariant mass of $\pi^0\pi^0$ pairs.

Distributions over the invariant mass of pairs of π^0 candidates used to determine the yield of K_S mesons are formed in different transverse momentum ranges and centrality classes and are approximated by the sum of a Gaussian function (describing the signal from K_S mesons) and a parabola (describing the background). The yield of K_S mesons is found by the area under the Gaussian function.

Due to limited acceptance of the detector, the effects of its operation, and the kinematic constraints used in analysis, K_S meson yields are corrected using the reconstruction efficiency. This quantity is calculated for K_S mesons by Monte Carlo simulation of the detector's response using the GEANT-3 software package [15].

Invariant yields of K_S mesons in collisions of uranium nuclei at $\sqrt{s_{NN}}$ = 192 GeV in different transverse momentum ranges and centrality classes are measured by the formula used in the study of π^0 meson production [8].

The main systematic error in measuring the yields of K_S mesons produced in collision of U + U nuclei is the error related to selecting the parameters for approximating invariant mass distributions: the approximation range, signal integration range and the polynomial degree during approximation. The error is 15.0–22.5% in different ranges of transverse momenta and in different centrality classes. A substantial contribution to systematic measurement error is also made by conversion of γ quanta in detector materials (10.4%).

Results and discussion

Fig. 1 shows invariant spectra of K_S meson production as function of transverse momentum in collisions of uranium nuclei (U + U) at $\sqrt{s_{NN}}$ = 192 GeV. The spectra were measured in four centrality classes and in a wide range of transverse momenta: up to 11 GeV/c in central collisions.

Fig. 2 shows a comparison of nuclear modification factors for K_S mesons produced in collisions of uranium nuclei (U + U) at $\sqrt{s_{NN}}$ = 192 GeV, gold (Au + Au) [16] and copper (Cu + Cu) nuclei [17] at $\sqrt{s_{NN}}$ = 200 GeV with an equal number of inelastic nucleon-nucleon collisions $\langle N_{coll}\rangle$. The values of $\langle N_{coll}\rangle$ for each system of colliding nuclei and each centrality class are given in Table. The nuclear modification factors of K_S mesons were calculated by formula (1).

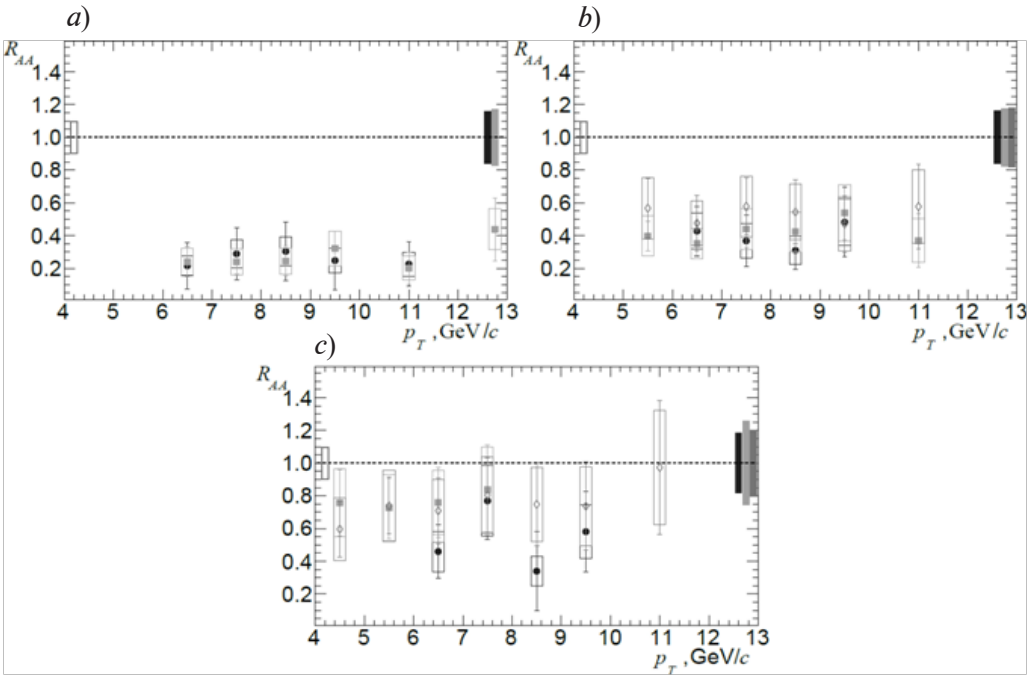

Fig. 2. Nuclear modification factors R_{AA} as function of transverse momentum p_T for K_S mesons in (U + U) interactions (solid circles), (Au + Au) interactions (solid squares) and (Cu + Cu) interactions (diamonds) [16, 17] at energies of 192 and 200 GeV, respectively (see Table)
Rectangles over the dashed lines indicate the systematic error for N_{coll}

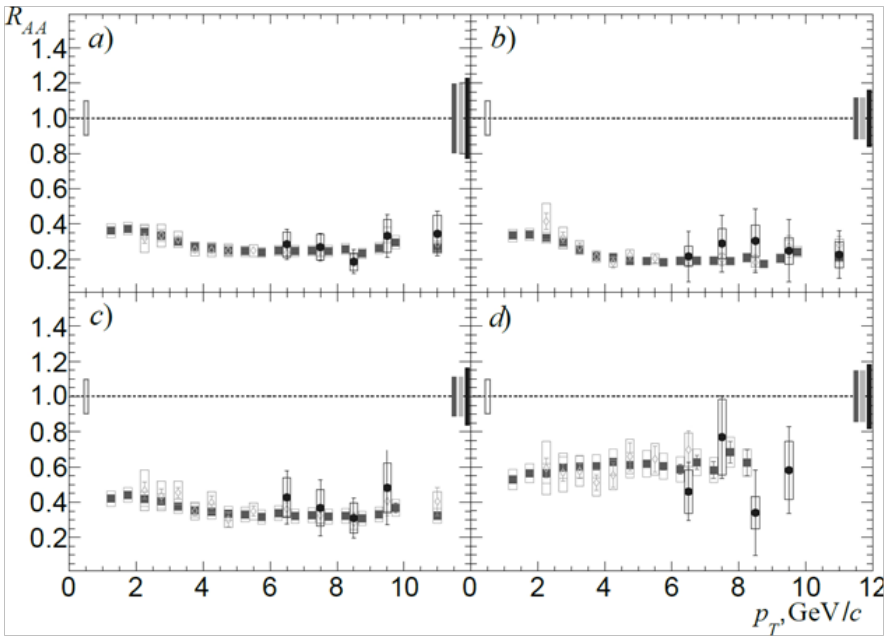

Fig. 3. Nuclear modification factor R_{AA} as function of transverse momentum p_T for π^0 mesons (squares), η mesons (diamonds) and K_S mesons (circles) in (U + U) interactions at $\sqrt{s_{NN}}$ = 192 GeV for different centrality classes, %: 0–80 (*a*), 0–20 (*b*), 20–40 (*c*), 60–80 for π^0 and η mesons, and 40–80 for K_S mesons (*d*). Rectangles over the dashed lines indicate the systematic error for N_{coll}

Table

Number of collisions N_{coll} as function of centrality for different types of interactions (see Fig. 2) [16, 17, 19]

Centrality, %	N_{coll}	Fig. 2
Au + Au, 200 GeV		
0–20	783.2±71.4	*a*)
20–60	300.8±32.6	*b*)
60–93	14.5±2.5	*c*)
Cu + Cu, 200 GeV		
0–20	151.8±16.1	*b*)
20–60	42.0±3.5	*c*)
U + U, 192 GeV		
0–20	934.5±97.5	*a*)
20–40	335.0±33.0	*b*)
40–80	56.7±5.0	*c*)

Note. Different variants possible for collisions of uranium nuclei are due to different degrees of deformation of the uranium nucleus in calculations of the nucleon numbers N_{coll} in the Glauber model [19].

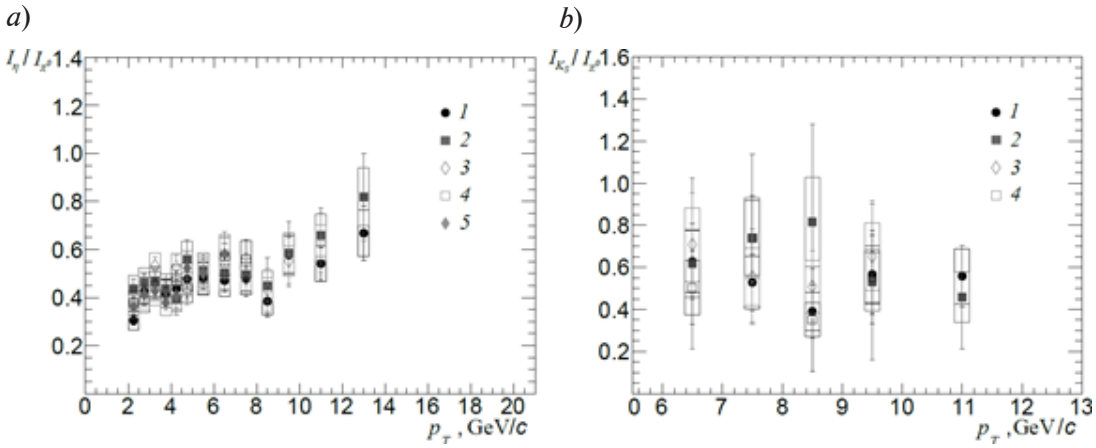

Fig. 4. Ratios of η meson to π^0 meson production spectra *(a)* and K_S meson to π^0 meson production spectra *(b)*, measured in U + U collisions at $\sqrt{s_{NN}}$ = 192 GeV, as functions of transverse momentum for different centrality classes, %: 0–80 (*1*), 0–20 (*2*), 20–40 (*3*), 40–60 for η/π^0 and 40–80 for K_S/π^0 (*4*), 60–80 (*5*)

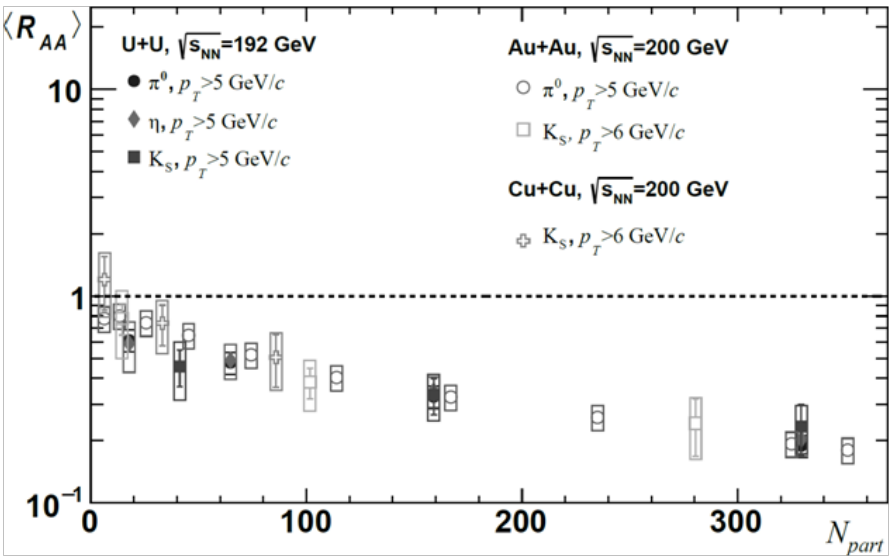

Fig. 5. Integral nuclear modification factors of π^0, η and K_S mesons in collisions of U + U, Au + Au and Cu + Cu nuclei [16, 17, 19] at $\sqrt{s_{NN}}$ = 192 GeV and 200 as functions of average number $\langle N_{part} \rangle$ of collision participants

The nuclear modifications factor of K_S mesons measured in collisions of uranium, gold and copper nuclei (U + U, Au + Au and Cu + Cu) at $\sqrt{s_{NN}}$ = 192 and 200 GeV coincide within the measurement error for all given values of $\langle N_{coll} \rangle$. A similar behavior of nuclear modification factors was observed in the study of yields of particles (π^0 mesons) that did not include the *s* quark [9], which indicates that the jet quenching effect does not depend on the geometric shape of colliding nuclei and the quark composition of the given light mesons in (U + U), (Au + Au) and (Cu + Cu) collisions at $\sqrt{s_{NN}}$ = 192 and 200 GeV.

Fig. 3 shows a comparison of nuclear modification factors of π^0, η and K_S mesons, measured in collisions of U + U nuclei at $\sqrt{s_{NN}}$ = 192 GeV in different centrality classes.

The nuclear modification factors of π^0,

η and K_S mesons, measured in collisions of U + U nuclei at $\sqrt{s_{NN}}$ = 192 GeV, coincide within the error in the entire range of transverse momenta and in all centrality classes.

The ratios of η to π^0 meson yields (η/π^0) and of K_S to π^0 meson yields (K_S/π^0), measured in collisions of uranium nuclei at $\sqrt{s_{NN}}$ = 192 GeV, in different centrality classes are shown in Fig. 4.

The behavior of η/π^0 and K_S/π^0 ratios measured in collisions of U + U nuclei at $\sqrt{s_{NN}}$ = 192 GeV does not depend on centrality and transverse momentum within the systematic error. The ratios η/π^0 and K_S/π^0 for the spectra coincide with the previously measured ratios within statistical and systematic error [17, 18]. The fact that the η/π^0 and K_S/π^0 ratios do not depend on the collision system indicates that fragmentation of hard partons does not depend on mass and quark composition of π^0, η and K_S mesons.

Fig. 5 shows the integral nuclear modification factors of π^0, η and K_S mesons produced in collisions of uranium, gold and copper nuclei at $\sqrt{s_{NN}}$ = 192 and 200 GeV [8, 14, 16–18]. The behavior of integral nuclear modification factors of π^0, η, and K_S mesons produced in collisions of U + U nuclei as functions of $\langle N_{part}\rangle$ does not differ, within the systematic error, from the behavior of integral nuclear modification factors of π^0, η and K_S mesons produced in collisions of Cu + Cu and Au + Au nuclei.

Conclusion

We have measured the invariant spectra of K_S meson production as function of transverse momentum in four centrality classes and the nuclear modification factors of K_S mesons in three centrality classes in collisions of uranium nuclei (U + U) at $\sqrt{s_{NN}}$ = 192 GeV.

Coinciding nuclear modification factors for the K_S mesons produced in collisions of uranium nuclei at $\sqrt{s_{NN}}$ = 192 GeV, gold and copper at $\sqrt{s_{NN}}$ = 200 GeV, with an equal average number of inelastic nucleon-nucleon collisions in the entire measured range of transverse momenta in all centrality classes indicates the absence of the jet quenching effect does not depend on the shape of colliding nuclei. A similar behavior of nuclear modification factors is observed in particles with a different quark composition (π^0 and η mesons) [8].

The behavior of the η/π^0 and K_S/π^0 ratios and the integral nuclear modification factors of π^0, η and K_S mesons indicates that fragmentation of hard partons does not depend on mass and composition of quarks of π^0, η and K_S mesons produced in collisions of U + U nuclei at $\sqrt{s_{NN}}$ = 192 GeV.

Measurements performed in (U + U) collisions at $\sqrt{s_{NN}}$ = 192 GeV for π^0, η and K_S mesons confirm that the geometric shape of colliding nuclei has no effect on jet quenching.

The results of this study were obtained within the framework of State Task of the Ministry of Education and Science of Russian Federation 3.1498.2017/4.6.

REFERENCES

1. **Arsene I., Dearden I.G., Beavis D., et al.,** Quark gluon plasma and color glass condensate at RHIC? The perspective from the BRAHMS experiment, Nuclear Physics. A. 757 (1–2) (2005) 1–27.

2. **Back B.B., Baker M.D., Ballintijn M., et al.,** The PHOBOS perspective on discoveries at RHIC, Nuclear Physics. A. 757 (1–2) (2005) 28–101.

3. **Adcox K., Adler S.S., Afanasiev S., et al.,** Formation of dense partonic matter in relativistic nucleus-nucleus collisions at RHIC: experimental evaluation by the PHENIX Collaboration, Nuclear Physics. A. 757 (1–2) (2005) 184–283.

4. **Adams J., Aggarwal M.M., Ahammed Z., et al.,** Experimental and theoretical challenges in the search for the quark gluon plasma: the STAR Collaboration's critical assessment of the evidence from RHIC collisions, Nuclear Physics. A. 757 (1–2) (2005) 184–283.

5. **Sultanov R.,** Jet measurements by ALICE at LHC, Physics of Atomic Nuclei. 78 (14) (2015) 1587–1590.

6. **Tarasov A.,** Jet quenching as a probe of the phases of QCD in relativistic nuclear collisions, Phys. Rev. C. 76 (5) (2007) 054902.

7. **Betz B.,** Jet quenching in relativistic heavy ion collisions, B. Eur. Phys. J.A. Ser. 48 (164) (2012) 1434–6001.

8. **Berdnikov A.Ya., Berdnikov Ya.A., Zharko S.V., et al.,** Experimental study of pion production in U + U interactions at 192 GeV, Bulletin of the Russian Academy of Sciences: Physics. 82 (10) (2018) 1262–1265.

9. **Tanabashi M., Hagiwara K., Hikasa K., et al.**, Review of particle physics, Physical Review, D. 98 (3) (2018) 030001.

10. **Iordanova A.,** U+U and Cu+Au results from PHENIX, Journal of Physics: Conference

Series. 458 (Aug) (2013) 012004.

11. **Allen M., Bennett M. J., Bobrek M., et al.,** PHENIX inner detectors, Nuclear Instruments and Methods in Physics Research, Section A: Accelerators, Spectrometers, Detectors and Associated Equipment. 499 (2–3) (2003) 549–559.

12. **Miller M.L., Reygers K., Sanders S.J., et al.,** Glauber modeling in high-energy nuclear collisions, Annual Review of Nuclear and Particle Science. 57 (2007) 205–243.

13. **Aphecetche L., Awes T.C., Banning J., et al.,** PHENIX calorimeter, Nuclear Instruments and Methods in Physics Research, Section A: Accelerators, Spectrometers, Detectors and Associated Equipment. 499 (2–3) (2003) 521–536.

14. **Berdnikov A.Ya., Berdnikov Ya.A., Kotov D.O., et al.,** Nuclear modification factors of π^0 and η mesons in U + U collisions at $\sqrt{s_{NN}}$ = 192 GeV, Journal of Physics: Conference Series. 1135 (2018) 012046.

15. **Adler S.S. Afanasiev S., Aidala C., et al.** (PHENIX Collaboration), PHENIX on-line and off-line computing, Nuclear Instruments and Methods in Physics Research, Section A: Accelerators, Spectrometers, Detectors and Associated Equipment. 499 (2–3) (2003) 593–602.

16. **Adare A. Afanasiev S., Aidala C., et al.** (PHENIX Collaboration), Production of ω mesons in $p+p$, d + Au, Cu + Cu and Au + Au collisions at $\sqrt{s_{NN}}$ = 200 GeV, Physical Review. C. 84 (4) (2011) 044902.

17. **Adare A., Afanasiev S., Aidala C., et al.** (PHENIX Collaboration), Measurement of K_{S0} and K^*_0 in $p+p$, d+Au, and Cu+Cu collisions at $\sqrt{s_{NN}}$ = 200 GeV, Physical Review. C. 90 (5) (2014) 054905.

18. **Adler S.S., Afanasiev S., Aidala C., et al.** (PHENIX Collaboration), High transverse momentum η meson production in $p+p$, d+Au, and Au+Au collisions at $\sqrt{s_{NN}}$ = 200 GeV, Physical Review, C. 75 (2) (2007) 024909.

19. **Adare A., Aidala C., Ajitanand N.N., et al.** (PHENIX Collaboration), Forward J/ψ production in U+U collisions at $\sqrt{s_{NN}}$ = 193 GeV, Physical Review. C. 93 (3) (2016) 034903.

Received 20.03.2019, accepted 01.04.2019.

THE AUTHORS

RADZEVICH Pavel V.
Peter the Great St. Petersburg Polytechnic University
29 Politechnicheskaya St., St. Petersburg, 195251, Russian Federation
radzevichp@gmail.com

BERDNIKOV Alexander Ya.
Peter the Great St. Petersburg Polytechnic University
29 Politechnicheskaya St., St. Petersburg, 195251, Russian Federation
alexber@phmf.spbstu.ru

BERDNIKOV Yaroslav A.
Peter the Great St. Petersburg Polytechnic University
29 Politechnicheskaya St., St. Petersburg, 195251, Russian Federation
berdnikov@spbstu.ru

ZHARKO Sergei V.
Peter the Great St. Petersburg Polytechnic University
29 Politechnicheskaya St., St. Petersburg, 195251, Russian Federation
zharkosergey94@gmail.com

KOTOV Dmitry O.
Peter the Great St. Petersburg Polytechnic University
29 Politechnicheskaya St., St. Petersburg, 195251, Russian Federation
dmitriy.kotov@gmail.com

СПИСОК ЛИТЕРАТУРЫ

1. **Arsene I., Dearden I.G., Beavis D., et al.** Quark gluon plasma and color glass condensate at RHIC? The perspective from the BRAHMS experiment // Nuclear Physics A. 2005. Vol. 757. No. 1–2. Pp. 1–27.

2. **Back B.B., Baker M.D., Ballintijn M., et al.** The PHOBOS perspective on discoveries at RHIC // Nuclear Physics A. 2005. Vol. 757. No. 1–2. Pp. 28–101.

3. **Adcox K., Adler S.S., Afanasiev S., et al.** Formation of dense partonic matter in relativistic nucleus-nucleus collisions at RHIC: experimental evaluation by the PHENIX Collaboration // Nucl. Phys. A. 2005. Vol. 757. No. 1–2. Pp. 184–283.

4. **Adams J., Aggarwal M.M., Ahammed Z., et al.** Experimental and theoretical challenges in the search for the quark gluon plasma: the STAR Collaboration's critical assessment of the evidence from RHIC collisions // Nuclear Physics A. 2005. Vol. 757. No. 1–2. Pp. 184–283.

5. **Sultanov R.** Jet measurements by ALICE at LHC// Physics of Atomic Nuclei. 2015. Vol. 78. No.14. Pp. 1587–1590.

6. **Tarasov A.** Jet quenching as a probe of the phases of QCD in relativistic nuclear collisions // Phys. Rev. C. 2007. Vol. 76. No. 5. P. 054902.

7. **Betz B.** Jet quenching in relativistic heavy ion collisions // B. Eur. Phys. J.A. 2012. Vol. 48. No. 164. Pp. 1434–6001.

8. **Бердников А.Я., Бердников Я.А., Жарко С.В., Котов Д.О., Радзевич П.В.** Экспериментальные исследования рождения π-мезонов в (U + U)-взаимодействиях при энергии 192 Гэв // Известия РАН. Сер. физическая. 2018. **Т**. 82. № 10. **С**. 1391–1394.

9. **Tanabashi M., Hagiwara K., Hikasa K., et al.** Review of particle physics // Physical Review. D. 2018. Vol. 98. No. 3. P. 030001.

10. **Iordanova A.** U+U and Cu+Au results from PHENIX // Journal of Physics: Conference Series. 2013. Vol. 458. P. 012004.

11. **Allen M., Bennett M. J., Bobrek M., et al.** PHENIX inner detectors // Nuclear Instruments and Methods in Physics Research. Section A: Accelerators, Spectrometers, Detectors and Associated Equipment. 2003. Vol. 499. No. 2–3. Pp. 549–559.

12. **Miller M.L., Reygers, K., Sanders S. J., et al.** Glauber modeling in high-energy nuclear collisions // Annual Review of Nuclear and Particle Science. 2007. Vol. 57. Pp. 205–243.

13. **Aphecetche L., Awes T.C., Banning J., et al.** PHENIX calorimeter // Nuclear Instruments and Methods in Physics Research. Section A: Accelerators, Spectrometers, Detectors and Associated Equipment. 2003. Vol. 499. No. 2–3. Pp. 521–536.

14. **Berdnikov A.Ya., Berdnikov Ya.A., Kotov D.O., Radzevich P.V., Zharko S.V.** Nuclear modification factors of π^0 and η mesons in U+U collisions at $\sqrt{s_{NN}}$ = 192 GeV // Journal of Physics: Conference Series. 2018. Vol. 1135. P. 012046.

15. **Adler S.S. Afanasiev S., Aidala C., et al.** (PHENIX Collaboration). PHENIX on-line and off-line computing // Nuclear Instruments and Methods in Physics Research. Section A: Accelerators, Spectrometers, Detectors and Associated Equipment. 2003. Vol. 499. No. 2–3. Pp. 593–602.

16. **Adare A., Afanasiev S., Aidala C., et al.** (PHENIX Collaboration). Production of ω mesons in $p + p$, d + Au, Cu + Cu and Au + Au collisions at $\sqrt{s_{NN}}$ = 200 GeV // Physical Review. C. 2011. Vol. 84. No. 4. P. 044902.

17. **Adare A., Afanasiev S., Aidala C., et al.** (PHENIX Collaboration). Measurement of K_{S0} and K_{*0} in $p + p$, d + Au, and Cu + Cu collisions at $\sqrt{s_{NN}}$ = 200 GeV // Physical Review. C. 2014. Vol. 90. No. 5. P. 054905.

18. **Adler S.S., et al.** (PHENIX Collaboration). High transverse momentum η meson production in $p + p$, d + Au and Au + Au collisions at $\sqrt{s_{NN}}$ = 200 GeV // Phys. Rev. C. 2007. Vol. 75. No. 2. P. 024909.

19. **Adare A., Aidala C., Ajitanand N.N., et al.** (PHENIX Collaboration). Forward J/ψ production in U+U collisions at $\sqrt{s_{NN}}$ = 193 GeV. Phys9 ical Review. C. 2016. Vol. 93. No. 3 P. 034903.

Статья поступила в редакцию 20.03.2019, принята к публикации 01.04.2019.

СВЕДЕНИЯ ОБ АВТОРАХ

РАДЗЕВИЧ Павел Владиславович – *аспирант кафедры экспериментальной ядерной физики Санкт-Петербургского политехнического университета Петра Великого.*
195251, Российская Федерация, г. Санкт-Петербург, Политехническая ул., 29
radzevichp@gmail.com

БЕРДНИКОВ Александр Ярославич – *кандидат физико-математических наук, доцент кафедры экспериментальной ядерной физики Санкт-Петербургского политехнического университета Петра Великого.*
195251, Российская Федерация, г. Санкт-Петербург, Политехническая ул., 29
alexber@phmf.spbstu.ru

БЕРДНИКОВ Ярослав Александрович – *доктор физико-математических наук, профессор, заведующий кафедрой экспериментальной ядерной физики Санкт-Петербургского политехнического университета Петра Великого.*
195251, Российская Федерация, г. Санкт-Петербург, Политехническая ул., 29
berdnikov@spbstu.ru

ЖАРКО Сергей Вячеславович – *ассистент кафедры экспериментальной ядерной физики Санкт-Петербургского политехнического университета Петра Великого.*
195251, Российская Федерация, г. Санкт-Петербург, Политехническая ул., 29
zharkosergey94@gmail.com

КОТОВ Дмитрий Олегович – *кандидат физико-математических наук, доцент кафедры экспериментальной ядерной физики Санкт-Петербургского политехнического университета Петра Великого.*
195251, Российская Федерация, г. Санкт-Петербург, Политехническая ул., 29
dmitriy.kotov@gmail.com

DOI: 10.18721/JPM.12210
УДК 539.12

ASYMPTOTIC EFFECTS IN DIJET PRODUCTION IN PROTON-PROTON COLLISIONS AT EXTREMELY HIGH ENERGIES

A.Yu. Egorov, Ya.A. Berdnikov

Peter the Great St. Petersburg Polytechnic University, St. Petersburg, Russian Federation

In the paper, the scope for the search of the Balitsky–Fadin–Kuraev–Lipatov (BFKL) evolution effects at future proton-proton colliders at center-of-mass energies of 14, 27 and 100 TeV has been analyzed for processes of dijets production with a large jet separation in rapidity at a dijet. Simulation of proton-proton collisions using Monte Carlo calculations performed with generator packages PYTHIA8 and HERWIG++ based on Dokshitzer–Gribov–Lipatov–Altarelli–Parisi evolution and with generator package HEJ+ARIADNE based on BFKL approach was carried out. The simulation observations pointed to a promise to reveal the BFKL effects experimentally under conditions established at future proton-proton colliders.

Keywords: quantum chromodynamics, BFKL approach, dijet production; large rapidity

Citation: Egorov A.Yu., Berdnikov Ya.A., Asymptotic effects in dijet production in proton-proton collisions at extremely high energies, St. Petersburg Polytechnical State University Journal. Physics and Mathematics. 12 (2) (2019) 118–125. DOI: 10.18721/JPM.12210

АСИМПТОТИЧЕСКИЕ ЭФФЕКТЫ ПРИ РОЖДЕНИИ ПАР АДРОННЫХ СТРУЙ В ПРОТОН-ПРОТОННЫХ СТОЛКНОВЕНИЯХ ПРИ СВЕРХВЫСОКИХ ЭНЕРГИЯХ

А.Ю. Егоров, Я.А. Бердников

Санкт-Петербургский политехнический университет Петра Великого,
Санкт-Петербург, Российская Федерация

В работе проанализированы возможности поиска эффектов эволюции Балицкого – Фадина – Кураева – Липатова (БФКЛ) на будущих протон-протонных коллайдерах при максимальных энергиях в системе центра масс протонов 27 ,14 и 100 ТэВ в процессах рождения пар адронных струй с большим разделением по быстроте между струями в паре. Выполнено моделирование протон-протонных столкновений в программных пакетах Монте-Карло, основанных на эволюции Докшицера – Грибова – Липатова – Альтарелли – Паризи PYTHIA8 и HERWIG++, а также в программном пакете HEJ+ARIADNE, основанном на приближении БФКЛ. Результаты моделирования указали на перспективность экспериментального обнаружения эффектов БФКЛ при условиях, созданных на будущих протон-протонных коллайдерах.

Ключевые слова: квантовая хромодинамика, приближение БФКЛ, рождение пар адронных струй, большая быстрота

Ссылка при цитировании: Егоров А.Ю., Бердников Я.А. Асимптотические эффекты при рождении пар адронных струй в протон-протонных столкновениях при сверхвысоких энергиях // Научно-технические ведомости СПбГПУ. Физико-математические науки. 2019. Т. 12. № 2. С. 121–129. DOI: 10.18721/JPM.12210

Introduction

Hard collisions of partons at extremely high center-of-mass energies ($\sqrt{s} \to \infty$), large momentum transfer ($Q \to \infty$) and a fixed ratio $Q/\sqrt{s} \sim x$ (this limit is called the Bjorken limit, and x is the scaling variable) are described in terms of perturbative quantum chromodynamics within collinear factorization. This provides factorization of the hadron-hadron cross section into a hard subprocess and parton distribution functions. This kinematic mode implies summation of the diagrams amplified by large logarithms of momentum transfer, namely, the terms of the perturbative series proportional to

$$(\alpha_s(Q^2)\ln Q^2)^n,$$

where $\alpha_s(Q^2)$ is the running coupling constant of strong interaction, n is the order of the term in the perturbative series.

Such summation in all orders of perturbation theory is achieved in the leading logarithmic approximation (LLA) in the Dokshitzer–Gribov–Lipatov–Altarelli–Parisi (DGLAP) equations [1–5] describing the evolution of parton distribution functions with the scale Q. Summing the terms proportional to $[\alpha_s(Q^2)]^n[\ln Q^2]^{n-1}$ leads to DGLAP equations in the logarithmic approximation next to LLA (NLLA).

The parton scattered in a hard subprocess emits bremsstrahlung, forming a partonic shower. The parton shower can also be described in different logarithmic approximations of DGLAP splitting functions. The emitting partons are ordered by the transverse momentum $p_\perp$, while preserving the same order of rapidity y:

$$y = 1/2\ln[(E + p_z)/(E - p_z)],$$

where E is the parton energy, p_z is the longitudinal momentum (momentum along the beam of colliding hadrons).

Parton shower and hadronization lead to production of jets. Inclusive production of jets agrees well with calculations in the framework of NLLA DGLAP approach in a wide range of transverse momenta, for all experimentally available energies currently obtained in the HERA (DESY, Germany) and Tevatron (Fermilab, USA) accelerators and in the Large Hadron Collider (LHC, CERN, Switzerland). However, agreement with the experiment deteriorates if jets are largely separated in rapidity [6].

When the collision energy $\sqrt{s}$ of the center-of-mass system tends to infinity, i.e., greatly exceeds the finite scale Q of hard interaction, such that $Q/\sqrt{s} \sim x \to 0$ (the Regge–Gribov limit), hard partons scatter at large rapidities y, while parton emission increases rapidly with an increase in the phase space accessible in rapidity. Such dynamics is due to diagrams enhanced by large logarithms:

$$\ln s \sim \ln(1/x).$$

Summation of these logarithms was obtained in LLA and NLLA in the Balitsky–Fadin–Kuraev–Lipatov (BFKL) evolution equations [7–9].

Searches for BFKL evolution in production of jets in proton-proton collisions were previously carried out at the Tevatron in the D0 experiment [10–12] for the energies $\sqrt{s}$ = 630 and 1800 GeV, and also at the LHC in the ATLAS [13, 14] and CMS [6, 15 – 17] experiments for the energy $\sqrt{s}$ = 7 TeV, reached in LHC Run I. While DGLAP evolution was well confirmed in the experiment in the Bjorken limit (high center-of-mass energies and large momentum transfers), experiments on searches for BFKL evolution which should dominate in semi-hard processes (high center-of-mass energies and moderate momentum transfers) have not yielded any definitive results. There are several reasons for this. For one, no Monte Carlo generator can currently simulate BFKL evolution in NLLA and no generator can run pure simulation in the DGLAP approximation. Existing Monte Carlo generators based on DGLAP equations include phenomenological model corrections partially simulating the BFKL effects such as color coherence phenomena, angular ordering in parton cascades and dipole parton showers. Additional uncertainty in searches for BFKL evolution is the theoretical uncertainty regarding the energy scale $\sqrt{s_0}$ on which the BFKL effects become dominant. Therefore, energies that are the most readily accessible experimentally are required to search for such effects.

In this study, we used Monte Carlo simulation to consider possible searches for BFKL effects at future hadron colliders at maximum center-of-mass energies, namely, $\sqrt{s}$ = 14 TeV. This is the nominal energy of the Large Hadron Collider (LHC), which it should reach in Run III. Energies $\sqrt{s}$ = 27 and 100 TeV, which are, respectively, the energy of the planned HE-LHC (High-Energy Large Hadron Collider) [18] and the planned FCC (Future Circular Collider), are also of interest [19].

Monte Carlo generators used

We used Monte Carlo generators based on DGLAP evolution and BFKL evolution to simulate proton collisions. The first type includes the PYTHIA8 (8153) generator [20] with Tune 4C [21] and the HERWIG++ (2.7.1) generator [22] with Tune UE-EE-3C [23]. The generators compute matrix elements in leading order of perturbation theory, refined by taking into account the parton shower in LLA DGLAP. The difference between the PYTHIA8 and HERWIG++ generators is that they use different phenomenological models for simulating parton showers and hadronization.

What is important for the purposes of this study is that these generators use different methods for accounting for color coherence effects in parton cascades, which partially emulate BFKL evolution:

PYTHIA8 uses a *dipole* cascade, ordered by *transverse momentum*;

HERWIG++ uses a *parton* cascade ordered by *angle*.

These effects only partially account for the dynamics of BFKL. The Monte Carlo simulation based on LLA BFKL was performed with the HEJ generator (1.4.0) [24] at the parton level. Hadronization at the parton level was performed with the ARIADNE (4.12J01) generator [25]. Predictions based on LLA BFKL are referred to as HEJ+ARIADNE below.

Simulations with Monte Carlo generators give predictions at the hadron level. Hadrons in the final state can produce jets carrying information about the parton subprocess. Infrared and collinear-safe cluster algorithms, including the anti-kT algorithm are considered to be the best for reconstructing jets [26]. The anti-kT algorithm used in our study was implemented in the FASTJET software package [27]. The value of the jet size parameter was chosen to be 0.5 in the space with pseudorapidty η and azimuthal angle ϕ. Pseudorapidity η is a dimensionless physical quantity:

$$\eta = -\ln[\mathrm{tg}(\theta/2)],$$

where θ is the azimuthal angle.

The selected parameter value corresponds to that used in measurements at the LHC with the center-of-mass energy $\sqrt{s} = 7$ TeV [15].

Observables sensitive to BFKL effects

One of the main difficulties in detecting BFKL effects is in selecting a value that can be actually measured conveniently. It was found in [28] for proton collisions that measurement of the cross section for production of dijets with large separation in rapidity is sensitive to BFKL effects. In this case, a pair of jets with the highest and lowest rapidities ($y_{\max}$ and $y_{\min}$) among the jets produced in a proton-proton collision, with transverse momenta above a certain threshold ($p_{\wedge} \geq p_{\wedge\min}$), is called a Mueller–Navelet (MN) dijet. The BFKL approximation was used in the study to calculate the ratio of the production cross section for an MN dijet to the Born cross section (MN K factor).

Notably, the K factor is defined as the ratio of the cross section calculated in higher orders of perturbation theory to the Born cross section. However, it is virtually impossible to measure the Born cross section, since it is impossible to kinematically forbid the virtual corrections. Nevertheless, an "exclusive" dijet cross section, i.e., the cross section of the process producing strictly two jets with transverse momenta above the threshold $p_{\perp\min}$, can be measured instead of the Born cross section.

The inclusive K factor, that is, the ratio of inclusive cross section for production of a dijet to the Born cross section, was calculated in [29] in framework of BFKL theory. All jets with transverse momenta above the threshold $p_{\perp\min}$ make pairwise contributions to the inclusive cross section for production of dijets. It seems preferable to measure the inclusive cross section for production of dijets rather than the MN cross section, since the rapidity of an MN dijet may fall beyond the detector's acceptance at high center-of-mass energies [29].

Notably, searches for BFKL effects should be performed at the highest possible center-of-mass energy and, at the same time, the lowest possible threshold $p_{\perp\min}$ for the transverse momentum. A lower cutoff is imposed on the transverse momentum of the jets in experimental measurements. The detector should be capable of detecting jets with large rapidities, because colliding beams cross at small angles. For example, the ATLAS measurements [13, 14] detected dijet observables sensitive to BFKL effects for the average pair transverse momentum

$$\langle p_\perp \rangle = (p_{\perp 1} + p_{\perp 2})/2 > 50(60)\ \mathrm{GeV}$$

with rapidity separation up to

$$\Delta y = |y_1 - y_2| = 6(8),$$

where y_1, y_2 are the dijet rapidities.

On the other hand, the CMS experiment [15–16] measured dijets with transverse momenta $p_\perp \geq 35$ GeV and rapidity separation

Δy = 9.4. Thus, CMS measurements are more sensitive to possible BFKL effects.

Ref. [16] reported on using the CMS detector to measure the quantities R^{incl} and R^{MN}, the ratios of cross sections for dijet production in proton-proton collisions at $\sqrt{s}$ = 7 TeV as functions of separation in rapidity Δy:

$$R^{incl} = \sigma^{incl}/\sigma^{excl}, \quad R^{MN} = \sigma^{MN}/\sigma^{excl}, \qquad (1)$$

where σ^{incl} is the inclusive cross section for dijet production with the transverse momentum $p_\perp \geq$ 35 GeV; σ^{excl} is the "exclusive" section for dijet production; σ^{MN} is the MN cross section for dijet production (MN dijet is a pair of jets with maximum separation in rapidity among the jets with transverse momenta $p_\perp \geq 35$ GeV produced in the event).

Events producing a single dijet with the transverse momentum $p_\perp \geq 35$ GeV contribute to the "exclusive" cross section. Measurement results were compared with Monte Carlo predictions in [15]. The predictions were obtained with the same generators that we used in this study. It was established in [15] that the PYTHIA8 (4C) generator adequately describes the experimental data, while HERWIG++ (UE-EE-3C) overestimates them in the region of large rapidities. The HEJ+ARIADNE generator considerably overestimates the experimental data. However, since LLA BFKL predicts a stronger rise in cross sections that actually observed, it is important to take into account the contribution of NLLA BFKL, which is known to predict a slower rise in cross sections.

Computational results and discussion

We carried out predictive calculations of quantities (1) by the Monte Carlo method as functions of rapidity separation $\Delta y = |y_1 - y_2|$, (y_1 and y_2 are the rapidities of the first and second jets in the dijet) with different generators (see the section "Monte Carlo generators used" for the description) for proton-proton collisions with energies $\sqrt{s}$ = 14, 27 and 100 TeV, accessible for future colliders. We used the PYTHIA8 (4C) and HERWIG++ (UE-EE-3C) models, calculating matrix elements in leading order of perturbation theory, matched to LLA DGLAP parton showers, and the HEJ+ARIADNE model, based on LLA BFKL. The jets were reconstructed using an anti-kT algorithm with the jet size of 0.5. The calculation results are shown in Fig. 1.

The dependences obtained for the ratios of cross sections for dijet production R^{incl} and R^{MN} versus rapidity separation $\Delta y = |y_1 - y_2|$ in the dijets have the predicted form. R^{incl} and R^{MN} were observed to increase with increasing rapidity separation Δy, which is associated with the phase space extending for emission of additional jets and with dynamic effects. The ratios decrease at the largest rapidity intervals, which is associated with kinematic restrictions imposed on production of jets with transverse momenta above the threshold $p_{\perp min}$ = 35 GeV, in addition to "exclusive" dijets. The ratios should equal unity with the maximum value of Δy, when all center-of-mass energy has been spent on production of an "exclusive" dijet.

The phase space available with respect to Δy extends with increasing center-of-mass energy. The maximum of the ratios is shifted towards large rapidity intervals.

Calculations with the HEJ+ARIADNE generator (based on LLA BFKL) predict considerably stronger rise of the rations with rapidity separation Δy, than calculations with the PYTHIA8 and HERWIG++ generators. However, LLA BFKL calculations can produce overestimated values for cross section rise.

Analyzing the results obtained using HEJ+ARIADNE, we concluded that a faster rise of ratios with the center-of-mass energy $\sqrt{s}$ is predicted in this case than when using the PYTHIA8 and HERWIG ++ generators. Consequently, an increase in the interaction energy makes the measurements more sensitive to BFKL effects.

The dynamics of DGLAP equations has no evolution in rapidity. Emission of partons (hadron jets) should be equally probable over the entire range of rapidities. Therefore, the cross section ratios should remain constant over the entire range of rapidities. The observed increase in the values calculated using the PYTHIA8 and HERWIG ++ generators (based on DGLAP) may be due to the phase space extending and to the phenomena partially emulating the BFKL effects, such as color coherence, angular ordering in the parton cascade and dipole cascade. The difference in the predictions obtained using the PYTHIA8 and HERWIG++ generators is because they are based on different color coherence models, in the first case, a dipole cascade ordered by transverse momentum, and in the second case, a parton cascade ordered by angle.

The obtained results indicate that these models predict different behavior of the calculated values with increasing center-of-mass energies. A stronger rise of ratios is predicted in the first case than in the second. Notably, the models taking into account color coherence were introduced into the calculations in DGLAP-based

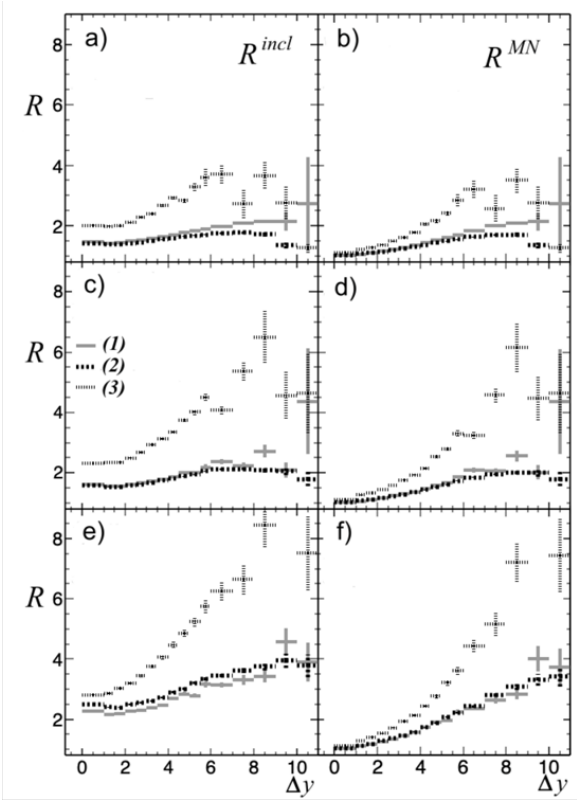

Fig. 1. Calculated R^{incl} (*a*, *c*, *e*) and R^{MN} (*b*, *d*, *f*) as functions of rapidity separation Δy in dijet events, with different energies $\sqrt{s_{NN}}$, TeV: 14 (*a*, *b*), 27 (*c*, *d*), 100 (*e*, *f*). Transverse momentum of jets: $p_\perp \geq 35$ GeV.
The generators used were HERWIG++ (*1*), PYTHIA8 (*2*) and HEJ+ARIADNE (*3*).

generators in order to improve agreement with the experiment in central rapidity regions, i.e., for calculations with small corrections. The simulation results demonstrated the unstable behavior of these corrections at large rapidities and high center-of-mass energies.

Comparing the ratios of R^{incl} and R^{MN}, we can conclude that the first of these quantities always exceeds the second, lying well above the second for small rapidity intervals and becoming comparable for large ones. A possible explanation for this is that MN dijets constitute a subset of inclusive pairs. Both MN dijets and pairwise combinations of jets lying in the rapidity interval between MN jets contribute to the inclusive cross section for dijet production. As follows from the results obtained, the rapidity interval in an MN pair can reach $\Delta y > 11$ at extremely high energies. These events are the most sensitive to BFKL effects. However, they are rather difficult to detect experimentally. At the same time, these events can contribute to the inclusive cross section due to jets produced together with an MN dijet, ordered by rapidity with smaller rapidity intervals.

Thus, inclusive cross sections for dijet production should be preferred in searches for BFKL effects at extremely high energies.

Conclusion

The simulation results obtained indicate that experimental searches for BFKL effects at future proton-proton colliders may be a promising endeavor.

More definitive and clear conclusions regarding the manifestation of BFKL effects can be drawn by obtaining pure predictions based on evolution of DGLAP without corrections partially emulating the BFKL effects. Furthermore, both analytical computations and Monte Carlo estimates should be developed based on BFKL evolution in the logarithmic approximation next to LLA (NLLA).

The results of this study were obtained within the framework of State Task of the Ministry of Education and Science of Russian Federation 3.1498.2017/4.6.

REFERENCES

1. **Gribov V.N., Lipatov L.N.,** Deep inelastic *e p* scattering in perturbative theory, Sov. J. Nucl. Phys. 15 (4) (1972) 438–450.

2. **Gribov V. N., Lipatov L.N.,** e^+ e^- pair annihilation and deep inelastic *e p*-scattering in perturbation theory, Yadern. Fiz. 15 (6) (1972) 1218–1237.

3. **Lipatov L.N.,** The parton model and perturbation theory, Sov. J. Nucl. Phys. 20 (1) (1974) 94–102.

4. **Altarelli G., Parisi G.,** Asymptotic freedom in parton language, Nuclear Physics, B. 126 (2) (1977) 298–318.

5. **Dokshitzer Y.L.,** Calculation of the structure functions for deep inelastic scattering and *e*+ *e*– annihilation by perturbation theory in quantum chromodynamics, Journal of Experimental and Theoretical Physics. 73 (4) (1977) 1216–1240.

6. **Chatrchyan S., Khachatryan V., Sirunyan A.M., et al.,** Measurement of the inclusive production cross sections for forward jets and for dijet events with one forward and one central jet in *pp* collisions at $\sqrt{s}$ = 7 TeV, Journal of High Energy Physics. 2012 (6) (2012) 36, 1–37.

7. **Kuraev E.A., Lipatov L.N., Fadin V.S.,** Multi-reggeon processes in Yang-Milles theory, Journal of Experimental and Theoretical Physics. 43 (3) (1976) 443–443.

8. **Kuraev E.A., Lipatov L.N., Fadin V.S.** Pomeranchuk singularity in non-abelian gauge theories, Journal of Experimental and Theoretical Physics. 72 (2) (1977) 377–389.

9. **Balitsky I.I., Lipatov L.N.,** The Pomeranchuk singularity in quantum chromodynamics, Sov J. Nucl. Phys. 28 (7) (1978) 822–829.

10. **Abachi S. et al.** (D0 Collaboration), Azimuthal decorrelation of jets widely separated in rapidity, Physical Review Letters. 77 (4) (1996) 595–600.

11. **Abbott B. et al.** (D0 Collaboration), Probing Balitsky-Fadin-Kuraev-Lipatov dynamics in the dijet cross section at large rapidity intervals in pp^- collisions at $\sqrt{s}$ = 1800 and 630 GeV, Physical Review Letters. 84 (25) (2000) 5722–5727.

12. **Abbott B. et al.** (D0 Collaboration), Probing hard color-singlet exchange in $p\bar{p}$ collisions at $\sqrt{s}$ = 630 GeV and 1800 GeV, Physics Letters, B. 440 (1–2) (1998) 189–202.

13. **Aad G., Abbott B., Abdallah J., et al.** (The ATLAS Collaboration), Measurement of dijet production with a veto on additional central jet activity in pp collisions at $\sqrt{s}$ = 7 TeV using the ATLAS detector, Journal of High Energy Physics. 2011 (9) (2011) 1–53.

14. **Aad G., Abbott B., Abdallah J., et al.** (The ATLAS Collaboration) Measurements of jet vetoes and azimuthal decorrelations in dijet events produced in *pp* collisions at root *s* = 7 TeV using the ATLAS detector, The European Physical Journal, C. 74 (11) (2014) 3117, 1–27.

15. **Chatrchyan S., Khachatryan V., Sirunyan A.M., et al** (The CSM Collaboration), Ratios of dijet production cross sections as a function of the absolute difference in rapidity between jets in proton-proton collisions at $\sqrt{s}$ = 7 TeV, The European Physical Journal, C. 72 (11) (2012) 2216–2234.

16. **Khachatryan V., Sirunyan A.M., Tumasyan A., et al.** (The CSM Collaboration), Azimuthal decorrelation of jets widely separated in rapidity in *pp* collisions at $\sqrt{s}$ = 7 TeV, Journal of High Energy Physics. 2016 (8) (2016) 139, 1–40.

17. **Sirunyan A.M., Tunasyan A., Adam W., et al.** (The CSM Collaboration), Study of dijet events with a large rapidity gap between the two leading jets in *pp* collisions at $\sqrt{s}$ = 7 TeV, The European Physical Journal, C. 78 (3) (2018) 242– 282.

18. **Zimmermann F. et al.,** Future circular collider study, Vol. 4: The high energy LHC (HE-LH), Tech. Rep. CERN-ACC-2018-0059, CERN, Geneva, 2018.

19. **Benedikt M. et al.,** Future circular collider: Vol. 3: The Hadron Collider (FCC-hh), No. CERN-ACC-2018-0058, 2018.

20. **Sjцstrand T., Mrenna S., Skands P.**, A brief introduction to PYTHIA 8.1, Computer Physics Communications. 178 (11) (2008) 852–867.

21. **Corke R., Sjцstrand T.,** Interleaved parton showers and tuning prospects, Journal of High Energy Physics. 2011 (3) (2011) 32, 1–51.

22. **Bähr M. et al.,** Herwig++ physics and manual, The European Physical Journal C. 58 (4) (2008) 639–707.

23. **Gieseke S. et al.,** Herwig++ 2.5 release note, arXiv preprint arXiv:1102. 1672, 2011.

24. **Andersen J.R., Smillie J.M.** Multiple jets at the LHC with high energy jets, Journal of High Energy Physics. 2011 (6) (2011) 10, 10–47.

25. **Lцnnblad L.,** ARIADNE version 4 –

A program for simulation of QCD cascades implementing the color dipole model, Comput. Phys. Commun. 71 (1–2) (1992) 15–31.

26. **Cacciari M., Salam G.P., Soyez G.,** The anti-*kt* jet clustering algorithm, Journal of High Energy Physics. 2008 (4) (2008) 63, 1 – 13.

27. **Cacciari M., Salam G. P., Soyez G.,** FastJet user manual, The European Physical Journal, C. 72 (3) (2012) 1896–1950.

28. **Mueller A.H., Navelet H.,** An inclusive minijet cross section and the bare pomeron in QCD, Nuclear Physics, B. 282 (1987) 727–744.

29. **Kim V.T., Pivovarov G. B.,** Balitskiĭ-Fadin-Kuraev-Lipatov QCD pomeron in high energy hadron collisions: Inclusive dijet production, Physical Review, D. 53 (1) (1996) 6–10.

Received 20.03.2019, accepted 01.04.2019.

THE AUTHORS

EGOROV Anatoliy Yu.
Peter the Great St. Petersburg Polytechnic University
29 Politechnicheskaya St., St. Petersburg, 195251, Russian Federation
egorov.a@spbstu.ru

BERDNIKOV Yaroslav A.
Peter the Great St. Petersburg Polytechnic University
29 Politechnicheskaya St., St. Petersburg, 195251, Russian Federation
berdnikov@spbstu.ru

СПИСОК ЛИТЕРАТУРЫ

1. **Грибов В.Н., Липатов Л.Н.** Глубоко неупругое *ep*-рассеяние в теории возмущений // Ядерная физика. 1972. Т. 15. № 4. С. 781–807.

2. **Грибов В.Н., Липатов Л.Н.** Аннигиляция e^+e^--пар и глубоко неупругое *ep*-рассеяние в теории возмущений // Ядерная физика. 1972. Т. 6 № .15. С. –1218 1237.

3. **Липатов Л.Н.** Партонная модель и теория возмущений // Ядерная физика. 1974. Т. 20. № 1 С. 181–198.

4. **Altarelli G., Parisi G.** Asymptotic freedom in parton language //Nuclear Physics. B. 1977. Vol. 126. No. 2. Pp. 298–318.

5. **Докшицер Ю.Л.** Вычисление структурных функций для глубоконеупругого рассеяния и e^+ e^- ании гиляции в теории возмущений квантовой хромодинамики // ЖЭТФ. 1977. Т. 73. № 4. С. 1216–1249.

6. **Chatrchyan S., Khachatryan V., Sirunyan A.M., et al.** Measurement of the inclusive production cross sections for forward jets and for dijet events with one forward and one central jet in *pp* collisions at $\sqrt{s}$ = 7 TeV // Journal of High Energy Physics. 2012. Vol. 2012. No. 6. P. 36. Pp. 1–37.

7. **Кураев Е.А., Липатов Л.Н., Фадин В.С.** Мультиреджеонные процессы в теории Янга – Миллса // ЖЭТФ. 1976. Т. 3 № .43. С. 855–840.

8. **Кураев Е.А., Липатов Л.Н.,** Фадин **В.С.** Сингулярность Померанчука в неабелевых калибровочных теориях // ЖЭТФ. 1977. Т. 72. № 2. С. 377–389.

9. **Балицкий Я.Я., Липатов Л.Н.** Сингулярность Померанчука в квантовой хромодинамике // Ядерная физика. 1978. Т. 28. № 7. С. 1597–1611.

10. **Abachi S. et al.** (D0 Collaboration). Azimuthal decorrelation of jets widely separated in rapidity // Physical Review Letters. 1996. Vol. 77. No. 4. Pp. 595–600.

11. **Abbott B. et al.** (D0 Collaboration). Probing Balitsky-Fadin-Kuraev-Lipatov dynamics in the dijet cross section at large rapidity intervals in *p pÏ* collisions at $\sqrt{s}$ = 1800 and 630 GeV // Physical Review Letters. 2000. Vol. 84. No. 25. Pp. 5722–5727.

12. **Abbott B. et al.** (D0 Collaboration). Probing hard color-singlet exchange in $p\bar{p}$ collisions at root s = 630 GeV and 1800 GeV // Physics Letters. B. 1998. Vol. 440. No. 1–2. Pp. 189–202.

13. **Aad G. et al.** (The ATLAS Collaboration). Measurement of dijet production with a veto on additional central jet activity in *pp* collisions at $\sqrt{s}$ = 7 TeV using the ATLAS detector // Journal of High Energy Physics.

2011. Vol. 2011. No. 9. P. 53. Pp. 1–53.

14. **Aad G., Abbott B., Abdallah J., et al.** (The ATLAS Collaboration). Measurements of jet vetoes and azimuthal decorrelations in dijet events produced in *pp* collisions at root *s* = 7 TeV using the ATLAS detector // The European Physical Journal. C. 2014. Vol. 74. No. 11. P. 3117. Pp. 1–27.

15. **Chatrchyan S., Khachatryan V., Sirunyan A.M., et al.** (The CSM Collaboration). Ratios of dijet production cross sections as a function of the absolute difference in rapidity between jets in proton-proton collisions at $\sqrt{s}$ = 7 TeV // The European Physical Journal. C. 2012. Vol. 72. No. 11. Pp. 2216–2234.

16. **Khachatryan V., Sirunyan A.M., TuM masyan A., et al.** (The CSM Collaboration). Azimuthal decorrelation of jets widely separated in rapidity in *pp* collisions at $\sqrt{s}$ = 7 TeV // Journal of High Energy Physics. 2016. Vol. 2016. No. 8. P. 139. Pp. 1–40.

17. **Sirunyan A.M., Tunasyan A., Adam W., et al.** (The CSM Collaboration). Study of dijet events with a large rapidity gap between the two leading jets in *pp* collisions at $\sqrt{s}$ = 7 TeV // The European Physical Journal. C. 2018. Vol. 78. No. 3. Pp. 242– 282.

18. **Zimmermann F. et al.** Future circular collider study. Vol. 4. The high energy LHC (HE-LHC). Tech. Rep. CERN-ACC-2018-0059. Geneva: CERN, 2018.

19. **Benedikt M. et al.** Future circular collider. Vol. 3. The hadron collider (FCC-hh). 2018. No. CERN-ACC-2018-0058.

20. **Sjцstrand T., Mrenna S., Skands P.** A brief introduction to PYTHIA 8.1 // Computer Physics Communications. 2008. Vol. 178. No. 11. Pp. 852–867.

21. **Corke R., Sjцstrand T.** Interleaved parton showers and tuning prospects // Journal of High Energy Physics. 2011. Vol. 2011. No. 3. P. 32. Pp. 1–51.

22. **Вдhr M., Gieseke S., Gigg M. A. et al.** Herwig++ physics and manual // The European Physical Journal C. 2008. Vol. 58. No. 4. Pp. 639–707.

23. **Gieseke S., Grellscheid D., Hamilton K. et al.** Herwig++ 2.5 release note //arXiv preprint arXiv:1102.1672. 2011.

24. **Andersen J.R., Smillie J. M.,** Multiple jets at the LHC with high energy jets // Journal of High Energy Physics. 2011. Vol. 2011. No. 6. P. 10. Pp. 10–47.

25. **Lцnnblad L.** ARIADNE version 4 – A program for simulation of QCD cascades implementing the color dipole model // Comput. Phys. Commun. 1992. Vol. 71. No. 1–2. Pp. 15–31.

26. **Cacciari M., Salam G. P., Soyez G.** The anti-*kt* jet clustering algorithm // Journal of High Energy Physics. 2008. Vol. 2008. No. 4. P. 63. Pp. 1–13.

27. **Cacciari M., Salam G. P., Soyez G.** FastJet user manual // The European Physical Journal C. 2012. Vol. 72. No. 3. Pp. 1896–1950.

28. **Mueller A.H., Navelet H.** An inclusive minijet cross section and the bare pomeron in QCD // Nuclear Physics. B. 1987. Vol. 282. Pp. 727–744.

29. **Kim V.T., Pivovarov G.B.** Balitskiĭ-Fadin-Kuraev-Lipatov QCD pomeron in high energy hadron collisions: Inclusive dijet production // Physical Review. D. 1996. Vol. 53. No. 1. Pp. 6 – 10.

Статья поступила в редакцию 20.03.2019, принята к публикации 01.04.2019.

СВЕДЕНИЯ ОБ АВТОРАХ

ЕГОРОВ Анатолий Юрьевич – ассистент кафедры экспериментальной ядерной физики Санкт-Петербургского политехнического университета Петра Великого.

195251, Российская Федерация, г. Санкт-Петербург, Политехническая ул., 29

egorov.a@spbstu.ru

БЕРДНИКОВ Ярослав Александрович – доктор физико-математических наук, профессор, заведующий кафедрой экспериментальной ядерной физики Санкт-Петербургского политехнического университета Петра Великого.

195251, Российская Федерация, г. Санкт-Петербург, Политехническая ул., 29

berdnikov@spbstu.ru

DOI: 10.18721/JPM.12211
УДК 539.3

THE EXACT SOLUTION OF THE PROBLEM ON A CRACK EMERGING FROM THE TOP OF TWO DISSIMILAR WEDGES

V.V. Tikhomirov

Peter the Great St. Petersburg Polytechnic University, St. Petersburg, Russian Federation

A closed connection of two different isotropic wedges has been considered within the scope of the anti-plane problem. A finite-length crack emerges from the top of this connection at an arbitrary angle to the symmetry axis of the structure. The exact solution of the problem was obtained through the problem's reducing to the Wiener – Hopf scalar equation. The dependence of the stress intensity factor (SIF) at the crack tip on the structural parameters was studied. The effects of an increase and a decrease in SIF were compared with those known for the case of a homogeneous medium. It was shown that the stress asymptotics near the junction vertex could have one or two singular terms determining both strong and weak singularities at this singular point.

Keywords: anti-plane crack, closed bimaterial wedge; strong singularity, weak singularity

Citation: V.V. Tikhomirov, The exact solution of the problem on a crack emerging from the top of two dissimilar wedges, St. Petersburg Polytechnical State University Journal. Physics and Mathematics. 12 (2) (2019) 126–134. DOI: 10.18721/JPM.12211

ТОЧНОЕ РЕШЕНИЕ ЗАДАЧИ ДЛЯ ТРЕЩИНЫ, ВЫХОДЯЩЕЙ ИЗ ВЕРШИНЫ ДВУХ РАЗНОРОДНЫХ КЛИНЬЕВ

В.В. Тихомиров

Санкт-Петербургский политехнический университет Петра Великого,

Санкт-Петербург, Российская Федерация

В рамках антиплоской задачи рассмотрено замкнутое соединение двух различных изотропных клиньев, из вершины которого выходит трещина конечной длины под произвольным углом к оси симметрии структуры. Путем сведения проблемы к скалярному уравнению Винера – Хопфа получено ее точное решение. Изучена зависимость коэффициента интенсивности напряжений (КИН) в вершине трещины от структурных параметров. Проанализированы эффекты увеличения и уменьшения КИН, по сравнению со случаем однородной среды. Показано, что асимптотика напряжений вблизи вершины соединения может иметь одно или два сингулярных слагаемых, определяющих как сильную, так и слабую особенности в этой особой точке.

Ключевые слова: антиплоская трещина, замкнутый биматериальный клин, сильная сингулярность, слабая сингулярность

Ссылка при цитировании: Тихомиров В.В. Точное решение задачи для трещины, выходящей из вершины двух разнородных клиньев // Научно-технические ведомости СПбГПУ. Физико-математические науки. 2019. Т. 12. № 2. С. 130–139. DOI: 10.18721/JPM.12211

Introduction

Inhomogeneous structures often have singularities where geometric parameters and mechanical properties of the structure's components change radically. Such points are, for example, the edges of interfaces between several wedge-shaped structures consisting of different materials. These structures can be closed if all of their interfaces are connected, or open, if there are notches. The stresses determined by linear theory of elasticity grow without bound at corner points and, therefore, such singularity points are sources of crack propagation.

A large number of studies starting from Williams and Bogy [1, 2], focused mainly on plane problems, have considered elastic fields in bimaterial and multimaterial wedges. The class of anti-plane problems has been studied far less.

The characteristics of a stress singularity in a semi-infinite crack terminating at the interface between two or three isotropic wedges were discussed in [3–6] within the framework of the anti-plane problem. It was found that stress singularity has a power-law behavior at this point (symmetric problem), different from the classical case where the exponent is 0.5 [3, 6]. The asymptotic behavior of stresses near the vertex can contain two singular terms in the asymmetric case [5, 6].

The stress singularity at the tip of a semi-infinite longitudinal crack located in a three-component medium with functionally gradient properties was analyzed in [7], finding two real eigenvalues determining the properties of elastic fields.

A crack of finite length, emanating from the tip of a sharp notch located in a composite wedge-shaped structure, was considered in [8–11]. It was established in [8, 9] that the solution for anisotropic materials of the structure can be obtained based on the solution constructed for the isotropic case by using a linear coordinate transformation.

The critical loads at which cracks evolve at the tip of a sharp notch under anti-plane loading were estimated in [12, 13].

However, the problem of cracks emanating from a closed interface between wedge-shaped structures under anti-plane deformation still remains largely unexplored.

As a first step to solving this problem, this paper considers a crack of finite length, emanating from the top of the interface between two connected wedges composed of different materials. Its exact solution is constructed by reducing the problem to the scalar Riemann problem. An analytical representation is obtained for the stress intensity factor (SIF) at the crack tip, and its dependence on the structure parameters is studied.

Aside from its own significance, the obtained exact solution of the problem is one of the basic elements in analysis of brittle fracture based on the so-called finite fracture mechanics [14], using approximate analytical methods for plane problems due to lack of exact solutions.

Problem statement; reducing the problem to the Wiener–Hopf equation

Let us consider a rectilinear mode III crack of length ε, emanating from the top of the interface between two wedge-shaped regions (Fig. 1). The materials of the wedges are assumed to be isotropic, homogeneous, and with shear moduli μ_1 and μ_2 ($\mu_3 = \mu_2$) in the regions Ω_k ($k = 1, 2, 3$). The materials are assumed to have perfect contact. A self-balanced load $g(r)$ is applied to the edges of the crack (r is the polar radius).

The geometry of the given elastic composite can be conveniently described by two parameters: the vertex angle α ($0 < \alpha < 2\pi$) of the region Ω_1 and the angle β between the direction of the crack and the axis of symmetry of the region Ω_1. Evidently, $|\beta| \le \pi - \alpha/2$. Varying the angle β with a fixed α causes the region Ω_1 to rotate around its vertex. Thus, the angle β characterizes the mutual orientation of the crack and the region Ω_1. For example, the problem is symmetric for $\beta = 0$. An interfacial crack corresponds to the values $\beta = \pm(\pi - \alpha/2)$, and a crack emanating from the vertex along the interface to $\beta = \pm\alpha/2$.

It is known that the displacements w_k in the regions Ω_k are harmonic functions in this case:

$$\frac{\partial^2 w_k}{\partial r^2} + \frac{1}{r^2}\frac{\partial^2 w_k}{\partial \theta^2} + \frac{1}{r}\frac{\partial w_k}{\partial r} = 0 \quad (k = 1, 2, 3), \tag{1}$$

and the stresses in polar coordinates r and θ are found by the formulas

$$\tau_{\theta zk} = \frac{\mu_k}{r}\frac{\partial w_k}{\partial \theta}, \ \tau_{rzk} = \mu_k \frac{\partial w_k}{\partial r}.$$

Elastic fields at the interfaces should satisfy the conditions of perfect contact:

$$w_1 = w_2, \ \tau_{\theta z1} = \tau_{\theta z2} \text{ with } \theta = \beta + \alpha/2, \tag{2}$$
$$w_1 = w_3, \ \tau_{\theta z1} = \tau_{\theta z3} \text{ with } \theta = \beta - \alpha/2,$$

and the following mixed conditions along the crack line:

$$\tau_{\theta z2}(r, \pi) = \tau_{\theta z3}(r, -\pi) = g(r) \ (0 \le r \le \varepsilon), \tag{3}$$
$$\tau_{\theta z2}(r, \pi) = \tau_{\theta z3}(r, -\pi) = \tau(r),$$
$$w_2(r, \pi) = w_3(r, -\pi) \ (\varepsilon < r < \infty) \tag{4}$$

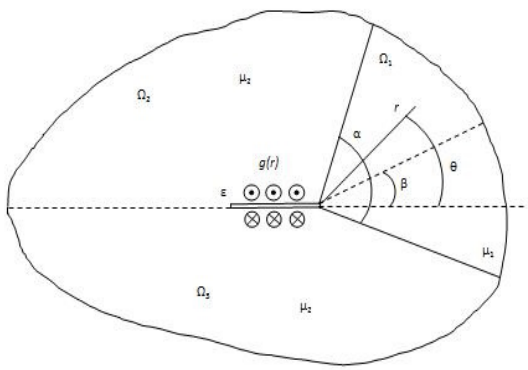

Fig. 1. Crack emanating from top of interface between two inhomogeneous wedges:
$g(r)$ is the load on the edges of the crack; μ_1 and μ_2 are the shear moduli of materials; Ω_1, Ω_2, Ω_3 are the wedge-shaped regions; ε is the distance from the top of the interface to the tip of the crack; α and β are the vertex angles of the wedges; r and θ are polar coordinates

Here $\tau(r)$ is an unknown function.

As in [15], we search for the solution to the problem in the form of Mellin integrals:

$$w_k(r,\theta)=\frac{1}{2\pi i}\int_L W_k(p,\theta)r^{-p}dp,$$
$$\tau_{\theta zk}(r,\theta)=\frac{1}{2\pi i}\int_L T_{\theta zk}(p,\theta)r^{-p-1}dp \quad (5)$$
$$(k=1,2,3),$$

where the transforms of displacements and stresses are found by the following formulas:

$$W_k(p,\theta) = A_k(p)\sin p\theta + B_k(p)\cos p\theta, \quad (6)$$
$$T_{\theta zk}(p,\theta) = \mu_k\, p[A_k(p)\cos p\theta - B_k(p)\sin p\theta]$$
$$(\mu_3=\mu_2).$$

Since regularity conditions are imposed for the solution with $r \to 0$ and $r \to \infty$, the integration path L is parallel to the imaginary axis in the strip $-\delta_1 < \mathrm{Re}\, p < \delta_2$ (δ_1, $\delta_2 > 0$).

Mixed conditions (3) and (4) lead to equalities

$$T_{\theta z2}(p,\pi) = T_{\theta z3}(p,-\pi) = [T_-(p) + G_+(p)]\varepsilon^{p+1}, \quad (7)$$
$$-p[W_2(p,\pi) - W_3(p,-\pi)] = U_+(p)\varepsilon^p,$$

where

$$T_-(p)=\int_1^\infty \tau(\varepsilon\rho)\rho^p d\rho,\ G_+(p)=\int_0^1 g(\varepsilon\rho)\rho^p d\rho, \quad (8)$$
$$U_+(p)=\int_0^1 \frac{\partial}{\partial\rho}\left[w_2(\varepsilon\rho,\pi)-w_3(\varepsilon\rho,-\pi)\right]\rho^p d\rho.$$

The function $T_-(p)$ is regular and has no zeroes in the half-plane Ω_- to the left of the path L and the functions $G_+(p)$ and $U_+(p)$ have no zeroes in the right half-plane Ω_+ [16].

Substituting expressions (6) into the left-hand sides of equalities (7) and conditions (2) modified by the Melling transform, after eliminating the quantities $A_k(p)$ and $B_k(p)$, we obtain the scalar Wiener–Hopf equation:

$$F(p)[T_-(p)+G_+(p)]+\frac{\mu_2}{2\varepsilon}U_+(p)=0\ (p\in L). \quad (9)$$

Here, the imaginary axis can be taken as the path L, while the function $F(p)$ has the form

$$F(p) = f(p)/\Delta(p), \quad (10)$$
$$f(p) = 2[\sin^2\pi p - m^2\sin^2(\pi-\alpha)p], \quad (11)$$
$$\Delta(p) = \sin 2\pi p + 2m\sin\alpha p\cos 2\beta p - m^2\sin 2(\pi-\alpha)p. \quad (12)$$

The elastic properties of the composite are reproduced in these formulas through a single bielastic constant

$$m = (\mu_1-\mu_2)/(\mu_1+\mu_2) = (\mu-1)/(\mu+1),$$

where $\mu = \mu_1/\mu_2$ is the relative hardness of the inclusion ($0 \le \mu < \infty$).

This quantity satisfies the inequality $|m| \le 1$ for all combinations of shear moduli of materials. If the inclusion material is harder than the matrix material, then $0 < m < 1$; otherwise (for a soft inclusion), this parameter lies in the interval $-1 < m < 0$. The value $m = 0$ corresponds to a homogeneous medium, and the values $m = \pm 1$ correspond to an absolutely hard inclusion and a wedge-shaped notch.

Notice that the zeroes of function (11) are eigenvalues of the anti-plane problem for an interface between two wedge-shaped regions with symmetric and antisymmetric (with respect to the ray $\theta = 0$) stress distributions. The zeroes of function (12) determine the characteristics of the stress singularity at the tip of a semi-infinite crack terminating at an elastic wedge-shaped inclusion [6].

Solution of the Wiener–Hopf equation

Factorization of the coefficient of Eq. (9) is carried out similarly to the procedure in [15]:

$$F(p)=pF_+(p)F_-^{-1}(p), \quad (13)$$

$$F_{\pm}(p)=\Phi_{\pm}(p)X_{\pm}^{-1}(p),$$

$$X_{\pm}(p)=\left[\frac{\Gamma(1+p)}{\Gamma(1/2+p)}\right]^{\pm 1},$$

$$\Phi_{\pm}(p)=\exp\left[-\frac{1}{2\pi i}\int_L \frac{\ln\Phi(t)}{t-p}dt\right]$$

$$(p\notin L),$$

where

$$\Phi(p) = [1- m^2 \sin^2 (\pi - \alpha)\, p \sin^{-2}\pi p]\times$$
$$\times[2 + 1m \sin \alpha p \cos 2\beta p \sin^{-1} 2\pi p$$
$$- m^2 \sin 2(\pi - \alpha)p \sin^{-1} 2\pi p]^{-1},$$

and $\Gamma(p)$ is the gamma function.

From here, using formulas (13) and applying the Liouville theorem [16] from Eq. (9), taking into account the behavior of the terms at infinity, we obtain:

$$\Phi_{-}^{-1}(p)X_{-}(p)T_{-}(p)+Q_{=}(p)=$$
$$=-\frac{\mu_2}{2\varepsilon p}U_{+}(p)\Phi_{+}^{-1}(p)X_{+}(p)-Q_{+}(p)=0, \quad (14)$$

where

$$Q_{\pm}(p)=\mp\frac{1}{2\pi i}\int_L \frac{Q(t)}{t-p}dt,$$
$$Q(t)=\frac{1}{t}X_{+}(t)\Phi_{+}^{-1}(t)F(t)G_{+}(t). \quad (15)$$

Then we find from Eqs. (14)

$$T_{-}(p)=-\Phi_{-}(p)X_{-}^{-1}(p)Q_{-}(p). \quad (16)$$

Given that, with $p\to\infty$,

$$X_{-}(p)\sim\frac{1}{\sqrt{-p}},\ Q_{-}(p)\sim-\frac{C}{p},$$
$$C=\frac{1}{2\pi i}\int_L \frac{X_{+}(t)G_{+}(t)}{t\Phi_{+}(t)}F(t)dt, \quad (17)$$

we obtain the asymptote

$$T_{-}(p)\sim -C\big/(i\sqrt{p}).$$

Then, by the Abel-type theorem [16], we conclude that the stress asymptote at $r\to\varepsilon+0$ has the form

$$\tau(r)\sim-\frac{C}{i\sqrt{\pi(1-\rho)}}=C\sqrt{\frac{\varepsilon}{\pi}}\frac{1}{\sqrt{r-\varepsilon}}. \quad (18)$$

Stress intensity factor

Let us find the stress intensity factor (SIF) at the crack tip $r=\varepsilon$ by the formula

$$K_{\mathrm{III}}=\lim_{r\to\varepsilon+0}\sqrt{2\pi(r-\varepsilon)\tau(r)}.$$

Then, using asymptote (16), we obtain that

$$K_{\mathrm{III}}(\alpha,\beta,m,\varepsilon)=\sqrt{2\varepsilon}C. \quad (19)$$

Let self-balanced concentrated forces T_0 be applied to the edges of the crack at a distance r_0 from the top of the interface, i.e.,

$$g(r) = T_0\delta(r - r_0),$$

where $\delta(r)$ is the Dirac delta function, and $\varepsilon < r_0 < \infty$.

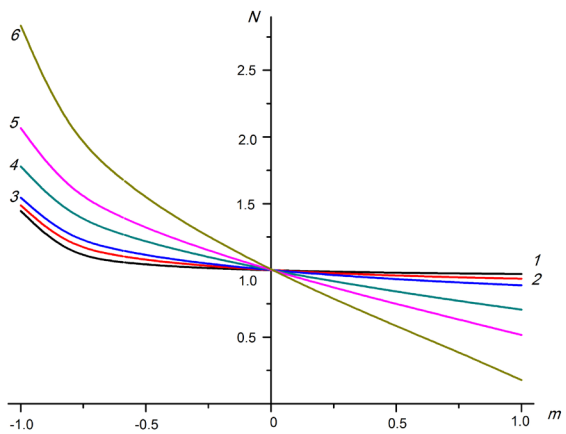

Fig. 2. Normalized stress intensity factor (NSIF) as function of parameter m at $\beta = 0$ and $r_0/\varepsilon = 0.5$ for different angles α: $\pi/4$ (*1*); $\pi/2$, $3\pi/2$ (*2*); $3\pi/4$, $5\pi/4$, $7\pi/4$ (*3*)

Then, calculating the function $G_+(t)$ by formula (8), combining the integration path with the imaginary axis in formula (17) and using the residue theorem in the region Ω_+, we obtain, according to equality (19):

$$K_{\text{III}} = -T_0\sqrt{\frac{2}{\varepsilon}}\sum_{k=1}^{n}\frac{X_+(p_k)f(p_k)}{p_k\Phi_+(p_k)\Delta'(p_k)}\left(\frac{r_0}{\varepsilon}\right)^{p_k}. \quad (20)$$

Here the prime denotes the derivative with respect to the variable p, and p_k are positive zeroes of function (12).

In case of a geometrically symmetric structure, with $\beta = 0$, series (20) is summed for some values of the bielastic constant m, and the expressions for SIF can be represented in a simple closed form. They have the following form for different cases:

$$K_{\text{III}}^0 = T_0\sqrt{\frac{2}{\pi\varepsilon}}\sqrt{\frac{r_0/\varepsilon}{1-r_0/\varepsilon}} \quad (21)$$

for a crack in a homogeneous medium ($m = 0$);

$$K_{\text{III}}^S = T_0\sqrt{\frac{2}{\pi\varepsilon a}}\frac{1}{\sqrt{1-(r_0/\varepsilon)^{1/a}}}$$

for a crack emanating from the tip of a notch ($\beta = 0$, $m = -1$);

$$K_{\text{III}}^H = T_0\sqrt{\frac{2}{\pi\varepsilon a}}\sqrt{\frac{(r_0/\varepsilon)^{1/a}}{1-(r_0/\varepsilon)^{1/a}}}$$

for a crack emanating from the vertex of an absolutely hard inclusion ($\beta = 0$, $m = 1$).

In these formulas,

$$a = 1 - \alpha/(2\pi),\ r_0/\varepsilon < 1.$$

Using formulas (20) and (21), let us introduce the normalized stress intensity factor (NSIF), which describes the variation of the SIF in a heterogeneous composite compared to the SIF at the tip of a similar crack in a homogeneous medium:

$$N = \frac{K_{\text{III}}}{K_{\text{III}}^0} = -\sqrt{\pi\left(1-\frac{r_0}{\varepsilon}\right)}\times \\ \times\sum_{k=1}^{n}\frac{X_+(p_k)f(p_k)}{p_k\Phi_+(p_k)\Delta'(p_k)}\left(\frac{r_0}{\varepsilon}\right)^{p_k-0.5}. \quad (22)$$

Roots of the characteristic equation

$$\Delta(p) = 0, \quad (23)$$

located in the strip $0 < \text{Re}\, p < 1$, were analyzed in detail in [6]. It was established that, depending on the parameters of the composite α, β and m, Eq. (23) can either have one root $p_1 < 0.5$ or $p_1 > 0.5$ in this strip, as well as two roots:

$$0 < p_1 < 0.5 < p_2 < 1,$$

or

$$0.5 < p_1 < p_2 < 1.$$

The characteristic equation in case of a symmetrical structure ($\beta = 0$) takes the form

$$\Delta_*(p) = \cos \pi p + m \cos(\pi - \alpha)\, p = 0$$

and has a single root in the interval (0, 1).

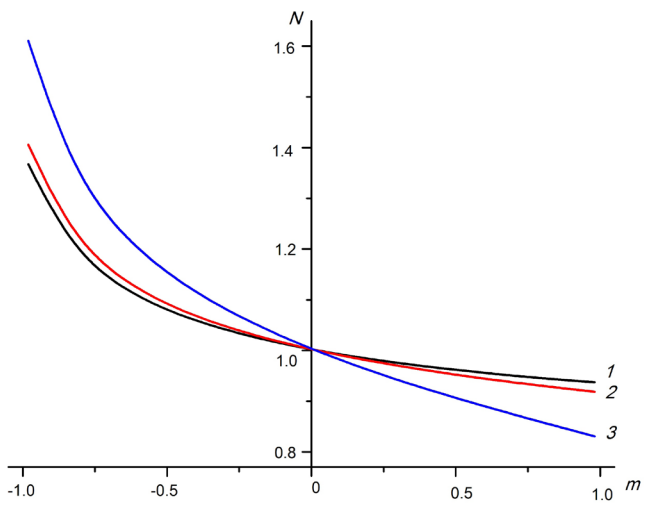

Fig. 3. NSIF as function of parameter m with $\alpha = \pi/2$ and $r_0/\varepsilon = 0.5$ for different angles β: 0 (*1*), $\pi/4$ (*2*), $\pi/2$ (*3*)

This root is larger than 0.5 with $m > 0$, and lies in the interval $0 < p_1 < 0.5$ with $m < 0$.

In this case, the NSIF exhibits a typical behavior depending on the parameter m at different values of the angle α and is a monotonically decreasing function over the entire variation range of the bielastic constant (Fig. 2). At the same time, an increase in NSIF compared with a homogeneous medium is observed if a crack is located in a harder material, when $\mu_2 > \mu_1$ and, therefore, $m < 0$. In contrast, there is a decrease in NSIF for a crack located in a relatively softer material ($m > 0$). These effects become more pronounced as the vertex angle α of the region Ω_1 increases. It follows then that a "symmetric" crack emanating from the top of the interface always propagates in a relatively harder medium.

The behavior of NSIF is less unambiguous in case of an asymmetric structure ($\beta \neq 0$). If the dimensionless parameter r_0/ε (characterizing how close to the top the load is applied) is not too small, then NSIF at the crack tip has a qualitatively similar behavior as in the symmetric case. Fig. 3 shows the variation of NSIF for the angle $\alpha = \pi/2$ and $r_0/\varepsilon = 0.5$ depending on m for different values of the asymmetry parameter β. These data indicate that the effects increasing and decreasing the NSIF intensify with increasing angle β.

However, when $r_0/\varepsilon \to 0$, the dominant term of series (22) is its first term. NSIF asymptote in this case takes the form

$$N \sim -\sqrt{\pi\left(1-\frac{r_0}{\varepsilon}\right)}\frac{X_+(p_1)f(p_1)}{p_1\Phi_+(p_1)\Delta'(p_1)}\left(\frac{r_0}{\varepsilon}\right)^{p_1-0.5}. \quad (24)$$

It follows then that if $p_1 > 0.5$ and $r_0/\varepsilon << 1$, then $(r_0/\varepsilon)^{p1-0.5} < 1$, $(r_0/\varepsilon)^{p1-0.5} > 1$, this leads to a decrease in NSIF. If $p_1 < 0.5$, then, for small values of the relative distance r_0/ε in expression (24), the factor $(r_0/\varepsilon)^{p1-0.5} > 1$, which leads to a decrease in NSIF.

An example of increasing NCIN for small r_0/ε is shown in Fig. 4 for the case $\alpha = \beta = \pi/2$. The first root of Eq. (23) is less than 0.5 with these values of the angles, both if $m < 0$ and if $m > 0$ [6, 15]. Analysis of the behavior of the curves indicates that the dependence $N(m)$ is not monotonous. The increase in NSIF becomes more pronounced with a decrease in the distance r_0/ε. Besides, if the crack is located in a softer medium, the SIF values may exceed those for a similar crack located in a homogeneous medium with a sufficiently small ratio r_0/ε, due to the influence of heterogeneity and geometry of the structure (as opposed to the symmetric case).

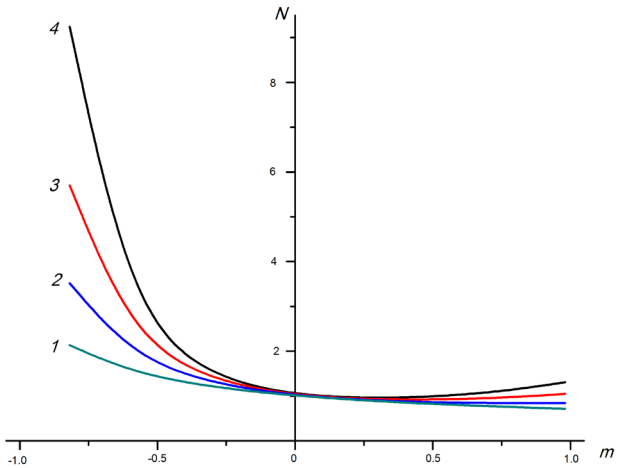

Fig. 4. NSIF as function of parameter m with $\alpha = \beta = \pi/2$ for small relative distance r_0/ε: 0.1 (*1*); 0.01 (*2*); 0.001 (*3*); 0.0001(*4*)

Stress singularity at the top of the interface between the wedges

Based on Eqs. (6)–(8), it is easy to obtain representations for the stresses in the regions Ω_j (j = 1, 2, 3):

$$\tau_{\theta zj}(r,\theta)=\frac{1}{\pi i}\int_L \frac{\tau_j(p,\theta)}{\Delta(p)}\left[T_-(p)+ +G_+(p)\right]\left(\frac{r}{\varepsilon}\right)^{-p-1}dp, \quad (25)$$

where

$$\tau_j(p,\theta) = a_j(p)\cos p\theta - b_j(p)\sin p\theta;$$

$$a_1(p) = (1+m)[\sin p\pi - m\cos 2p\beta \sin p(\pi-\alpha)];$$

$$b_1(p) = (1+m)m\sin 2p\beta \sin p(\pi-\alpha);$$

$$a_n(p) = \sin p\pi + m\sin p\alpha \cos[p(\pi + + (-1)^n 2\beta)] - m^2 \cos p\alpha \sin p(\pi-\alpha);$$

$$b_n = (-1)^n m \sin p\alpha\{\sin p(\pi-\alpha) - - \sin[p(\pi+(-1)^n 2\beta]\} \ (n = 2, 3).$$

Substituting representations (15), (16) into integrand (25) and given that the transform of the concentrated load at the edges of the crack has the form

$$G_+(p) = T_0/\varepsilon(r_0/\varepsilon)^p,$$

we obtain the following expression for stresses:

$$\tau_{\theta zj}(r,\theta)=\frac{T_0}{\varepsilon\pi i}\int_L \frac{\tau_j(p,\theta)}{\Delta(p)}\left[\left(\frac{r_0}{\varepsilon}\right)^p - -\frac{\Phi_-(p)}{X_-(p)}Q_-^*(p)\right]\left(\frac{r}{\varepsilon}\right)^{-p-1}dp, \quad (26)$$

where

$$Q_-^*(p)=\frac{1}{2\pi i}\int_L \frac{F(t)}{t(t-p)}\frac{X_+(p)}{\Phi_+(p)}\left(\frac{r_0}{\varepsilon}\right)^t dt.$$

By applying the theorem of the residues (calculated by the zero roots p_k of function (12) located in the left half-plane of the path L) to integral (26) we obtain with $r < r_0$:

$$\tau_{\theta zj}(r,\theta)=\frac{2T_0}{r_0}\left[\sum_{k=1}^{\infty}\frac{\tau_j(-p_k,\theta)}{\Delta'(-p_k)}\left(\frac{r}{r_0}\right)^{p_k-1} - -\frac{r_0}{\varepsilon}\sum_{k=0}^{\infty}\frac{\tau_j(-p_k,\theta)}{\Delta'(-p_k)}\frac{\Phi_-(-p_k)}{X_-(-p_k)}\times \times Q_-^*(-p_k)\left(\frac{r}{\varepsilon}\right)^{p_k-1}\right]. \quad (27)$$

Notably, the first sum in this formula determines the stress distribution in case of a semi-infinite crack emanating from the top of a closed interface between the wedges [6]. The second sum is due to finite length of the given crack.

It follows from representation (27) that the stresses at the top of the interface have a singularity described by the power law. Depending on the structure parameters, the asymptotic behavior of stresses with $r \to 0$ can have one or two singular terms, determined by the roots of Eq. (23), located in the interval (0, 1). The singularity exponents $\lambda_k = 1 - p_k$ (k = 1, 2) can be both larger and smaller than 0.5 and, therefore, generate both strong and weak singularities at this point.

Conclusion

We have obtained an exact solution for the problem of an anti-plane crack emanating from a closed interface between two wedge-shaped regions based on the Mellin integral transform and the Wiener–Hopf method. We have analyzed the behavior of the stress intensity factor (SIF) at the tip of a crack upon variation of elastic properties and geometry of the structure, which can lead to an increase or decrease in SIF, compared with a homogeneous medium. We have observed a dependence of SIF on the relative hardness of the materials that is not characteristic for the symmetric case in the absence of geometric symmetry of the structure, for some values of the composite parameters and a concentrated load applied at a sufficiently small distance from the top of the interface. In particular, the SIF for a crack located in a relatively softer material may exceed the SIF for a similar crack in a homogeneous medium. Examining the stress singularity at the corner point of the interface, we have confirmed that this singularity can be both strong and weak.

REFERENCES

1. **Williams M.,** Stress singularities resulting from various boundary conditions in angular corners of plates in extension, Trans. ASME, Ser. E, J. Appl. Mech., 74 (4) (1952) 526–528.

2. **Bogy D.B.,** Two edge-bonded elastic wedges of different materials wedge angles under surface tractions, Trans. ASME, Ser. E, J. Appl. Mech. 38 (2) (1971) 377–386.

3. **Schovanec L.,** A mode III crack problem in a bonded composite material, Eng. Fract. Mech. 31 (3) (1988) 437–449.

4. **Pageau S.S., Joseph P.F., Biggers S.B.,** Singular antiplane stress fields for bonded and disbanded three-material junctions, Eng. Fract. Mech. 52 (5) (1995) 821–832.

5. **Misuris G., Kuhn G.,** Comparative study of an interface crack for different wedge-interface models, Archive Appl. Mech. 71 (11) (2001) 764–780.

6. **Tikhomirov V.V.,** Longitudinal shear crack terminating at a wedge-shaped elastic inclusion, St. Petersburg Polytechnical University Journal. Physics and Mathematics. (2(194)) (2014) 110–119.

7. **Linkov A., Rybarska-Rusinek L.,** Evaluation of stress concentration in multi-wedge systems with functionally graded wedges, Int. J. Eng. Sci. 61 (1) (2012) 87– 93.

8. **Beom H.G., Jang H.S.,** A wedge crack in an anisotropic material under antiplane shear, Int. J. Eng. Sci. 49 (9) (2011) 869–880.

9. **Beom H.G., Jang H.S.,** Interfacial wedge cracks in dissimilar anisotropic materials under antiplane shear, Int. J. Eng. Sci. 56 (1) (2012) 49–62.

10. **Beom H.G., Jang H.S.,** A crack emanating from a wedge in dissimilar anisotropic materials under antiplane shear, Int. J. Fract. 177 (2) (2012) 191–198.

11. **Shen M.H., Lin C.P., Hung S.Y.,** Edge crack in front of anisotropic wedge interacting with anti-plane singularity, Theor. Appl. Fract. Mech. 58 (1) (2012) 1–8.

12. **Trefi M., Oyadiji O.,** Strain energy approach to compute stress intensity factors for isotropic homogeneous and bimaterial V-notches, Int. J. Solids Struct. 50 (14–15) (2013) 2196–2212.

13. **Tikhomirov V.V.,** Sharp V-notch fracture criteria under antiplane deformation, St. Petersburg Polytechnical University Journal. Physics and Mathematics. 11 (3) (2018) 99–107.

14. **Carpinteri A., Cornetti P., Pugno N., Sapora A.,** On the most dangerous V-notch, Int. J. Solids Struct. 47 (7–8) (2010) 887–893.

15. **Tikhomirov V.V.,** Mode III crack approaching to the wedge-shaped elastic inclusion, St. Petersburg Polytechnical University Journal. Physics and Mathematics. 10 (2) (2017) 99–109.

16. **Noble B.,** Method based on the Wiener – Hopf technique for solution of partial differential equations, Pergamon Press, Oxford, 1958.

Received 15.03.2019, accepted 19.03.2019.

THE AUTHOR

TIKHOMIROV Victor V.
Peter the Great St. Petersburg Polytechnic University
29 Politechnicheskaya St., St. Petersburg, 195251, Russian Federation
victikh@mail.ru

СПИСОК ЛИТЕРАТУРЫ

1. **Williams M**. Stress singularities resulting from various boundary conditions in angular corners of plates in extension // Trans. ASME. Ser. E. J. Appl. Mech. 1952. Vol. 74. No. 4. Pp. 526–528.

2. **Bogy D.B.** Two edge-bonded elastic wedges of different materials wedge angles under surface tractions // Trans. ASME. Ser. E. J. Appl. Mech. 1971. Vol. 38. No. 2. Pp. 377–386.

3. **Schovanec L.** A mode III crack problem in a bonded composite material // Eng. Fract. Mech. 1988. Vol. 31. No. 3. Pp. 437–449.

4. **Pageau S.S., Joseph P.F., Biggers S.B.** Singular antiplane stress fields for bonded and disbanded three-material junctions // Eng. Fract. Mech. 1995. Vol. 52. No. 5. Pp. 821–832.

5. **Misuris G., Kuhn G.** Comparative study of

an interface crack for different wedge-interface models // Archive Appl. Mech. 2001. Vol. 71. No. 11. Pp. 764–780.

6. **Тихомиров В.В.** Трещина продольного сдвига, упирающаяся в клиновидное упругое включение // Научно-технические ведомости СПбПУ. Физико-математические науки. 2014. № 2 (194). С. 110 – 119.

7. **Linkov A., Rybarska-Rusinek L.** Evaluation of stress concentration in multi-wedge systems with functionally graded wedges // Int. J. Eng. Sci. 2012. Vol. 61. No. 1. Pp. 87– 93.

8. **Beom H.G., Jang H.S**. A wedge crack in an anisotropic material under antiplane shear // Int. J. Eng. Sci. 2011. Vol. 49. No. 9. Pp. 869–880.

9. **Beom H.G., Jang H.S.** Interfacial wedge cracks in dissimilar anisotropic materials under antiplane shear // Int. J. Eng. Sci. 2012. Vol. 56. No. 1. Pp. 49–62.

10. **Beom H.G., Jang H.S.** A crack emanating from a wedge in dissimilar anisotropic materials under antiplane shear // Int. J. Fract. 2012. Vol. 177. No. 2. Pp. 191–198.

11. **Shen M.H., Lin C.P., Hung S.Y.** Edge crack in front of anisotropic wedge interacting with anti-plane singularity // Theor. Appl. Fract. Mech. 2012. Vol. 58. No. 1. Pp. 1–8.

12. **Trefi M., Oyadiji O.** Strain energy approach to compute stress intensity factors for isotropic homogeneous and bimaterial V-notches // Int. J. Solids Struct. 2013. Vol. 50. No. 14–15. Pp. 2196– 2212.

13. **Тихомиров В.В.** Критерии разрушения острого выреза в условиях антиплоской деформации // Научно-технические ведомости СПбПУ. Физико-математические науки. 2018. Т. 11. № 3. С. 99–107.

14. **Carpinteri A., Cornetti P., Pugno N., Sapora A.** On the most dangerous V-notch // Int. J. Solids Struct. 2010. Vol. 47. No. 7–8. Pp. 887–893.

15. **Тихомиров В.В.** Трещина моды III, приближающаяся к упругому клиновидному включению // Научно-технические ведомости СПбПУ. Физико-математические науки. 2017. Т. 10. № 2. С. 99–109.

16. **Noble B.** Method based on the Wiener–Hopf technique for solution of partial differential equations. Oxford: Pergamon Press, 1958.

Статья поступила в редакцию 15.03.2019, принята к публикации 19.03.2019.

СВЕДЕНИЯ ОБ АВТОРЕ

ТИХОМИРОВ Виктор Васильевич – *кандидат физико-математических наук, заместитель директора по образовательной деятельности Санкт-Петербургского политехнического университета Петра Великого.*

195251, Российская Федерация, г. Санкт-Петербург, Политехническая ул., 29
victikh@mail.ru